

Abstract

Title of Dissertation/Thesis: Core/Shell and Alloy Nanoparticles of
Transition Metals for Heterogeneous Catalysis:
Bridging the Gap between Experiment and Theory

Selim Alayoglu, Doctor of Philosophy, 2009

Thesis Directed By: Professor Bryan W. Eichhorn
Department of Chemistry and Biochemistry

This thesis describes the structural and catalytic properties of the architecturally-controlled bimetallic nanoparticles (NPs) of transition metals. In this study, bimetallic nanoparticles with well-defined architectures were synthesized, characterized and evaluated toward various heterogeneous reactions. Random alloy nanoparticles were compared to the core/shell nanoparticles ($M@M'$ NPs where M is the core metal and M' is the shell metal), which is the synthetic counterpart of the theoretically well-studied Near Surface Alloys (NSAs). Thus, the long existing experimental gap with the theory can be bridged via the systematic evaluation of such architecturally-controlled bimetallic NPs.

The $M@Pt$ ($M=Ru, Rh, Ir, Pd$ and Au) and $Ru@M'$ ($M'=Rh$ and Pd) core/shell NPs of tunable core sizes and shell thicknesses, and the PtRu alloy and PtRh alloy NPs of various compositions were prepared via poly-ol reduction reactions by using sequential deposition techniques. Seed NPs for the core/shell systems were synthesized via either poly-ol or $NaBH_4$ reduction reactions. The wet-chemical co-deposition technique was employed to synthesize the alloy NPs.

The core/shell and alloy NPs were characterized by using a combination of TEM, STEM-EDS, XRD, and FT-IR and Micro Raman -CO probe experiments. Full structural analysis employing techniques such as Extended X-Ray Absorption Fine

Structure (EXAFS) and atomic Pair Distribution Function (PDF) was also performed for the 4.1 nm Ru@Pt NPs comprising of 3.0 nm cores and 1-2 MLs thick shells and the 4.4 nm Pt₅₀Ru₅₀ alloy NPs. Through collaborations, the nanoparticle structures were also modeled through EXAFS analyses, PDF fits, Rietveld Refinements and Debye Function simulations.

The well-characterized core/shell and alloy NPs were evaluated for preferential oxidation of CO in H₂ feeds (PROX). Catalytically, the core/shell NPs were superior to their alloy counterparts with similar particle sizes and identical compositions. The PROX reactivities of the M@Pt (M=Ru, Rh, Ir, Pd and Au) core/shell NPs increased in the order of Au@Pt < Pd@Pt < Ir@Pt < Rh@Pt < Ru@Pt, which is predicted by the NSA theory. Density Functional Theory (DFT) calculations performed by Prof. Mavrikakis at the University of Wisconsin helped elucidate the thermo-chemistry beyond the enhanced PROX activities and the observed surface reactivity trends for the core/shell architectures. The decreased equilibrium surface coverage of CO as well as the new H₂-assisted O₂ dissociation pathway on the electronically-altered Pt shells were suggested to bring on the room temperature CO oxidation and the subsequent H₂ activation with enhanced PROX selectivity.

The surface reactivities toward PROX and benzene hydrogenation reactions of the composition series of the PtRu alloy NPs exhibited the 'Volcano' behavior, which invoked the Hammer-Norskov theory. The preliminary benzene hydrogenation results on the Ru@Pt NPs system presented in this study also showed a structure dependent correlation in surface activity.

Core/Shell & Alloy Nanoparticles of Transition Metals for Heterogeneous Catalysis:
Bridging the Gap between Experiment and Theory

By

Selim Alayoglu

Dissertation submitted to the Faculty of the Graduate School of the
University of Maryland, College Park, in partial fulfillment
of the requirements for the degree of
Doctor of Philosophy

2009

Advisory Committee:
Professor Bryan W. Eichhorn, Chair
Professor Robert Walker
Professor Lawrence R. Sita
Professor Michael Zachariah
Associate Professor Gregory Jackson

© Copyright by Selim Alayoglu 2009

Dedication

In memory of my grandmother Nebahat Alayoglu and Grandfather Sabahattin Doras, always be remembered. To my loving wife, Pinar Damla Alayoglu, and to my family, for always standing by me.

Acknowledgements

I would like to express my thanks to Prof. Eichhorn for his guidance, support and suggestions he has given me and the valuable discussions we have been through throughout my research. I have been greatly inspired by his approach to scientific problems and way of problem-solving. It was a great honor working with him for these many years.

I would like to thank Prof. Greg Jackson and Dr. Seyed-Abdolreza Seyed-Reihani for their helps in operating the catalysis rig, and Prof. Robert Walker for the valuable discussions on spectroscopy-related subjects. I am indebted to Prof. Mavrikakis and Dr. Anand Nilekar for performing the DFT calculations and helping elucidate the PROX chemistry on core/shell NPs which were in the heart of my Ph.D. research. The discussions with Prof. Mavrikakis were very helpful in understanding the chemistry related to my work. I am also grateful to Dumesic Group members, Dr. Edward Kunkes and Mr Mark Tucker for collecting the chemisorption and benzene hydrogenation reaction data.

I would like to thank to Dr. Peter Zavalij for his valuable suggestions in performing Rietveld fits, generating model clusters that I used in PDF fits and all the crystallographic and structural background he provided with me. I also would like to thank to Prof. Anatoly Frenkel and Dr. Qi Wang for collecting and fitting the EXAFS data, Dr. Peter Chupas for collecting the PDF data, and Dr. Bryan Toby for collecting the Synchrotron XRD data. I am also grateful to Dr. Wen-an Chiou and his assistant Larry Lai in the UMD Nanocenter, and Tim Miguel in the UMD Biological Ultrastructure Laboratory for giving me the instructions and TEM training upon which I have built my

growing knowledge of electron microscopy. Here, I would like to express my enormous appreciation to Larry Lai for helping me collecting the STEM-EDS data. Thanks to Dr. Bindu Varughese for helping me collecting and analyzing the XPS data.

To my past and present lab mates and friends, I want to bestow a tremendous amount of gratitude. To those I have worked with, Dr. Melanie Moses, Dr. Chad Stoltz, Dr. Emren Nalbant-Esenturk, Dr. Shenghu Zhou, Dr. Oktay Demircan, Dr. Mary Sukeshini, Sanem Kocak, Tony Dylla, Jordan Halsig, Dr. Zhufang Liu and Dr. Chunjuan Zhang, Pavan Bellamkonda, Domonique Downing, Dr. Suleyman Can, Dr. Albert Ephystein, Dr. Okan Esenturk, thanks for helping me carry this heavy burden, called being a graduate student; and thanks for making life memorable for me during my time here at the University of Maryland.

To my beloved family, Sinan Alayoglu, Sibel Alayoglu, Selin Sarac, Serkan Sinik and Sertan Sinik, and friends, Gokhan Metan, Demet Metan, Arda Diker, Alper Bircan, Gokhan Arikan, Taner Ozel, Oktay Demircan and Suleyman Can to whom I owe my personality, without your support and understanding you provided with me throughout my life, I would not be the person who I am today.

To my loving wife, Pinar Damla Alayoglu, to whom this work is dedicated, words possibly can not begin to describe what it means to have you in my life. Without your eternal love in my heart and your never-ending support to free my mind off the obstacles to my path, it would not be possible writing this thesis.

Table of Contents

Dedication	i
Acknowledgements	ii
Table of Contents	iv
List of Tables	xi
List of Figures	xii
List of Schemes	xxxiii
List of Abbreviations	xxxiv
Chapter 1	1
Introduction	1
1.1. Introduction.....	1
1.2. Metal Nanoparticles.....	4
1.3. Multi-metallic Nanoparticles.....	9
1.3.1. Bimetal nanoparticle architectures.....	10
1.3.2. Thermodynamics and kinetics of formation and stability.....	13
1.3.3. Magic Numbers for size and composition control.....	18
1.3.4. Synthesis of Bimetallic NPs.....	20
1.3.5. Characterization of Bimetallic NPs.....	25
1.3.5.1. X-rays for bulk structural/chemical analysis.....	26
1.3.5.2. Infrared surface probe studies.....	32
1.3.5.3. Electron Microscopy for single (multi) particle analysis.....	33
1.4. Importance and applications.....	35
1.5. Overview of the Thesis.....	41

Chapter 2.....	43
Synthesis and characterization of nano-structured Ru-Pt bimetallic particles for heterogeneous catalysis.....	43
2.1. Introduction.....	43
2.2. Experimental.....	49
2.2.1. Materials.....	49
2.2.2. Sample characterization of the proposed nanostructures.....	50
2.2.2.1. Powder X-ray Diffraction.....	50
2.2.2.2. Powder X-Ray Diffraction simulations by Debye Function (DF).....	50
2.2.2.3. Powder X-Ray Diffraction Refinements.....	53
2.2.2.4. Atomic Pair Distribution Function Analysis.....	53
2.2.2.5. Extended X-Ray Absorption Fine Structure (EXAFS) and X-Ray Absorption Near Edge Structure Studies (XANES).....	55
2.2.2.6. X-Ray Photoelectron Spectroscopy.....	56
2.2.2.7. Fourier Transformed-Infrared Spectroscopy.....	56
2.2.2.8. Micro-Raman Spectroscopy.....	57
2.2.2.9. Transmission Electron Microscopy.....	57
2.2.2.10. Scanning Transmission Electron Microscopy (STEM) and Energy Dispersive Spectroscopy (EDS).....	58
2.2.3. Evaluation for heterogeneous catalysis.....	58
2.2.3.1. Catalytic evaluation for PROX reaction.....	58
2.2.3.2. Catalytic evaluation for Rich/Lean NO _x reduction.....	59
2.2.3.3. Catalytic evaluation for benzene hydrogenation.....	60

2.2.3.4. Density Functional Theory (DFT) calculations	61
2.2.4. Synthesis of bimetallic Ru-Pt NPs with various architectures.....	61
2.2.5.1. Synthesis of Ru@Pt core/shell NPs with various core sizes and shell thicknesses	64
3.2.5.2. Synthesis of PVP free Ru@Pt core/shell NPs	65
3.2.5.3. Synthesis of Pt _x Ru _{1-x} (x=0,1).....	65
2.3. Results.....	66
2.3.1. Synthesis of Ru@Pt core/shell and Pt _x Ru _{1-x} alloys NPs with or without PVP66	
2.3.2. Size, shape and distribution by Transition Electron Microscopy	69
2.3.3. Composition and architecture by Scanning Transition Electron Microscopy	76
2.3.4. Structure evaluation of core/shell and alloys NPs by X-rays	79
2.3.4.1. Powder X-ray Diffraction	79
2.3.4.2. Extended X-Ray Absorption Fine Structure (EXAFS) and.....	88
X-Ray Absorption Near Edge Structure (XANES) Studies	88
2.3.4.3. Atomic Pair Distribution Function Analysis.....	100
2.3.5. Chemical analysis by X-Ray Photoelectron Spectroscopy.....	109
2.3.6. Surface probing by CO-sorption.....	111
2.3.6.1. Fourier Transformed-Infrared Spectroscopy measurements	111
2.3.6.2. Micro-Raman measurements	117
2.3.7. Catalytic evaluation of the bimetallic Pt/Ru NPs	118
2.3.7.1. Preferential Oxidation (PROX) of CO.....	118
2.3.7.1.1. Experiment.....	118
2.3.7.1.2. Density Functional Theory (DFT) calculations	127

2.3.7.2. NO _x Reduction	132
2.3.7.3. Benzene Hydrogenation.....	136
2.4. Discussions	142
Chapter 3.....	151
Synthesis and characterization of nano-structured Rh-Pt bimetallic particles for PROX reaction.....	151
3.1. Introduction.....	151
3.2. Experimental	154
3.2.1. Materials	154
3.2.2. Sample characterization of the proposed nanostructures.....	154
3.2.2.1. Powder X-ray Diffraction	155
3.2.2.2. Debye Function Simulations.....	155
3.2.2.3. Fourier Transformed-Infrared Spectroscopy	156
3.2.2.4. Micro-Raman Spectroscopy.....	156
3.2.2.5. Transmission Electron Microscopy	157
3.2.2.6. Scanning Transmission Electron Microscopy-Energy Dispersive Spectroscopy.....	157
3.2.3. Catalytic evaluation for PROX reaction	158
3.2.4. Synthesis of bimetallic Rh-Pt NPs with various architectures.....	158
3.2.4.1. Synthesis of Rh@Pt core/shell NPs with various core sizes and shell thicknesses	160
3.2.4.2. Synthesis of PVP free Rh@Pt core/shell NPs	162
3.2.4.3. Synthesis of Pt _x Rh _{1-x} (x=0,1).....	162

3.2.5. Preparation of γ -Al ₂ O ₃ supported catalysts.....	162
3.3. Results.....	163
3.3.1. Synthesis of Rh@Pt core/shell and Pt _x Rh _{1-x} alloys NPs with or without PVP	163
3.3.2. Size, shape and distribution by Transition Electron Microscopy	165
3.3.3. Composition and architecture by Scanning Transition Electron Microscopy	171
3.3.4. Surface-adsorbed CO probing by FT-IR.....	173
3.3.5. Micro Raman for surface probing.....	178
3.3.6. Structure by XRD	179
3.3.7. Catalytic Evaluation of supported Pt/Rh bimetallic catalysts in PROX/CO oxidation	184
3.4. Discussion	189
Chapter 4.....	193
Synthesis and characterization of other M@Pt (M=Ir, Pd and Au) and Ru@M' (M'=Pd and Rh) core/shell NPs and their distinguishing PROX properties	193
4.1. Introduction.....	193
4.2. Experimental	197
4.2.1. Materials	197
4.2.2. Sample Characterization	198
4.2.3. Density Functional Theory (DFT) calculations	198
4.2.4. Synthesis of M@Pt (M=Ir, Pd and Au) and Ru@M (M=Pd and Rh) core/shell NPs.....	199

4.2.4.1. Synthesis of Ir@Pt NPs	199
4.2.4.2. Synthesis of Pd@Pt NPs.....	201
4.2.4.3. Synthesis of Au@Pt NPs	202
4.2.4.4. Synthesis of Ru@Pd NPs.....	203
4.2.4.5. Synthesis of Ru@Rh NPs	204
4.2.4.6. Preparation of γ -Al ₂ O ₃ supported catalysts.....	205
4.3. Results.....	206
4.3.1. Synthesis of M@Pt (M=Ir, Pd and Au) core/shell NPs	206
4.3.2. Synthesis of Ru@M (M=Pd and Rh) core/shell NPs.....	207
4.3.3. Size and size distribution analysis by TEM.....	208
4.3.4. Composition and architecture by Scanning Transition Electron Microscopy	214
4.3.5. Structural evaluation by XRD.....	218
4.3.6. Surface-adsorbed CO probing by FT-IR.....	224
4.3.6. Micro Raman for structure analysis and surface probing	232
4.3.7. Catalytic Evaluation of supported M@Pt NP catalysts in PROX/CO oxidation	233
4.3.7.1. M@Pt NPs (M=Ru, Rh, Ir, Pd, Au).....	233
4.3.7.2. Ru@M NPs (M=Pt, Rh and Pd)	239
4.3.7.3. M@Pt@Pd NPs (M=Ru and Ir).....	245
4.3.8. Density Functional Theory (DFT) Calculations	250
4.4. Discussions	260
Chapter 5.....	269

Conclusion	269
5.1. ‘Catalysis by design’ strategy for improved catalytic properties.....	270
5.2. Architecturally-controlled Pt-free bimetallic NP catalysts	272
5.3. Structure-reactivity correlations in heterogeneous catalysis.....	273
Appendix.....	276
Chapter 4.....	276
References.....	288

List of Tables

Table 1.1. 1 st Shell coordination numbers comparing EXAFS-derived data and cluster model-calculations.	31
Table 2.1. Table showing Schmid model-derived core size, shell thickness and composition parameters of some Ru@Pt core/shell cluster series.	68
Table 2.2. Structure parameters and estimated error bars from EXAFS analysis of the Ru@Pt core/shell and Pt ₅₀ Ru ₅₀ alloy NPs.	97
Table 2.3. Coordination numbers (1 st -4 th , Pt-Pt) from EXAFS experiment vs. modeling for Ru@Pt core/shell structure.	99
Table 2.4. XPS data for the Pt/Ru system.	110
Table 2.5. Calculated PW91 binding energies of various species at ¼ ML coverage and the activation energy barriers of different elementary steps on Pt(111) and Pt*/Ru(0001).	131
Table 2.6. Benzene hydrogenation data on the Ru _x @Pt _{1-x} , Pt _{1-x} Ru _x , Pt, Ru, and the mixtures of monometallic Pt and Ru NPs catalysts.	141
Table 3.1. Comparative PROX selectivities ^a for the different Rh-Pt and the Ru@Pt core/shell ^b catalysts.	191
Table 4.1. Comparative PROX selectivities ^a for the M@Pt core/shell and monometallic Pt NP catalysts.	264
Table 4.2. Comparative PROX selectivities ^a for the Ru@M ^b core/shell NP catalyst.	267

List of Figures

Figure 1.1. TEM pictures of (a) Au NPs of various geometric shapes; cubes, triangles, hexagons, rods, etc. Representative HR-TEM pictures of the nanocrystalline (b) Au polyhedron, (c) Pt cube, and (d) Fe tetrahedron.	6
Figure 1.2. Schematic illustrations of (a) a model alloy cluster of 35 Å diameter and ~1700 atoms, (b) the radial distribution function. (c) The representative structure function of the alloy cluster depicted in (a). (d) The atomic pair distribution function calculated from (c) by using the equation 1.7 represents the atomic correlations of the alloy cluster depicted in (a).	29
Figure 2.1. TEM images of (a) Pt, (d) Ru, (g) Ru@Pt (1:1) and (k) Pt ₅₀ Ru ₅₀ NPs; (b, e, h, l) HR-TEM images, showing crystallinity and/or twinning; (c, f, i, m) particle size histograms of the NPs in (a, d, g, k), respectively. Insets show the Fast Fourier Transforms (FFTs) of the HR-TEM images.	70
Figure 2.2. TEM images of (a) 3.7 nm Ru@Pt NPs with sub-monolayer coverages of Pt shells and 4.4 nm Ru@Pt NPs with ca. 2-3 ML thick Pt shells that are synthesized using (d) as-received EG and (g) rigorously dried EG; (b, e and h) HR-TEM images given next to each TEM image, showing crystallinity and/or twinning; (c, f and i) particle size histograms of the NPs in (a, d and g), respectively.	71
Figure 2.3. TEM images of (a) sequentially grown 4.2 nm Ru NPs and (d) 4.7 nm Ru@Pt NPs with ca. 1-layer thick Pt shells; (b and e) HR-TEM images, showing twinning and nano-crystallinity; (c and f) particle size histograms of the respective NPs.	72

Figure 2.4. TEM images of (a) 5.7 nm Ru NPs, (d) 6.2 nm Ru@Pt NPs with ca. 1 ML thick Pt shells and (g) 7.6 nm Ru@Pt NPs with multiple layers of Pt shells; (b, e and h) HR-TEM images, showing nano-crystallinity and multiple twinning; (c, f and i) particle size histograms of the NPs in (a, d and g), respectively, indicating the gradual size increase. 72

Figure 2.5. TEM images of (a) 2.0 nm Pt NPs and (d) 3.0 nm Ru@Pt NPs with ca. 1-2 layers thick Pt shells; (b and e) HR-TEM images, showing Pt 111 planes; and (c and f) particle size histograms of the NPs in (a and d), respectively. 73

Figure 2.6. TEM images of (a) PVP-free Pt, (d) PVP-free Ru, and (g) PVP-free Ru@Pt (1:1) NPs; (b, e and h) HR-TEM images, showing nano-crystallinity and/or twinning; (c, f and i) particle size histograms of the NPs in (a, d and g), respectively..... 74

Figure 2.7. TEM images of (a) Pt₆₆Ru₃₄ NPs, (d) Pt₃₄Ru₆₆ NPs and (f) Pt₈₀Ru₂₀ NPs; (b) HR-TEM image of Pt₆₆Ru₃₄ indicating nano-crystallinity and 111 planes; (c, e and g) particle size histograms of the NPs in (a, d and f), respectively. Fast Fourier Transform (FFT) of the HR-TEM image in (b) is given inset..... 75

Figure 2.8. Representative STEM-EDS line spectra of (a) a 4.1 nm Ru@Pt NP with 3.0 nm Ru core and 1-2 MLs thick Pt shells, (b) a 4.2 nm PVP-free Ru@Pt NP, (c) a 4.4 nm Pt₅₀Ru₅₀ alloy nanoparticle, and (d) a 4.4 nm Ru@Pt NP with 3.0 nm Ru core and ca. 2-3 MLs thick Pt shells. Relative atomic % composition (vertical axis) of Pt (red) and Ru (blue) are plotted against the line scan probe position (horizontal axis) and are given next to STEM images. A 1.5 nm probe was used to trace 10 – 25 nm scans across each particle. The particle center is at ~ 5 nm in (a), ~ 8 nm in (b), ~7 nm in (c), and ~12 nm in (d)..... 77

Figure 2.9. A representative STEM-EDS point analysis of a 4.1 nm Ru@Pt nanoparticle with a ca. 1-2 MLs thick Pt shell, showing three spectra: one from the top edge of the particle (left), one from the center (middle), and another from the right edge (right)..... 78

Figure 2.10. A representative STEM-EDS point analysis of a 4.4 nm Pt₅₀Ru₅₀ alloy nanoparticle (also see Figure 2.8c), showing three spectra in the order given in the table: one from the center of the particle(left), one from the bottom edge (middle), and another from the right top edge (right). 78

Figure 2.11. XRD profiles comparing 4.1 nm Ru@Pt NPs and 4.4 nm Pt₅₀Ru₅₀ NPs. Blue vertical lines represent the HCP Ru phase (JC-PDS file 06-0663), and red vertical lines the FCC Pt phase (JC-PDS file 04-0802)..... 80

Figure 2.12. (a) Rietveld refinement on synchrotron data of 4.4 nm Pt₅₀Ru₅₀ NPs, and LeBail fits on molybdenum K_α data of (b) 4.4 nm Pt₅₀Ru₅₀ NPs and (c) 4.1 nm Ru@Pt NPs. The experimental data are shown by markers and the fits by solid lines. The residual patterns are given below each. 82

Figure 2.13. Debye Function simulations of the 40 Å diameter core/shell clusters with (A) a 2 MLs thick Pt shell, (B) a 1 ML thick Pt shell (B), and (C) a 50:50 mixture of 1 ML and 2 MLs thick Pt shells. Debye Function simulations of Pt-skin clusters are also shown with dashed lines below each respective core/shell cluster. XRD pattern of the 4.1 nm Ru@Pt NPs is shown in (D). JC-PDS peak positions for Pt (black) and Ru (red) are also presented..... 83

Figure 2.14. Patterns showing (A) experimental XRD from the 4.4 nm Pt₅₀Ru₅₀ NPs and (B) simulated XRD from a 44 Å diameter random alloy cluster. JC-PDS peak positions for Pt (red) are also presented. 84

Figure 2.15. XRD profiles of (a) 4.1 nm Ru@Pt NPs after anneal at 500 °C for 12 h, (b) as-synthesized Ru@Pt NPs, (c) PtRu alloy nanoparticles and (d) as-prepared mixtures of monometallic Pt NPs and Ru NPs, and (e) physical mixtures after anneal at 500 °C for 12 h. Blue vertical lines represent the HCP Ru phase (JC-PDS file 06-0663), and red vertical lines the FCC Pt phase (JC-PDS file 01-1194). 85

Figure 2.16. XRD profiles of (a) sequentially grown 4.2 nm Ru NPs and 4.7 nm Ru@Pt NPs with ca. 1 ML thick Pt shells and (b) 5.7 nm Ru NPs via the co-deposition method and 6.2 nm Ru@Pt NPs with ca. 1 ML Pt shells, showing the transient Pt deposition. Blue vertical lines represent the HCP Ru phase (JC-PDS file 06-0663), and red vertical lines the FCC Pt phase (JC-PDS file 01-1194). 86

Figure 2.17. XRD profiles of (a) Ru@Pt NPs with 3.0 nm Ru cores and varying layers of Pt shells synthesized using rigorously dried EG, showing the correlation between the intensity of Pt 111 reflection and the Pt content, and (b) Ru@Pt NPs with varying Ru core sizes and approximately 1-2 MLs thick Pt shells. JC-PDS peak positions for Pt (red) and Ru (blue) are also presented. 87

Figure 2.18. XRD profiles of the Pt_xRu_{1-x} ($x=0.33-0.8$) NPs. Arrows show shifts in $2-\theta$ to high angles with increasing Ru content. Vegard's plot of XRD-derived unit cell parameters of the Pt_xRu_{100-x} alloy NPs is shown in the inset. Line shows the ideal Vegard's behavior, and circles the data points. JC-PDS peak positions for Pt (red) are also presented. 88

Figure 2.19. XANES spectra of (a) Ru@Pt NPs, $Pt_{50}Ru_{50}$ NPs and Pt foil at Pt L edge and (b) Ru@Pt NPs, $Pt_{50}Ru_{50}$ NPs, Ru mesh and RuO_2 powder at Ru K edge. 90

Figure 2.20. XAFS functions in k-space of (a) Ru@Pt core/shell, Pt ₅₀ Ru ₅₀ alloy NPs and Pt foil at Pt L edge, and (b) Ru@Pt core/shell, Pt ₅₀ Ru ₅₀ alloy NPs, Ru mesh and RuO ₂ powder at Ru K edge.....	92
Figure 2.21. Fourier Transforms of EXAFS functions of (a) Ru@Pt core/shell, Pt ₅₀ Ru ₅₀ alloy NPs and Pt foil at Pt L edge, and (b) Ru@Pt core/shell, Pt ₅₀ Ru ₅₀ alloy NPs, Ru mesh and RuO ₂ powder at Ru K edge.	93
Figure 2.22. FEFF6 fits (red) to the FT-EXAFS data at (a) Pt edge and (b) Ru edge for the 4.1 nm Ru@Pt core/shell particles, and at (c) Pt edge and (d) Ru edge for the Pt ₅₀ Ru ₅₀ alloy NPs.....	94
Figure 2.23. (a) Experimental PDFs of monometallic Ru, Pt ₅₀ Ru ₅₀ alloy and Ru@Pt core/shell NPs, and (b) theoretical PDFs of the respective models calculated with no physical constraints.....	102
Figure 2.24. PDF refinements of the Pt ₅₀ Ru ₅₀ NPs using (a) the spherically truncated periodic model, and (b) ATOMS generated model cluster of a 44 Å diameter random alloy. The experimental data are shown by markers and the fits by solid lines. The residual PDFs are presented below each.....	104
Figure 2.25. PDF refinements of the Ru NPs using (a) the spherically truncated periodic model, and (b) the ATOMS generated model cluster of a 30 Å diameter HCP Ru. The experimental data are shown by markers and the fits by solid lines. The residual PDFs are presented below each.....	105
Figure 2.26. PDF refinements of the Ru@Pt core/shell NPs using ATOMS generated model clusters of (a) a 40 Å diameter 1356 atoms Pt-skin, (b) a single-phase 40 Å diameter Ru@Pt with 30 Å diameter Ru core and 2-layers thick Pt shell and (c) a two-	

phase 40 Å diameter Pt-skin and 30 Å diameter Ru. The experimental data are shown by markers and the fits by solid lines. The residual PDFs are given below each..... 107

Figure 2.27. PDF refinements of the Ru@Pt NPs using ATOMS generated model clusters of (a) a two-phase 40 Å diameter 1 ML thick Pt-skin and 35 Å Ru, and (b) a two-phase 40 Å diameter 2 ML thick Pt-skin and 30 Å Ru. The experimental data are shown by markers and the fits by solid lines. The residual PDFs are given below each..... 108

Figure 2.28. FT-IR spectra of CO-saturated colloidal suspensions of monometallic Pt NPs and monometallic Ru NPs, 4.1 nm Ru@Pt core/shell NPs, and 4.4 nm Pt₅₀Ru₅₀ NPs. 111

Figure 2.29. FT-IR spectra of CO-saturated colloidal suspensions of PVP-free Ru NPs, PVP-free Pt NPs and PVP-free Ru@Pt NPs in EG. 112

Figure 2.30. FT-IR spectra of CO-saturated colloidal suspensions in EG of the Pt shell series of the 3.0 nm Ru NPs under (a) normal reaction conditions (b) the anaerobic reaction conditions. Pt:Ru compositions are shown in parentheses, and approximate Pt shell thicknesses are given next to them. FT-IR spectrum of CO-saturated colloidal suspension of the anaerobically synthesized Ru NPs is also shown in (b). The progressive spectral shift to higher wavelengths with the increasing Pt content in (b) is indicated by the arrow. 114

Figure 2.31. FT-IR spectra of CO-saturated colloidal nanoparticles of approximately ML thick Pt shells over (a) 1.5-2.5 nm Ru, (b) sequentially grown 4.2 nm Ru, and (c) 5.7 nm Ru. (d) FT-IR spectra showing $\nu(\text{Pt-CO})$ s on different Ru@Pt core/shell NPs with ca. 1-2 layers thick Pt shells and varying Ru core sizes. FT-IR spectra of CO-saturated colloidal suspensions of the sequentially grown Ru NPs are also shown in (b)..... 115

Figure 2.32. FT-IR spectra of CO-saturated colloids of the Pt_xRu_{1-x} ($x=0.33-0.8$) NPs. arrow shows the progressive shift of the $\nu(CO)$ to higher wavenumbers with increasing Pt content..... 116

Figure 2.33. Micro-Raman spectra of the PVP-free Pt NPs, PVP-free Ru@Pt NPs and PVP-free Ru NPs (from top to bottom) under flowing 25% vol. CO/air mixture (a) in the $\nu(M-C)$ region and (b) $\nu(C-O)$ region. 117

Figure 2.34. TPR plots for the PROX reaction showing H_2O formations 2000 ppm CO level of (a) three different batches of the 4.1 nm Ru@Pt core/shell NP catalysts, and (b) the 4.1 nm Ru@Pt core/shell NP catalyst with the intermediate activity (1st in (a)), the 4.4 nm $Pt_{50}Ru_{50}$ alloy NP catalyst and the mixtures of monometallic Pt and Ru NPs catalyst. (c)TPR plots for the PROX reaction showing H_2O formations 2000 ppm CO level of the 4.1 nm Ru@Pt core/shell NP catalyst with the intermediate activity, the 4.4 nm $Pt_{50}Ru_{50}$ alloy NP catalyst and the mixtures of monometallic Pt and Ru NPs catalyst..... 120

Figure 2.35. TPR plots for the PROX reaction showing (a) H_2O formation at 1000 ppm CO level, and (b) O_2 formation and CO selectivity at 10000 ppm CO level for the as-synthesized core/shell NP catalyst, the alloy NP catalyst and the mixtures of monometallic Pt and Ru NPs catalyst. The gas hourly space velocity is $2.3 \cdot 10^5$ mL/g/h. in (a), and $1.2 \cdot 10^5$ mL/g/h in (b). The gas mixture for the PROX reaction was composed of 0.2% CO, 0.5% O_2 , 50% H_2 , and balance Ar in (a), and 1% CO, 1% O_2 , 50% H_2 , and balance Ar in (b). % of maximum O_2 conversion is shown by open triangles and selectivity by lines in (b)..... 121

Figure 2.36. (a) TPR plots for the PROX reaction at 1000 ppm CO level on the Pt_xRu_{100-x} ($x=40-80$) alloy NPs, showing the rates of H_2O formation. (b) The temperatures at 50% of H_2O formation in (a) is plotted versus % atomic Pt.	123
Figure 2.37. TPR plots for the PROX (with 50% H_2) and CO oxidation (with 0% H_2) reactions at 2000 ppm CO level on the Ru@Pt core/shell NPs catalyst showing the effect of humidified gas feeds on the CO_2 formation rates.....	124
Figure 2.37. TPR plots for the PROX reaction at 2000 ppm CO level showing (a) H_2O and (b) CO_2 formations on the Ru@Pt NPs catalyst with 3.0 nm Ru cores and Pt shells varying between <1 ML and 3 MLs.	125
Figure 2.38. TPR plots for the PROX reaction at 2000 ppm CO level showing (a) H_2O and (b) CO_2 formations on the Ru@Pt NPs catalyst with ca. 1-2 MLs thick Pt shells and different Ru core sizes varying between 2.0 nm and 5.7 nm, showing the rates of H_2O formations and CO concentrations. For comparison, the PROX conversions for the 2.0 nm Pt NPs catalyst are also given.....	127
Figure 2.40. TPR plots for NO_x reduction reaction on (a) 4.1 nm Ru@Pt NPs catalyst and (b) 4.4 nm $Pt_{50}Ru_{50}$ NPs catalyst in $NO/H_2 = 4$. % N_2 Selectivity is defined as N_2 yield over % NO concentration.....	133
Figure 2.41. TPR plots for NO_x reduction reaction on (a) 4.1 nm Ru@Pt NPs catalyst and (b) 4.4 nm $Pt_{50}Ru_{50}$ NPs catalyst in $NO/H_2 = 1$. % N_2 Selectivity is defined as N_2 yield over % NO concentration.....	135
Figure 2.42. Plots of (a) TOFs based on TEM-projected surface areas vs. % atomic Pt, (b) Mass activities vs. % atomic Pt, and (c) Mass activities vs. Pt-M distances for the benzene hydrogenation reaction on the $Ru_x@Pt_{1-x}$, $Pt_{1-x}Ru_x$ ($x=0.2-0.66$) NPs catalysts as	

well as monometallic Pt NPs and monometallic Ru NPs and the mixtures of monometallic NPs catalysts. 138

Figure 3.1. TEM images of (a) 2.7 nm Rh, (d) 3.3 nm sequentially-grown Rh, and (g) 3.9 nm sequentially-grown Rh particles. (b, e and h) HR-TEM images and (c, f and i) particle size histograms of the particles shown in (a, d and g), respectively. 166

Figure 3.2. Representative TEM images of (a) 3.2 nm Rh@Pt NPs with 2.7 nm Rh cores and ca. 1 ML thick Pt shells, (d) 3.5 nm Rh@Pt NPs with 2.7 nm Rh cores and ca. 1-2 layers thick Pt shells, (g) 4.3 nm Rh@Pt NPs with 3.3 nm Rh cores and ca. 2 ML thick Pt shells, (j) 4.4 nm Rh@Pt NPs with 3.9 nm Rh cores and ca. 1 ML thick Pt shells and (m) 5.1 nm Rh@Pt NPs with 3.9 nm Rh cores and ca. 2 ML thick Pt shells. (b, e, h, k and n) HR-TEM images and (c, f, i, l and o) particle size histograms of the particles shown in (a, d, g, j and m), respectively. 169

Figure 3.3. (a) TEM and (b) HR-TEM images, (c) FFT and (d) particle size histogram of Pt₅₀Rh₅₀ NPs. 169

Figure 3.4. Representative TEM images of (a) 2.2 nm PVP-free Rh NPs, (d) PVP-free 2.7 nm Rh@Pt NPs comprising 2.2 nm Rh cores and ca. 1 ML thick Pt shells, and (g) PVP-free 3.3 nm Rh@Pt NPs comprising 2.2 nm Rh cores and ca. 2 ML thick Pt shells. High resolution images and particle size histograms of the particles in a, d and g are shown directly next to each figure. 170

Figure 3.5. Representative STEM-EDS line spectra of (a) a 5.1 nm Rh@Pt NP with 3.9 nm Rh core and 2 ML Pt shell, and (b) a 5 nm Pt₅₀Rh₅₀ alloy nanoparticle. Relative atomic % composition (vertical axis) of Pt (red) and Rh (blue) are plotted against the line scan probe position (horizontal axis) and are given next to STEM images. A 1.5 nm

probe was used to trace 10 - 15 nm scans across each particle. The particle center is at ~ 6.5 nm in (a) and ~ 5.5 nm in (b). 172

Figure 3.6. A representative STEM-EDS point analysis of a 5 nm Rh@Pt core/shell nanoparticle with ~2 ML thick Pt shells, showing two spectra: one from the center of the particle (top), and another from the edge (bottom). 172

Figure 3.7. (a) The *ex-situ* FT-IR spectra of CO-saturated colloidal suspensions sampled as a function of time during the synthesis of the Rh@Pt NPs. The stacked plots show (i) parent Rh core NPs at 0 min, (ii) Rh@Pt NPs in 10th min, (iii) in 40th min, (iv) in 160th min, (v) and 240th min. (b) FT-IR spectra of CO saturated colloidal suspensions comparing core-shell (red), 50:50 alloy (blue) and a mixture of monometallic Rh and Pt nanoparticles (green). 175

Figure 3.8. FT-IR spectra of CO-saturated colloids of PVP-free Rh NPs, PVP-free Rh@Pt NPs with ca. 1 ML thick Pt shells and PVP-free Rh@Pt NPs with ca. ca. 2 ML thick Pt shells. 176

Figure 3.9. FT-IR spectra of CO-saturated colloids of (a) Rh NPs of different sizes and 177
(b) Rh@Pt NPs comprising different core sizes and shell thicknesses..... 177

Figure 3.10. 633 nm micro-Raman spectra of CO-saturated PVP-free NPs showing (a) the $\nu(\text{M-C})$ region (M = Pt, Rh), and (b) the $\nu(\text{CO})$ region. The data were recorded for 2.2 nm Pt NPs (black), 2.2 nm Rh NPs (green), and 2.7 nm Rh@Pt NPs (red) in 2.5 : 1 air-to-CO gas mixtures. 179

Figure 3.11. XRD profiles comparing (a) Rh NPs via polyol reduction of $\text{Rh}(\text{NO}_3)_3 \cdot 2\text{H}_2\text{O}$ to give, (i) 2.7 nm as-synthesized Rh NPs, (ii) 3.3 nm Rh NPs and (iii)

3.9 nm Rh NPs grown from sequential deposition. (b) XRD profiles of Rh@Pt core-shell (blue pattern) and Pt₅₀Rh₅₀ alloy (purple pattern) NPs of similar particle diameters. The inset shows an enlargement of the 111 and 200 reflections. JC-PDS lines for Pt (black), Rh (green), and Pt₅₀Rh₅₀ alloy (purple) are also shown..... 180

Figure 3.12. (a) XRD profiles and (b) DF simulations of Rh@Pt NPs of various core diameters and shell thicknesses. Red - 2.7 nm Rh core, 1 ML Pt shell; Reddish brown – 2.7 nm Rh core, 2 ML thick Pt shell; Light blue – 3.9 nm Rh core, 1 ML Pt shell; Orange – 3.3 nm Rh core, 2 ML Pt shell; Dark blue – 3.9 nm Rh core, 2 ML Pt shell. JC-PDS peak positions for Pt (black), 1:1 RhPt alloy (purple) and Rh (green) are also presented. 181

Figure 3.13. XRD profiles of PVP-free 2.2 nm Rh particles and PVP-free Rh@Pt NPs comprising 2.2 nm Rh cores and various shell thicknesses..... 182

Figure 3.14. TPR plots showing (a) H₂O formation, and (b) CO₂ formation for monometallic Pt NPs, monometallic mixtures of Pt NPs and 2.7 nm Rh particles, 4.9 nm Pt₅₀Rh₅₀ alloy NPs and 3.2 nm Rh@Pt NPs for H₂ streams contaminated with 2000 ppm CO. Percent of maximum H₂O formation was calculated from the limiting reactant, O₂, and % of maximum CO₂ formation is relative to the CO inlet concentration. See the text for details. 186

Figure 3.15. TPR plots showing CO₂ formation for 5 different supported catalysts from 4 different Rh@Pt NPs batches of colloids. The blue and green catalysts were prepared from the same colloid preparation. The red plot is the one presented in Figure 3.7 of the text..... 187

Figure 3.16. TPR plots showing % maximum CO₂ formation (connected dots) in PROX reactions for the three different Rh-Pt catalysts described in the text. The PROX feed is composed of 1% CO, 1% O₂, 50% H₂ and an Ar balance. The solid lines denote the corresponding PROX selectivity, defined as $[\chi_{\text{CO}_2}/(\chi_{\text{CO}_2}+\chi_{\text{H}_2\text{O}})] \times 100$ where χ_{CO_2} is the fraction of O₂ used to convert CO to CO₂ and $\chi_{\text{H}_2\text{O}}$ is the fraction of O₂ used to convert H₂ to H₂O. CO₂ and H₂O were used to calculate selectivities due to their superior sensitivity to mass spectrometric detection relative to O₂ and CO. 187

Figure 3.17. TPR plots showing % CO₂ conversions (connected dots) in PROX reactions for the three Rh@Pt and Ru@Pt catalysts described in the text. The PROX feed is composed of 1% CO, 1% O₂, 50% H₂ and an Ar balance. The solid lines denote the corresponding PROX selectivity, defined as $[\chi_{\text{CO}_2}/(\chi_{\text{CO}_2}+\chi_{\text{H}_2\text{O}})] \times 100$ where χ_{CO_2} is the fraction of O₂ used to convert CO to CO₂ and $\chi_{\text{H}_2\text{O}}$ is the fraction of O₂ used to convert H₂ to H₂O. CO₂ and H₂O were used to calculate selectivities due to their superior sensitivity to mass spectrometric detection relative to O₂ and CO. 188

Figure 4.1. TEM images of (a) Ir NPs, and (d) Ir@Pt (4:5) NPs. HR-TEM images of (b) Ir NPs, and (e, g and h) Ir@Pt NPs. 111 planes with inter-planar spacing of 0.210 Å for an iridium nanoparticle are shown in (b). 111 planes of a Ir@Pt nanoparticle is also shown in (e). (h) HR-TEM showing a Ir@Pt NP with the hexagonal packing, and another Ir@Pt NP with the face center cubic packing. FFT of the Ir@Pt nanoparticle with the FCC packing is given in (i). Particle size histograms of the Ir NPs and Ir@Pt NPs are shown in (c) and (f), respectively. 210

Figure 4.2. TEM images of (a) PVP-free Ir@Pt NPs, and (d) PVP-protected Ir@Pt@Pd NPs. HR-TEM images of (b) PVP-free Ir@Pt NPs, and (e) PVP-free Ir@Pt NPs. 111

planes with inter-planar spacing of 0.215 nm for both PVP-free Ir@Pt and Ir@Pt@Pd nanoparticles are also shown in (b) and (e), respectively. Particle size histograms are given in (c) and (f). 211

Figure 4.3. TEM images of (a) Ru@Pd (1:1) NPs with ca. 1-2 MLs thick Pd shells (d) Ru@Pd (1:2) NPs with ca. 2-3 MLs thick Pd shells (g) Ru@Pt@Pd (3:2:5) NPs with sandwiched Pt shells at sub-monolayer coverage and Pd shells of 1-2 MLs thick. (c, f and i) HR-TEM images, and (b, e and h) particle size histograms of NPs shown in (a, d and g), respectively. 213

Figure 4.4. Representative STEM-EDS line spectra of a ~8.0 nm Au@Pt NP with ~6.0 nm Au core and 3-4 layers thick Pt shells. Relative atomic % composition (vertical axis) of Au (blue) and Pt (red) are plotted against the line scan probe position (horizontal axis) and are given next to STEM image. A 1.5 nm probe was used to trace 15 – 20 nm scans across each particle. The particle center is at ~ 15. Representative EDS spectrum is given below STEM image. 215

Figure 4.5. Representative STEM-EDS line spectra of a 5.0 nm Ru@Pd NP comprising of a 3.0 nm Ru core and ca. 2-3 layers thick Pd shells. Relative atomic % composition (vertical axis) of Ru (blue) and Pd (red) are plotted against the line scan probe position (horizontal axis) and are given next to STEM images. A 1.5 nm probe was used to trace 15 – 20 nm scans across each particle. The particle center is at ~ 9 nm in (b). 216

Figure 4.6. Representative STEM-EDS line spectra of a 4.8 nm Ru@Pt@Pd particle with 3.0 nm Ru core, sandwiched Pt shells at sub-monolayer coverage and 1-2 MLs thick Pd shells. Relative atomic % composition (vertical axis) of Ru (blue), Pt (red) and Pd (green) are plotted against the line scan probe position (horizontal axis) and are given next to

STEM images. A 1.5 nm probe was used to trace ~11 nm scans across the particle. The particle center is at ~ 6 nm. 217

Figure 4.7. STEM-EDS point analysis of two randomly chosen Ru@Pt@Pd NPs, showing (a) edge spectrum and (b) core spectrum. EDS spectra are shown next to each STEM image along with the table, showing the % compositions from the spectra. 217

Figure 4.8. Powder XRD patterns of (a) PVP-protected 2.0 nm Ir particles and their Pt shell series, and (b) PVP-free Ir NPs and 2.5 nm Ir@Pt (3:4) particles. JC-PDS lines for Pt (blue) and Ir (red) are also presented. 219

Figure 4.8. Transient powder XRD patterns of nano-crystalline Au@Pt particles collected ex-situ at 1st min, 60th min and 180th min of Pt growth reaction at 100 °C compared to powder diffraction pattern of 2.5 nm Au NPs. * show the major reflections of (unreacted) PtCl₂. JC-PDS lines for Pt (blue) and Au (red) are also presented. 221

Figure 4.9. Powder XRD patterns of (a) Ru@Rh NPs with the 3.0 nm Ru cores and varying Rh shell thicknesses compared to those of monometallic 2.7 nm Rh NPs and 3.0 nm Ru nanoparticle seeds, and (b) Ru@Pd NPs with the 3.0 nm Ru cores and varying Pd shell thicknesses compared to that of 3.0 nm Ru particle seeds and the 4.8 nm Ru@Pt@Pd NPs. JC-PDS lines for Pt (black), Ru (blue), Rh (red) and Pd (purple) are also presented. 223

Figure 4.10. FT-IR spectra of CO-saturated colloids of (a) 2.0 nm PVP-protected Ir particles and Ir@Pt NPs of varying Ir:Pt ratios: 1:1, 2:3 and 1:2; and (b) PVP-free Ir NPs, 2.2 nm PVP-free Pt and 2.5 nm PVP-free Ir@Pt particles. Asterisks show free-CO in the colloidal suspension. 225

Figure 4.11. FT-IR spectra of CO-saturated colloids of (a) EG-reduced Pd NPs, NaBH₄-reduced Pd NPs, 4.0 nm NaBH₄-reduced Pd particles after NaBr treatment and 4.5 nm Pd@Pt core/shell particles with 4.0 nm Pd cores and ca. 1 ML thick Pt shells; and (b) bimetallic Pd/Pt NPs with alternating Pt and Pd layers at ca. 1 ML coverage, namely Pd@Pt, Pd@Pt@Pd, and Pd@Pt@Pd@Pt core/shell NPs. 227

Figure 4.12. FT-IR spectra of CO-saturated colloids of 2.0 nm Ir particles, 2.5 nm Ir@Pt particles, 3.0 nm Ir@Pt@Pd NPs with 2.5 nm Ir@Pt cores and ca. 1 ML thick Pd shells, and 3.0 nm Ir@Pt NPs after two-step Pt growth. 228

Figure 4.13. FT-IR spectra of CO-saturated colloids of (a) 3.0 nm Ru particles, 2.7 nm Rh particles, 3.9 nm Ru@Rh particles with ca. 1-2 MLs thick Rh shells, and 4.3 nm Ru@Rh particles with ca. 2-3 MLs thick Rh shells; and (b) 3.0 nm Ru particles, 4.0 nm Pd particles, 4.5 nm Ru@Pd particles with ca. 1-2 layers thick Pd shells, and 5.0 nm Ru@Pd particles with ca. 2-3 MLs thick Pd shells 4.0 nm Pd particles. 230

Figure 4.14. FT-IR spectra of CO-saturated colloids of 3.0 nm Rh particles, 3.7 nm Ru@Pt particles with submonolayer coverage of Pt, 4.8 nm Ru@Pt@Pd NPs with ca. 1-2 MLs thick Pd shells. For control, FT-IR spectrum of CO-saturated colloids of Ru@Pt@Ru NPs with 3.7 nm Ru@Pt cores and ca. 1-2 MLs thick Ru shells is also shown. 231

Figure 4.15. Micro-Raman spectra of PVP-free Ir, PVP-free Pt and PVP-free Ir@Pt (3:4) NPs in the (a) M-C stretch region and (b) C-O stretch region. 232

Figure 4.16. TPR plots for the PROX reaction showing (a) H₂O formations and (b) CO concentrations at 1000 ppm CO level of the M@Pt (M=Ru, Rh, Ir, Pd and Au) core/shell NPs with ca. 1 ML thick Pt shells and the 2.5 nm Pt particle catalysts. The gas hourly

space velocity is 2.3×10^5 mL/g/h. The gas mixture for the PROX reaction was composed of 0.1% CO, 0.5% O ₂ , 50% H ₂ , and balance Ar.....	235
Figure 4.17. TPR plots for the PROX reaction showing (a) H ₂ O formations and (b) CO concentration at 2000 ppm CO level of the M@Pt (M=Ru, Rh, Ir, Pd and Au) core/shell NPs with ca. 1 ML thick Pt shells and the 2.5 nm Pt particle catalysts. The gas hourly space velocity is 2.3×10^5 mL/g/h. The gas mixture for the PROX reaction was composed of 0.2% CO, 0.5% O ₂ , 50% H ₂ , and balance Ar. Arrow shows % of unreacted CO.....	236
Figure 4.18. TPR plots for the PROX reaction showing CO ₂ (open triangles) and H ₂ O (open circles) formations at 2000 ppm CO level of the 3.4 nm core/shell Au@Pt and 2.2 nm monometallic Pt catalysts.	237
Figure 4.19. TPR plots for the PROX reaction showing O ₂ consumption and CO selectivity at 10000 ppm CO level of the M@Pt (M=Ru, Rh, Ir and Au) core/shell NPs with ca. 1 ML thick Pt shells and the 2.5 nm Pt particle catalysts. The gas hourly space velocity is 2.3×10^5 mL/g/h. The gas mixture for the PROX reaction was composed of 1.0% CO, 0.5% O ₂ , 50% H ₂ , and balance Ar. CO selectivity is defined as $100 \times (\chi_{CO_2} / (\chi_{CO_2} + \chi_{H_2O}))$. % of maximum O ₂ consumptions is shown by solid circles, and % selectivities for CO by lines.....	238
Figure 4.20. TPR plots for the PROX reaction showing (a) H ₂ O formations and (b) CO concentration at 2000 ppm CO level of the Ru@M (1:1) (M=Pt, Pd and Rh) core/shell NPs with ca. 1-2 MLs thick M shells. The gas hourly space velocity is 2.3×10^5 mL/g/h. The gas mixture for the PROX reaction was composed of 0.2% CO, 0.5% O ₂ , 50% H ₂ , and balance Ar.....	240

Figure 4.21. TPR plots for the PROX reaction showing (a) H₂O formations and (b) CO concentrations at 2000 ppm CO level of the Ru@M (1:2) (M=Pt, Pd and Rh) core/shell NPs with ca. 2-3 MLs thick M shells. The gas hourly space velocity is 2.3*10⁵ mL/g/h. The gas mixture for the PROX reaction was composed of 0.2% CO, 0.5% O₂, 50% H₂, and balance Ar. Arrows show % of unreacted CO. 241

Figure 4.22. TPR plots for the PROX reaction showing CO₂ formations and CO selectivities at 10000 ppm CO level of (a) the Ru@M (1:1) (M=Pt, Pd and Rh) core/shell NPs with ca. 1-2 layers thick Pt shells catalysts, and (b) the Ru_x@M_{1-x} (M=Pt and Rh; x=0.33 and 0.5) core/shell NPs catalysts. The gas hourly space velocity is 2.3*10⁵ mL/g/h. The gas mixture for the PROX reaction was composed of 1.0% CO, 0.5% O₂, 50% H₂, and balance Ar. CO selectivity is defined as 100*($\chi_{CO_2} / (\chi_{CO_2} + \chi_{H_2O})$). % of maximum CO₂ formation is shown by open squares, and % selectivities by lines. 243

Figure 4.23. TPR plots for the PROX reaction showing (a) H₂O formations and (b) CO concentrations at 2000 ppm CO level of the Ru_x@Rh_{1-x} (x=0.33 and 0.5) NPs, 2.7 nm Rh particles and 3.0 nm Ru particles catalysts. The gas mixture for the PROX reaction was composed of 0.2% CO, 0.5% O₂, 50% H₂, and balance Ar. 245

Figure 4.24. TPR plots for the PROX reaction showing (a) H₂O formations and (b) CO concentrations at 2000 ppm CO level of the 4.4 nm Ru@Pd@Pt core/shell1/shell2 particles, Ru_x@Rh_{1-x} (x=0.33 and 0.5) NPs, and 3.7 nm Ru@Pt particles catalysts. The gas mixture for the PROX reaction was composed of 0.2% CO, 0.5% O₂, 50% H₂, and balance Ar. 247

Figure 2.25. TPR plots for the PROX reaction showing (a) H₂O formations and CO concentrations at 2000 ppm CO level and (b) CO₂ formation and selectivity at 1.0% CO

and 0.5% O₂ for the 3.0 nm Ir@Pt@Pd core/shell1/shell2 particles, 3.0 nm Ir@Pt@Pt core/shell particles, and 2.5 nm Ir@Pt particles catalysts. The gas hourly space velocity is 2.3*10⁵ mL/g/h. 249

Figure 4.26. (a) Cross-section and a-top views of the optimized geometries of CO adsorbed on Pt(111) at various coverages. Red, black and gray spheres represent O, C and Pt atoms, respectively. As a guide to the eye the unit cell drawn with white lines. (b) Differential binding energy for CO as a function of CO coverage on various Pt*/M model (111) or (0001) surfaces. A positive differential BE indicates that the respective state is not stable on the surface..... 251

Figure 4.27. (a) the activation energy barrier (E_a) and (b) heat of reaction (ΔH) for H₂ dissociation as a function of CO coverage on Pt*/M and Pt(111) on a four-layered slab in a (√3 x 2√3) surface unit cell. 253

Figure 4.28. (a) Binding energy (BE) of different reaction intermediates and (b) the activation energy (E_a) for different PROX elementary steps on Pt*/M and Pt(111) on four-layer slabs with a (2 x 2) surface unit cell. 257

Figure 4.29. (a) TPR plots for the PROX reaction showing CO₂ formations at 2000 ppm CO level on the core/shell M@Pt (M=Ru, Rh, Ir, Pd and Au) and monometallic Pt NPs. (b) The activation energies, E_as, for the rate limiting reaction step of CO oxidation on the Pt*/M NSAs and Pt(111) are plotted against temperatures of 50% CO₂ formation on the core/shell M@Pt and monometallic Pt NPs (M=Ru, Rh, Ir, Pd and Au). 259

Figure A4.1. TEM images of (a) Pd NPs, and (d) Pd@Pt NPs. HR-TEM images of (b) Pd NPs, and (e) cubic Pd@Pt NPs. Particle size histograms of (a) and (d) are shown in (c) and (f), respectively. 276

Figure A4.2. TEM images of Ru@Rh NPs with nominal Rh:Ru ratios of (a) 1:1, and (d) 2:1 . HR-TEM images of Ru@Rh NPs with nominal Rh:Ru ratios of (b) 1:1, and (e) 2:1). Particle size histograms of (a) and (d) are also shown in (c) and (f), respectively. 277

Figure A4.3. TEM images of (a) 6.0 nm Au NPs, (d) 7.8 nm Au@Pt NPs with multiple monolayers of Pt shells, (g) 2.5 nm Au NPs, and j) 3.4 nm Au@Pt NPs with ca. 1-2 MLs thick Pt shells. HR-TEM images of (b) several nano-crystalline Au cubes, (e) a 7.8 nm Au@Pt NPs, (h) a 2.5 nm Au icosahedra, and k) a nanocrystalline Au@Pt spheroid. Size histograms of the particles in (a), (d), (g) and (j) are shown in (c), (f), (i) and (l), respectively. 280

Figure A4.4. STEM-EDS point analysis of 10 randomly chosen Au@Pt NPs supported on γ -Al₂O₃ after conditioning at 200 °C for several hours under PROX reaction. Representative EDS spectrum of the particle 5 is shown below STEM image. Table shows particle composition, and statistical parameters. 281

Figure A4.5. Representative STEM-EDS line spectrum of a ~3.5 nm Au@Pt NP with ~2.5 nm Au core and 1-2 MLs thick Pt shells. Relative atomic % composition (vertical axis) of Au (red) and Pt (blue) are plotted against the line scan probe position (horizontal axis) and are given next to STEM image. A 1.0 nm probe was used to trace 15 – 20 nm scans across each particle. The particle center is at ~ 7 nm. 282

Figure A4.6. Representative STEM-EDS line spectra of a 4.3 nm Ru@Rh NP with 3.0 nm Ru core and 2-3 MLs thick Rh shells. Relative atomic % composition (vertical axis) of Ru (blue) and Rh (red) are plotted against the line scan probe position (horizontal axis) and are given next to STEM images. A 1.5 nm probe was used to trace 15 – 20 nm scans across each particle. The particle center is at ~ 8 nm. 283

Figure A4.7. Micro-Raman spectra showing $\nu(\text{M-O})$ s ($\text{M}=\text{Ru}, \text{Rh}, \text{Pd}$ and Pt) of (a) the Ru@M NPs with ca. 1-2 MLs thick M shells and (b) the 4.8 nm Ru@Pt@Pd particles with sandwiched layer of Pt at sub-monolayer coverage and ca. 1-2 MLs thick Pd shells, the parent 3.7 nm Ru@Pt particles and the 4.5 nm Ru@Pd NPs with ca. 1-2 MLs thick Pd shells. Dashed lines mark the positions of Raman active $\nu(\text{Ru-O})$ s of as-synthesized Ru NPs. \circ marks the $\nu(\text{Ru-O})$ s in the respective bimetallic NP systems, \bullet the $\nu(\text{Rh-O})$ s in the Ru@Rh NPs, \blacktriangledown the $\nu(\text{Pd-O})$ s in the Ru@Pd NPs and \blacklozenge the single $\nu(\text{Pt-O})$ at ca. 590 cm^{-1} . (\leftarrow , \rightarrow) arrows show the direction of shifts in $\nu(\text{M-O})$ s of the bimetallic NPs relative to those of the monometallic NPs. 287

List of Schemes

Scheme 1.1. Diagram showing the poly-ol oxidation reaction network.	7
Scheme 1.2. Schematic illustration of alloy clusters with (a) ordered, (b) random disordered and (c) cluster-in-cluster architectures.	11
Scheme 1.3. Schematic illustration of core/shell clusters with (a) overlayer and (b) sandwich type architectures.	12
Scheme 1.4. Schematic illustration of bimetallic clusters of (a) hetero-dimer, and (b) and (c) hetero-aggregate architectures.	13
Scheme 1.5. Schematic illustration of the sequential method employed by the poly-ol (i.e. ethelene glycol) reduction technique, showing the two-step reaction.	23
Scheme 1.6. Schematic illustration of some metal nucleation pathways; delayed-nucleation vs. co-nucleation.	24
Scheme 1.7. Schematic illustration showing the formation of core/shell nanoparticles via a transmetallation reaction route.	25
Scheme 1.8. Schematic illustration of thermally-induced phase transformation of 36 atom PtRu5 cluster studied by Nuzzo and co-workers.	30
Scheme 2.1. Schematic illustration of various bimetallic particle architectures.	44
Scheme 2.2. Schematics illustration showing (a) Frank van-der Merwe and (b) Volmer-Weber type heterogeneous growth mechanisms.	144
Scheme 3.1. Schematic illustration of various bimetallic particle architectures.	152

List of Abbreviations

acac	acetylacetonate
PVP	polyvinylpyrrolidone
EG	ethylene glycol
°C	degree Celcius
nm	nanometer
NP	nanoparticle
NC	nanocrystal
mmol	millimole
mL	milliliter
TEM	transmission electron microscope
HRTEM	high-resolution transmission electron microscope
STEM	scanning transmission electron microscope
EDS	energy dispersive spectroscopy
XRD	x-ray diffraction
JC-PDS	powder diffraction database file
FCC	face-centered cubic
HCP	hexagonal close packed
EXAFS	extended x-ray absorption fine structure
XANES	x-ray absorption near edge structure
CN	coordination number
PDF	pair distribution function
DFA	debye function analysis

ATOMS	software for atomic-structure display
DISCUS	software for diffuse scattering defect-structure simulation
XPS	x-ray photoelectron spectroscopy
FT-IR	fourier transformed infrared
TPR	temperature programmed reaction
TPD	temperature programmed desorption
GHSV	gas hourly space velocity
TOF	turnover frequency
ppm	part per million
PROX	preferential oxidation
WGS	water gas shift
PEMFC	polymer electrolyte membrane fuel cell
DMFC	direct methanol fuel cell
PGM	platinum group metal
NSA	near surface alloy
DFT	density functional theory
BE	binding energy
ML	monolayer

Chapter 1

Introduction

1.1. Introduction

Nanoscience and nanotechnology date back to late 80s, although some nanoscale objects and submicron size bacteria have been known and recognized for decades before. The recent burst of research in design and fabrication of materials at the nanoscale is partly attributed to the fascinating properties of nano-materials, and also to demand for ‘smaller’ and higher performance technologies. Applications and utilization of nanomaterials range from drug delivery² to disease recognition and diagnosis³ in medicine and life sciences; from heterogeneous catalysis to electronic circuit devices,^{4,5} optics⁶ and magnetic storage media^{7,8} in engineering and physical sciences. Having such a wide spread influence throughout many disciplines of science and technology, the number of topics currently under investigation is countless, and volume of studies that have been squeezed into that short period of time is enormous.

A nanoparticle can be defined as particle of the nanosize irrespective of their physical and chemical properties such as shape, geometry, architecture, structure, elemental identity, oxidation state and composition. Nanoclusters refer to nanoparticles with symmetry-defined geometries, and should be distinguished from molecular clusters by their sizes above 1 nm. There are other terms such as nanodisc, nanowire, nanotube, etc. which refer to certain geometrical shapes of nanoparticles.

Materials in nanosize are distinguished from their bulk analogues by their physical and chemical properties. Nanomaterials at certain size limit lie between bulk materials and molecular assemblies and clusters. In this sense, they bridge the two worlds of material design. In their embryonic and development stages, nanomaterials exhibit challenges in fabrication and characterization. Yet, they offer new scopes in material design, and thus make what is thought difficult and impossible easy and possible. The most fundamental understanding beyond their distinct properties is surface-to-volume ratio. For spherical nanoparticles, sizes below 10 nm exhibits drastic increase of surface area with respect to bulk volume. Secondly, the quantum confinement effect is used in a more scientific way to explain observed material properties of nanoparticles. In bulk materials orbitals in atoms and molecules combine to form finite bands. It is this band formation that gives solid state phenomena its characteristics. Nanomaterials are comprised of a smaller amount of material compared to the bulk so that bands show finite size effects, and thus usually fail to exhibit solid state properties.⁹

A brief visit to thermodynamics would be useful to understand why nanoparticles exist and how they form. Nanoparticles have large surface areas relative to bulk volume, so that they possess high excess of surface free energies which make nanoparticles unstable below a critical size. Briefly, surface excess free energy is always positive and linearly increases with surface area. Volume excess free energy, on the other hand, is positive and scales with volume, so the enthalpy of formation should be negative above a critical diameter at which the absolute value of volume free energy exceeds surface free energy.¹⁰ This reasoning is valid for spherical particles however the thermodynamic description becomes less clear for non-spherical and other pseudo-1-D

particle shapes. In these more complex systems, crystallization kinetics becomes an important driving force.

Crystallization phenomena as defined in classical theory for macroscopic materials can be extended to include nanoparticle formation. Crystallization has two distinct processes: nucleation and growth. Nucleation by itself is described by the two opposing terms of thermodynamics, namely surface tension and volume free energy. The two works against each other in the nucleation step to give stable nuclei whose diameter is greater than the critical size.^{10,11} The growth process provides a pathway for kinetic phases of otherwise spherical nanoparticles to form. The timescale and temperature of a reaction provide sensitive interplay between nucleation and growth steps that cause size diversity and assorted shape distributions of particles. This is fundamental to how branched or single nanowires, and other geometrically related structures are made.¹²

Having the formation phenomena of nanoparticles established, making distinctions between various types of nanoparticles is of fundamental importance for the sake of simplicity. Among all the different materials including semiconducting metal oxides,¹³⁻¹⁵ light emitting metal chalcogenides,¹⁶⁻¹⁸ optically-active semiconductor-polymer hybrids¹⁹ and gas sensing metal-polymer hybrids,²⁰ transition group metals draw our attention regarding their unique catalytic behavior toward various heterogeneous reactions. From a catalysis point of view, metal nanoparticles usually exhibit the highest rank in activity and selectivity. They are the choice of materials in catalyzing various gas phase reactions such as olefin and aromatic hydrogenations,²¹⁻²⁶ steam reforming,²⁷⁻³⁰ water-gas-shift,^{29,31} NO_x reduction,³²⁻³⁴ and preferential oxidation of CO (PROX),³⁵⁻³⁷ etc. Also, platinum group metals (PGMs) such as platinum and ruthenium are the only

materials employed in low temperature fuel cells, such as polymer electrolyte membrane fuel cells (PEMFC)³⁸⁻⁴⁵ and direct methanol fuel cells (DMFC).⁴⁶⁻⁴⁸

1.2. Metal Nanoparticles

Metal nanoparticles can be categorized with respect to their structural and chemical properties such as particle geometry, elemental make-up, elemental composition, architectural arrangement at both atomic and intra-particle level. Monometallic nanoparticles are composed of a single phase with a little sophistication. On the other hand, bi-metallic and other multi-metallic nanoparticles represent a high level of sophistication in terms of permutations of all possible structural and compositional aspects. Generally speaking, particle size and shape are the only properties that one can vary in a monometallic nanoparticle without invoking any complications on material make-up. Engineering the material properties comes into play at a later stage at which structural make-up is considered and offers endless possibilities in material design.

Monometallic nanoparticles can be synthesized via various methods ranging from vapor deposition techniques to wet chemical routes. Each and every method has its own advantages and disadvantages in cost, simplicity and applicability. Among them, wet chemical methods are widely accepted and employed as primary method of synthesis. In this approach, a metal precursor salt is dissolved in a proper solvent and reduced using a reducing agent in the presence of a ligand. The role of the ligand is to protect the particle against uncontrolled growth.^{49,50} The ligand also stabilizes nanoparticles by providing inter-particle separation in form of steric bulk and/or electrical repulsion.⁴⁹ Other functions of ligands are to preferentially cap high energy surface sites and to navigate

particle growth in one or more of crystallographic directions,^{51,52} and to passivate the particle surface by altering its chemical structure.⁴⁹ Ligands may hinder catalytic reactivity and selectivity by blocking surface-active sites, and thus their strength and reversibility of binding plays an important role in nanoparticle synthesis.⁵³ The power of reducing agent plays a central role in controlling reaction kinetics. Strong reducing agents like superhydrides induce fast nucleation. The growth process is, however, shut down and nanoparticle formation becomes diffusion-limited because monomer concentration quickly drops below the supersaturation limit during the nucleation stage.⁵⁴ The result is small particles with a broad size distribution.^{11,54,55} When a weak reducing agent is employed, growth process can compete with nucleation, so that the result is larger, but more monodisperse nanoparticles via inter-particle monomer diffusion.^{11,56} Additionally, other kinetic phases with isotropic non-spherical particle geometries, such as triangles, cubes and hexagons⁵⁷ or anisotropic particle shapes such as rods and wires may become accessible by controlling growth of certain facets (see Figure 1.1).^{51,52}

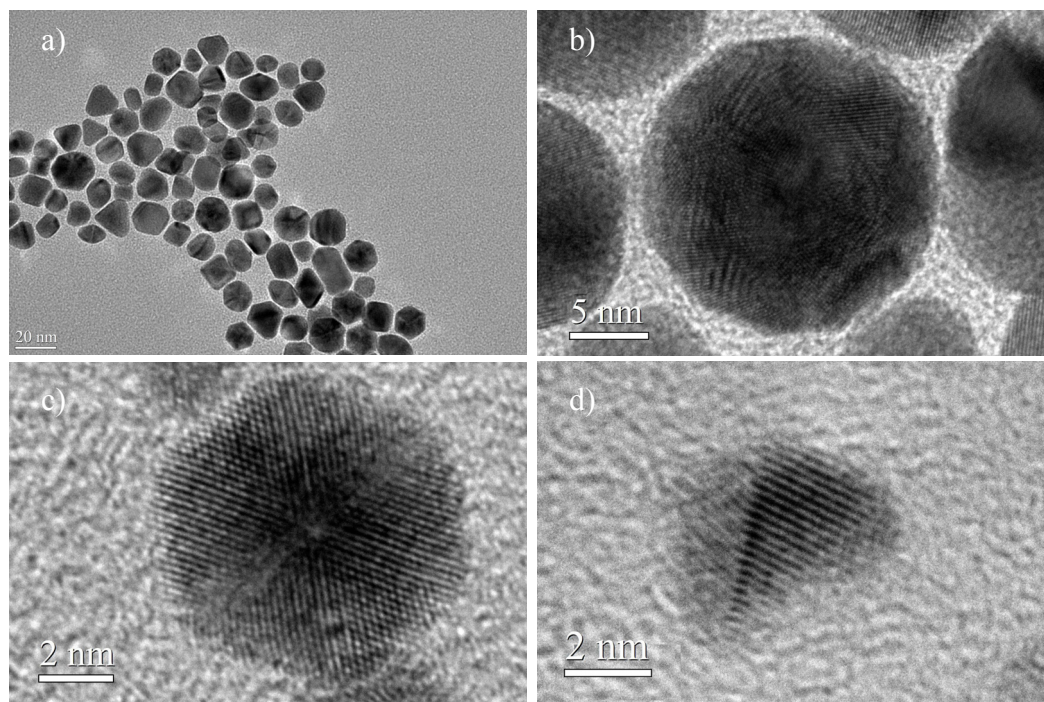
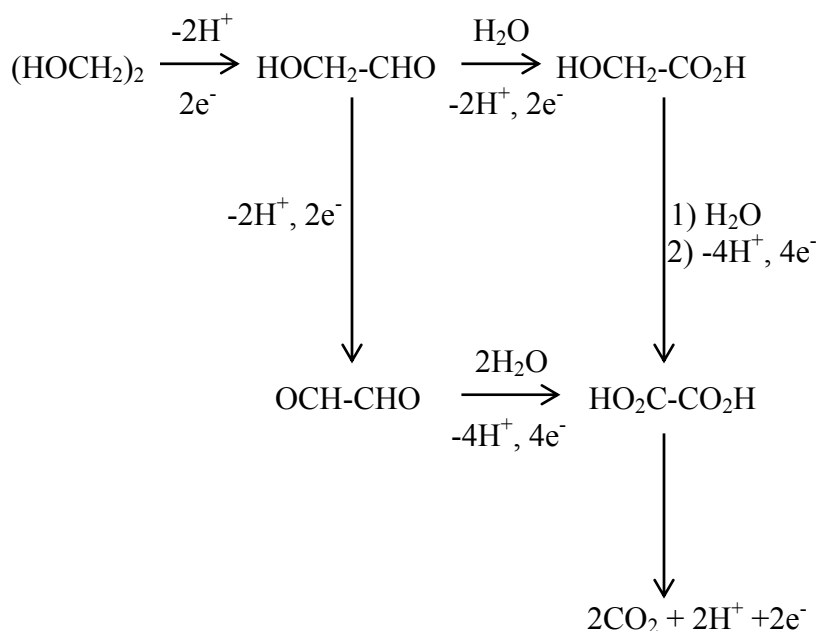


Figure 1.1. TEM pictures of (a) Au NPs of various geometric shapes; cubes, triangles, hexagons, rods, etc. Representative HR-TEM pictures of the nanocrystalline (b) Au polyhedron, (c) Pt cube, and (d) Fe tetrahedron.

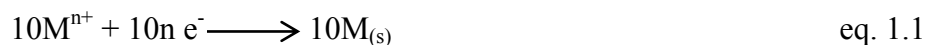
Certain solvents and/or their oxidation by-products may also act as protecting agents, and therefore stabilize nanoparticles without use of secondary ligands.⁵⁸ Some solvents are used as reducing agents at elevated temperatures so that use of such solvents provides further control over reaction kinetics, and helps in tuning particle size^{59,60} and shape.^{60,61} Poly-ol solvents, particularly ethylene glycol, (EG) are reducing at elevated temperatures, and also act as protecting agent at certain pH values. EG is thus environmentally safe and high boiling, and has strong temperature dependence on viscosity over a wide temperature window which affects solubility and supersaturation. The poly-ol reduction method satisfies many aspects of synthesis, and thus is widely used to synthesize monometallic nanoparticle in a broad range of sizes⁶² and shapes.^{61,63,64} For

example, PGMs including Pt, Rh and Ir with well-defined surface morphology and particle shape have been reported to be synthesized in EG at pHs above 10 without any secondary ligand stabilization.⁵⁸

Scheme 1.1. Diagram showing the poly-ol oxidation reaction network.



The redox mechanism involving EG is pH dependent. The oxidation of EG, however, is reported to follow the general reaction network (Scheme 1.1).⁶⁵ In alkaline solutions, the reaction is found to go to completion, and thus the product is CO₂ with a total of 10e⁻ oxidation. CO₃⁻ intermediate has also been detected by FT-IR spectrum of the reaction products.⁶⁵ CaCO₃ sediments upon adding CaCl₂ into reaction filtrate have also been detected by XRD.⁶⁶ For the complete oxidation of EG, the typical redox reaction is given in equation:⁶⁶



Monometallic NPs can be used as-synthesized or after supported in certain metal oxides as catalysts. The main area of interest that metal nanoparticles find application in catalysis is heterogeneous transformations of small molecules such as NO_x ,²⁵ CO ,^{25,37,67,68} and hydrogenation of olefins²⁴ and aromatic hydrocarbons.^{22,24,69,70} Reductive removal of exhaust gases like NO_x is performed commercially on three-way catalysts comprising of Pt NPs and Rh NPs supported on CeO_2 .⁷¹ Rh NPs catalysts are widely employed for hydrogenation of aromatic hydrocarbons.^{22,26,70,72-74} Ir NP ionic liquid hybrid catalysts⁷⁵ and phenanthroline-stabilized Pd NP catalysts⁷⁶ greatly increase the kinetics of olefin hydrogenation. Monometallic Pt NPs are also considered the most active electro-catalyst known to low temperature fuel cells running on pure H_2 .^{77,78}

Catalytic properties such as activity and selectivity are solely determined by identity of elements and greatly enhanced by size and surface geometry for given element type. For example, 100 crystallographic surface sites on single crystal Pt are found to be more selective toward benzene hydrogenation to cyclohexane than 111 surface sites.⁷⁹ Having structure dependence of reactivity in mind, Pt NPs with truncated octahedron geometry are far less selective in catalyzing benzene hydrogenation than Pt nanocubes of similar particle diameters.⁸⁰ Similarly, nanoparticulate Rh tetrahedrons with exclusively 100 crystallographic surface sites are more active and selective toward benzene hydrogenation to cyclohexane than any other monometallic Rh NPs.⁷⁰ Somorjai and co-

workers have recently shown for ethylene hydrogenation on shape/morphology controlled NPs of Pt⁸¹ and Rh⁶⁰ the enhanced surface reactivity.

Bimetallic NPs, or multi-metallic NPs in general, offer unpredictable improvements in physical, chemical and catalytic properties which any of the constituent elements by themselves do not show. Thus, these properties can be tuned by changing variables such as elemental composition, particle architecture and structural make-up. The next section will focus entirely on possible permutations on material properties introduced by two or more present metals and potential implications in materials design and engineering of such degree of complexity.

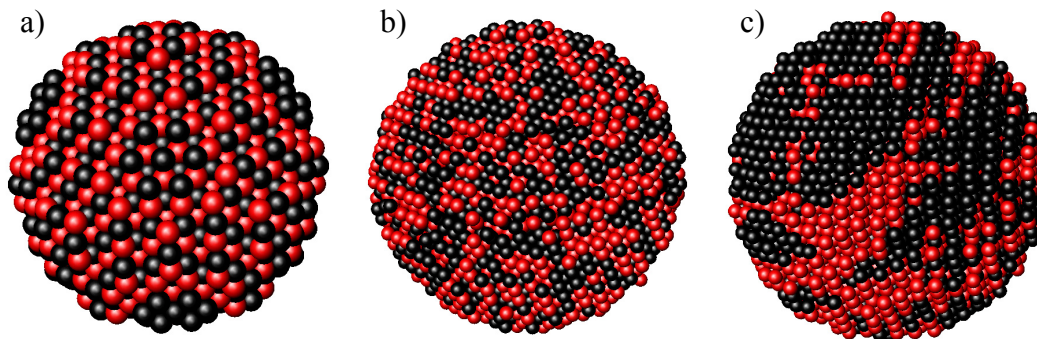
1.3. Multi-metallic Nanoparticles

When a second (or more) metal is integrated into a monometallic structure the result is a bimetallic (multi-metallic) system irrespective of the form and degree of interaction between the two. Bulk binary alloy phases of transition group metals have been known to metallurgy since the 1900s and to heterogeneous catalysis since the 1950s.⁸² Thermodynamic phase diagrams exist to show compositional correlations between metals as a function of temperature.⁸³ At the nanoscale, in contrast, phase relationships between metals are generally unknown. However, a case study published by Nuzzo et. al. on nanoparticles of bimetallic PtRu shows the complex nature of alloying between Pt and Ru at the nanosize.⁸⁴

1.3.1. Bimetal nanoparticle architectures

The most studied and the best understood multi-metallic systems are alloys, which can be described as solid solutions of two or more metals at certain compositions. There are several possible ways of arranging two elements confined to a sphere of finite diameter at various compositions. Checkerboard type arrangement of atoms of two metal types is usually called ordered phase of alloying, or an intermetallic (Scheme 1.2a), and face-centered tetragonal (FCT) CoPt NPs⁸⁵ upon thermal aging of Co@Pt core/shell NPs is a representative of such a model. As shown in Scheme 1.2, disordered phases may exhibit either homogeneous random (b) or inhomogeneous cluster-in-cluster arrangements (c).⁸⁶ AuPd NPs⁸⁷ synthesized via sequential reduction of Au and subsequently Pd has been found to exhibit composition gradient-like in the cluster-in-cluster structure. Similarly, AuPd nanowires (NWs) synthesized via galvanic replacement of alkylamine-stabilized Pd NWs has shown to have Au-rich cores at the early stage of the reaction. By addition of excess Au monomers, AuPd NWs with dominantly cluster-in-cluster structures are observed to transform into random alloy phases.⁸⁸ The number of heteroleptic interactions decreases in favor of homoleptic ones in the order of ordered alloy > random disordered alloy > random cluster-in-cluster alloy.⁸⁶

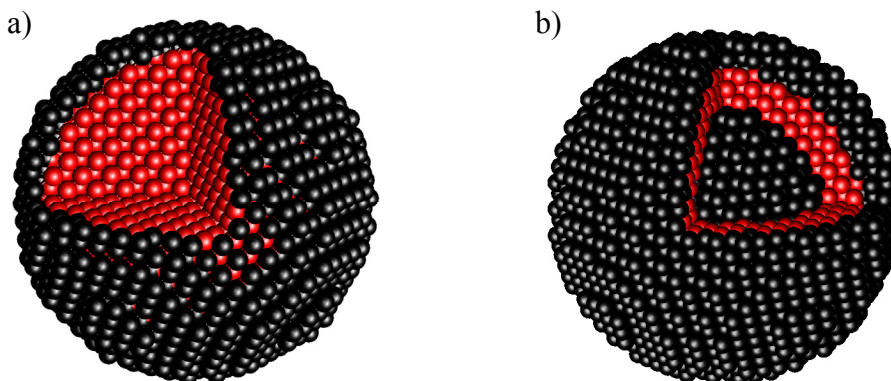
Scheme 1.2. Schematic illustration of alloy clusters with (a) ordered, (b) random disordered and (c) cluster-in-cluster architectures.



Next, bimetallic NPs with core/shell architectures are the second most studied system. They are structurally more sophisticated than bimetallic alloy with similar compositions. From a certain perspective, the core/shell architecture can be treated as a special alloy structure with intra-particle segregation. The bimetallic core/shell architecture allows heteroleptic interaction only at the interface between core and shell.⁸⁶ In this sense, it exhibits a lower level of heteroatom correlation than any alloy structure. Generally, there are two core/shell structures that are worthy of mentioning here: heteroatomic metal overlayers^{86,89,90} as in core/shell structure with the general formula of $M@M'$, and sandwich structure (see Scheme 1.3).^{86,90,91} The former has been defined as a shell of one guest metal at exactly one monolayer coverage over a core of another host metal.⁹⁰ This description should be extended to include shell thicknesses beyond one monolayer coverage. One of the few well-characterized examples of bimetallic core/shell NPs includes $Au@Pd$ NPs by Schmid,⁹² and $Pd@Pt$ NPs by Toshima.⁹³ Throughout this paper, core/shell structure will be used as a reference to the overlayer structure. Similarly,

sandwich structure can be formulized as core/shell1/shell2. However, shell2 atoms can be identical to or different from core atoms. For bimetallic systems, only the former may exist, but trimetallic and other multi-metallic systems may have all three layers composed of different elements, and thus in theory as many shell layers as combinations of the present elements. Another structure determining factor in sandwich type structure is the thicknesses of successive layers. Shell thickness is determined by fine-tuning the synthesis methods, and therefore is an important variable in material design. Because of synthetic difficulties, thermodynamic and kinetic limitations, there are only a few reported bimetallic nanoparticles with the sandwich structure.⁹¹ Nevertheless, it is an open area of synthetic chemistry, and in the light of recent advances in nanoparticle synthesis, it is likely that there will be more reports on such systems in the near future.

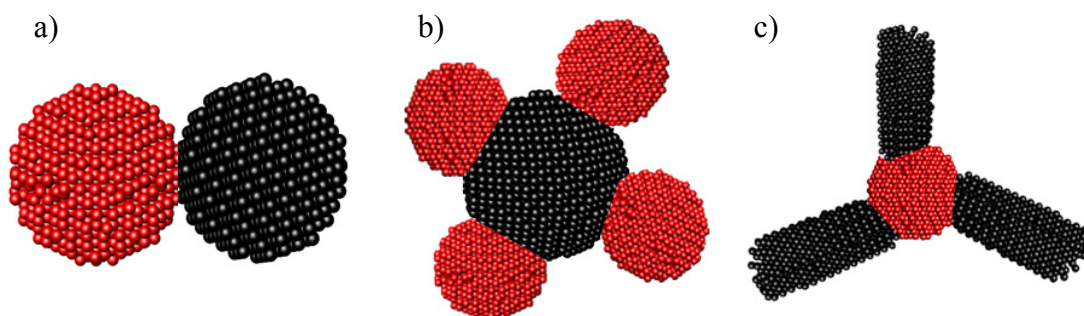
Scheme 1.3. Schematic illustration of core/shell clusters with (a) overlayer and (b) sandwich type architectures.



Lastly, contact heteroaggregates are distinct architectures from alloys and core/shell structures (Scheme 1.4). They serve as a transition between cluster-in-cluster

alloys (or core/shell overlayers NPs) and physical mixtures of monometallic NPs by means of their negligibly few number of heteroleptic bonds. Typically, two related structures with this architecture can be distinguished: contact dimers and dendritic aggregates. The former has been nicely shown by Gu et. al. on the Au/PtFe NPs system.⁹⁴ Nanocrystalline heteroaggregates of Au/Pt with Au nanoparticle cores and dendritic Pt nanoarms protruding over it exemplifies the later.⁹⁵

Scheme 1.4. Schematic illustration of bimetallic clusters of (a) hetero-dimer, and (b) and (c) hetero-aggregate architectures.



1.3.2. Thermodynamics and kinetics of formation and stability

Similar to monometallic NPs as discussed above, bimetallic NPs are stabilized in colloidal suspensions by ligation and solvation effects. Differently, structural stability of bimetallic nanoarchitectures strongly depends on the thermochemistry of metal atoms with their local environment. Atoms in bimetallic nanoparticles are energetically correlated to each other in the bulk and on the surface, and to ligands and other adsorbate molecules on the surface. Structural incoherency defines the degree of

mixing of any two metals. Thus, cohesive energy, which is defined as energy gained by arranging atoms in a crystal, can be used as a measure of relative stability of any bimetallic phase. Molecular Dynamic calculations and TEM observations on Au/Pd bimetallic NPs have shown that cohesive energy varies for different bimetallic architectures.⁹⁶ Therefore, structural preference of Pd@Au core/shell NPs over PdAu alloys and inverse Au@Pd core/shell NPs in a mixture of bimetallic Au/Pd NPs is solely attributed to maximum structural incoherency of the former.⁹⁶ High structural incoherency of monometallic phases partially accounts for the lack of thermodynamically stable binary alloy phases in the solid state of 2nd and 3rd group middle TMs, such as Ru, Rh and Ir, etc.⁹⁷ Cohesive energy is maximized for these elements and thermodynamic pathway of alloy formation is shut down.

Thermodynamic stability in the solid state dictates what can be fabricated and what can not be in a bulk alloy under thermodynamically controlled conditions. At the nanoscale, surface effects become dominant, so that surface-related crystallization kinetics are determining in formation of phases that are otherwise thermodynamically unfavorable. Kinetic variables such as monomer diffusion and atomic adsorption, and entropy are in favor of mixing for growing nuclei below a critical size. Certain kinetic phases then become synthetically accessible by adjusting reaction conditions. One such kinetic phase is the AuPt alloy.⁹⁸ The thermodynamic binary phase diagram overrules the formation of the AuPt alloy phase at any composition of Au and Pt below 900 °C. However, colloidal AuPt alloy NPs has been reported to form at temperatures well below 300 °C.⁹⁸ Fast nucleation and subsequent slow growth, induces random alloying of Pt and Au atoms. Given the low coordination number of surface atoms and the critical size of

the individual clusters, energy lowering via formation of hetero-nuclei is greatly enhanced.⁸⁶ Similarly, PtRu alloy NPs can be synthesized at any composition and size under kinetic control although thermodynamics dictates mixtures of Pt and Ru under identical temperature and pressure conditions in solid state.⁸⁴

Other kinetic variables related to metal-metal bonding such as lattice mismatch and thermal diffusion usually determine the stability of bimetallic phases: especially those with core/shell and heteroaggregate architectures. Lattice mismatch puts a thermodynamic barrier to miscibility of two metal atoms. Metal atoms crystallize in close packed lattices, and employ one of the close-packed structures, namely body-centered cubic (BCC), face-centered cubic (FCC) and hexagonal close-pack (HCP). Atomic sizes as well as crystal structures of individual phases cause a misfit at the interface of lattices. Implications of such a mismatch on alloy architectures are partial segregation to cluster-in-cluster structures, or total transition to core/shell architecture. For nanoparticles employing the core/shell architecture, this effect is less pronounced due to the release of lattice strain via a defect/vacancy-induced distortion/relaxation mechanism while still retaining the architecture.⁹⁹ However, different modes of hetero-nucleation, namely layer-by-layer epitaxial growth and pseudo-morphic growth are partially governed by lattice mismatch between the core and shell.¹⁰⁰ Lattice strain induced by misfit epitaxial and pseudo-morphic growth mechanisms have been studied and shown on various bimetallic systems.^{99,101-103} Jacob et al. have recently reported on Pt overlayers on HCP Ru crystal the pseudo-morphic growth of Pt shells to 3-5 layers off the surface. The FCC Pt unit crystal is larger than HCP Ru unit crystal by 2.7%, which generates a mismatch of lattices, so that Pt atoms feel strain as they are nucleated on Ru.

First, Pt atoms claim the hexagonal packing with the lattice parameters of the Ru crystal. In other words, the Pt lattice is distorted to accommodate the lattice strain. Then, as strain is relaxed via outgrowing layers, the FCC Pt lattice is restored from distorted pseudo-morphic phase.⁹⁹ Other examples from surface science includes Pd overlayers on a Ru crystal.¹⁰⁴ Bimetallic NPs bridge surface science and nanoscience. Bimetallic Au/Pd and Pd/Pt NPs are the most studied examples. Au@Pd NPs are thermodynamically stable and thus deposition of Pd shells on Au core follows a heterogeneous epitaxial pathway.¹⁰⁰ Pseudo-morphically grown overlayers of Au on Pd cores are, on the other hand, kinetically stabilized.¹⁰⁰ The non-epitaxial nature of deposition of Pd on the Au nanoparticle core is explained by a combination of relative sizes of the metal atoms and magnitude and sign of cohesive energies.^{96,100} Similarly, epitaxially grown Pd@Pt core/shell NPs and inverse Pt@Pd core/shell NPs are accessible via kinetic synthesis routes. Only Pt@Pd core/shell NPs can be synthesized by epitaxial type of growth given the smaller structural coherency of the inverted core/shell structure.¹⁰⁰ However, stable Pd@Pt nanoparticle colloids can also be synthesized by a small modification of reaction conditions. Slow reduction of Pt precursor salt by use of a mild reducing agent combined with the negligible lattice mismatch surpasses the shortcomings of thermodynamics, and helps in forming an otherwise inaccessible bimetallic phase.¹⁰⁵

Kinetic stabilization via a combination of temperature and diffusion effects of bimetallic phases at nanoscale has also been reported. One example is the kinetically stable Cu@Pt core/shell NPs by Zhou et al.³⁴ Cu and Pt are miscible in the whole composition range at temperatures below 700 °C, so that the thermodynamic phase of bimetallic Cu/Pt is the ordered alloys. In contrast to what solid state thermodynamics

dictates, both Cu@Pt core/shell NPs and inverse Pt@Cu core/shell NPs can be synthesized via low-temperature solution methods, such as poly-ol reaction. However, upon annealing, only Cu@Pt NPs maintain stability against alloy formation.³⁴ The apparent stability against such transformation is shown to be rooted in the relative thermal diffusion rates of Cu and Pt atoms, which invokes nanoscale Kirkendall effect.¹⁰⁶ The Kirkendall effect in bulk material arises from thermal diffusivity difference of two phases constituting a binary phase. In the Cu@Pt NPs example, nanoparticle cores of Cu atoms with the lower melting point and higher vacancy concentration at a given temperature is kinetically trapped inside shells of Pt atoms with small inward diffusion rate.³⁴ On the other hand, lack of such a kinetic stabilization effect for the inverted core/shell NPs, makes them prone to phase transformation to thermodynamically stable structure. Similar reasoning holds in understanding the morphological stability and selective formation of spherical nanocrystals vs. dense/hollow rods of ordered Sn_xM_y alloys (M=Co, Ni, Cu, Ag, Pt, Ru; $x=0.2-0.75$, $y=0.8-0.25$).¹¹ Based on their systematic study on ordered alloy phases with the formula Sn_xM_y alloys (M=Co, Ni, Cu, Ag, Pt, Ru; $x=0.2-0.75$, $y=0.8-0.25$), Chou et al. has suggested use of relative diffusion rates as a predictive guideline to reaction temperature for morphology and composition of nanocrystalline bimetallic structures.¹⁰⁷

Finally, kinetic control over formation and stability of bimetallic nanoparticles to be discussed here is introduced by ligands and other small molecules such as H_2 , O_2 and CO. Adsorbate-induced formation of bimetallic NPs has been reported by Toshima et al. on the Pd@Pt core/shell NPs.⁹³ In their inspiring study, H_2 gas that is bubbled through the colloidal solution of Pd NPs and Pt precursor salt sacrificially and

selectively reduces Pt ions on the surface of Pd nanoparticle cores, and thus helps hetero-nucleation of Pt.⁹³ NO₂ gas bubbled through or generated by the reaction of HCl and HNO₃ is also shown in an independent study to have a similar effect on the formation of Pt@Pd NPs. Furthermore, preferential binding of NO₂ to oxygen-adsorbed 111 surface facets of Pt is used to hinder Pd growth over (111) direction, and to synthesize Pt@Pd nanowires, exclusively.¹⁰⁸ Most recently, Somorjai and co-workers have shown on the size-controlled Rh₅₀Pd₅₀ gradient alloy nanoparticles with Rh-rich surfaces the adsorbate-induced surface restructuring.¹⁰⁹ In their study, the surface composition and particle architecture (Rh-rich pseudo-core/shell vs. 50:50 alloy) and surface chemical state (mostly oxidized vs. mostly metallic) of alloy nanoparticles have been reversibly controlled by using reactive gases such as NO, CO and O₂.¹⁰⁹

1.3.3. Magic Numbers for size and composition control

Size and composition are correlated for bimetallic nanoparticles, and thus size follows a geometrical pattern. Molecular metal clusters, which are the building blocks of larger nanoparticles, composed of successive structural shells of atoms arranged in a geometrically controlled way around a central core atom, so that they form symmetry-defined structures. Metallic nanocrystals are, similarly, constructed by layer-by-layer closed-packing or non closed-packing of hard spheres and are extended in larger spatial dimensions than molecular clusters usually are. Algorithms exist for counting atoms in a cluster with a definite symmetry.

Some particle shapes with definitive symmetries and shell-growth patterns are the icosahedron, cuboctahedron, octahedron, tetrahedron, decahedron, etc. The

cuboctahedron, octahedron and decahedron exhibit the face-centered cubic (FCC) closed-packing of atoms. The cuboctahedron, which is one of the most frequently observed form of nanoparticle shapes has the layer sequence of abcabca... Every third layer is on top of one another in a close-packed arrangement.¹¹⁰ The number of atoms, N , in each shell is given by the formula,^{110,111}

$$N=10n^2 + 2 \quad \text{eq. 1.3}$$

The total number of atoms, N_T in whole cluster is then,¹¹¹

$$N_T= 10\Sigma(n^2+2) + 1 = 5*n*(n+1)*(2n+1)/3 + 2n + 1 \quad \text{eq. 1.4}$$

with n being the shell index. One famous example is the Pd₋₅₆₁ cuboctahedra, which is composed of 5 shells of Pd atoms around a central core atom.^{92,112}

Another related layer sequence is ababa... which describes hexagonal closed-packing of the icosahedra.

The icosahedral structure has the same magic numbers as the cuboctahedron. In contrast to cuboctahedron, it has 5-fold lattice symmetry and thus no translational symmetry. Thus is not HCP. Au₅₅ nanoclusters have shown to adopt an icosahedron geometry with well-defined ligand shells.¹¹¹ Other non-close-packed particle shapes with a 5-fold symmetry is the decahedron, and it has a different shell growth algorithm than that of the icosahedron.¹¹⁰

Examples of bimetallic core/shell and or alloy nanoclusters with well-defined particle shapes and geometries are very scarce due to statistical distribution of particle sizes and compositional inhomogeneities related to kinetic and diffusion limitations. Au@Pd core/shell nanocubes,^{100,108} and Au@Ag core/shell truncated nanocubes¹⁰⁰ with a well defined Au octahedral in the core are two among a few reported symmetry-defined

nanoclusters. Nanoparticles vary in size and atomic arrangement in a colloidal suspension, shell growth algorithms can only be used in approximating the average structural and compositional make-up that nanoparticle colloids exhibit. In reality, “Magic Numbers”¹¹¹ are only a guide to synthetic chemists, and should not be taken as real picture of existence of nanoparticle colloids. In their study of the synthesis of Pd@Pt NPs, Wang et al. have employed a particle size weighed “Magic Number” approach to estimate the composition of Pd@Pt nanoparticle colloids with ca. monolayer coverage of Pt.⁹³ They have used the formula,

$$R = \frac{\sum_{f_i=f_{\min}}^{f_i} f_i [(10(n_i+1)^2 + 2)]}{\sum_{f_i=f_{\min}}^{f_i} f_i [5n_i(n_i+1)(2n_i+1)/3 + 2n_i + 1]} \quad \text{eq. 1.5}$$

where R is the molar ratio, f_i the number density of atoms with particle size, d_i and number of shells, n_i , assuming a particle shape of cuboctahedron and bulk metal-metal bond distances.⁹³

1.3.4. Synthesis of Bimetallic NPs

Synthesis of bimetallic NPs of various architectures can be achieved via wet chemical routes, in particular, the poly-ol reduction method can be universally employed to selectively synthesize different architectures of transition group bi-metallic NPs. The poly-ol method is a generic name referring to use of poly-ol solvents, usually di-ols, such as ethylene glycol, 1,2-propanediol, and 1,4-butanediol formation of ligand stabilized

nanoparticle formation. Ethylene Glycol is commonly the choice of solvent in bimetallic nanoparticle synthesis of platinum group metals (PGMs), because of its high boiling point (198 °C, 1 atm), low viscosity at boiling and high solubility of transition metal salts. EG thus provides strong reducing power at temperatures as low as 80 °C.

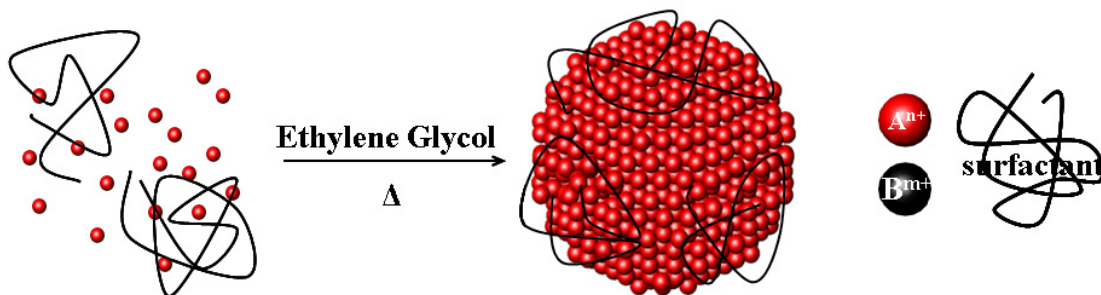
Other solvents and wet chemical methods that are widely employed in synthesis of NPs in catalytically-relevant sizes are water, as is used in chemical and electro-chemical reduction methods, high boiling hydrocarbons such as octadecene, hexadecane, octyl ether and diphenyl ether. Water has unique physical properties which makes it solvent of choice in synthesis of nanocomposites especially of biological and medicinal importance. Water-based bimetallic nanoparticle synthesis offers advantages in performing electro-chemistry. On the other hand, it fails to provide structurally and chemically stable colloids for nanocomposites of oxophilic TMs. Air-sensitive 1st group metals and 2nd early group metals should be protected from oxidative chemical environments (and structural) transformations through the way of high boiling dry hydrocarbon solvents by strongly binding ligands. Other pronounced advantages of performing synthesis in high boiling hydrocarbon solvents is the variety of particle shapes and structures that are kinetically accessible, and the functional diversity of soluble ligands and the broad window of reaction temperatures to control the formation of such phases.

In contrast to monometallic NPs, the synthesis of bimetallic NPs requires strict control over reaction conditions and synthetic techniques in order to access the desired particle architectures by design. There is no well-established generic method to synthesize NPs with core/shell architecture, especially those that possess catalytic

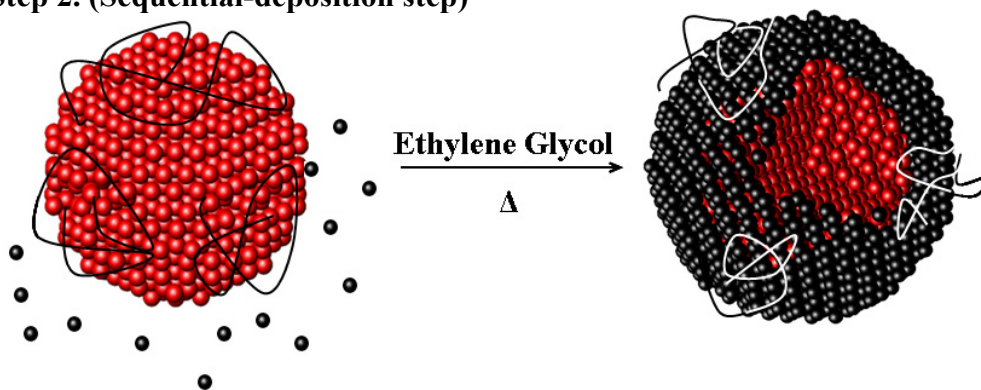
activity. One strategy is the sequential deposition of one metal type over pre-synthesized nanoparticle seeds of the other. In the sequential deposition method,^{93,113} reaction conditions should be manipulated to favor hetero-nucleation of the guest metal atoms over the preformed seeds of the host atom. Scheme 1.5 shows a schematic illustration of the sequential deposition method using poly-ol reduction technique. Thus, the nucleation step should be slowed down and the growth step should be almost simultaneous. Employing temperatures that the host metal precursor salt will not self-nucleate, but will slowly and controllably be nucleated on the surface of the seed particle greatly satisfies this criterion. The seed-mediated growth method as described by Fan et. al. in their study of epitaxially grown Au@M (M=Pt and Ag) nanocrystals,¹⁰⁰ the seeded growth methods reported by Lim et. al. for the synthesis of nanocrystalline Pd@Pt core/shell plates,¹⁰⁵ and by Habas et. al. for the inverted Pt@Pd core/shell nanocrystals¹⁰⁸ are different names given in the literature of the sequential deposition/reduction techniques.

Scheme 1.5. Schematic illustration of the sequential method employed by the poly-ol (i.e. ethylene glycol) reduction technique, showing the two-step reaction.

Step 1.

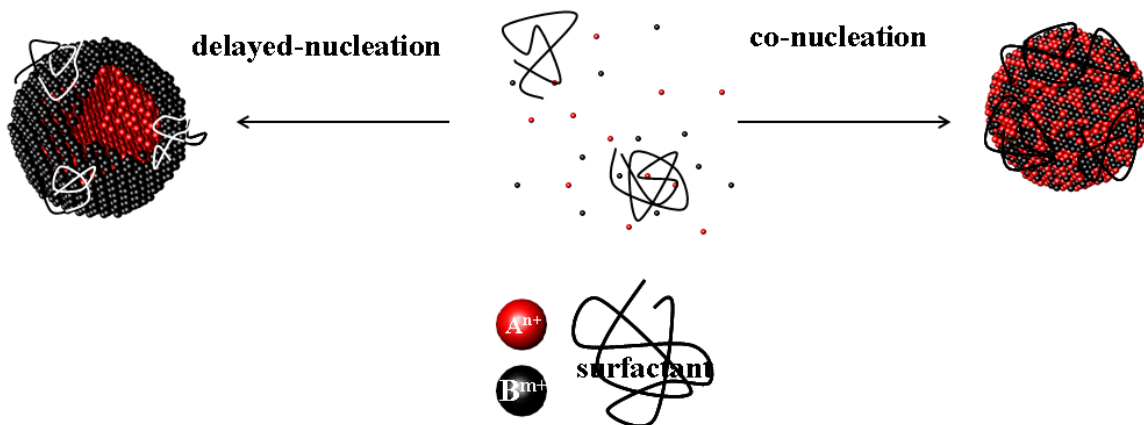


Step 2. (Sequential-deposition step)



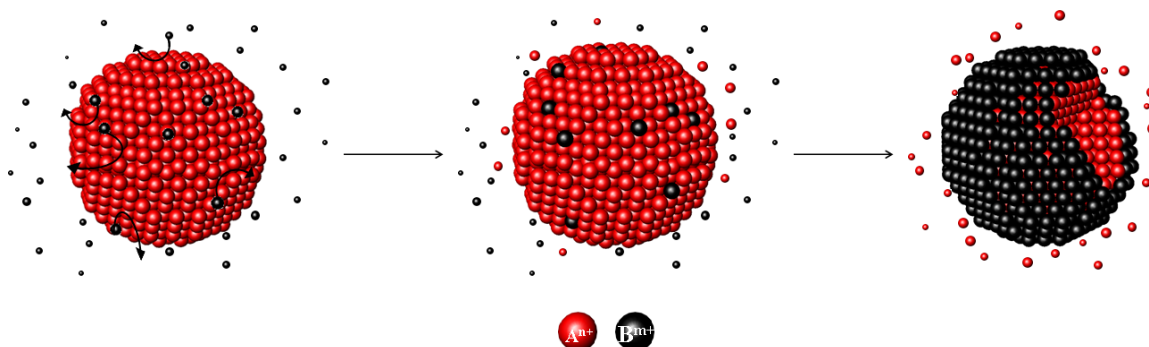
However, the sequential deposition method is not the only route to the core/shell architecture. There are reports of core/shell nanoparticle formation by the way of delayed-nucleation method. Metal salt precursors differ by their reduction potentials and thus temperatures of nucleation from their supersaturated solutions. In the delayed-nucleation approach, proper metal precursor salts are chosen by design and implemented in synthesis of the core/shell NPs (see Scheme 1.6). ‘Delayed-nucleation’ of the metal monomers with higher reduction potentials and higher kinetic barrier to nucleate at certain temperatures has been demonstrated by Garcia-Gutierrez et. al. on a study of Au@Pt core/shell NPs in EG.¹¹⁴

Scheme 1.6. Schematic illustration of some metal nucleation pathways; delayed-nucleation vs. co-nucleation.



In addition, redox reaction pathways lead to the formation of core/shell architectures. Chemical displacement of the core metals on the surface by the guest metal ions of higher reduction potentials can simultaneously take place (See Scheme 1.7). Such a transmetalation route to the formation of metallic shells at monolayer coverage has been reported.¹¹⁵ A sacrificial hydrogen reduction strategy on the surface of Pd nanoparticle seeds has been employed to protect Pd atoms from being displaced from the surface by Pt ions.⁹³ Similarly, galvanic displacement of surface atoms of the preformed nanoparticle seeds also leads to core shell architecture similar to transmetalation routes. Nanocomposite Au/Pd via galvanic replacement by $AuCl_3$ in toluene of thin Pd nanowires have been reported to adopt an alloy structure,⁸⁸ showing rich and unpredictable nature of chemical/galvanic atomic displacement reactions.

Scheme 1.7. Schematic illustration showing the formation of core/shell nanoparticles via a transmetallation reaction route.



1.3.5. Characterization of Bimetallic NPs

It is also difficult to characterize as-synthesized bimetallic nanoparticle colloids and show the actual particle architecture which might be different from the one proposed, and the actual chemical composition which also might deviate from the nominal one. To fully characterize a bimetallic nanoparticle system, it generally requires a thorough analysis that has been performed carefully by employing various analytical, diffraction and imaging techniques. Transmission electron microscopy (TEM), scanning electron microscopy (SEM) are a few techniques that give morphological information of nanoparticles. TEM in the diffraction mode is capable of giving crystallographic structure; in the scanning mode, additionally giving compositional and architectural make-up of nanoparticles. Powder X-ray diffraction (XRD) is a bulk technique to determine the crystal structure of materials, therefore, is also useful in determining average particle size, composition and structure of nanocrystalline materials. Next, spectroscopic investigation of surface-adsorbed probe molecules such as CO is well-established and widely-applied to distinguish between different metal atoms on the

surface of nanocomposites. The $\nu(\text{CO})$ modes are sensitive to the identity and electronic structure of metal atoms that it binds, so that the electronic make-up of bimetallic nanoparticles can in theory be traced by CO-probing IR and/or Raman spectroscopy. Another surface sensitive technique is UV-Vis spectroscopy as applied to Surface Plasmon active metals such as Au, Cu and Ag. Finally, it is sometimes necessary to complement experimental results with simulations in an attempt to fit a model structure. In this section, some experimental techniques and theoretical tools that are in current use or have potentials to be used in characterization of bimetallic nanoparticles will be in detail investigated.

1.3.5.1. X-rays for bulk structural/chemical analysis

One of the most commonly employed X-ray technique in the field of nanoscience is the powder XRD and is mainly used for phase identification and structure evaluation of nanocrystals. One particular use of the XRD technique is to distinguish alloy nanocrystals with the ordered structures (i.e. intermetallics) from their disordered counterparts (i.e. random alloy nanocrystals). For example, it has been recently shown by Schaak and co-workers a new nanocrystalline intermetallic phase of Sn/Ni system. XRD technique has been used to refine the crystal structure of $\beta\text{-SnNi}_3$ NCs by replacing the Pt atoms by Ni in the known $\beta\text{-SnPt}_3$ phase.¹¹⁶

Relative peak intensities of X-ray diffraction patterns are subject to change by surface effects, so that even the determination of nanoparticle morphology is possible. Middle transition metals crystallize in FCC structure. XRD pattern of FCC metals give rise to two peaks at 2θ angles below 50° : 111 reflections and 200 reflections with ca.

40% relative intensity in solid state. At the nanoscale, as the particle size decreases, the surface-to-volume ratio increases, so that 111 vs. 200 reflections become strongly dependent on the morphology. Such phenomena have been observed on Au@Pd core-shell nanocubes grown over Au nano-octahedra.¹⁰⁰ Au octahedra have exclusively (111) surfaces. Thus, 111 reflections dominate the XRD pattern. Cube-shaped Au@Pd NPs with multiple monolayers of Pd shells, on the other hand, have dominant 200 reflections for the Pd phase as expected for exclusively (100) Pd surfaces.¹⁰⁰

The XRD pattern of bimetallic nanocrystals as well as monometallic nanocrystals can be simulated by use of Debye function, which has the form:

$$I_N(Q) = \sum_{n,m=1}^N \frac{f_m f_n [\sin(2\pi Q r_{mn})]}{[2\pi Q r_{mn}]} \quad \text{eq. 1.6}$$

where θ is the Bragg's angle, λ the wavelength of X-rays, f_n and f_m are the scattering amplitudes of atoms m and n , and r_{mn} the distances run over pairs of m and n . The Debye function can be computed for model clusters of definitive sizes and shapes. The so-called Debye Function Analysis (DFA) is a fitting procedure to extract structural information regarding lattice parameters and mass fraction of diffracting phases. This analysis has proven to be useful in the full structural analysis of bimetallic Pt/Ni NPs.

Another simulation tool that is derived from X-ray diffraction is atomic pair distribution function (PDF), which is usually described as histograms of interatomic distances and similar to the radial distribution function, -probability of finding atoms in a radius, r , from another atom, depicted in Figure 1.2b. The need for PDF analysis is urged from the fact that scattering from non-periodic materials like nanocrystals has a diffuse

contribution that is equally important as the Bragg diffraction, and is thus contributing to total scattering. Pair distribution function, $G(r)$, is the Fourier transform of the experimental scattered intensity (Figure 1.2c and 1.2d). Experimentally, it requires use of synchrotron sources, highly energetic monochromatic X-rays, and therefore various polarization, absorption and scattering corrections have to be applied to the data. Basically, the structure function, $S(Q)$, as a function of diffraction angle, θ , (i.e. $Q=4\pi\sin\theta/\lambda$, in the reciprocal space) is first derived from the scattered intensity data as measured by XRD and PDF, $G(r)$, in the real space is then calculated according to the formula:¹¹⁷

$$G(r) = \int_{Q_{\min}}^{Q_{\max}} Q[S(Q)-1]\sin(Qr)dQ \quad \text{eq. 1.7}$$

PDF analysis is promising in local structure determination of nanocrystalline composites as small as a few hundred atoms. However, constituting model clusters with sophisticated bimetallic architectures like core/shell and refining them against the experimental data have built-in difficulties, so that its use is at the moment limited.

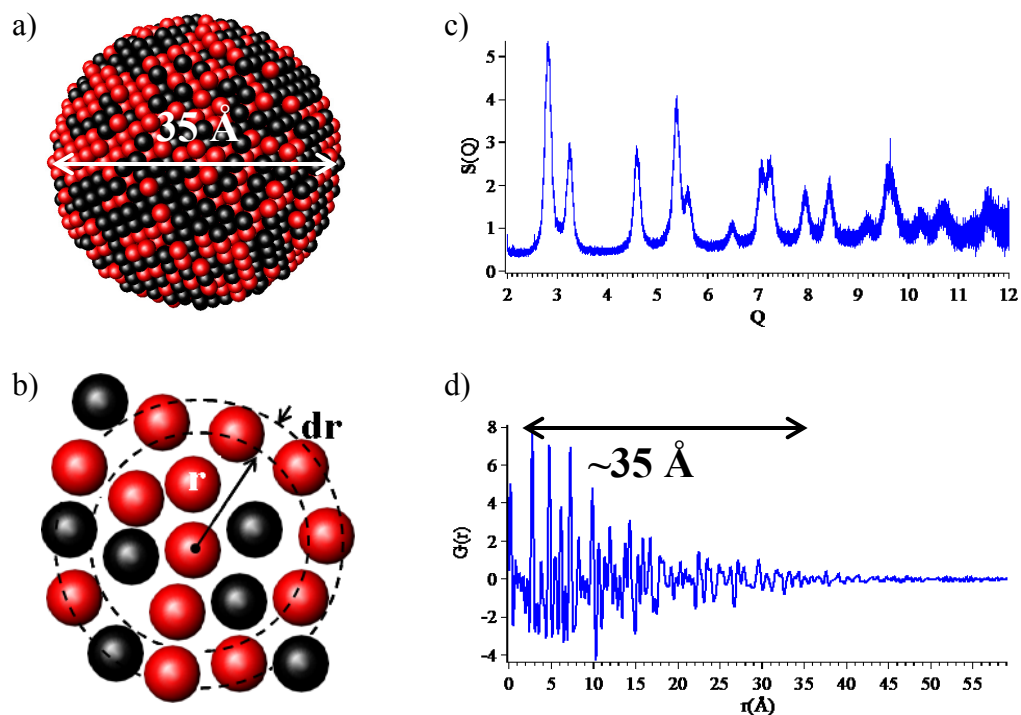


Figure 1.2. Schematic illustrations of (a) a model alloy cluster of 35 Å diameter and ~1700 atoms, (b) the radial distribution function. (c) The representative structure function of the alloy cluster depicted in (a). (d) The atomic pair distribution function calculated from (c) by using the equation 1.7 represents the atomic correlations of the alloy cluster depicted in (a).

Extended X-ray absorption fine structure (EXAFS) analysis, which uses a similar intensity function as that of PDF, is a fundamentally different technique. It is based on X-ray absorption rather than diffraction. Transition metals like other elements have unique inner core electronic structures. Metals have closed-packing arrangement of atoms with small thermal distortions from their equilibrium positions. In such a closed-packed rigid environment, absorption of X-rays from atoms scattering off back and forth from the surrounding atoms can be mapped to determine the local structure. Multi-scattering from atoms complicates the X-ray absorption spectrum in the form of

oscillations, but intensity dampening follows an inverse square law of distances, which falls off rapidly to allow real-space data analysis. C-supported bimetallic PtRu nanoclusters have been studied by EXAFS to elucidate their local structural make-up.¹¹⁸⁻¹²⁰ A core shell inversion upon annealing has been found in the case of 1.5 nm PtRu alloy clusters (see Scheme 1.8), which shown how powerful the EXAFS can be for characterizing small alloy clusters.¹²⁰ In their study, the reductive decomposition of the molecular PtRu₅ precursor salt produced bimetallic PtRu₅ alloy nanoparticles with Pt-rich surfaces at 100 °C, and Pt-rich cores at 400 °C (Scheme 1.8 and Table 1.1), as monitored in-situ by EXAFS.¹²⁰

Scheme 1.8. Schematic illustration of thermally-induced phase transformation of 36 atom PtRu₅ cluster studied by Nuzzo and co-workers.¹²⁰

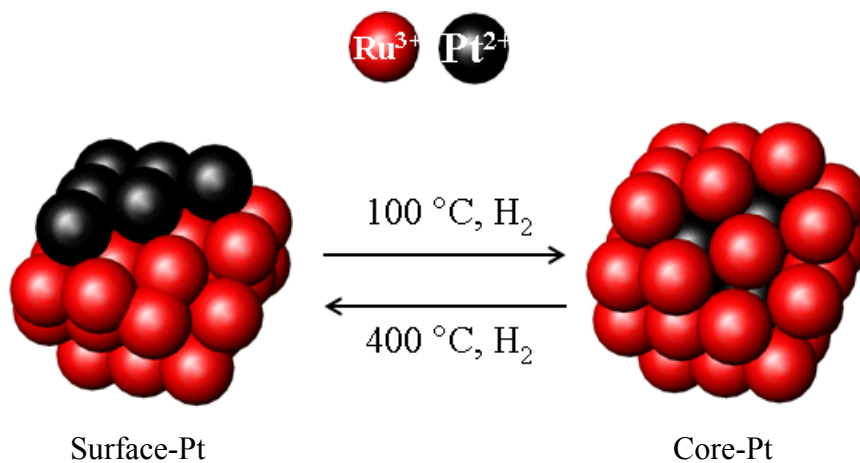


Table 1.1. 1st Shell coordination numbers comparing EXAFS-derived data and cluster model-calculations

	1.5 nm PtRu ₅ at 400 °C	36 atom PtRu ₅ Surface-Pt	1.5 nm PtRu ₅ at 100 °C	36 atom PtRu ₅ Core-Pt
N _{Ru-Ru}	5.9(6) ^a	7.3 ^b	2.74(1) ^a	4.8 ^c
N _{Ru-Pt}	0.9(3) ^a	0.7 ^b	2.63(2) ^a	1.7 ^c
N _{Pt-Pt}	2.1(7) ^a	1.6 ^b	3.8(1.3) ^a	4.0 ^c
N _{Pt-Ru}	4.4(1.4) ^a	3.3 ^b	2.7(7) ^a	8.0 ^c

^a Reference 119. ^b calculated from ATOMs-generated 36 atom PtRu₅ cluster (Surface-Pt cluster in Scheme 1.8) using DISCUS.¹ ^c calculated from ATOMs-generated 36 atom PtRu₅ cluster (Core-Pt cluster in Scheme 1.8) using DISCUS. The 1st shell coordination numbers are presented as N_{Ru-Ru}, N_{Ru-Pt}, N_{Pt-Pt} and N_{Pt-Ru}.

Finally, X-ray photoelectron spectroscopy (XPS) is a technique based on absorption of X-rays by composite materials and detection of the emitted electrons, which are elemental fingerprints. Elemental identity, chemical states and atomic compositions of nanocomposites can be elucidated using XPS. Because inelastic mean free paths of electrons are in the range of 1-10 nm, only those coming from the topmost layers of material can be detected. Wieckowski and co-workers have recently studied by XPS various architectures of Pt/Ru nanoparticles, namely PtRu alloys, Ru@Pt core/shell and inverse Pt@Ru core/shell NPs, to determine the electro-chemically most active architecture and chemical state. They have concluded that the Pt@Ru core/shell NPs with

the fully reduced metallic Ru have exhibited the highest activity for methanol oxidation.¹²¹ Furthermore, XPS equipped with Ar⁺ plasma etching can be used to map the elemental and chemical make-up of nanoparticles. Zhou et al. have used XPS depth-profiling to demonstrate the stability of kinetically trapped phase of 8.8 nm Cu@Pt core/shell nanoparticles as compared to thermally-driven gradient alloy formation of the inverse core/shell phase.³⁴

1.3.5.2. Infrared surface probe studies

Another characterization method employed to bimetallic nanoparticles is CO adsorption and subsequent determination of CO stretching frequencies in FT-IR. CO is a well-known probe for distinguishing between different types of a metal and bimetallic alloy NPs, but rarely applied to the field of core/shell materials. CO molecules bind to metal via σ -bonding. In addition to π -back bonding from a transition metal causes a decrease in CO bond order and thus the CO stretching frequency shifts to a lower wavenumber IR. The degree of the π -back donation depends on the d-electron density of the metal, and varies from metal to metal.¹²² For example, CO stretching frequencies on monometallic Pt and Ru nanoparticles have been documented to differ by ca. 30 cm⁻¹.¹²³ A study of composition series of PtRu alloy nanoparticles by Chaudret and co-workers have determined single phonon modes whose $\nu(\text{CO})$ positions are intermediate to those on Pt and Ru, and therefore scale with the nanoparticle composition.¹²⁴ There are also different binding geometries available for CO, which contribute to complexity of spectral interpretation. In contrast to the dominantly linear mode of CO binding to Pt, CO prefers bridging mode of binding on Pd. Toshima and co-workers studied a complete

architectural series of the Pd/Pt bimetallic NPs. What they have found regarding feasibility and reliability of CO-probed FTIR spectroscopy technique is inspirational to design of architecturally controlled bimetallic NPs. However, there are other shortcomings and complications of minor importance to the CO-probing approach. Shifts in $\nu(\text{CO})$ that are induced by ‘lateral effects’ can occur which makes electronic interpretation of IR spectrum difficult. Lateral effects are mainly caused by differential CO coverage, which can be of electronic origin and/or can be related to passivation by ligand and solvent molecules, and solvation. However, surface probing at the atomic level still offers a technique to qualitatively distinguish between architecturally distinct bimetallic nanoparticles.

1.3.5.3. Electron Microscopy for single (multi) particle analysis

TEM is widely used in analysis of particle size distributions and particle morphologies. Particle size analysis is usually performed by counting finite numbers of particles, which provides statistically poor results. On the hand, XRD size determination using a Debye-Scherrer analysis can be complemented to TEM analysis in order to improve statistics of counting. Another shortcoming of particle size determination using TEM is that electron images from TEM analysis are two-dimensional, and thus only projected areas can be used to measure particle diameter and/or shape factors, which is not necessarily the three dimensional size.

Apart from its function as being an imaging tool, TEM helps elucidate the crystal structure of nanocomposites in the bright field mode of operation. Electron beams that are elastically scattered in or close to the Bragg’s angles reveal crystallographic

planes, generally named as Moire patterns. Thus, lattice parameters in the form of interplanar spacings can be calculated. Crystallographic elements such as defects, dislocations, twinning and preferred orientation can also be evaluated. For FCC metals, the (111) surface is crystallographically the lowest energy (thermodynamically the most favorable) surface, so that multiple (111) twinning is suggested to be a mechanism of self-control in the formation of low energy surface morphologies. PVP-stabilized Rh NPs in 1,4-butanediol have been shown by TEM to be thermodynamically stable polygons such as hexagons, pentagons and trigons of Rh NPs that are multiply (111) twinned.⁶⁰ Similarly, nanoprisms and nanorods of Au with high surface energy (110) and (100) facets are thermodynamically stabilized by halide ion adsorption, which is believed, based on a through TEM analysis, to reduce surface energy during the preferred growth of Au.¹²⁵ Translation of these findings to bimetallic systems has been documented using TEM on spontaneously nucleated PVP stabilized nanoparticles of Pd/Au. It has been proposed for the formation of structurally incoherent, in other words thermodynamically unfavorable, bimetallic phase of Pd@Au that lattice defects in the form of crystal twinning introduces partial compensation for the structural instabilities. Thus, multiply (111) twinned Au overlayers on Pd core lowers free energy of formation of the structurally incoherent Pd@Au core/shell phase.⁹⁶

Scanning transmission electron microscopy (STEM) operating in the dark field mode, -conventional dark field (DF) and/or high angle annular dark field (HAADF) form of operations, can also be used to study the core/shell architecture. The conventional dark field technique is based on Bragg's scattering of electrons from atoms. The HAADF technique is known as Z-contrast imaging, because it physically describes a Rutherford-

like scattering of electrons from atomic nuclei which exhibits a Z^2 -power law.¹²⁶ Its use can be expanded to elements with similar atomic numbers if the so-called strain field is present at the interface of two core shell metals. Such a lattice distortion exists due to lattice misfit between Pt and Au, such that the Au@Pt core/shell NPs can be characterized by performing HAADF.^{114,126} Finally, STEM equipped with an energy dispersive spectroscopy attachment (EDS) is both an analytical and structural tool that provides elemental analysis as well as structural characterization via elemental mapping. STEM-EDS in the scanning mode is a sophisticated technique that provides mapping of the individual phases of a multi-elemental nanostructure. Compositional distribution of elements across a single nanoparticle can be plotted vs. inter-particle distances to deduce a two-dimensional picture of the nanostructure. The epitaxially grown Pd@Pt core/shell nanoplates,¹⁰⁵ and Au@Pd nanocubes with Au octahedral cores and epitaxially grown Pd shells have been characterized beyond a doubt by interpretation of such line spectra.

1.4. Importance and applications

Theories that computational chemist and surface scientists have developed can be the starting point for material scientists to design and subsequently synthesize their nanoparticle catalysts. The reactivity series of metals, structural dependence on particle architecture, and molecular pathways to reaction products and mechanistic evaluation of reaction conditions can now be determined by theoretical calculations, such that nanoparticle synthesis can be built upon these foundations. Coupled to advances in surface science, theoretical calculations will be better models for ‘catalysis by design’.

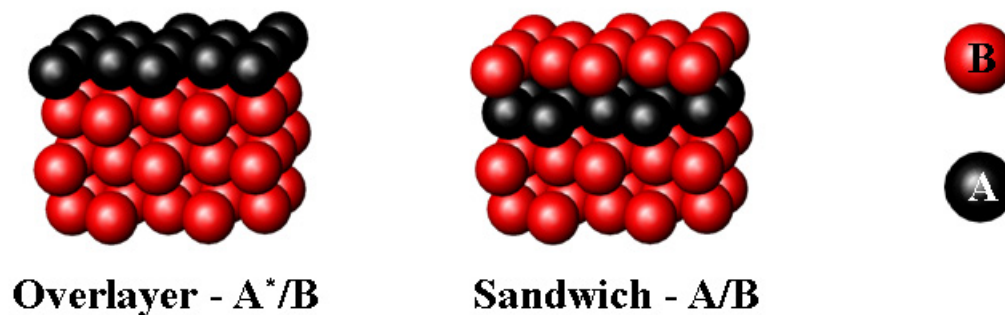
Historically, Goodman and co-workers have started what is known today as electronic structural effects in bimetallic catalysis. Goodman, Campbell and Rodriguez have studied the metal adlayers at monolayer coverages on single crystal metal surfaces using XPS. They have found in Cu, Ni and Pd overlayers on Rh(100), Ru(0001) and W(110) that the XPS core level binding energies shift from their respective bulk values. Thus, the extent that core level binding energy shifts correlate with the desorption temperatures of CO from the respective overlayer surfaces.¹²⁷ They have explained the observed trends in terms of the electronic perturbation that are induced by a combination of adlayer-adlayer and adlayer-substrate interactions.¹²⁸ Later, they reported an activity series in CO adsorption energies on Pd overlayers at monolayer coverage over Ta(110), Mo(110), W(110), Re(0001) and Ru(0001). Pd 3d_{5/2} binding energies have observed to shift to higher values in the order of Ru<Re<Mo<W<Ta. Goodman and co-workers have attributed this trend to charge transfer interactions between the substrates and the Pd adlayer. In contrast to bulk alloys, which electronegativities of the constituting metal atoms dictate the direction of charge transfer, they have proposed a different type of interaction model between bimetallic parts.¹²⁹ The electron rich Pd has acted as electron donor, and thus the magnitude of charge transfer from Pd adlayer to electron poor substrates has occurred at the extent of their electron accepting abilities.¹²⁹ It has also been documented on Cu monolayers over various single crystal metal substrates that Cu has accepted charge from electron rich Ru, Rh and Pt substrates and have donated charge to electron poor Ta and Mo substrates.¹²⁹⁻¹³¹

Later, Hammer and Norskov have correlated the core level binding energy shifts to the variations of d-band center in metal overlayer structures using ab initio

Density functional Theory (DFT) calculations.¹³² According to the surface chemisorption and reactivity model developed by Hammer and Norskov, the surface reactivity can be measured by the position of d-band center relative to the Fermi energy,¹³³ such that the extent of the shift of d-band center below the Fermi level determines the strength of the interaction of surface-adsorbed H atom with the Pd/Re alloy.¹³⁴ Furthermore, Koper and coworkers have recently shown on bimetallic overlayers¹³⁵ and alloys^{135,136} of Pt/Ru system that the d-band model holds to explain CO and OH adsorption enthalpies, however, metal carbon and/or carbon oxygen bond strengths are not necessarily a measure of the surface reactivity of such adsorbates.¹³⁵

Recently, Mavrikakis and co-workers have reported weaker binding energies of H and lower dissociation energies, at the same time, in overlayers and subsurface alloys at monolayer coverage of TMs (Scheme 1.9), which they have called Near Surface Alloys (NSAs).⁹⁰ Their findings suggest that altered electronic structure by substrate of NSAs accounts for a new class of bimetallic structure which can bridge the high H₂ activation on PGMs and low H binding enthalpies on noble metals.^{90,137}

Scheme 1.9. Schematic illustrations of NSA overlayer and sandwich structures.



Bimetallic systems have thus been found to have the potential to have higher activity and selectivity. Experimental studies by Goodman and Somorjai on overlayers at varying monolayer coverage over single crystal metal surfaces have partially revealed the basics of catalytic enhancement. The reason beyond catalytic enhancement has long been explained as a relationship between electronic/geometric structure and catalytic functionality. From the experimentalist point of view, the electronic/geometric structure of bimetallic systems can be tuned to alter the chemical properties of individual metals. Given the different functionality of TMs for various catalytic reactions, the choice of metals along with the degree and form that they are incorporated are of fundamental importance. For example, Cu is known to be inactive in CO Methanation and ethane hydrogenolysis to form methane. Therefore, a decrease in the catalytic activity of the surface with CO coverage is to be expected for Cu/Ru(0001), simply because of blocking effect of Cu. Similarly, the role of Au diluents on Au/Pt(111) alloys and Au overlayers at submonolayer coverage over Pt(111) in the cyclohexane dehydrogenation reaction is to decrease the rate of carbon coking and in turn increase the rate of benzene hydrogenation.¹³¹

One bimetallic system used for electro-chemical methanol⁴⁶ and CO⁴⁵ oxidation reactions, which are the key reactions for the development of fuel cells, is PtRu alloy electrocatalyst, and were reported in the 1970s by Watanabe and Motoo. They observed an enhancement in CO tolerance of the Pt electrodes modified by Ru adatoms. They attributed this phenomenon to the bi-functional theory.⁴⁵ The authors have described it as the promotional effect of the more oxiphilic Ru adatoms in activation of H₂O toward CO oxidation. CO preferentially adsorbed on Pt surface sites are more

readily oxidized by OH molecules adsorbed on Ru surface sites irrespective of surface structure. In this sense, the so-called bi-functional theory invokes the structure insensitivity of bimetallic catalysis. Recently, Watanabe and co-workers have fabricated via a combinatorial sputtering approach bimetallic alloy electrodes of TMs, and studied their CO oxidation behavior.⁴¹ They have documented three classes of alloy surfaces in terms of the electro-catalytic activity. The most pronounced effect of alloying has been measured for bimetallic electrodes with the more oxophilic non-PGMs, which means that the bifunctional mechanism can not account for the observed activities at high cell potentials. The Pt-skin structures at such high potentials invoke a ‘ligand’ effect. In other words, the subsurface alloy structure induces an electronic alteration on the surface Pt, which in return changes CO coverage and CO oxidation kinetics.⁴¹ More recently, similar trends on bimetallic Pt₃M (M=Ni, Co, Fe, etc.) electrodes for the oxygen reduction reaction (ORR), which is the other half-cell reaction in fuel cells, has been reported.¹³⁸ The authors, in parallel with the findings of Watanabe and co-workers, have found an increasing ORR activity with the electronegativity of adatom, M, and thus attributed this to the electronically-induced reduction of the OH coverage.¹³⁸

Similar to the surface science view of heterogeneous catalysis, theoretical models based on first principle quantum chemical methods first derived the ‘catalysis by design’ strategy. Surface science derives its generic understanding of heterogeneous catalysis from an empirical approach rather than a rational design strategy. NSA theory and Norskov-Hammer theory of the surface reactivity are derived from first principle quantum mechanical calculations and therefore predict qualitatively the reactivity trends and activation series of bimetallic overlayers of TMs. In parallel with the findings of

surface science, DFT calculations lead to the structure insensitive nature of ethylene hydrogenation on the surface of bimetallic systems, such that alloys and overlayers improves the reaction kinetics by only shutting down some unwanted paths like coking. Sabatier principle which manifests a trade-off between high surface reactivity and high catalytic activity, dictates that optimum reaction kinetics will be achieved when reactive and noble metals are used in a certain bimetallic form.^{21,139}

The Norskov-Hammer theory of the surface reactivity can rationalize the activity trends in ethylene hydrogenation calculated for monolayers of Pd on single crystal substrates, M (M=Re(0001), Ru(0001) and Au(111)). Pd/Au(111) with the smallest gap between its Pd d-band center and the Fermi level is the most active surface, because ethylene and hydrogen adsorption and bond formation correlate with the Pd d-band center.²¹ Similarly, Pt overlayers at monolayer coverage on Cu(111) is modeled using NSA theory and DFT calculations to be a promising water-gas-shift (WGS) reaction, which is a key reaction in H₂ production from CO and H₂O.³¹

The theory is not clear when moving from single crystal surfaces and alloy electrodes to catalytically relevant nanoparticles in terms of the surface reactivity. The electronic ‘ligand’ effect is the most pronounced mechanism of enhancement for the catalytic activity of core/shell nanoparticles, which is the synthetic counterpart of NSAs. 8.8 nm Cu@Pt NPs with multiple overlayers of Pt exhibits a superior catalytic behavior toward rich-NO_x reduction reaction than monometallic Pt NPs with smaller sizes. Since the Pt shells are multi-layer thick, the electronic alteration by the substrate effect should be minimal as well documented for the CO chemisorption temperatures on Pd/Ru(111) at various Pd coverages above monolayer.¹³¹ The Cu/Pt NSA with Pt overlayers at

monolayer coverage has also been evaluated for the WGS reaction, and has been found to show the optimum reactivity.³¹ Similarly, the geometrical effects are known to diminish at the long spatial extents.^{99,101} Similar arguments can be derived for the CO tolerant behavior of AuPt alloy NPs,⁹⁸ but the PROX behavior of PtRu alloy NPs is irrespective of size and structure. The most pronounced bi-functional effect is seen with PtRu alloy NPs as CO and methanol oxidation electro-catalysts, however, the relative role of the ‘ligand’ effect is still not well understood.

In order to understand the catalysis phenomena at nanoscale, the synthesis of well-characterized nanoparticle catalysts are of fundamental importance. Bimetallic nanoparticles with architecturally controlled structures and compositions can now be achieved, such that core/shell, alloys and hetero-aggregate structures can be catalytically evaluated for basic surface reactions. Through this route, the necessary fundamentals to bridge the existing gap with the surface science studies and the DFT-calculated theories can be learned and can further be used to develop better catalysts.

1.5. Overview of the Thesis

In this Thesis, the syntheses, characterization and application to various heterogeneous catalysis reactions, such as PROX, de-NO_x and benzene hydrogenation of the bimetallic nanoparticles will be presented.

In Chapter 2, the synthesis and characterization of the Ru@Pt core/shell NPs comprising of various core sizes and shell thicknesses, as well as the PtRu alloy NPs with various compositions will be given. The full structure analyses of the 4.1 nm Ru@Pt NPs with ca. 1-2 MLs thick Pt shells and the 4.4 nm Pt₅₀Ru₅₀ NPs will also be presented. The

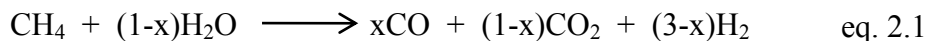
full catalytic evaluations for PROX and benzene hydrogenation reactions will be discussed. The preliminary catalysis results for de-NO_x reaction will also be presented. Chapter 3 presents the synthesis, characterization application to PROX reaction of the Rh@Pt core/shell NPs with a focus on the 3.2 nm Rh@Pt NPs comprising of ca. 1-2 MLs thick Pt shells. In Chapter 4, PROX reaction on the core/shell NPs with the general formula of M@Pt (M=Ir, Pd and Au; 1-2 MLs thick Pt shells) and Ru@M (M=Pt, Pd and Rh; 1-2 MLs and 2-3 MLs thick Pt shells, separately) will be presented and discussed in corroboration with the DFT calculation performed by Prof. Mavrikakis and Dr. Nilekar at the University of Wisconsin. Finally, the fully characterized Ru@Pt@Pd NPs with the sandwiched Pt shells at submonolayer coverages will be given along with a brief introduction to the heterogeneous catalysis using the trimetallic core/shell NPs. Chapter 5 is the conclusion of this Thesis.

Chapter 2

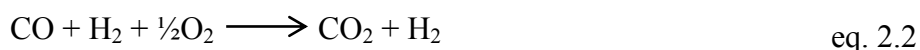
Synthesis and characterization of nano-structured Ru-Pt bimetallic particles for heterogeneous catalysis

2.1. Introduction

We describe the synthesis and characterization of a new Ru-core/Pt-shell nanoparticle (NP) catalyst (Ru@Pt) and demonstrate its unique properties by way of preferential CO oxidation in hydrogen feeds (PROX); a key reaction for the practical implementation of hydrogen fuel cells.¹⁴⁰ The PROX reaction is of importance since the majority of the world's hydrogen supply is currently obtained by reforming methane (see equation 1 below).



This “reformat” hydrogen contains significant quantities of CO (1000 – 10,000 ppm) that poison current fuel cell devices. The PROX reaction removes the CO through selective (preferential) oxidation according to the equation:

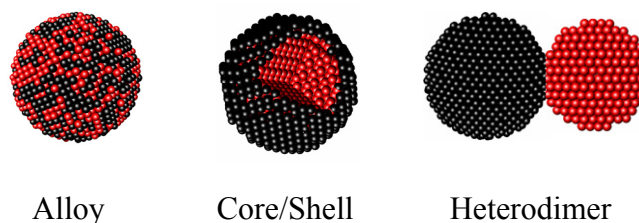


The difficulty of this process is to obtain a high rate of reaction while keeping a very high selectivity for oxidizing CO instead of H₂. The Ru@Pt NP catalyst accomplishes this task to give enhanced CO oxidation activity with high selectivity.

The development of bimetallic heterogeneous catalysts has historically been achieved mainly through chemical intuition and empirical synthetic approaches. Catalytic reforming,^{27,141} fuel cell electrocatalysis,^{141,142} hydrodesulfurization⁷¹ and

partial alkene oxidation¹⁴³ are a few examples of important technologies that rely on bimetallic systems^{89,130} developed over the last several decades. Recent advances in surface science techniques, analytical instrumentation and first-principles calculations provide mechanistic insight into the atomistic surface chemistry governing the catalytic activity and offer the groundwork for true rational design of heterogeneous catalysts.^{27,90,144-150} However, to develop bulk scale catalysts beyond fundamental surface science studies, it is necessary to develop and couple new NP synthesis methods with first principles theoretical design and surface science modeling studies. We report here a new nanoparticle (NP) catalyst comprising a Ru core covered with a shell of Pt atoms (*i.e.* a Ru@Pt core-shell NP) that has predictable catalytic properties that are markedly different from nanoparticles of “bulk” PtRu alloys or monometallic Pt and Ru mixtures of identical loadings and compositions. Graphical representations of the bimetallic nanoparticles are shown schematically below.

Scheme 2.1. Schematic illustration of various bimetallic particle architectures.



DFT studies reveal the origin of the enhanced activity for the core-shell NP's and provide a fundamental mechanistic explanation of the hydrogen-promoted CO oxidation reaction at low temperatures. The results presented in this chapter show that the

electronic structure, catalytic activity and chemical selectivity of bimetallic heterogeneous catalysts can now be designed, implemented and tuned through a combination of theoretical analysis and core-shell NP synthesis.

Expanding further on earlier experimental evidence,^{89,130} and by using Density Functional Theory (DFT), it has been shown recently that Pt monolayers on base metals, (*i.e.* bimetallics known as near surface alloys or NSAs), sustain the high activity of pure Pt for H₂ activation kinetics, whereas at the same time bind adsorbates (*e.g.* CO) much weaker than pure Pt.^{90,151} The core-shell architecture highlighted in this work can be seen as a synthetic counterpart of the NSAs, where only one type of atoms is present on the surface, and thus invokes a combination of “ligand” and surface strain effects without any mechanistic complications of the alloy surface bifunctionality. The latter refers to more common bimetallic catalysts, where both alloy components are present on the surface. In such bimetallic systems, the more oxophilic metal acts as an oxygen activator (*i.e.* to form surface OH), which facilitates the oxidation of the CO adsorbed on neighboring, less oxophilic metal centers.^{44,152-156} For example, it is well established in PtRu bimetallics that OH selectively binds to Ru to form Ru-OH and CO to Pt to form Pt-CO. In contrast, core-shell NSA catalysts have only one type of surface metal but their electronic structure and catalytic properties are substantially modified because of the interactions of the shell atoms with the core atoms. The kinetically-stabilized core-shell structure has already proven itself as a novel architecture for NO_x reduction over the PtCu bimetallic system.³⁴ *In situ* chemical¹⁵⁷ and electrochemical^{152,158} deposition of Pt and other metals onto core NPs (including Ru) has been reported but the resulting catalyst NP structure / architecture is difficult to assess in these systems. Nevertheless, the

electrocatalytic performance of electrochemically prepared Pt-on-Ru NP electrocatalysts for CO-tolerant H₂ electro-oxidation first reported by Adzic *et al.* is quite encouraging.¹⁵² However, the lack of controlled bulk synthetic procedures and the limited structural and spectroscopic information for Ru@Pt systems hinders mechanistic interpretation and direct comparison with other NP architectures.

The architectural control over NP synthesis is in the heart of the design and fabrication of the new generation catalysts, and therefore DFT calculations may guide the design to some extent. However, the synthesis is still the focus of developing catalysis research. Nano-sized materials with the desired physical and chemical properties can now be designed from first principles, and fabricated using various techniques, of which the chemical routes have some advantages. The poly-ol synthesis of monometallic phases in nanometer size has been known for a long time, and recently been implemented to multimetallic systems.¹⁵⁹⁻¹⁶² The geometrical and structural properties of nanoparticle phases can be controlled and tuned to some extent in the poly-ol method.^{63,64,163-166} The architectural control of bimetallic nanoparticles is, in contrast, not trivial, and thus requires understanding of thermodynamic properties, metal-metal bonding, ligand-metal interactions and nucleation/growth phenomena.¹⁰⁰ The correlation between these variables is of such a complex function, and therefore the knowledge of the measured and tabulated parametric data is so scarce that the optimal synthetic conditions should be empirically determined. Even thermodynamically meta-stable phases can be made accessible in solution by employing appropriate reaction conditions. To make structurally different architectures of bimetallic nanoparticles, namely alloys, core/shell and contact dimers (i.e. hetero-aggregates), the poly-ol method should be blended with various

particle growth techniques. Overlayers of metals can be deposited on host metals of the same type or other types employing the 'sequential growth'^{105,108} technique along with the poly-ol reduction method, or two or more metals can be co-deposited to make alloys of desired compositions. Schmid cluster model^{110,111} and/or density and volume values of the close-packed metal atoms can independently be used to estimate the starting molar ratios of bimetallic phases. Schmid model is a good starting point to tune the relative sizes of core and shell phases.⁹³

Even though the synthesis of different NP phases with the desired architecture can be achieved, well-characterized NP structures are essential to better understanding of their catalytic properties. Multiple techniques are required to study architecturally-controlled bimetallic nanoparticles. Recently, advances in instrumental techniques have offered material scientists new scopes in characterization. Analytical tools such as TEM in the scanning mode alone can be used to distinguish alloys and core/shell architectures.¹⁰⁰ However, STEM-EDS analyses are limited to the probe size and severely affected by sample drift and formation of carbonaceous species and thus the smallness of NPs under investigation solely determine the success of experimentation. Moreover, surface-adsorbed CO probed with Raman and/or FT-IR is a powerful tool to distinguish between alloys and core/shell architectures.^{93,167,168} However CO probing lacks the structural information that X-Ray techniques can provide. X-Ray techniques include diffraction as in XRD and absorption as in EXAFS. Nano-crystalline bimetallic particles are in the focus of sophisticated analysis techniques using X-rays because of their interesting structural properties. Strain/stress induced lattice distortions^{99,102-104,128,129,169} at the interface of core/shell NPs can be studied using XRD. Atomic

arrangements via a sense of coordination numbers can be deduced from EXAFS.^{86,120,170} When combined with modeling and simulations, they offer valuable and unique structural insight into sophisticated NP structures such as core/shell architecture may have.^{88,120} Model clusters can be derived from mean particle sizes (TEM) with the proposed particle architecture. Thus, Debye Function (DF) of the model clusters to simulate XRD pattern provides not only the most fundamental, but also the most valuable picture of the structural properties. Similar to EXAFS, but derived from whole powder diffraction, atomic Pair Distribution Function (PDF) reveals distributions of atomic distances in average within nano-crystalline particles, for which long range order and periodicity are missing,^{171,172} such that 3-D construction of the particle structure^{173,174} becomes possible.

In this chapter, the synthesis and full characterization of a Ru@Pt core-shell NP catalyst that is distinctly different from the PtRu alloy and from the mixed monometallic systems of the same composition will be presented. Bimetallic Pt/Ru NPs with well-defined particle architectures, namely Pt_xRu_{1-x} ($x=0.33-0.8$) alloys and $Ru_x@Pt_{1-x}$ ($x=0.33-0.66$) core/shells, are synthesized via modified poly-ol reduction methods. Composition series of the alloys NPs, and core size and shell thickness series of core/shell NPs are then characterized using an array of diffraction, spectroscopic, imaging techniques and other analytical tools and theoretical analyses. Finally, they are catalytically evaluated for both scientifically and industrially important reactions under the reaction conditions of common practice.

In PROX reactions, the Ru@Pt NPs are far more active and selective for CO oxidation at room temperature than alloy and monometallic NP catalysts. Because the Ru metal is confined and kinetically trapped inside a Pt shell, the conventional bifunctional

mechanism cannot be implicated since CO oxidation necessarily occurs entirely on the Pt surface sites; no Ru is exposed on the NP's surface. Since no promoter such as a reducible oxide support has been employed, we have attributed this distinguishing behavior to the NP architecture. Through DFT modeling, it is shown that the enhanced CO oxidation is achieved through modification of the electronic structure of the Pt surface by the presence of subsurface Ru. This modification significantly destabilizes CO on Pt, leading to a lower CO saturation coverage, thereby providing more adsorbate-free active sites where O₂ and H₂ can be activated. At the same time, this electronic modification greatly accelerates the CO oxidation reaction through a substantial destabilization of the adsorbed reactive intermediates.

2.2. Experimental

2.2.1. Materials

All reactions were carried out under N₂ atmosphere using standard Schlenk line on a Fisher Scientific Isotherm hot plate stirrer with a temperature control unit using a Teflon coated K-type thermocouple. Chemicals, PtCl₂ (Engelhard, Pt 73.09%), Pt(acac)₂ (Strem, 98%, acac=acetylacetonate), Rh(NO₃)₃.2H₂O (Alfa Aesar, 99.9% pure, Rh 31.1%), Ru(acac)₃ (Engelhard, Rh 39.46%), Ru₂(CO)₄Cl₂ (Fluka, >97%), polyvinylpyrrolidone (Aldrich, typical M_w=55000), ethylene glycol (VWR, H₂O >0.02%), acetone (Pharmco Aaper, HPLC-UV Grade), ethanol (Pharmco Aaper, 200 proof) and γ-Al₂O₃ (Alfa Aesar, 99.97% metal basis) were purchase and used as received unless otherwise stated. Ethylene glycol was distilled over Na (Aldrich, 99%) to make it dry.

2.2.2. Sample characterization of the proposed nanostructures

The colloidal suspensions described below were diluted with acetone and centrifuged at 6000 rpm using a Hermle Z 300 centrifuge. The supernatants were clear. The precipitates were washed with acetone and acetone-ethanol mixture upon sonication using a Fisher Scientific FS30H sonicator bath. The cycles of dilution by acetone-ethanol mixtures, sonication and centrifugation were repeated 4-5 times. The precipitates were dried in open air prior to characterization.

2.2.2.1. Powder X-ray Diffraction

A Bruker C2 Discover (Parallel Beam) General Area Diffraction Detection (GADDS) system was used for powder diffraction detection. The monochromatic Cu $K\alpha$ radiation source that was biased at 40 mV and 40 mA was employed along with Bruker ACS Hi-Star detector. The diffraction patterns were acquired between 33-90° by integrating four frames with 14° 2 θ per frame. The samples were oscillated in the xy-axis to homogenize the diffracting grains.

2.2.2.2. Powder X-Ray Diffraction simulations by Debye Function (DF)

Powder diffraction patterns were simulated using the DISCUS software package.¹ The ATOMS program was used to generate the spherical core/shell nanoclusters of desired Ru core sizes and Pt shell thicknesses. Fractional atom coordinates in a P₁ cubic lattice of 100 Å cell size were simulated using the Debye function with no symmetry constraints.

Model clusters were generated using ATOMS software package. First, FCC Ru and Pt unit cells were created in GSAS with the lattice parameters from JC-PDS files and the fractional coordinates of a FCC unit cell. The .gsas file for Pt cell was read from ATOMS, and single unit cell was expanded to a spherical nanocluster of desired particle diameter. The generated atomic coordinates were opened in EXCEL to calculate the atomic distances. Atoms with distances that were equal to and smaller than the diameter of the corresponding Ru cluster were deleted. The remaining atoms that constitute the Pt skin were saved as a .pdb file. Finally, the two, namely Ru core cluster and Pt skin cluster, were opened in the same EXCEL sheet to generate the core/shell clusters. The fractional coordinates were generated from the atomic coordinates for a 100 Å cell. The atom labels, the fractional coordinates, and the thermal parameters with user-defined values of 0.01 Å⁻² for both Ru and Pt atoms were saved as a 5-column DISCUS .stru file. The unit cell was defined as 100 Å, and the spacegroup as P₁. The .stru file was read in DISCUS.

Two core/shell clusters of 40 Å particle diameters were generated: one with 1605 Ru atoms and 810 Pt atoms i.e. 35 Å Ru core ~1 ML thick Pt shell and another with 922 Ru atoms and 1356 Pt atoms i.e. 30 Å Ru core and ~2 ML thick Pt shells. The ATOMS-generated core/shell clusters further distorted to register Ru and Pt atoms using DISCUS' Reverse Monte Carlo (RMC) function. The atoms were moved in harmonic potentials, according to the equation:

$$E_h = \sum_j \sum_n k_n * [d_{jn} - \gamma_{jn} * d_0]^2 \quad \text{eq. 2.3}$$

where j was the site index, n the neighbors around site j , d_{jn} the distance between neighboring atoms, d_0 the average distance and γ_{jn} the distortion. The sums were taken over all sites j and all neighbors n around site j . The force constant k_n was fixed at an arbitrary value of 10 for all nearest neighbor pair interactions. The Hamiltonian was normalized using a restoring force constant k_0 i.e. a situation where $\gamma_{jn}=0$, which was also arbitrarily fixed at 15 for all nearest neighbor pair interactions. EXAFS-measured metal-metal distances of $d_{Pt-Pt}=2.743$ Å, $d_{Pt-Ru}=2.690$ Å and $d_{Ru-Ru}=2.665$ were used. Pt atoms were allowed to shift isotropically by 0.005 Å and Ru atoms by 0.015 Å. Thermal factors (i.e. Debye-Waller parameters) were also taken into account in the RMC simulations. Simulated atom-atom distances were found to be converged to EXAFS-derived distances at cycles between $5 \cdot 10^5$ and 10^6 .

The alloy cluster of 44 Å diameter was generated as described above, with the exception that the FCC Pt cluster was first generated with the EXAFS-derived unit cell parameters and randomly replaced by Ru atoms with a probability of 0.5 using DISCUS' CHEM function. The alloy cluster was further distorted as described above with the EXAFS-measured metal-metal distances of $d_{Pt-Pt}=2.740$ Å, $d_{Pt-Ru}=2.718$ Å and $d_{Ru-Ru}=2.690$ and the distortions of $\gamma_{Pt}=\gamma_{Ru}=0.005$ Å.

The powder diffractions are simulated using 'powder' subroutine with built-in 'Debye' function in DISCUS. Periodic diffractions from the model clusters were also evaluated.

2.2.2.3. Powder X-Ray Diffraction Refinements

General Structure Analysis System (GSAS) package was employed to analyze and refine the powder diffraction data obtained with X-rays. Rietveld fit sub-routine was employed to refine the synchrotron data of the Pt₅₀Ru₅₀ alloy NPs, and LeBail fit sub-routine for the Mo K_α data of the Pt₅₀Ru₅₀ alloy NPs and Ru@Pt core/shell NPs. For the core/shell sample, atomic parameters for the Ru and Pt atoms of space groups Fm-3m and P63/mmc, respectively, were first entered. Then, a single Pt atom with the fractional coordinates of 0,0,0 and a single Ru atom with the fractional coordinates of 0.333,0.666,0.25 were generated. Symmetry-equivalent atom sites and multiplicity were automatically generated from these single-atom phases. Isotropic thermal parameters were set to 0.0025 Å² for both Pt and Ru atoms. The fit was performed for the periodic unit cell, and atomic parameters only for the Pt phase were refined. For the alloy sample, two atoms each of Pt and Ru were generated with occupancies of f₀=0.5 each. The unit cell was initially set to a₀=3.874 Å, the space group to Fm-3m, and the fractional coordinates to 0,0,0. The unit cell parameter was refined provided that it was coupled to the occupancy using the equation:

$$a^* = a_0 \times (1+f^*) \quad \text{eq. 2.4}$$

where a* is the refined unit cell parameter and f* the refined occupancy.

2.2.2.4. Atomic Pair Distribution Function Analysis

The data collection for the atomic pair distribution function analysis of the alloy and core/shell NPs was conducted at the 11-ID-B beamline at the National

Synchrotron Light Source of Argonne National Laboratory by Dr. Peter Chupas. A monochromatic Si(311) beam with an energy range of 58-59 keV and energy resolution of 0.001 eV was used. Independently, a Bruker Smart1000 Single Crystal Diffractometer using a Mo K_α source and Smart1000 area detector was employed to collect the X-Ray data. This experiment was conducted at the X-Ray Crystallographic Center at the University of Maryland under the supervision of Dr. Peter Zavalij. The data analysis was carried out using PDFGETX2 and PDFGUI software packages. First, the intensity function, $I(Q)$, was calculated from the raw X-ray data using PDFGETX2. The intensity function was corrected for the sample and instrument effects such as Compton scattering, Laue diffuse scattering, self-absorption, X-ray polarization, and weighting after background subtraction. The corrected intensity function was then used to calculate first the structure function, $S(Q)$, and then the reduced structure function, $S((Q)-1)$. Finally, the reduced structure function was Fourier-transformed to the pair distribution function, $G(r)$. Only X-ray polarization and weighting corrections were applied to the data from Mo K_α . A model cluster of Pt and Ru atoms were refined against the calculated pair distribution functions for the alloy NPs. A model cluster of Pt and Ru atoms were created at Wyckoff positions of multiplicity 4 of group 225 (Fm-3m),¹⁷⁵ and expended in space to 44 Å diameter using PDFGUI software package. Occupational probability of each atom site was initially set to 0.5 and temperature factors to 0.001 Å⁻² for all Pt and Ru atoms i.e. a 50:50 alloy. Multiple variables including low-r cut-off factor and Q damping factor were used in refinement. The ATOMS generated core/shell clusters (see above section) and the Pt-skin clusters of 810 Pt atoms and 1356 Pt atoms with 40 Å outer diameters were independently refined against the pair distribution function for the core/shell NPs.

Similarly, 3055-atom Pt₅₀Ru₅₀ alloy cluster with a particle diameter of 44Å were also refined against the pair distribution function for the alloy NPs. Only structural parameters that were used in refinement were temperature factors, and were initially set to 0.001 Å⁻².

2.2.2.5. Extended X-Ray Absorption Fine Structure (EXAFS) and X-Ray Absorption Near Edge Structure Studies (XANES)

XANES characterization of NPs was carried out at the X18B beamline at the National Synchrotron Light Source of Brookhaven National Laboratory by Prof. Anatoly Frenkel and Dr. Qi Wang. Nanoparticle and RuO₂ specimens were prepared by grinding the powders with a mortar and pestle, brushing them onto adhesive tape and folding it several times for adequate uniformity and thickness for transmission EXAFS measurement. Metal foils were measured in reference modes for energy calibration and as data analysis references. EXAFS analysis was done model-independently and the results were not biased in favor of any assumed model about the short range order of elements in these samples. Data for each edge were fitted with FEFF6 theory^{119,120} concurrently, by employing physically reasonable constraints between the fitting parameters. Modeling for the core/shell sample was performed at BNL using cuboctahedron clusters, and at UMD using the ATOMS generated spherical clusters of comparable sizes and number of atoms. The coordination numbers for the 1st through 4th coordination shells of the model core/shell clusters were calculated using ‘CHEM’ subroutine in DISCUS package. The model clusters were generated using ATOMS software as described above.

2.2.2.6. X-Ray Photoelectron Spectroscopy

XPS measurements were performed on a Kratos Axis 165 Spectrometer using Mg K_{α} radiation in a vacuum of 2×10^{-10} Torr. The hybrid mode was applied for measurements of 10 scans with a step size of 0.1 eV and sweep time of 60 sec. for each of Pt 4f, Ru 3d, Ru 4p, O 1s and Cl 2s regions. The spectra were recorded in the FAT analyzer mode with the pass energy of 80 eV. The data processing was performed using graphical analysis package with minimum number of mixed Lorentzian/Gaussian peaks after linear background subtraction.

2.2.2.7. Fourier Transformed-Infrared Spectroscopy

For the IR-CO probe experiments, the colloidal solutions of the desired nanoparticles were bubbled with CO using a stainless steel needle submerged in the solution at a flow rate between 20 and 40 sccm for ca. 20 minutes. A 100 μ L aliquot of CO saturated colloidal solution was filled in a liquid IR cell and monitored in a Nexus 870 FT-IR spectrometer. The liquid IR cell consisted of a 0.5 mm Teflon spacer sandwiched between two rectangular-shaped CaF_2 windows. The colloidal solution prior to CO bubbling was used for the background spectrum.

2.2.2.8. Micro-Raman Spectroscopy

A Renishaw Raman Microscope was employed to measure the micro-Raman spectra of CO saturated nanoparticles. The nanoparticle powders were dispersed on glass slides and then sealed in a gas-tight Linkam temperature control stage. A 632.8 nm He:Ne or 488 nm Ar ion laser was focused on the particles through 0.5 mm quartz window using Leica N plan L50x/0.50 objective lens. The backscattered light was monitored with a resolution of 20 exposures per second between 300 and 2400 cm^{-1} . The power was set to 12.5 mW. The power density was calculated to be $2.5 \times 10^{11} \text{ J} \cdot \text{m}^{-2} \cdot \text{s}^{-1}$. The particles were dosed with CO, CO/air or CO/Argon mixtures for about 20 minutes. The spectra were recorded under flowing gas streams. No significant graphite formation was detected by Raman.

2.2.2.9. Transmission Electron Microscopy

TEM samples were prepared directly from the reaction mixtures by diluting 20 μL of colloids to $\sim 2 \text{ mL}$ with deionized water. 3 μL of such mixtures were drop-cast and dried on continuous carbon film-deposited copper grids. A Zeiss CM10 TEM operating at 80 keV was used for high contrast imaging. A Jeol 2100F Field Emission TEM with an ultra-high resolution aperture operating at 200 keV was used in high magnification high contrast imaging. A JEM 2100 LaB6 TEM operating at 200 kV was used for both low and high resolution imaging.

2.2.2.10. Scanning Transmission Electron Microscopy (STEM) and Energy Dispersive Spectroscopy (EDS)

A Jeol 2100F Field Emission Transmission Electron Microscope (FE-TEM) equipped with an Inca Energy Dispersive Spectrometer (EDS) was used for line and point spectrum of nanoparticles. The FE-TEM was operated at 200 kV and in the scanning mode.

2.2.3. Evaluation for heterogeneous catalysis

2.2.3.1. Catalytic evaluation for PROX reaction

Catalysis runs were carried out using 105 mg of catalyst charges in all cases. A standard fixed bed flow-through reactor was employed. The reactor was made of quartz and had a diameter of 6.8 mm.^{95,98,176} The reactor bed, on the bottom, was composed of a layer of ca.100 mm long quartz beads and a thin layer of quartz wool to homogenize and disperse gas mixtures. The catalyst was loaded on top of the quartz wool layer and was 5.5 mm in height. The catalyst layer was supported on the top by another thin layer of quartz wool and a ca. 100 mm long layer of quartz beads. An inlet velocity for gases of 0.21 m/s, and a total flow rate of 400 NmL/min was employed. The gas hourly space velocity (GHSV) was calculated to be $2.3 \times 10^5 \text{ mL} \cdot \text{g}^{-1} \cdot \text{h}^{-1}$ with a corresponding residence time about 35 milliseconds. The PROX experiments described in this study uses three sets of gas mixtures. Namely, the first set is composed of 0.1% CO (99.5% pure, Al tank), 0.5% O₂ (99.999% pure), 50% H₂ (99.999% pure), and 49.4% Ar

(99.999% pure), the second set, 0.2% CO (99.5% pure, Al tank), 0.5% O₂ (99.999% pure), 50% H₂ (99.999% pure), and 49.3% Ar (99.999% pure), and the third set 1.0% CO (99.5% pure, Al tank), 1.0% O₂ (99.999% pure), 50% H₂ (99.999% pure), and 48.0% Ar (99.999% pure). The catalysts were reduced in 50% H₂-Ar mixture at 200°C prior to catalysis. The temperature was set to 200°C and the heating ramp was 1.8 °C/min. The gases were introduced to the reactor using carefully calibrated mass flow controllers. The product compositions were calculated from calibrated ion sensitivities. The ion-cracking patterns of the analyzed gases were also taken into account in calculations. The % of maximum CO₂ formation was based on the limiting CO, and the % of maximum H₂O formation, based on the limiting O₂. The gas products were monitored online using a Prima δB mass spectrometer. C and O balances were used to validate % conversions.

2.2.3.2. Catalytic evaluation for Rich/Lean NO_x reduction

The catalytic evaluation of γ -Al₂O₃ supported NPs catalysts toward rich-NO_x and lean-NO_x reduction reactions were carried out for 105 mg of supported catalyst charges of each bimetallic NPs system. Supported catalysts were loaded in the reactor bed of a quartz flow-through reactor tube, and were stabilized below and above by a thin layer of quartz wool and 100 mm long packed quartz sand. An inlet velocity for gases of 0.16 m/s, and a total flow rate of 300 NmL/min was employed. The gas hourly space velocity (GHSV) was calculated to be $1.7 \cdot 10^5 \text{ mL} \cdot \text{g}^{-1} \cdot \text{h}^{-1}$ with a corresponding residence time about 47 milliseconds. In order to vary flow rates and thus fix reactor residence time computer-controlled and carefully calibrated mass flow controllers were used. The gas

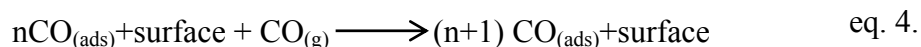
mixtures for rich-NO_x reaction was 0.75-3.0% H₂, 0.75% NO, and balance Ar, and for lean-NO_x reaction 0.75-3.0% H₂, 0.75% NO, 5.0% O₂, and balance Ar. All gases were ultra-high purity (+99.9999%) grade. The catalysts were reduced in 50% H₂-Ar mixture at 200 °C prior to catalysis. The high temperature was set to 400 °C and the heating ramp was from 25 to 400 °C ~2.1 °C/min. The gas products were monitored online using a Prima δB mass spectrometer. The product compositions were calculated from calibrated ion sensitivities and ion-cracking patterns of the analyzed gases. N, O and H balances were sought in the validation of % conversions.

2.2.3.3. Catalytic evaluation for benzene hydrogenation

The benzene hydrogenation experiments were conducted at the Department of Chemical and Biological Engineering in Prof. James Dumas Laboratory at the University of Wisconsin for 100 mg charges of γ -Al₂O₃ supported bimetallic NPs catalysts. Supported catalysts were conditioned at 200 °C under air-N₂ mixtures for 6 hours prior to reactions. Catalysts were placed in a round bottom flask. Then, 10 mL 5% benzene in hexadecane solution was admitted to the flask. H₂ gas was introduced to the reactor at room temperature. The H₂ outlet was closed until the pressure reached ~1-2 PSI above atmospheric. Finally, the H₂ inlet was closed, and the magnetic stirrer was started to mix the reactants. The product composition was periodically analyzed ex-situ in a gas chromatograph. 500 μ L aliquots of reaction mixture were sampled in each turn. The sampled suspension was cooled down to well below 0 °C in an acetone-liquid N₂ bath, catalyst was centrifuged and precipitated, and the composition of supernatant was analyzed in a gas chromatograph.

2.2.3.4. Density Functional Theory (DFT) calculations

The self-consistent DFT calculations were carried out using DACAPO,^{177,178} a total-energy code and was performed by Prof. Mavrikakis and Dr. Nilekar at University of Wisconsin-Madison. Unless otherwise stated, four-layer metal slabs with a 2×2 surface unit cells were employed. The equivalent of five layers of vacuum was used to separate periodic images of metal slabs in the z-direction of the unit cell. Adsorption is allowed on only one of the two exposed surfaces, and the electrostatic potential is adjusted accordingly.¹⁷⁹ All degrees of freedom for the top two layers of slab atoms and for all adsorbate atoms were relaxed. Differential binding energy was defined as the energy change for the reaction:



over a range of initial CO coverages; the highest CO coverage for which the differential binding energy of CO is still negative defines the CO-saturation coverage on the respective surface.

2.2.4. Synthesis of bimetallic Ru-Pt NPs with various architectures

3.0. nm Ru NPs. In a typical synthesis, 40.0 mg Ru(acac)₃ was dissolved in 20 mL EG in a 50 mL 3-neck round bottom flask along with 28.0 mg PVP₅₅₀₀₀. The Rh³⁺ precursor salt was loaded in a dry box; all other transfers were done on a Schlenk line under N₂ atmospheres. The mixture was heated to ~80°C and kept isothermal 10-15 min.

to dissolve the contents of the reaction mixture. The brick-red solution was brought to boiling EG temperature, and refluxed for about 90 min. in flowing N₂ with vigorous stirring. The solution turned black and colloidal at temperature range of 150-170°C. The reaction was quenched over ice. The colloids are stable for months without any precipitation.

~2.0 nm Ru NPs. It is a modified NaBH₄ reduction/nucleation in EG, and follows a two-pot reaction protocol. In a typical reaction, 42.0 mg anhydrous RuCl₃ and 56.0 mg PVP₅₅₀₀₀ were dissolved in 10 mL EG in a 50 mL 2-neck round bottom flask at about 100°C in flowing N₂. In a 100 mL 3-neck flask, 30 mL EG was brought to 130°C in flowing N₂. Next, ~40 mg granular NaBH₄ was added into hot EG. Temperature was set to 200°C, and when temperature reached to ~150°C, Ru³⁺ solution was syringed into NaBH₄ solution. Solution instantly turned black colloidal. The colloidal suspension was refluxed for about 90 min. in flowing N₂. The reaction was quenched on ice. Ru NPs colloids are stable for months without any precipitation.

4.2 nm Ru NPs. Typically, 33.6 mg Ru(acac)₃ (2x Ru³⁺-equivalent of Ru colloids) was dissolved in 8 mL Ru NPs suspension (see above) and diluted to 16 mL by EG at 80°C in flowing N₂ to make 4.2 nm Ru NPs. The deposition temperature was first set to 110°C, and then slowly ramped to 170°C. The colloidal suspension was allowed to age 2 hours at 170±2°C. The reaction was quenched by immersing the flask in an ice bath.

5.7 nm Ru NPs. In a typical synthesis, 20.2 mg Ru(acac)₃, 13.3 mg Ru₂(CO)₆Cl₄ and 28.3 mg PVP₅₅₀₀₀ were dissolved in 20 mL EG. The red solution was heated to ca. 80°C at which was held isothermal for 30 min. Then, the temperature was

quickly ramped to boiling EG temperature less than 10 min. The solution turned black and colloidal in a temperature range between 160°C and 180°C. The colloidal suspension was refluxed for 90 min. and then the reaction was quenched in an ice-water bath. The Ru NPs were 5.7 nm in diameter in average and highly faceted. When 100 μ L of 0.1 M NaBr dissolved in EG was admitted into the colloidal suspension at or under reflux, the resulting Ru nanoparticles had a mean size of 4.1 nm, and were splendid in shape.

3.1 nm PVP-free Ru NPs. 46.0 mg Ru(acac)₃ were dissolved in 22.5 mL EG in a 50 mL 3-neck round bottom flask in Schlenk line under positive N₂ pressure. The solution was slowly ramped to ca. 130°C over a period of 2 hours. The solution slowly turned dark and became colloidal. The colloidal suspension was aged for 15 min. Then, the reaction was quenched in an ice-water bath. Some degree of aggregation/precipitation occurred after the reaction was quenched, but the colloidal suspension was restored with stirring.

6.1 nm Pt NPs. In a typical synthesis, 54.0 mg PtCl₂ and 55.0 mg PVP₅₅₀₀₀ in 40 ml EG were refluxed for 1 hour. To prepare the physical mixture, the monometallic colloidal suspensions of Pt and Ru NPs were mixed and stirred overnight.

2.2 nm PVP free Pt NPs. 126.1 mg H₂PtCl₆ was dissolved in 22 mL EG. Temperature was slowly ramped to 130°C. The yellow solution turned black and colloidal upon aging it at 130 \pm 3°C for 90 min. The colloidal suspension of Pt NPs was aged 30 min. The reaction was stopped in a cold H₂O ice bath. The colloids were not stable in suspension, and precipitated in a few hours.

2.2.5.1. Synthesis of Ru@Pt core/shell NPs with various core sizes and shell thicknesses

4.1 nm Ru@Pt NPs with ca. 1-2 MLs thick Pt shells. In a typical synthesis, 14.0 mg PtCl₂ was dissolved in 10 mL of 3.0 nm Ru NP colloidal suspension along with 10 mL EG. The mixture was stirred at ~60°C to dissolve Pt²⁺ precursor salt. The solution was brought to boiling EG temperature with an average temperature ramp of 1°C/min and aged for 2 hours. The reaction was quenched over ice. The Ru@Pt nanoparticle colloids were not stable in solution, and precipitated after a day.

3.7 nm Ru@Pt NPs with sub-monolayer thick Pt shells. The synthesis is the same as above, except that 10.0 mg PtCl₂ was dissolved in 10 mL of 3.0 nm Ru NPs suspension and just 6 mL EG.

4.4 nm Ru@Pt NPs with ca. 2-3 MLs thick Pt shells. In a typical reaction, PtCl₂ (22.4 mg PtCl₂) was dissolved in 12 mL EG. 8 mL of 3.0 nm Ru NPs suspension was added under flowing N₂ atmosphere at room temperature. The mixture was heated to 80°C and held for 15 min. Then the temperature was ramped to 130°C and finally to boiling EG temperature with an average ramping rate of 1 °C/min. The mixture was aged at reflux for 1.5 hours, and then quenched to room temperature in an ice bath.

4.7 nm Ru@Pt NPs with ca. 1-2 MLs thick Pt shells. Typically, 10 mL of 4.2 nm Ru nanoparticle colloids were added to 16.2 mg PtCl₂ in 10 mL EG at room temperature. The colloidal suspension was quickly heated to 80 °C. Temperature was then ramped to boiling EG temperature with a heating ramp of ca. 1 °C/min. it was held isothermal under reflux for 1 hour before the reaction was quenched in an ice bath.

6.2 nm Ru@Pt NPs with ca. 1-2 MLs thick Pt shells. 10 mL of 5.7 nm Ru nanoparticle colloids was added to 7.1 mg PtCl₂ in 10 mL EG at room temperature. The reaction was carried out according to a slightly modified version of one described above, except, the suspension was heated from 130 °C with a temperature ramp of ca. 1 °C/min. The nanoparticle colloids are stable for a several hours in the suspension.

3.0 nm Ru@Pt NPs with ca. 1-2 MLs thick Pt shells. In a typical synthesis, 42.1 mg PtCl₂ in 10 mL EG was admitted to 10 mL of 2.0-2.5 nm Ru nanoparticle colloids at room temperature and under N₂ atmosphere, and reacted as described above. The nanoparticle colloids are stable in the suspension for several days.

3.2.5.2. Synthesis of PVP free Ru@Pt core/shell NPs

4.2 nm PVP-free Rh@Pt NPs with ca. 1 ML thick Pt shells. Typically, 42 mg H₂PtCl₆·6H₂O was dissolved in 16 mL of PVP-free 3.0 nm Ru NPs suspension. The temperature was slowly ramped to ca. 100°C, and hold isothermal for 1 h. The reaction was stopped, and the colloidal suspension was let aside to cool down under vigorous stirring. The PVP-free colloids have very short shelf-lives and precipitate over a few hours unless stirred.

3.2.5.3. Synthesis of Pt_xRu_{1-x} (x=0,1)

PtRu (1:1) alloy NPs. To prepare 4.4 nm Pt₅₀Ru₅₀ alloy nanoparticles, 40.9 mg Pt(acac)₂ and 26.5 mg Ru₂(CO)₄Cl₂ salts were dissolved in 20 mL EG along with 28.0 mg PVP₅₅₀₀₀. The temperature was first ramped to 80°C at which the red solution was

held for about 30 min. Then, it was quickly brought to boiling EG temperature in less than 10 min. The solution turned black colloidal at a temperature range of 135-165°C. The colloids was refluxed for about 2 hours and quenched over ice. TEM shows 4-5 nm particles of irregular shapes (mostly spheroids with aspect ratios of 1-2). To prepare alloy nanoparticles with the generic formula of $Pt_xRu_{(100-x)}$ ($x=80-34$), namely $Pt_{80}Ru_{20}$, $Pt_{66}Ru_{34}$, $Pt_{34}Ru_{66}$ and $Pt_{40}Ru_{60}$, certain amounts of $Pt(acac)_2$ and $Ru_2(CO)_6Cl_4$ were reacted as described for the $Pt_{50}Ru_{50}$ NPs.

2.3. Results

2.3.1. Synthesis of Ru@Pt core/shell and Pt_xRu_{1-x} alloys NPs with or without PVP

The Ru@Pt core-shell NPs were synthesized by using a sequential polyol process.^{93,113} $Ru(acac)_3$ (acac = acetylacetonate) was initially reduced in refluxing glycol in the presence of PVP stabilizers (MW = 55,000). The resulting Ru NPs (mean particle size = 3.0 nm) were subsequently coated with Pt by adding $PtCl_2$ to the Ru/glycol colloid and slowly heating to 200 °C. Pt self-nucleates at temperatures between 130-170 °C, so that employing temperatures below 130 °C is essential to favor hetero-nucleation of Pt shells over Ru cores. On the other hand, inhomogeneous Pt shells were observed under diffusion control of the Pt monomer. Thus, provided that thicker Pt shells i.e. 4.4 nm Ru@Pt NPs with 2-3 ML thick Pt shells were sought over Ru cores, the deposition temperature was set to 130 °C. To grow thin Pt shells i.e. 4.1 nm Ru@Pt NPs, the temperature was brought to a boil via a rather slow ramping between 130-170 °C, such

that self-nucleation of Pt was avoided as well as Ru cores could be coated by homogeneous layers of Pt shells. Synthesis using rigorously dried EG had no or little effect on the physical and chemical properties of the core/shell NPs (*vide infra*).

Larger Ru NPs seeds were synthesized via two independent routes, and are shown to be equivalently efficient. The first route employs a sequential growth method to deposit Ru over the preformed Ru NP seeds. 4.3 nm Ru NPs can be grown over 3.0 nm Ru NPs by having a 2 to 1 starting ratio of Ru³⁺ precursor salt to Ru colloids (see Figures 2.3). Ru(acac)₃ was the best Ru³⁺ source for this growth process. The latter route involves co-deposition of a Ru²⁺ precursor salt, namely Ru₂(CO)₆Cl₄ and a Ru³⁺ precursor salt, namely Ru(acac)₃ at reflux. The Ru NPs are 5.7 nm in diameter in average, and exhibit crystallographic facets (Figure 2.4). There also observed <0.1% by moles triangular plates of ca. 20 nm edges and ca. 2 nm height. Etching the 5.7 nm Ru NPs with NaBr removes the high surface energy facets results in size reduction down to 5.0 nm. Pt deposition over large Ru NPs seeds follows identical synthetic approaches, but under-reflux growth conditions are proven to be more robust for homogeneously and thoroughly deposited Pt overlayers. To achieve ca. 1 ML thick Pt shells, molar ratio of Pt²⁺ precursor to Ru colloids is less than 1. Molar ratio of Pt²⁺ precursor to Ru colloids to achieve ca. 1-layer Pt shell over 2.0 nm and 3.0 nm Ru nanoparticle cores is calculated using the Schmid cluster model.¹¹¹ Schmid model defines a layer-by-layer growth of successive shells, providing well-defined particle geometries, such as cuboctahedra, truncated octahedron and icosohedron, and related growth algorithms. On the other hand, polyhedron or sphere describes the best particle geometries beyond a certain nanoparticle size, and therefore it is how multiply-twinned nanoparticles are considered. Thus, volume

and density of closely-packed Ru and Pt metals are used to calculate relative molar ratio of Pt Ru for 4.3-5.7 nm Ru nanoparticle cores, as well as Schmid model. Table 2.1 shows Schmid model-derived structure and composition parameters of certain core/shell cluster series. Furthermore, mean particle sizes from TEM measurements are used to predict average number of atoms in Ru NPs. TEM images of the resulting core/shell NPs support the eligibility of such models and the success of growth reactions.

The PtRu alloy NPs is synthesized via co-reduction of the $[\text{Ru}(\text{CO})_3\text{Cl}_2]_2$ dimer and $\text{Pt}(\text{acac})_2$ with glycol and PVP stabilizer at 200 °C. The resulting NPs are 4.4 nm in diameter in average, and exhibit some shape and size anisotropy (see Figure 2.1). Ru-rich $\text{Pt}_{34}\text{Pt}_{66}$ alloy NPs show identical mean particle sizes. In contrast, Pt-rich $\text{Pt}_{66}\text{Ru}_{34}$ and $\text{Pt}_{80}\text{Ru}_{20}$ NPs are larger in average (see Figure 2.7).

Table 2.1. Table showing Schmid model-derived core size, shell thickness and composition parameters of some Ru@Pt core/shell cluster series.

# of shells (Ru-core)	# of core atoms	Center-to-center Ru core size (nm)	Edge-to-edge Ru core size (nm) (TEM)	ML coverage resulting from 1:1 ratio of Ru:Pt	ML coverage resulting from 1:2 ratio of Ru:Pt	ML coverage resulting from 2:1 ratio of Ru:Pt	Ratio of Pt to Ru to achieve 1 ML coverage	Total Particle (edge-to-edge) Size for 1 ML thick Pt shell	Total Particle (edge-to-edge) Size for 2 ML thick Pt shell
2	55	1.1	1.4	0.67	0.11	0.30	1.67	1.9	2.5
3	147	1.6	1.9	0.91	1.52	0.46	1.1	2.4	3.0
4	309	2.2	2.4	1.16	2.01	0.62	0.81	3.0	3.5
5	561	2.7	3.0	1.40	2.42	0.78	0.65	3.5	4.1
6	923	3.2	3.5	1.67	2.87	0.94	0.53	4.1	4.6
7	1415	3.8	4.1	1.96	-	1.10	0.45	4.6	5.1
8	2057	4.3	4.6	2.21	-	1.27	0.39	5.1	5.7
9	2869	4.8	5.1	2.45	-	-	0.35	5.7	6.2

Some of the monometallic and bimetallic clusters that are relevant to this work are highlighted blue.

2.3.2. Size, shape and distribution by Transition Electron Microscopy

TEM particle sizes were evaluated for the Ru@Pt NPs with different Ru core sizes and Pt shell thicknesses, as well as the individual Ru NPs. All the Ru@Pt NPs showed increase of the average particle diameters compared to those of the respective core metals. In general, particle size distributions were uniform and Gaussian. Furthermore, relative increases in particle sizes were consistent with the Schmid's cluster model,¹¹¹ and thus supported the core/shell structures. The Pt_xRu_{1-x} (x=0.33-0.8) alloy NPs also exhibited composition dependent variations in their average particle sizes in the range of 4.3-6.4 nm.

The Ru@Pt NPs from 3.0 nm Ru NPs with 1 to 1 stoichiometry of the elements show a mean particle size of 4.1 nm (Figure 2.1g and 2.1i), which is larger than that of monometallic Ru NPs (Figure 2.1a), and smaller than that of monometallic Pt NPs (Figure 2.1d). The HR-TEM image in the Figure 2.1h shows a typical Ru@Pt nanoparticle with lattice fringes. The bulk PtRu alloy NPs show an average size of 4.4 nm (Figures 2.1k and 2.1m). The HR-TEM images of the PtRu alloy NPs also show prominent FCC lattice fringes (Figure 2.1l). Using the shell model of Schmid,¹¹¹ the composition of the particles and taking into account the precision of the TEM measurements, we conclude that the Pt shell of the Ru@Pt NPs is 1-2 MLs thick, which we have found to be the Pt-coverage yielding optimal catalytic activity (*vide infra*).

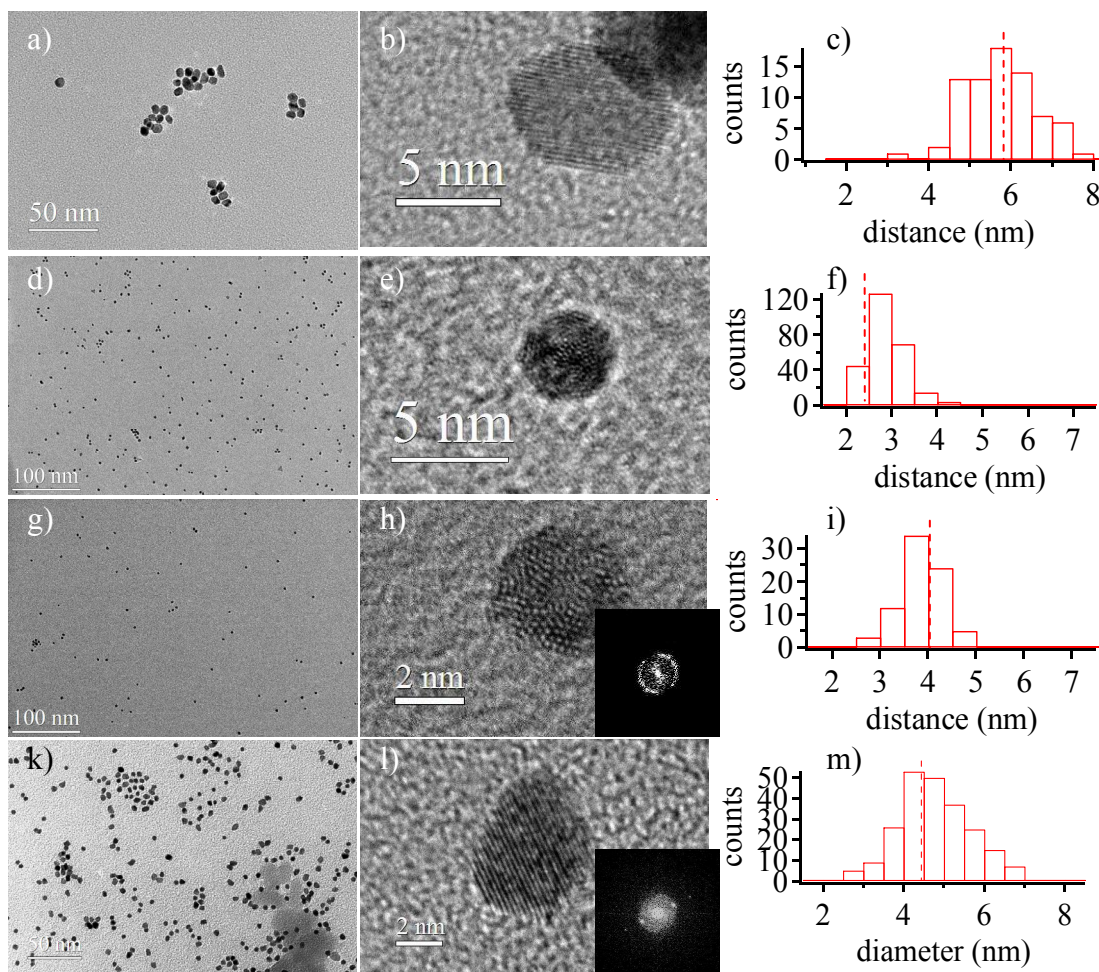


Figure 2.1. TEM images of (a) Pt, (d) Ru, (g) Ru@Pt (1:1) and (k) Pt₅₀Ru₅₀ NPs; (b, e, h, l) HR-TEM images, showing crystallinity and/or twinning; (c, f, i, m) particle size histograms of the NPs in (a, d, g, k), respectively. Insets show the Fast Fourier Transforms (FFTs) of the HR-TEM images.

Representative TEM analysis of 3.7 nm Ru@Pt NPs with submonolayer coverages of Pt shells, 4.4 nm Ru@Pt NPs with ca. 2-3 ML thick Pt shells are shown in Figure 2.2. 4.4 nm Ru@Pt NPs that are synthesized using rigorously dried EG are virtually identical to those synthesized using as-received EG.

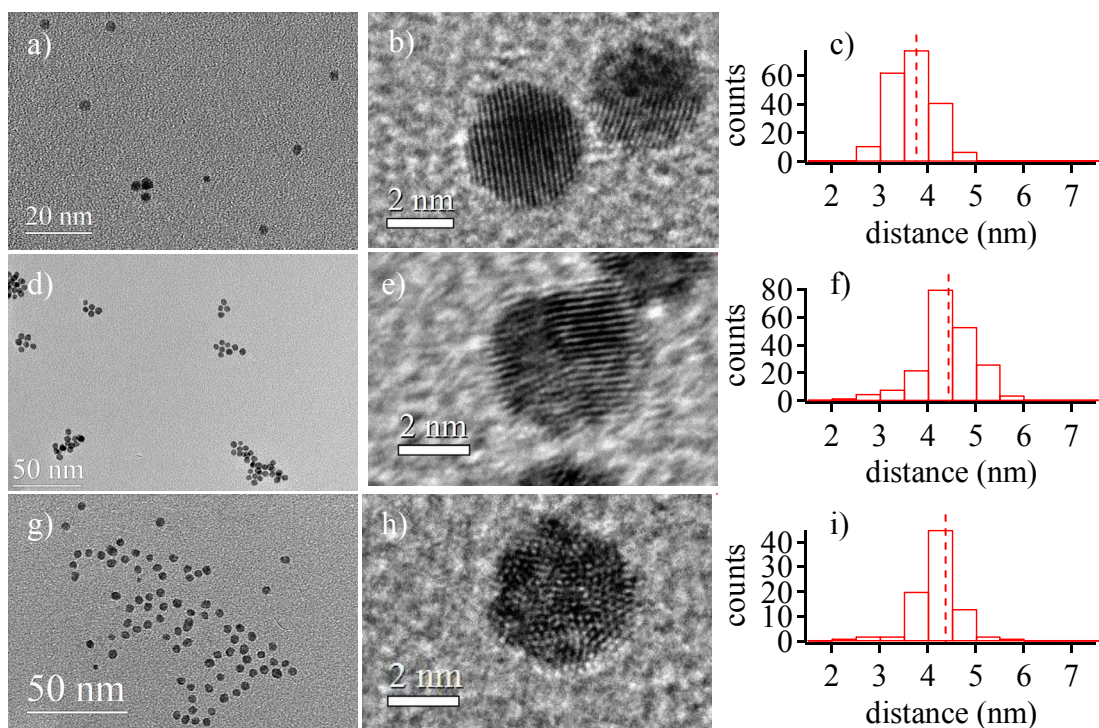


Figure 2.2. TEM images of (a) 3.7 nm Ru@Pt NPs with sub-monolayer coverages of Pt shells and 4.4 nm Ru@Pt NPs with ca. 2-3 ML thick Pt shells that are synthesized using (d) as-received EG and (g) rigorously dried EG; (b, e and h) HR-TEM images given next to each TEM image, showing crystallinity and/or twinning; (c, f and i) particle size histograms of the NPs in (a, d and g), respectively.

Figure 2.3 shows representative TEM analysis of sequentially grown 4.2 nm Ru NPs and 4.7 nm Ru@Pt NPs with ca. 1 ML thick Pt shells. TEM analysis of 5.7 nm Ru NPs and 6.2 nm Ru@Pt NPs with ca. 1 ML thick Pt shells, and 7.6 nm Ru@Pt NP with ca. 3-4 ML thick Pt shells is shown in Figure 2.4. Ru@Pt NPs derived from the sequentially grown 4.2 nm Ru NPs or 5.7 nm Ru NPs show size changes whose relative magnitudes are well predicted by volume/density calculations of the closely-packed metal phases.

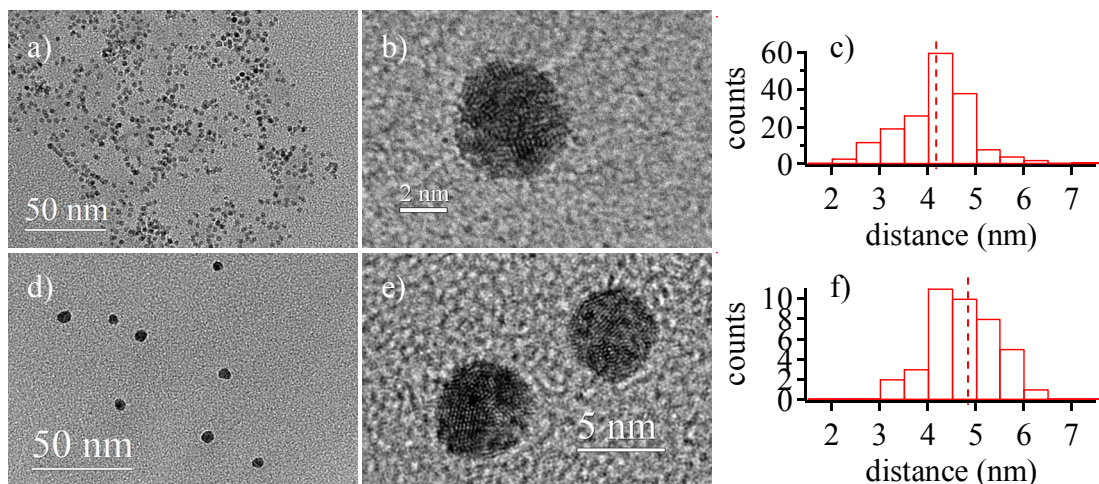


Figure 2.3. TEM images of (a) sequentially grown 4.2 nm Ru NPs and (d) 4.7 nm Ru@Pt NPs with ca. 1-layer thick Pt shells; (b and e) HR-TEM images, showing twinning and nano-crystallinity; (c and f) particle size histograms of the respective NPs.

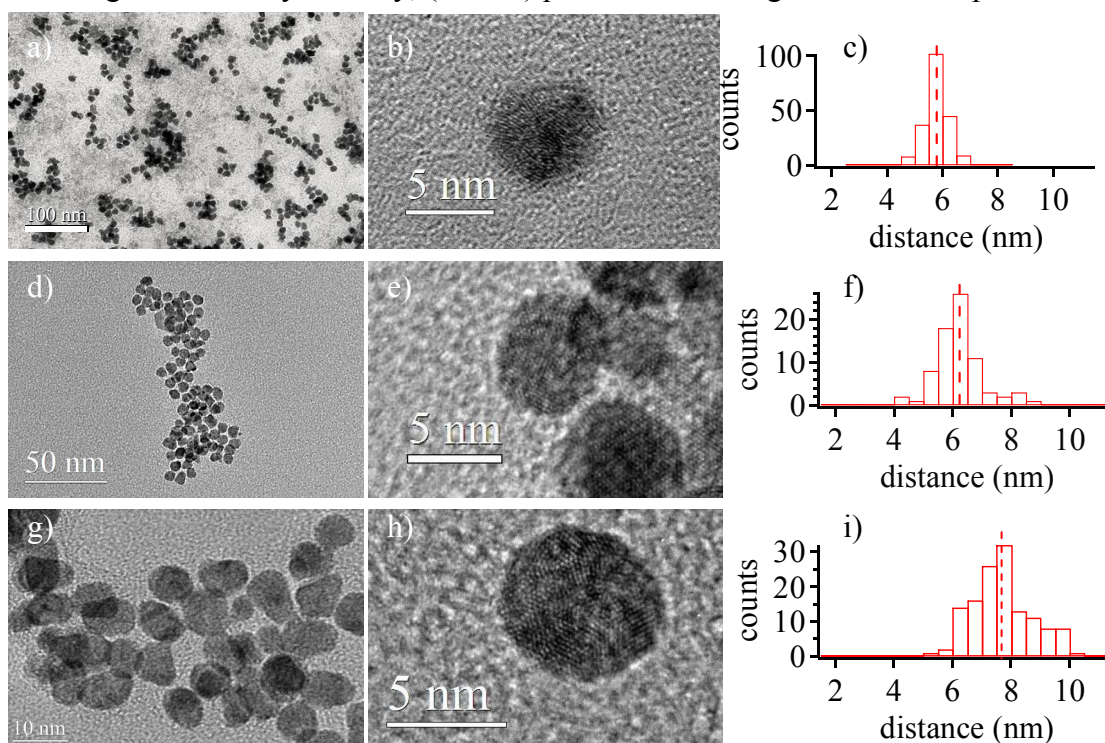


Figure 2.4. TEM images of (a) 5.7 nm Ru NPs, (d) 6.2 nm Ru@Pt NPs with ca. 1 ML thick Pt shells and (g) 7.6 nm Ru@Pt NPs with multiple layers of Pt shells; (b, e and h) HR-TEM images, showing nano-crystallinity and multiple twinning; (c, f and i) particle size histograms of the NPs in (a, d and g), respectively, indicating the gradual size increase.

Small Ru NPs via the NaBH_4 reduction of RuCl_3 showed little contrast on carbon supported Cu grid, and no particle size analysis could be performed. The particles were found to be in a size range of 1.0-2.5 nm (and possibly with particles <1.0 nm). The Ru@Pt NPs from the small Ru NPs seeds with a Ru:Pt molar ratio of 1:2 show a mean particle size of 3.0 nm, which correspond to a ca. 1-2 MLs thick Pt shells (Figures 2.5d and 2.5f). To compare and contrast, Pt NPs were also synthesized via NaBH_4 reduction in EG. Pt NPs exhibited a broad size distribution in a size range of 1-5 nm with a mean at 2.0 nm, as shown in Figures 2.5a and 2.5c. HR-TEM images show some twinning and reveals nanocrystallinity (Figures 2.5b and 2.5e).

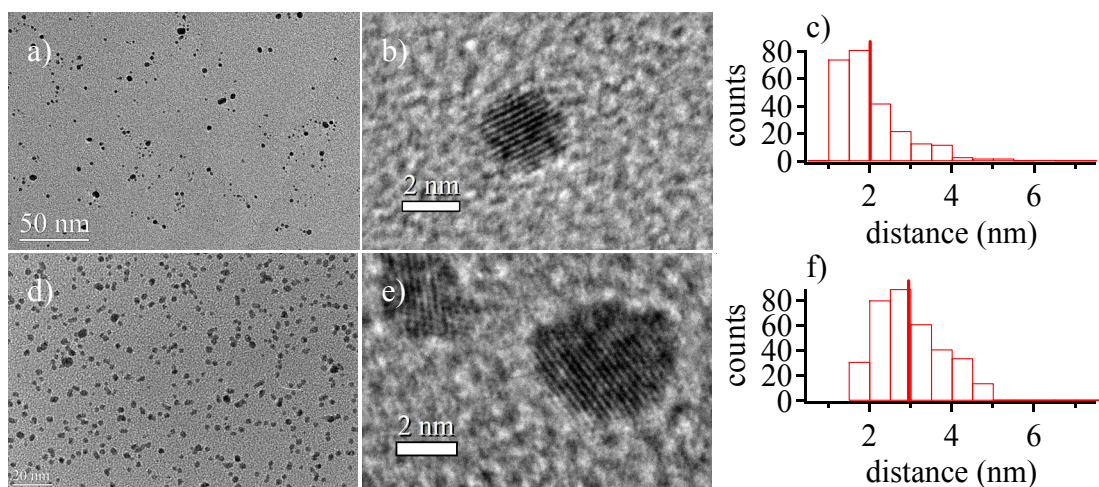


Figure 2.5. TEM images of (a) 2.0 nm Pt NPs and (d) 3.0 nm Ru@Pt NPs with ca. 1-2 layers thick Pt shells; (b and e) HR-TEM images, showing Pt 111 planes; and (c and f) particle size histograms of the NPs in (a and d), respectively.

PVP-free Ru NPs are ca. 3.1 nm in diameter, but there is a small fraction of >4 nm particles (Figures 2.6a and 2.6c). NPs are nano-crystalline in nature, as revealed in Figure 2.5b. PVP-free nano-crystalline Pt particles have ca. 2.2 nm size and smaller relative to PVP-protected ones under similar reaction conditions (Figures 2.6d through

2.6e). PVP-free Ru@Pt NPs are uniform in size with an average of 4.3 nm (Figures 2.6g and 2.6i). The size histogram reveals size focusing compared to the parent Ru NPs. HR-TEM image in Figure 2.6g show multiple twinning of NPs.

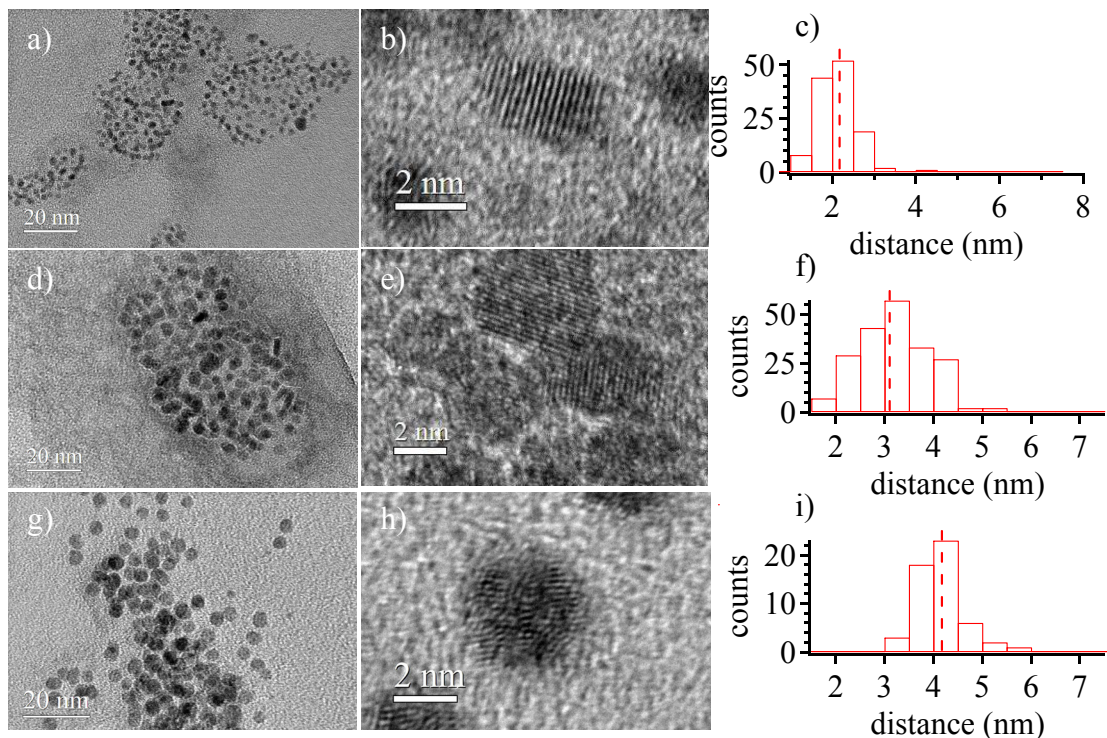


Figure 2.6. TEM images of (a) PVP-free Pt, (d) PVP-free Ru, and (g) PVP-free Ru@Pt (1:1) NPs; (b, e and h) HR-TEM images, showing nano-crystallinity and/or twinning; (c, f and i) particle size histograms of the NPs in (a, d and g), respectively.

Finally, Pt_xRu_{1-x} alloys NPs of various compositions that are designated by x ($x=0.33-0.80$) have been evaluated in TEM. Nano-structured PtRu alloy particles with 50:50 starting stoichiometry of the constituent atoms show a mean particle size of 4.4 nm (see Figures 2.1k through 2.1m). The $Pt_{66}Ru_{34}$ alloy NPs exhibit a mean particle diameter of 4.9 nm, and show nano-crystalline order rather in long range (Figures 2.7a through 2.7c). The $Pt_{34}Ru_{66}$ alloy NPs are, similarly, 4.4 nm in diameter in average. $Pt_{80}Ru_{20}$ alloy

NPs show the largest average size (6.4 nm) of the all alloy compositions studied. All Pt_xRu_{1-x} alloy NPs show a broad size distribution ranged between 3 nm and 8 nm.

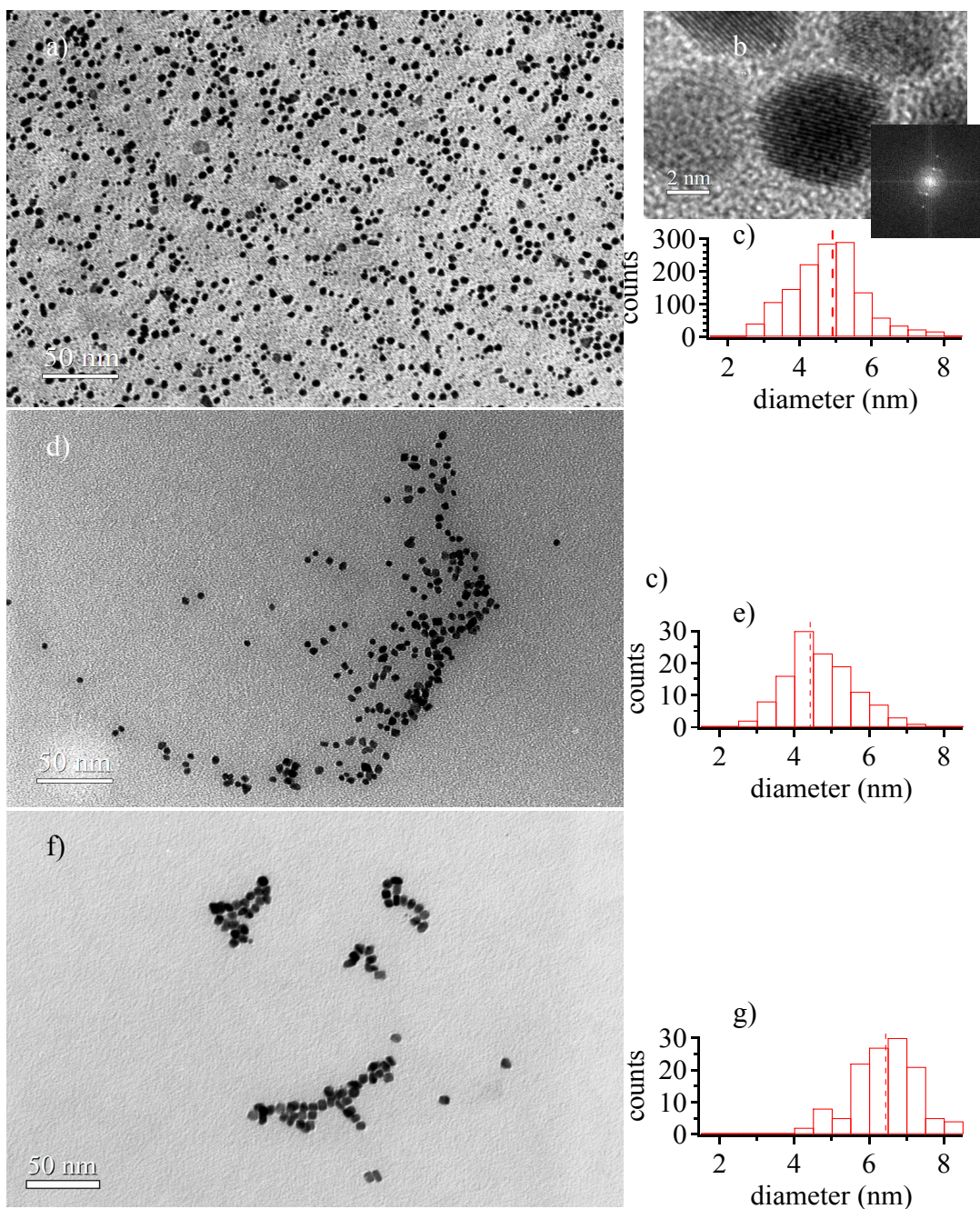


Figure 2.7. TEM images of (a) $Pt_{66}Ru_{34}$ NPs, (d) $Pt_{34}Ru_{66}$ NPs and (f) $Pt_{80}Ru_{20}$ NPs; (b) HR-TEM image of $Pt_{66}Ru_{34}$ indicating nano-crystallinity and 111 planes; (c, e and g) particle size histograms of the NPs in (a, d and f), respectively. Fast Fourier Transform (FFT) of the HR-TEM image in (b) is given inset.

2.3.3. Composition and architecture by Scanning Transition Electron

Microscopy

The composition and architecture (core-shell vs. alloy) were evaluated using a 1.5 nm EDS probe in a JEOL 2100 FE TEM operating in the STEM mode. Multiple single-particle EDS analysis of core-shell and alloy NPs from various syntheses confirmed that all particles are bimetallic in nature and stray monometallic particles were not observed in any of the samples. STEM-EDS line scans were recorded from 4.1 nm Ru@Pt NPs containing 3.0 nm Ru cores and 1 ML Pt shells (Figure 2.8a) clearly show the Pt M line with a bimodal Pt distribution that reaches a maximum at the edge of the particle (i.e. the shell). The Ru L line shows maximum Ru concentration at the center of the particle. STEM-EDS point spectra acquired from different regions of a distinct Ru@Pt NP show the highest atomic % Pt at the edges with more atomic % Ru at the center (Figure 2.9), which is consistent with the EDS line scan. Similarly, 4.4 nm Ru@Pt NPs with 3.0 nm Ru core and ca. 2-layer Pt shells show the bi-modal Pt distribution and the Ru distribution which is localized at the center of the particle (Figure 2.8d). In Figure 2.8b, a STEM-EDS line scan for ca. 6 nm PVP-free Ru@Pt nanoparticle is shown with the characteristic spectral features of the core/shell architecture. In contrast, the PtRu alloy NPs show Gaussian distributions of X-rays across the particle for both elements, as expected from the random arrangement of atoms on the surface and in the bulk of the particle (Figure 2.8c). STEM-EDS point spectra acquired from different regions of the same particle also reveals the random arrangement of Pt and Ru atoms across the particle (Figure 2.10).

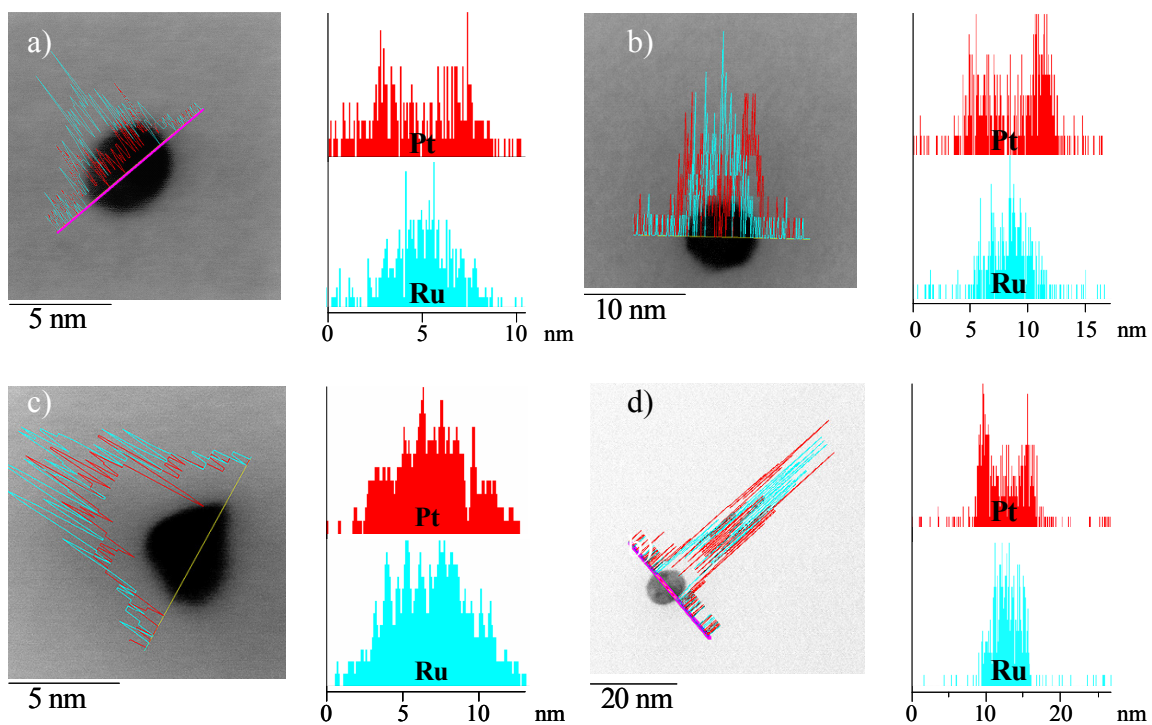


Figure 2.8. Representative STEM-EDS line spectra of (a) a 4.1 nm Ru@Pt NP with 3.0 nm Ru core and 1-2 MLs thick Pt shells, (b) a 4.2 nm PVP-free Ru@Pt NP, (c) a 4.4 nm Pt₅₀Ru₅₀ alloy nanoparticle, and (d) a 4.4 nm Ru@Pt NP with 3.0 nm Ru core and ca. 2-3 MLs thick Pt shells. Relative atomic % composition (vertical axis) of Pt (red) and Ru (blue) are plotted against the line scan probe position (horizontal axis) and are given next to STEM images. A 1.5 nm probe was used to trace 10 – 25 nm scans across each particle. The particle center is at ~ 5 nm in (a), ~ 8 nm in (b), ~7 nm in (c), and ~12 nm in (d).

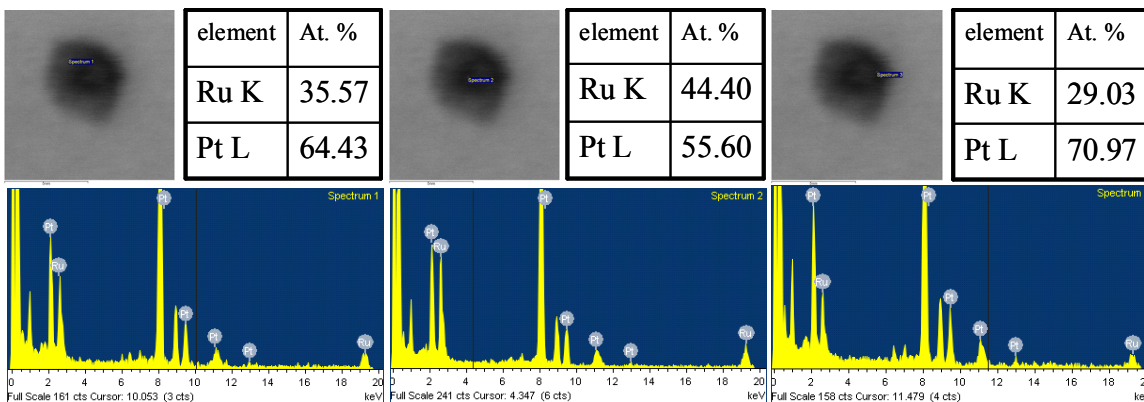


Figure 2.9. A representative STEM-EDS point analysis of a 4.1 nm Ru@Pt nanoparticle with a ca. 1-2 MLs thick Pt shell, showing three spectra: one from the top edge of the particle (left), one from the center (middle), and another from the right edge (right).

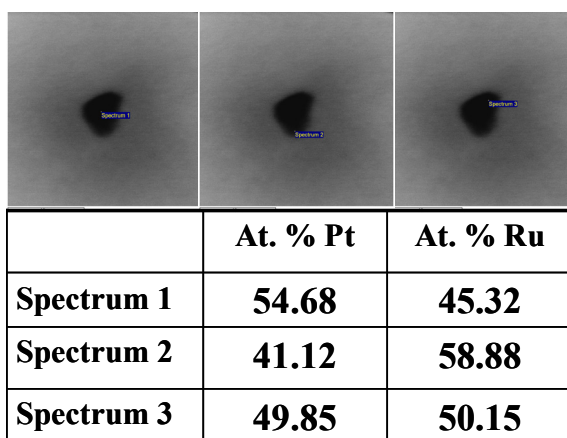


Figure 2.10. A representative STEM-EDS point analysis of a 4.4 nm Pt₅₀Ru₅₀ alloy nanoparticle (also see Figure 2.8c), showing three spectra in the order given in the table: one from the center of the particle(left), one from the bottom edge (middle), and another from the right top edge (right).

2.3.4. Structure evaluation of core/shell and alloys NPs by X-rays

2.3.4.1. Powder X-ray Diffraction

The XRD profiles of the Ru@Pt NPs (Figure 2.11) show face centered cubic (FCC) diffraction peaks for the Pt shell with an additional reflection at $\sim 19^\circ$ (a shoulder next to the Pt (111) peak at 18.3°) that arises from the poorly-crystalline HCP Ru core (Figure 2.11). The refined Pt lattice parameter for the Pt shell of the Ru@Pt particles gives a $3.897(1)$ Å FCC lattice constant (Figure 2.12c), which is slightly compressed from that of pure Pt at 3.923 Å.¹⁸⁰ While diffraction from monolayer films has been well described in a theoretical framework, it is rarely observed due to the lack of scattering matter from a thin film surface.¹⁸¹ Bulk samples of monolayer-coated NPs provide a higher density of scattering matter and enhanced X-ray diffraction relative to thin film samples. The XRD data for the Ru@Pt particles with approximate monolayer coverage show relatively strong Pt 111 diffraction peak whose peak position is shifted to higher 2θ compared to bulk Pt and is consistent with a compressed lattice. Additionally, the 002 reflection of Ru@Pt is shifted from its normal position to lower 2θ and has a lower intensity relative to bulk Pt. Monometallic Pt NPs synthesized under identical conditions show bulk Pt diffraction patterns with no anomalies in their peak positions. As the Pt shell becomes thicker with additional overlayers, the peak positions for the 111 diffraction shift to their “normal” position with increasing intensities. We attribute the anomalies in the diffraction data for the monolayer shells to incomplete lattice formation and distortions from bulk Pt phase associated with the 2D structure.¹⁸² These anomalies also suggest that the observed diffraction peaks do not arise from low concentrations of pure Pt NPs in the Ru@Pt sample.

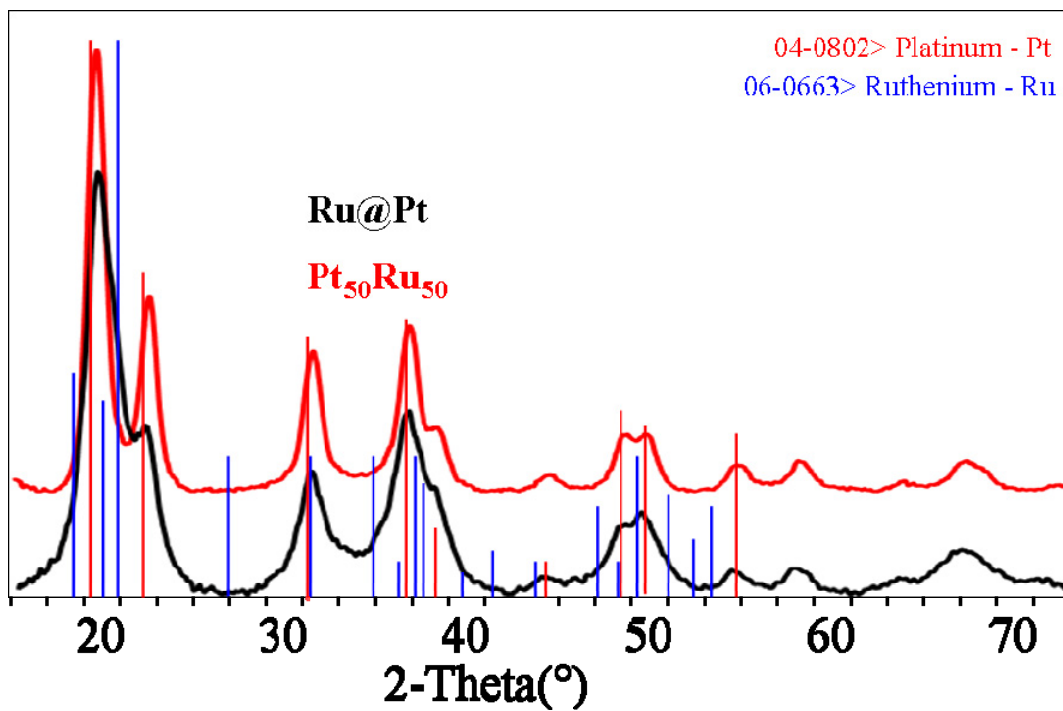


Figure 2.11. XRD profiles comparing 4.1 nm Ru@Pt NPs and 4.4 nm Pt₅₀Ru₅₀ NPs. Blue vertical lines represent the HCP Ru phase (JC-PDS file 06-0663), and red vertical lines the FCC Pt phase (JC-PDS file 04-0802).

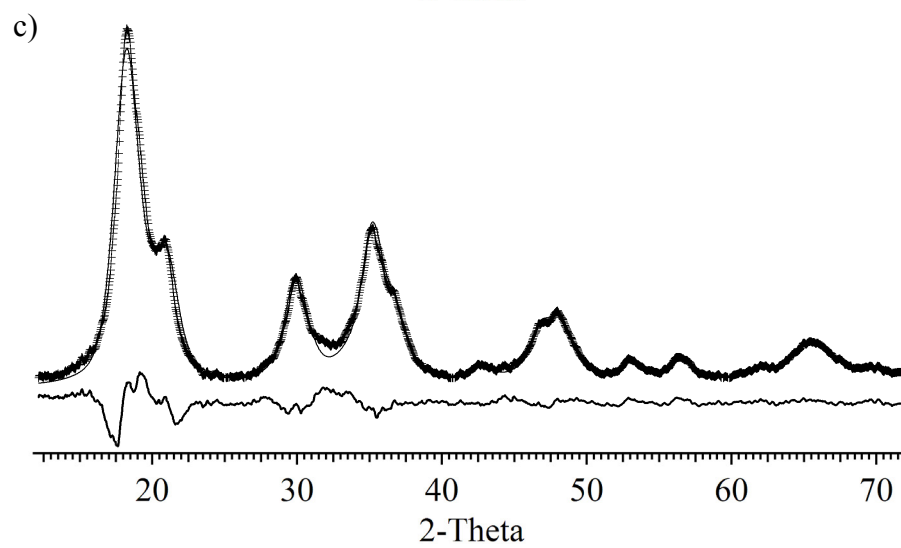
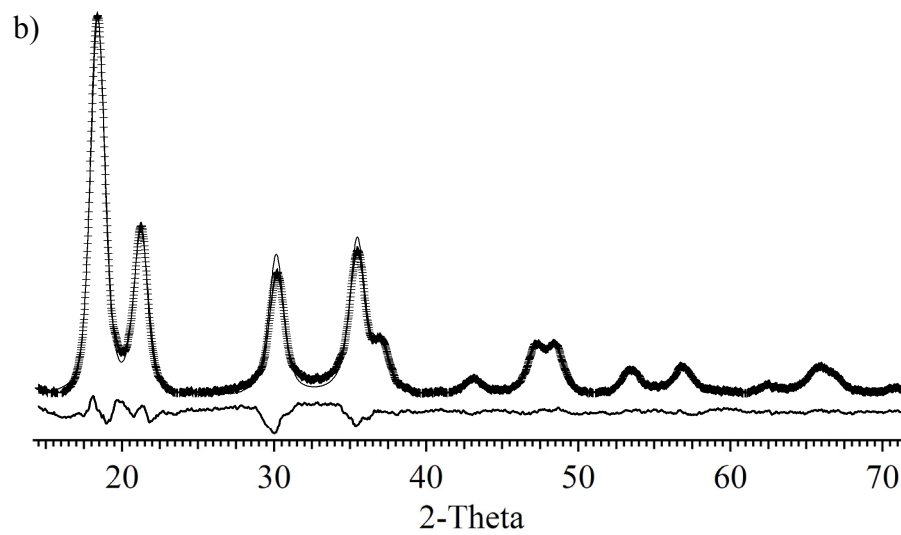
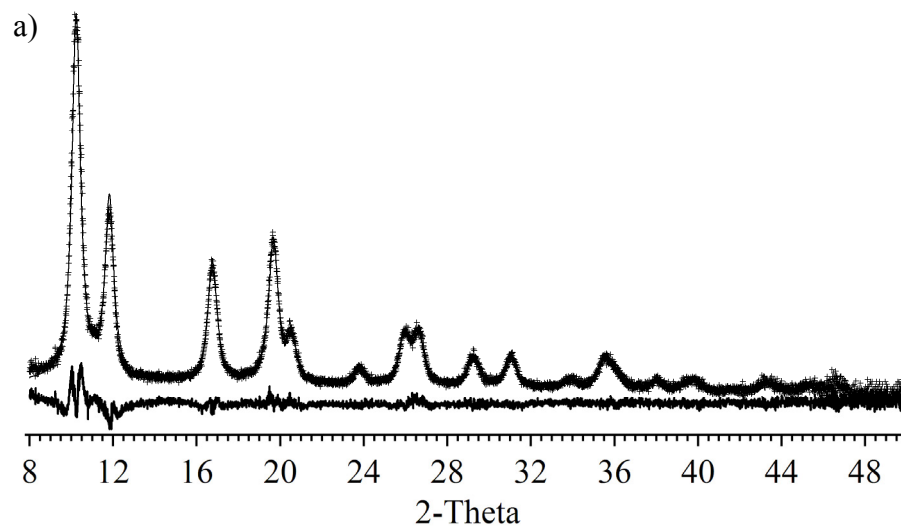


Figure 2.12. (a) Rietveld refinement on synchrotron data of 4.4 nm Pt₅₀Ru₅₀ NPs, and LeBail fits on molybdenum K_α data of (b) 4.4 nm Pt₅₀Ru₅₀ NPs and (c) 4.1 nm Ru@Pt NPs. The experimental data are shown by markers and the fits by solid lines. The residual patterns are given below each.

X-ray diffraction patterns for 4.1 nm Ru@Pt core/shell NPs with ca. 1-2 MLs thick Pt shells and 4.4 nm Pt₅₀Ru₅₀ alloy NPs were simulated using the Debye function sub-routine in DISCUS.¹ It was found that the TEM and EXAFS-derived core/shell cluster with thin Pt shell, i.e. 1 ML, underestimated the diffracting Pt volume and the model cluster with thick Pt shell, i.e. 2 ML, overestimated it (see Figure 2.13A and 2.13B). The simulated Pt-skin-only diffraction patterns were also given for comparison to the simulated core/shell diffraction patterns, and thus demonstrated a rather small contribution of the respective Ru cores to the overall diffraction. Moreover, the number average of the two model clusters, namely 40 Å core/shell cluster with 1 ML Pt shell and 40 Å core/shell with 2 ML Pt shell, exhibited a better visual match with the observed XRD pattern (Figure 2.13C). Likewise, the 1-layer and 2-layers core/shell structures were found to co-exist in the sample based on the EXAFS analysis of the measured and calculated coordination numbers (*vide infra*). Furthermore, the simulated XRD pattern of the alloy model cluster in Figure 2.14B was visually different from that of the core/shell model clusters, and matched with the experimental data (Figure 2.14A). In overall, the powder diffraction simulations qualitatively showed the diffraction from an approximately monolayer thick Pt shell around a disordered Ru core, which was consistent with the observed diffraction pattern.

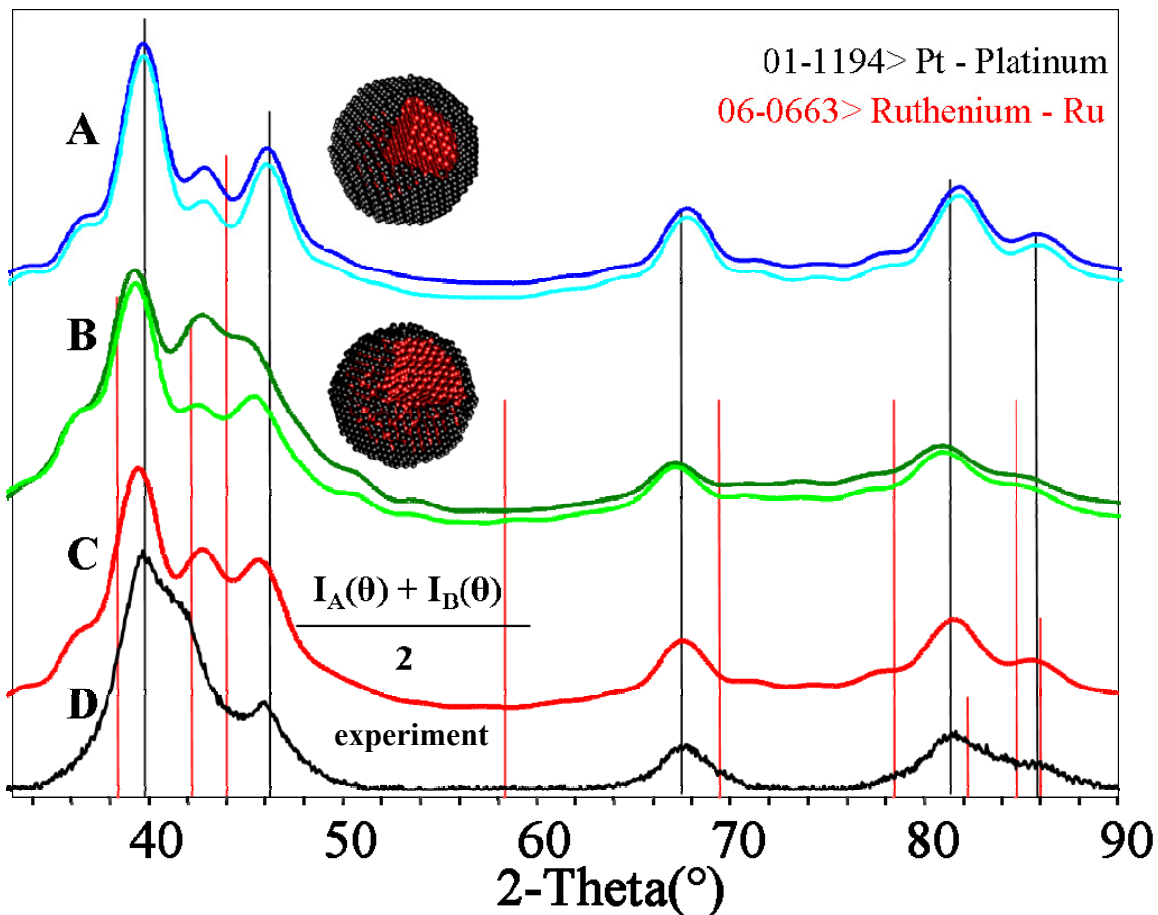


Figure 2.13. Debye Function simulations of the 40 Å diameter core/shell clusters with (A) a 2 MLs thick Pt shell, (B) a 1 ML thick Pt shell (B), and (C) a 50:50 mixture of 1 ML and 2 MLs thick Pt shells. Debye Function simulations of Pt-skin clusters are also shown with dashed lines below each respective core/shell cluster. XRD pattern of the 4.1 nm Ru@Pt NPs is shown in (D). JC-PDS peak positions for Pt (black) and Ru (red) are also presented.

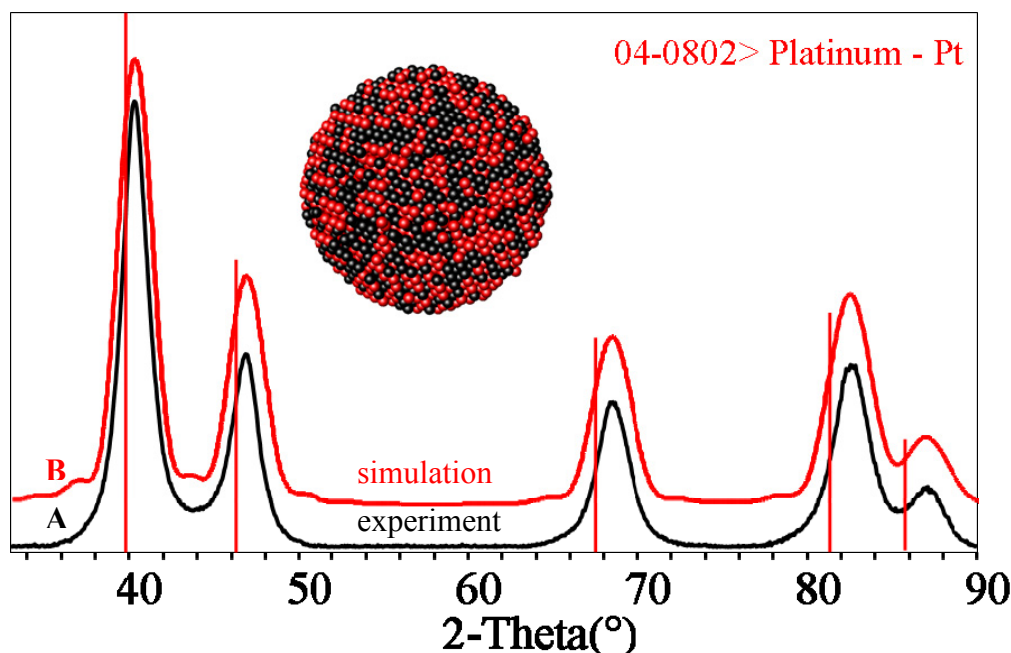


Figure 2.14. Patterns showing (A) experimental XRD from the 4.4 nm Pt₅₀Ru₅₀ NPs and (B) simulated XRD from a 44 Å diameter random alloy cluster. JC-PDS peak positions for Pt (red) are also presented.

Annealing the Ru@Pt NPs at 500°C in vacuum induces alloy formation, which is identical to that of the authentic alloy and its corresponding lattice parameter ($a = 3.8771(3)$ Å). As expected,^{183,184} both alloys (authentic and annealed Ru@Pt) show unit cells that are intermediate to pure Pt and Ru phases. In contrast, the physical mixtures of monometallic Pt and Ru NPs show well-resolved two-phase pattern of FCC Pt and HCP Ru upon annealing, indicating thermodynamic immiscibility as binary phase diagrams suggest (Figure 2.15).

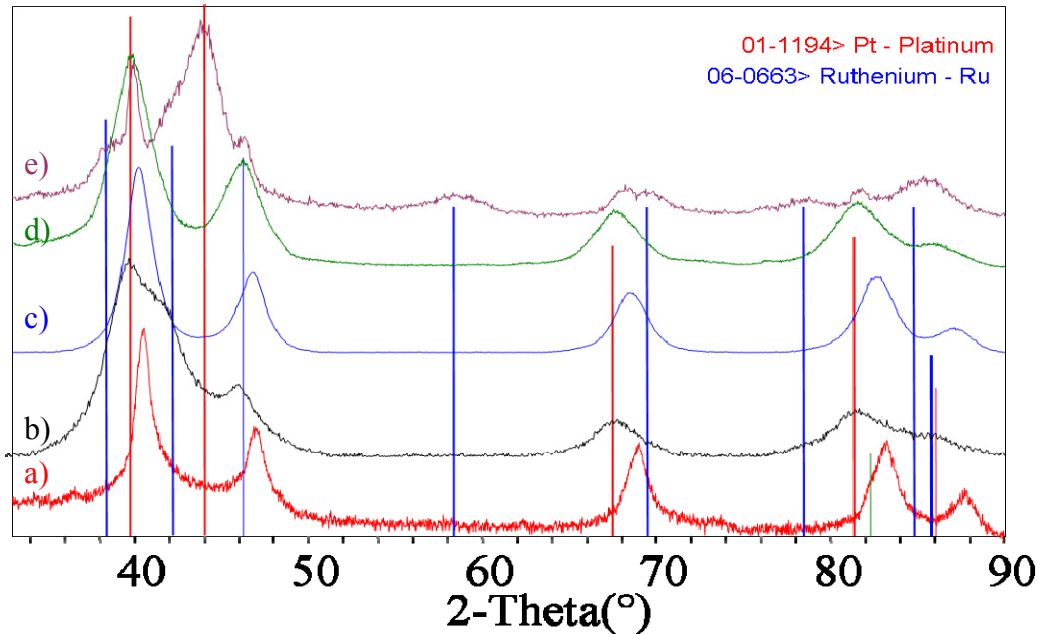


Figure 2.15. XRD profiles of (a) 4.1 nm Ru@Pt NPs after anneal at 500 °C for 12 h, (b) as-synthesized Ru@Pt NPs, (c) PtRu alloy nanoparticles and (d) as-prepared mixtures of monometallic Pt NPs and Ru NPs, and (e) physical mixtures after anneal at 500 °C for 12 h. Blue vertical lines represent the HCP Ru phase (JC-PDS file 06-0663), and red vertical lines the FCC Pt phase (JC-PDS file 01-1194).

4.2 nm Ru NPs synthesized from 3.0 nm Ru NPs via sequential deposition show a more crystalline HCP phase than the parent structure. Upon deposition of Pt shells of ca. 1 ML thick, the resulting XRD shows diffractions of mainly FCC Pt phase (Figure 2.16a). All, but 200 reflection of FCC Pt phase are in their bulk positions. The 200 reflection, on the other hand shifted to low 2- θ probably because of strain induced distortion of the FCC unit cell as shown in Figure 2.16a. 5.7 nm Ru NPs synthesized via co-deposition show a crystalline HCP phase. Both low and high angle peaks are prominent. Furthermore, Pt growth was monitored ex-situ using XRD. It was shown that the diffraction from FCC Pt shells increased in intensity as Pt was aged in the Ru colloidal suspension (Figure 2.16b). It was also found that the diffraction from FCC Pt

shells exhibited gradual increase with increasing thickness (Figure 2.17a). Similarly, the HCP Ru phase became more prominent with increasing mean Ru core sizes provided that Pt shells affixed at ca. 1-2 MLs (Figure 2.17b).

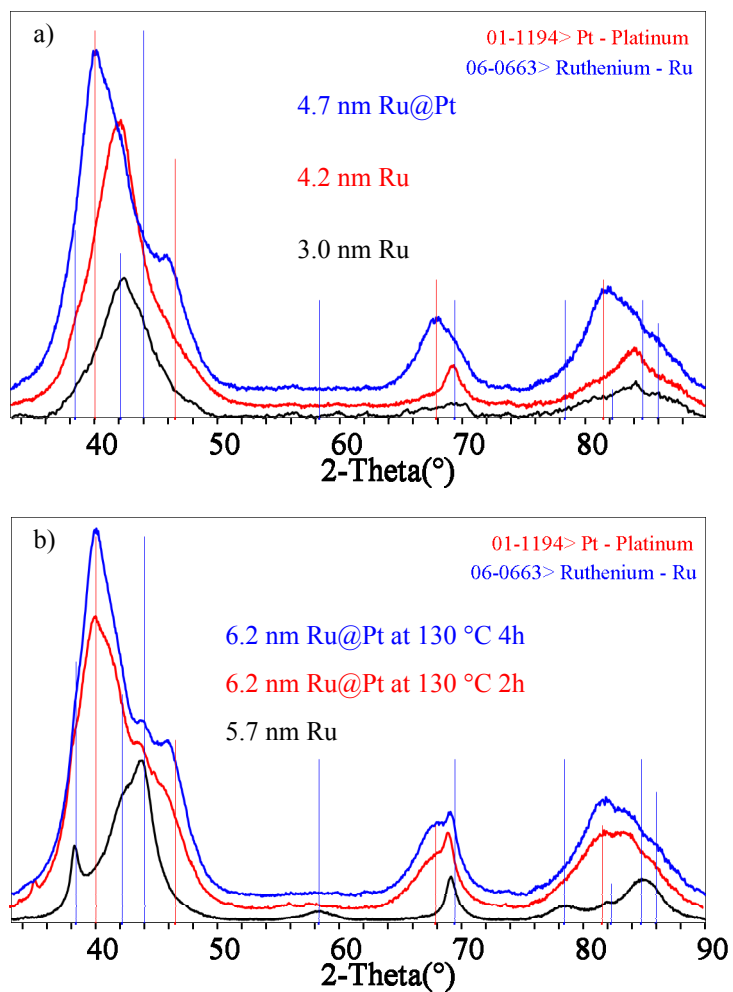


Figure 2.16. XRD profiles of (a) sequentially grown 4.2 nm Ru NPs and 4.7 nm Ru@Pt NPs with ca. 1 ML thick Pt shells and (b) 5.7 nm Ru NPs via the co-deposition method and 6.2 nm Ru@Pt NPs with ca. 1 ML Pt shells, showing the transient Pt deposition. Blue vertical lines represent the HCP Ru phase (JC-PDS file 06-0663), and red vertical lines the FCC Pt phase (JC-PDS file 01-1194).

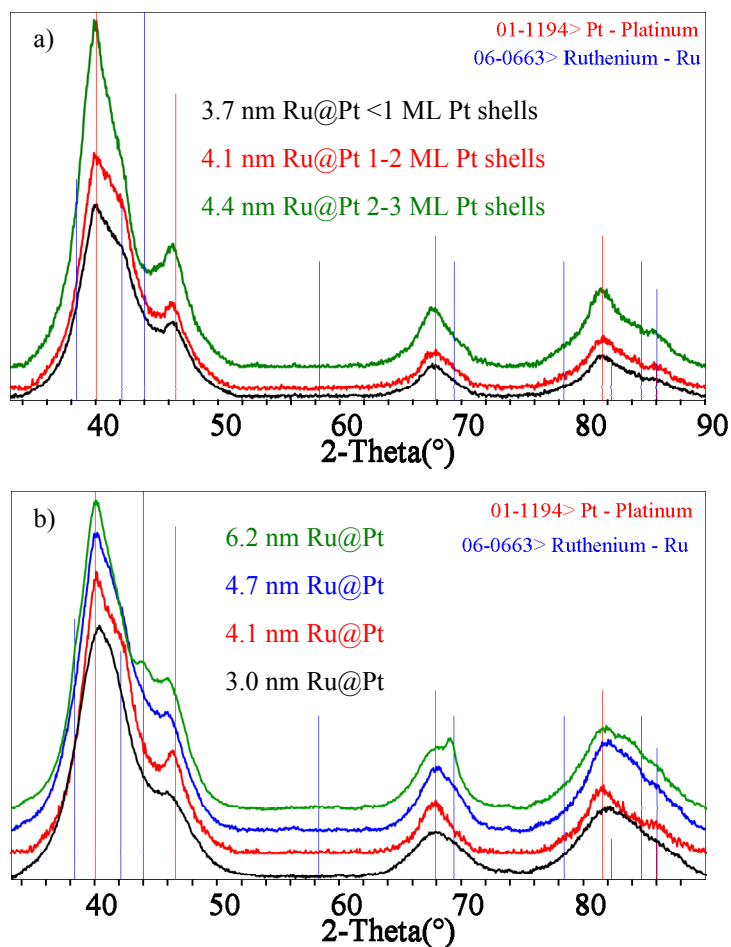


Figure 2.17. XRD profiles of (a) Ru@Pt NPs with 3.0 nm Ru cores and varying layers of Pt shells synthesized using rigorously dried EG, showing the correlation between the intensity of Pt 111 reflection and the Pt content, and (b) Ru@Pt NPs with varying Ru core sizes and approximately 1-2 MLs thick Pt shells. JC-PDS peak positions for Pt (red) and Ru (blue) are also presented.

Figure 2.18 shows the XRD profiles of the $\text{Pt}_x\text{Ru}_{100-x}$ ($x=34\text{-}80$) NPs. Vegard's law was used to estimate the composition of different $\text{Pt}_x\text{Ru}_{100-x}$ alloy phases.

¹⁸⁵ As shown by arrows in Figure 2.18, X-ray reflections, especially those at high angles because of their inverse $\sin 2\theta$ dependence ($2\theta > 90^\circ$), exhibited progressive shifts to higher angles with increasing Ru contents, as predicted by Vegard's Law (Figure 2.18 inset).

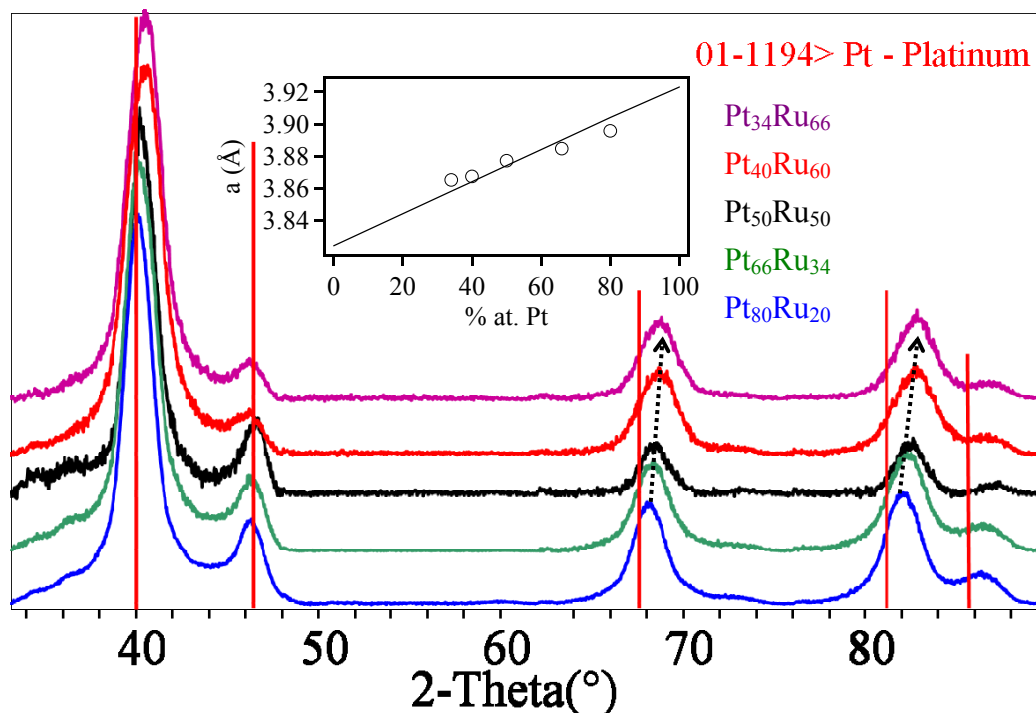


Figure 2.18. XRD profiles of the Pt_xRu_{1-x} ($x=0.33-0.8$) NPs. Arrows show shifts in 2- θ to high angles with increasing Ru content. Vegard's plot of XRD-derived unit cell parameters of the Pt_xRu_{100-x} alloy NPs is shown in the inset. Line shows the ideal Vegard's behavior, and circles the data points. JC-PDS peak positions for Pt (red) are also presented.

2.3.4.2. Extended X-Ray Absorption Fine Structure (EXAFS) and X-Ray Absorption Near Edge Structure (XANES) Studies

The bimetallic Pt/Ru NPs were studied in EXAFS and XANES to evaluate their three dimensional atomic structure governed by short range order (SRO). EXAFS data were collected by Prof. Frenkel and Dr. Wang at the X18B beamline at the National Synchrotron Light Source of Brookhaven National Laboratory on both Pt and Ru edges.

The multi-energy data analysis to account for multiple-scattering was also carried out by the same group. Modeling was partially performed at University of Maryland.

First, XANES was run for the bimetallic Pt₅₀Ru₅₀ alloy and Ru@Pt core/shell NPs, and compared to bulk Pt, Ru and RuO₂. XANES spectra of the bimetallic NPs consistently exhibited increasing white line intensities as well as shifts to higher energies than bulk Pt and Ru, but both samples were predominantly in the metallic state. Pt in both core/shell and alloy nanoparticles were more oxidized than in bulk Pt, and moreover, shell-Pt was more oxidized than alloyed Pt (Figure 2.19a). Ru also exhibited some degree of oxidation, especially in the alloy structure, because of the higher white line intensity and broader bandwidth of its XANES spectrum compared to that of bulk Ru (Figure 2.19b).

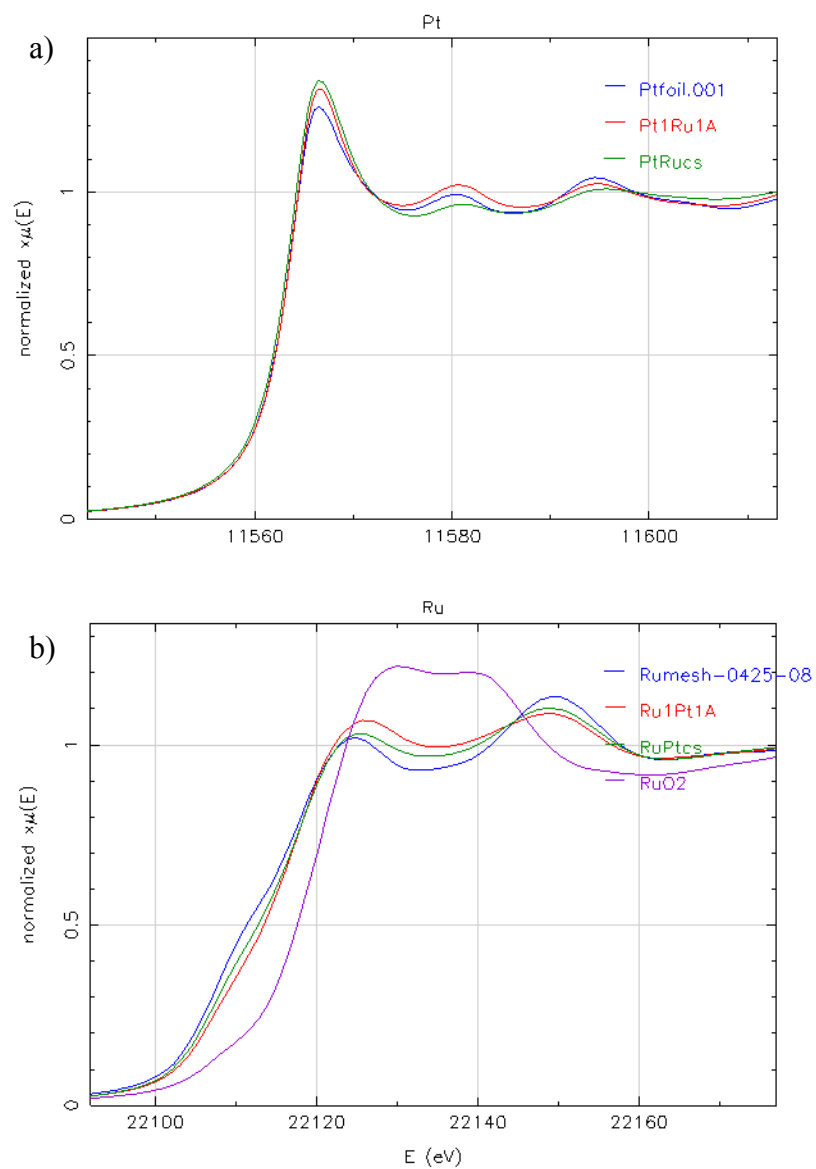


Figure 2.19. XANES spectra of (a) Ru@Pt NPs, Pt₅₀Ru₅₀ NPs and Pt foil at Pt L edge and (b) Ru@Pt NPs, Pt₅₀Ru₅₀ NPs, Ru mesh and RuO₂ powder at Ru K edge.

EXAFS spectra were acquired at both Pt and Ru edges for the bimetallic Pt₅₀Ru₅₀ alloy and Ru@Pt (1:1) core/shell NPs. The EXAFS data clearly reveal the distinct nano-crystalline nature of the core/shell versus alloy particles of similar average particle sizes and identical elemental compositions (Figure 2.20 and 2.21).

The EXAFS oscillations in k-space, shown in Figure 2.20, at each absorption edge showed amplitude drop compared to bulk Pt and Ru, respectively. Lower amplitudes were solely attributed to the finite size effect of nanoparticles. The EXAFS oscillations in the core/shell nanoparticles were in-phase with bulk metals at each absorption edge, showing phase-segregation consistent with the segregated metals in the structure. On the other hand, the alloy nanoparticles showed phase differences at each edge, which was consistent with an alloy structure of Pt and Ru (Figures 2.20a and 2.20b).

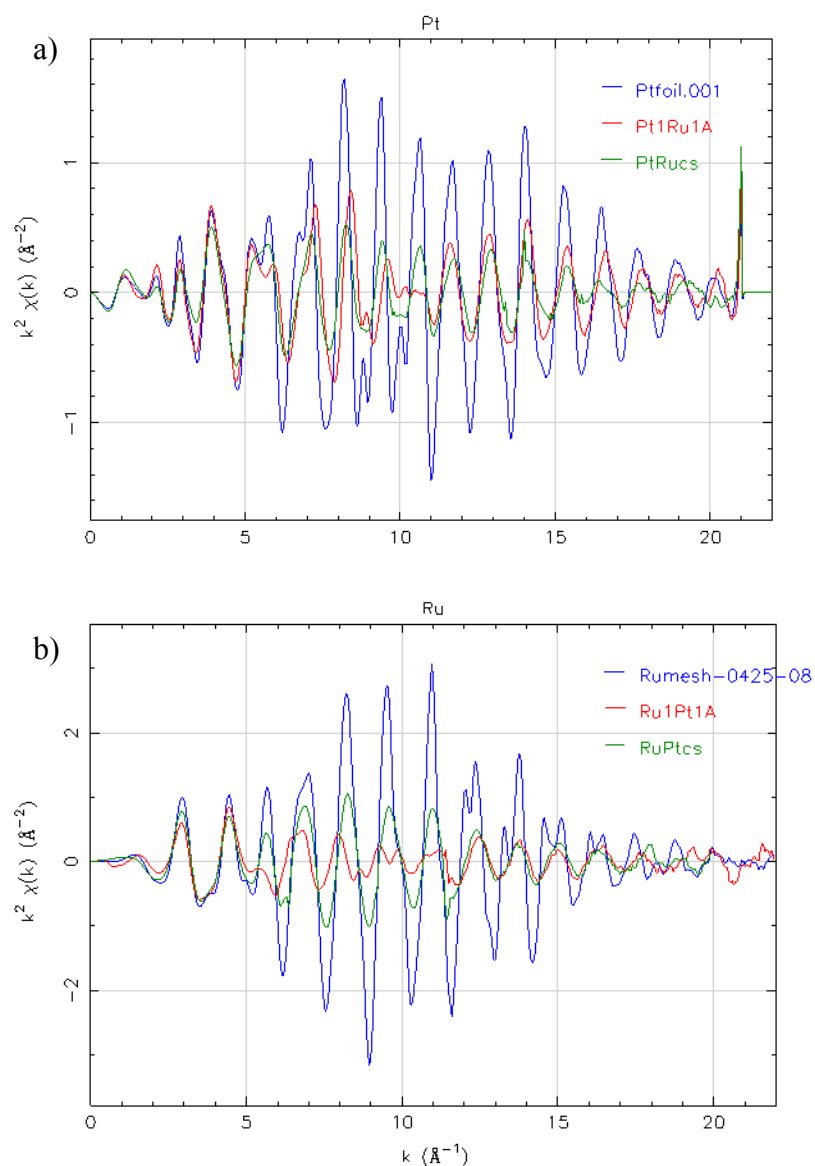


Figure 2.20. XAFS functions in k-space of (a) Ru@Pt core/shell, Pt₅₀Ru₅₀ alloy NPs and Pt foil at Pt L edge, and (b) Ru@Pt core/shell, Pt₅₀Ru₅₀ alloy NPs, Ru mesh and RuO₂ powder at Ru K edge.

Figure 2.20 showed the Fourier Transformed EXAFS spectra of the bimetallic nanoparticles and bulk references. The finite size effect caused the lower amplitudes of the 1st nearest neighbors at ca. 2.7 Å in case of the bimetallic alloy and

core/shell particles compared to the reference material. The r-space data indicated alloying in the alloy nanoparticles, and phase-segregation in the core/shell nanoparticles (Figure 2.21).

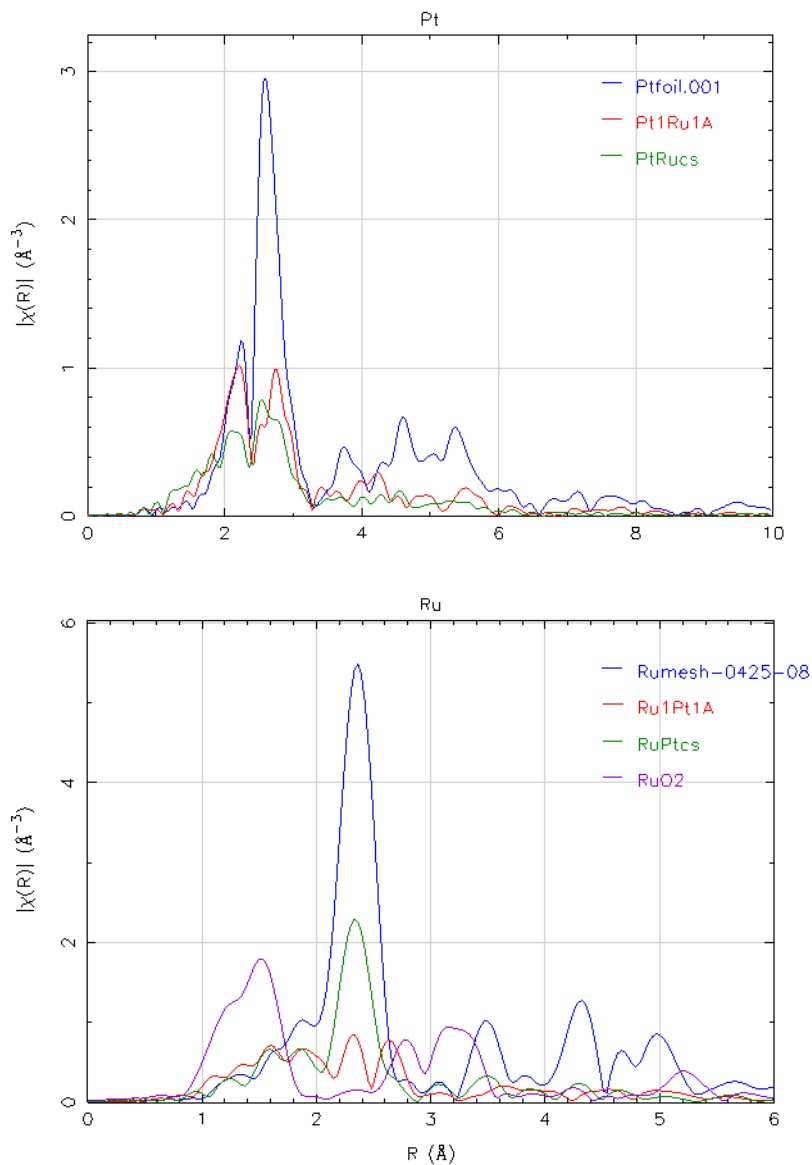


Figure 2.21. Fourier Transforms of EXAFS functions of (a) Ru@Pt core/shell, Pt₅₀Ru₅₀ alloy NPs and Pt foil at Pt L edge, and (b) Ru@Pt core/shell, Pt₅₀Ru₅₀ alloy NPs, Ru mesh and RuO₂ powder at Ru K edge.

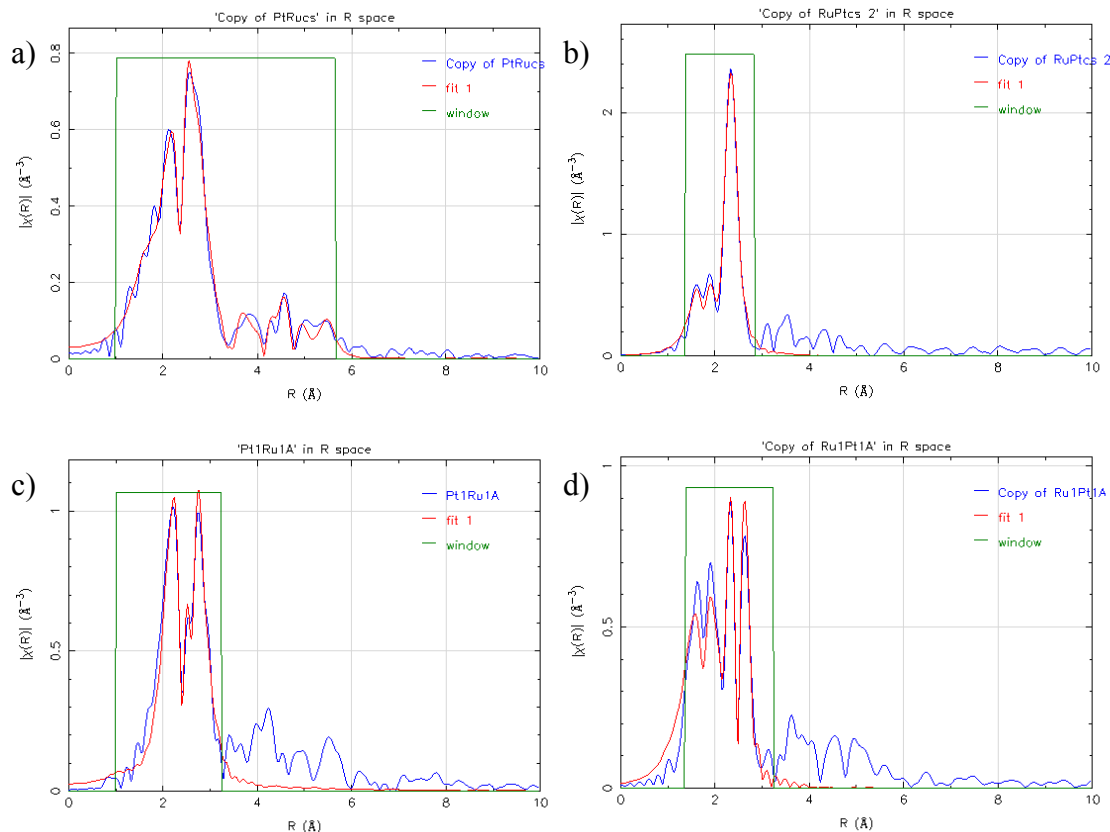


Figure 2.22. FEFF6 fits (red) to the FT-EXAFS data at (a) Pt edge and (b) Ru edge for the 4.1 nm Ru@Pt core/shell particles, and at (c) Pt edge and (d) Ru edge for the Pt₅₀Ru₅₀ alloy NPs.

EXAFS data analysis was carried out assuming Pt-Pt and Pt-Ru interactions for Pt edge data, and Ru-Ru and Ru-Pt interactions for Ru edge data by Prof. Frenkel and Dr. Wang at the Brookhaven National Laboratory. FEFF6 fits to the FT-EXAFS data for each Pt L edge and Ru K edge^{119,120} of the core/shell and alloy NPs were shown in Figure 2.22. Data for each edge were fitted by using FEFF6 theory concurrently, by employing physically reasonable constraints between the fitting parameters. For the core/shell nanoparticles, multiple-scattering contributions to Pt edge data were also included, such that data at higher r-range could be fitted to extract structural parameters beyond the 1st

coordination shell (Figure 2.22a). For Ru edge data, however, the absence of such contributions was taken as evidence of the disordered core structure (Figure 2.22b). The results of the FEFF6 fits were summarized in Table 2.2. The coordination numbers (CN) of Pt-metal (M) and Ru-metal (M) bonds were defined as

$$CN_{Pt-M} = CN_{Pt-Pt} + CN_{Pt-Ru}$$

$$CN_{Ru-M} = CN_{Ru-Ru} + CN_{Ru-Pt}$$

where CN_{Pt-Pt} , CN_{Pt-Ru} , CN_{Ru-Ru} , CN_{Ru-Pt} stood for partial coordination numbers due to Pt-Pt, Pt-Ru, Ru-Ru and Ru-Pt bonds, respectively. The total coordination numbers for the bimetallic nanoparticles were smaller than 12 (bulk) because of truncation effect of finite size particles. For the alloy, CN_{Pt-M} and CN_{Ru-M} were equal within the error,

$$CN_{Pt-M} = 6.52(41) + 2.8(32) = 9.3(5)$$

$$CN_{Ru-M} = 4.01(83) + 4.28(1.15) = 8.3(1.4)$$

which is indicative of a homogeneous alloy. The bulk composition was estimated from the equation,

$$X_{Pt}/X_{Ru} = CN_{Ru-Pt}/CN_{Pt-Ru}$$

The calculated X_{Pt}/X_{Ru} value of 1.4(3) was close to those from STEM-EDS (see section 2.3.3) and XPS measurements, and XRD and PDF refinements (see sections 2.3.5, 2.3.4.1

and 2.3.4.3, respectively). There was also significant Ru-O contribution, but no measurable Pt-O contribution (see Table 2.2).

Similarly, the total coordination numbers of Pt-metal and Ru-metal bonds in the core/shell nanoparticles were

$$\text{CN}_{\text{Pt-M}} = \overset{\text{Pt-Pt}}{7.17(42)} + \overset{\text{Pt-Ru}}{0.26(14)} = 7.4(5)$$

$$\text{CN}_{\text{Ru-M}} = \overset{\text{Ru-Ru}}{7.48(49)} + \overset{\text{Ru-Pt}}{0.42(27)} = 7.9(6)$$

The small Pt-Ru interactions were attributed to intended interactions of the core/shell interface. These data are in excellent agreement with the model structures that show a total of $\text{CN}_{\text{Pt-Ru}}=0.46$ for 4.1 nm structures used in this study. In contrast to the alloy, there was little contribution from Ru-O interactions, but significant contributions from Pt-O interactions.

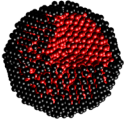
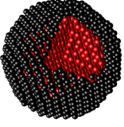
Table 2.2. Structure parameters and estimated error bars from EXAFS analysis of the Ru@Pt core/shell and Pt₅₀Ru₅₀ alloy NPs.

	Pt	PtRu alloy	Ru@Pt core-shell *	RuO ₂	Ru
N _{Pt-Pt (1st)}	12	6.52 (41)	7.17 (42)		
N _{Pt-Pt (2nd)}	6		2.06 (73)		
N _{Pt-Pt3 (ms)}	48		17.41 (8.4)		
N _{Pt-Pt5 (3rd)}	24		5.45 (1.79)		
N _{Pt-Pt8 (4th)}	12		3.08 (1.00)		
N _{Pt-O}			1.11 (35)		
N _{Pt-Ru}		2.80 (32)	0.26 (10)		
N _{Ru-Pt}		4.01 (83)	0.42 (27)		
N _{Ru-Ru}		4.28 (1.15)	7.49 (49)		12 (6+6)
N _{Ru-O}		1.12 (83)	0.54 (25)	6	
R(Å) _{Pt-Pt (1st)}	2.774(2)	2.740 (3)	2.743 (3)		
R(Å) _{Pt-Pt (2nd)}			3.878 (16)		
R(Å) _{Pt-Pt3 (ms)}			4.181 (19)		
R(Å) _{Pt-Pt5 (3rd)}			4.787 (11)		
R(Å) _{Pt-Pt8 (4th)}			5.533 (12)		
R(Å) _{Pt-O}			1.998 (15)		
R(Å) _{Pt-Ru}		2.718 (4)	2.690 (10)		
R(Å) _{Ru-Pt}		2.718 (4)	2.690 (10)		
R(Å) _{Ru-Ru}		2.689 (8)	2.665 (3)	3.119 (4)	2.648 (2) 2.707 (2)
R(Å) _{Ru-O}		1.966 (29)	1.967 (15)	1.919 (3) 2.017 (3)	
σ ² (Å ²) _{Pt-Pt (1st)}	0.0050 (1)	0.0054 (2)	0.0076 (3)		
σ ² (Å ²) _{Pt-Pt (2nd)}			0.0089 (17)		
σ ² (Å ²) _{Pt-Pt3 (ms)}			0.0020 (18)		
σ ² (Å ²) _{Pt-Pt5 (3rd)}			0.0089 (17)		
σ ² (Å ²) _{Pt-Pt8 (4th)}			0.0094 (21)		
σ ² (Å ²) _{Pt-O}			0.0116 (46)		
σ ² (Å ²) _{Pt-Ru}		0.0049 (6)	0.0027 (14)		
σ ² (Å ²) _{Ru-Pt}		0.0049 (6)	0.0027 (14)		
σ ² (Å ²) _{Ru-Ru}		0.0069 (16)	0.0061 (4)	0.0039 (6)	0.0032 (2)
σ ² (Å ²) _{Ru-O}		0.0027 (51)	0.0000 (18)	0.0001 (7) 0.0016 (7)	
ΔE ₀ (eV) _{Pt}	9.09 (36)	8.08 (40)	8.27 (59)		
ΔE ₀ (eV) _{Ru-Ru}		-5.90 (1.22)	-5.96 (63)	2.48 (81)	-4.54 (49)

Data for each edge were fitted with FEFF6 theory concurrently, by employing physically reasonable constraints between the fitting parameters at the Brookhaven National Laboratory. R_{Pt-Ru} is equal to R_{Ru-Pt} and σ²_{Pt-Ru} to σ²_{Ru-Pt}. Uncertainties are indicated in parentheses (e.g., 7.17(42) = 7.17 ± 0.42).

Furthermore, coordination numbers in the 1st through 4th coordination shells for the core/shell nanoparticles were simulated using model core/shell clusters. Model clusters based on the average TEM size, and core diameters and shell thicknesses from FCC lattices truncated in spherical structures that best simulated the observed TEM data were generated. The number distributions of metal-metal pair distances were tabulated from atomic coordinates. Finally, the coordination numbers of 1st through 4th coordination shells were calculated from the pair distributions projected on the radial distances and the number of atoms of each element. Given the strong disorder in the core (XRD and EXAFS analysis), Ru was not included in modeling. Instead, Pt-skin clusters with 40 Å outer diameter, and 1 ML and 2 MLs thick Pt shells were employed. The best agreement with the experiment was reached when a 50:50 mixture of the 40 Å clusters with the 1 ML and 2 MLs thick Pt shells were employed (see Table 2.3). The only other model phase whose coordination numbers matched with those measured was a 1.1 nm Pt cluster. However, no particles at or close to that size were observed in either the TEM, XRD or IR-CO probe experiments, leaving the core/shell structure the only existing phase.

Table 2.3. Coordination numbers (1st-4th, Pt-Pt) from EXAFS experiment vs. modeling for Ru@Pt core/shell structure

Coordination Shell	Experiment	1-layer Pt shell (810at) 35 Å Ru core (1650at) 	2-layer Pt shell (1356at) 30 Å Ru core (922at) 	Mixed 1 & 2 layer shell (0.5 each)*
1 st	7.4 (5)	6.17	8.68	7.43
2 nd	2.1(7)	2.28	3.64	2.96
3 rd	5.5 (1.8)	7.35	12.58	9.97
4 th	3.1 (1.0)	3.34	5.5	4.42

It was also hypothesized for the Ru core that the core-shell interface strengthened the disorder in the Ru nanoparticles. Incommensurate structures between the non-close packed Ru and close-packed Pt enhanced the strain at the interface. Due to large standard deviation of Ru-Ru bond distances, the most strongly disordered Ru-Ru bonds in the pair distribution function did not contribute to the EXAFS signal, and thus the result was the measured Ru-M coordination numbers were smaller than those expected for 3.0 nm Ru nanoparticles. Therefore, a modified pair distribution function picture was consistent with the PDF pattern of monometallic Ru NPs compared to that of Ru@Pt core/shell NPs which suggested a partial or complete loss of Ru-Ru pair distributions upon shelling with Pt (see PDF section). XRD pattern for the core/shell NPs

with the strain-induced shifts of certain Pt reflections was also complemented by the strain-induced disorder in the Ru core (see XRD section).

2.3.4.3. Atomic Pair Distribution Function Analysis

Bimetallic Pt/Ru NPs as well as monometallic Ru NPs were analyzed using Atomic Pair Distributions (PDF). The synchrotron X-ray diffraction was performed by Dr. Chupas at Argonne National Lab. All data analysis and PDF fits were carried out at University of Maryland. For the PDF refinements, distorted model clusters as well as periodic phases were used. PDF analysis provided the medium to compare/contrast the experimental pair distribution functions of the bimetallic NPs with different particle architectures and those simulated from their cluster models. Experimental PDFs were found to be strongly structure sensitive over long intra-particle distances (20 Å), such that a three-dimensional model of the average Ru@Pt core/shell particle could be generated and be further used in other X-ray analysis (see EXAFS section above and XRD section below).

Atomic pair distribution function (PDF) is derived from X-ray diffraction, and is usually described as histograms of interatomic distances.¹¹⁷ The need for PDF analysis is urged from the fact that scattering from non-periodic materials like nanocrystals has a diffuse contribution that is equally important as Bragg's diffraction, and is thus contributing to total scattering. Pair distribution function, $G(r)$, is the Fourier Transform of the experimental scattered intensity, and is given by the equation:

$$G(r) = \int_{Q_{\min}}^{Q_{\max}} Q[S(Q)-1]\sin(Qr)dQ \quad \text{eq. 2.5}$$

where $S(Q)$ is the structure factor, $Q[S(Q)-1]$ the reduced structure factor. Q is given by $4\pi\sin\theta/\lambda$ where θ is the diffraction angle and λ the wavelength of the incident X-rays. Experimentally, PDF requires use of synchrotron sources, highly energetic monochromatic X-rays, and therefore various polarization, absorption and scattering corrections have to be done on the data. PDF analysis is promising in local structure determination of nanocrystalline composites as small as a few hundred atoms with high structural sensitivity.

Experimental PDFs of monometallic Ru, bimetallic $\text{Pt}_{50}\text{Ru}_{50}$ and $\text{Ru}@Pt$ NPs were shown in Figure 2.23a. PDFs were also simulated by using model clusters and employing unconstrained fit parameters and thus the calculated PDFs exhibited qualitative match with the observed data (Figure 2.23b). Long range order beyond $r=20$ Å exists in 4.4 nm $\text{Pt}_{50}\text{Ru}_{50}$ particles. In contrast, 3.0 nm Ru particles showed short range order extending over only a few atoms. Furthermore, pair correlations dropped quickly with no or little pair contributions at $r>8$ Å. At the low- r ($r<10$ Å) region, pair correlations showed a small decay with distance for the $\text{Pt}_{50}\text{Ru}_{50}$ NPs. Moreover, the $\text{Pt}_{50}\text{Ru}_{50}$ peak pair distances were intermediate to the Ru and $\text{Ru}@Pt$ ones, which agreed with the EXAFS results. Experimental PDF of the core/shell NPs were virtually different from those of the alloy and monometallic Ru NPs, and exhibited mainly Pt-Pt pair correlations, which was also consistent with the EXAFS data (see section 2.3.3.2)

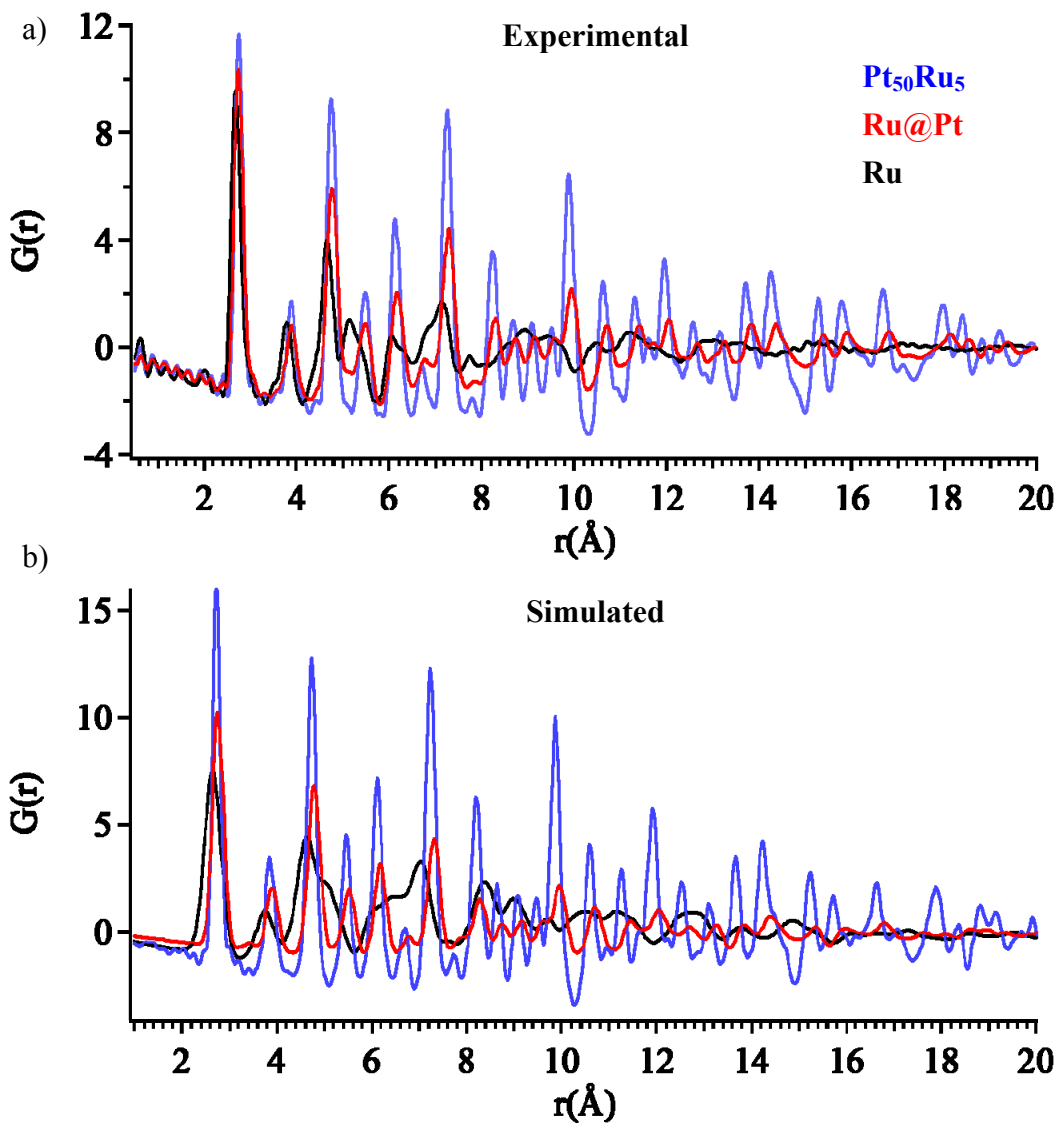


Figure 2.23. (a) Experimental PDFs of monometallic Ru, $\text{Pt}_{50}\text{Ru}_{50}$ alloy and Ru@Pt core/shell NPs, and (b) theoretical PDFs of the respective models calculated with no physical constraints.

PDFs of monometallic Ru and bimetallic $\text{Pt}_{50}\text{Ru}_{50}$ NPs were refined using PDFGUI software¹¹⁷ for PDF fit analysis to extract the crystal parameters. First, the periodic Pt FCC model with partial occupancy of 0.5 for each Pt and Ru and corresponding Wyckoff positions of multiplicity 4^{175} was used to fit the experimental PDF

of the alloy nanoparticles (Figure 2.24a). The lattice parameter was refined to 3.8785(1) Å and the occupational numbers to 0.52 and 0.48 for Ru and Pt, respectively, which were in accord with the Rietveld refinement¹⁸⁶ on the powder diffraction pattern (see Figures 2.12a and 2.12b). Similarly, PDF refinement from periodic model for the monometallic Ru NPs yielded physically reasonable lattice parameters. The quality of periodic model fit was, however, poor for the monometallic Ru NPs, especially beyond $r > 5$ Å. High level of disorder in the Ru lattice was believed to be at least partially responsible for this.

Although alloy and pure metals can easily be fitted with periodic model, more sophisticated structures such as core/shell can only be fitted by using cluster model. In cluster model, however, TEM and EXAFS-derived atom clusters were generated in a certain unit cell. This unit cell introduced an artificial background oscillating above the average pair correlations at low- r and below it at high- r regions. A thorough comparison of the fit residuals of periodic model and cluster model for the alloy in Figure 2.24 and for the monometallic Ru in Figure 2.25 demonstrated such an effect. Likewise, cluster model fits from TEM and EXAFS-derived core/shell clusters to the experimental PDF data exhibited fit residuals virtually similar to those observed in the alloy and monometallic Ru cluster model fits. On the other hand, position and intensity matched well between the experiment and cluster model fits (Figures 2.26 and 2.27).

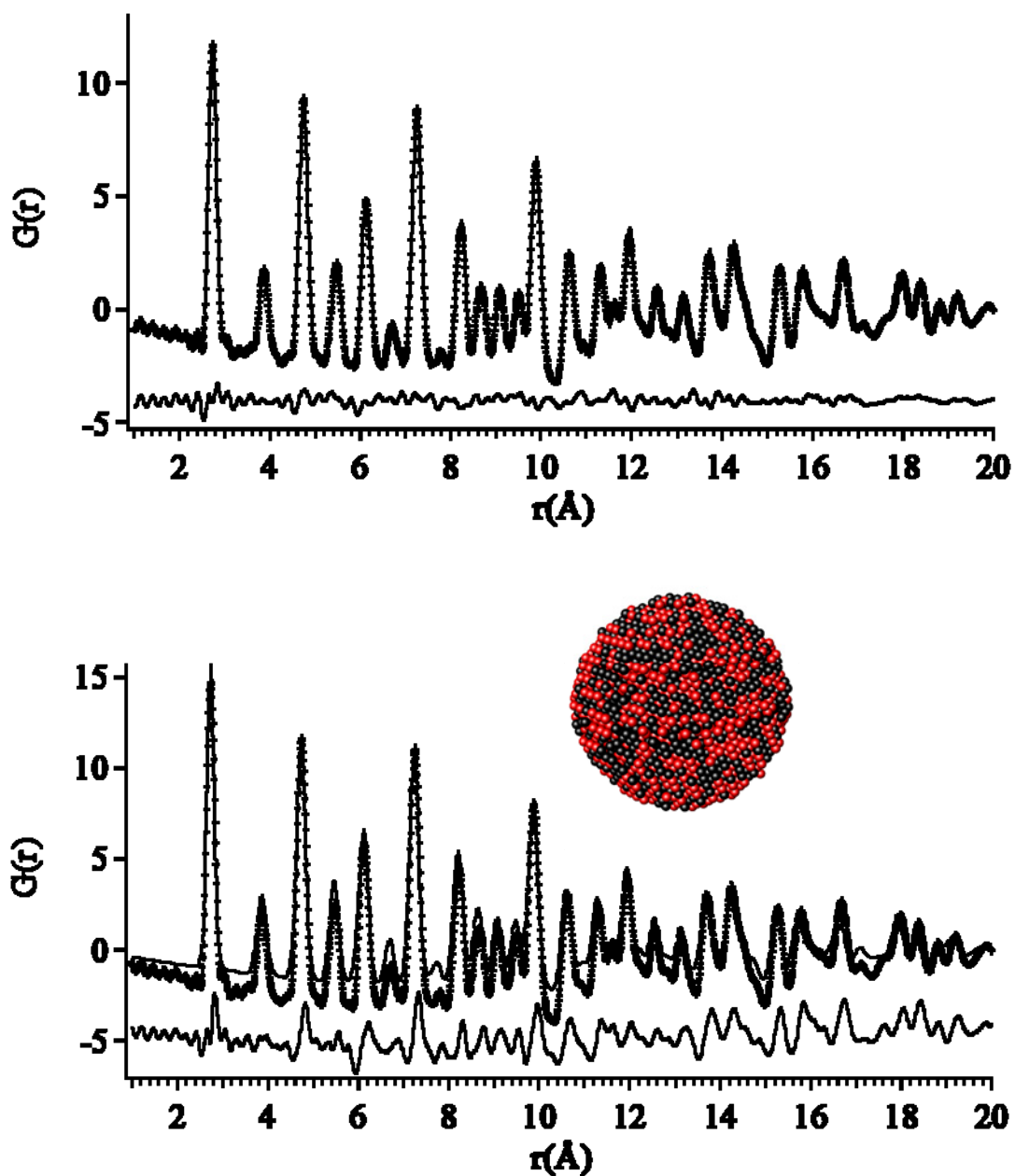


Figure 2.24. PDF refinements of the $\text{Pt}_{50}\text{Ru}_{50}$ NPs using (a) the spherically truncated periodic model, and (b) ATOMS generated model cluster of a 44 \AA diameter random alloy. The experimental data are shown by markers and the fits by solid lines. The residual PDFs are presented below each.

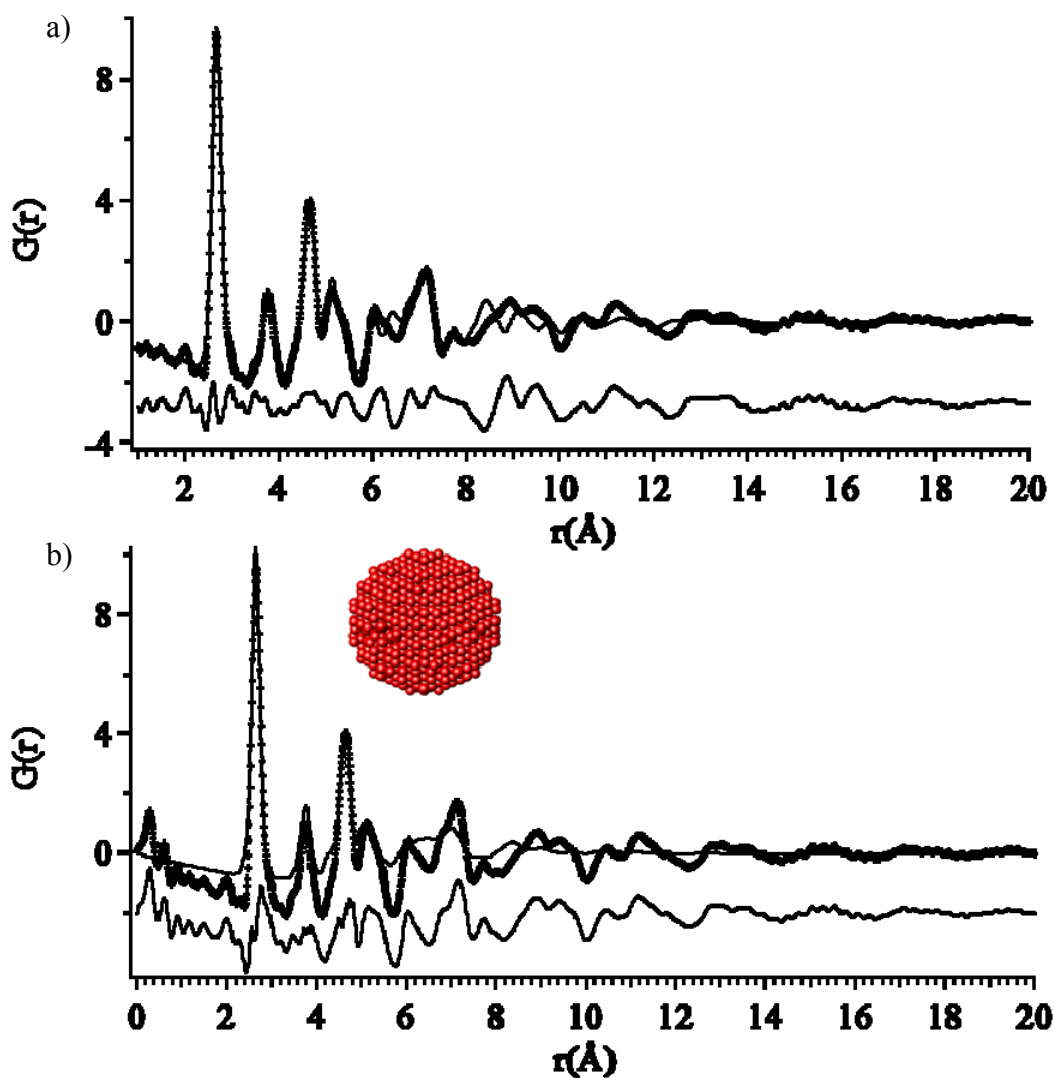


Figure 2.25. PDF refinements of the Ru NPs using (a) the spherically truncated periodic model, and (b) the ATOMS generated model cluster of a 30 \AA diameter HCP Ru. The experimental data are shown by markers and the fits by solid lines. The residual PDFs are presented below each.

PDF refinements with single-phase core/shell and two-phase Ru-core Pt-skin models were performed independently and compared to the Pt-skin only model (Figure 2.26a). The major contrast between the two phase models was the reversal of low- r ($r < 10 \text{\AA}$) and high- r ($r > 10 \text{\AA}$) pair populations. The single-phase core/shell model was unable to

catch the relatively high populations of high-r pair distributions due to embedded Ru cluster with shorter Ru-Ru distances which, in reality, did not contribute at the high-r (Figure 2.26b). Furthermore, the single-phase model overestimated the main pair correlations because of the unrealistic weighing of the Ru phase. The two-phase model had Pt and Ru unregistered and freely contributed, such that the weighing of the Ru phase could be adjusted for the better fit at both low-r and high-r regions (Figure 2.26c). The best fit with the experiment was reached with a relative scale factor of ~ 0.1 for the Ru phase. This is in qualitative agreement with the XRD data and EXAFS analysis predicting Pt shells that were incommensurate with the highly disordered Ru core. In other words the relative contribution to the total scattering of the Ru cores was negligible.

Finally, the two-phase models of 1-layer Pt skin and 2-layers Pt skin clusters with the respective Ru clusters and 40 Å outer diameters were evaluated against the experimental core/shell PDF. The refined PDF of the cluster model with the 2-layers Pt skin and 30 Å Ru core gave the best fit at low-r region, but no difference between the two could be observed at high-r, which supported the presence of mixtures, as shown in Figure 2.27.

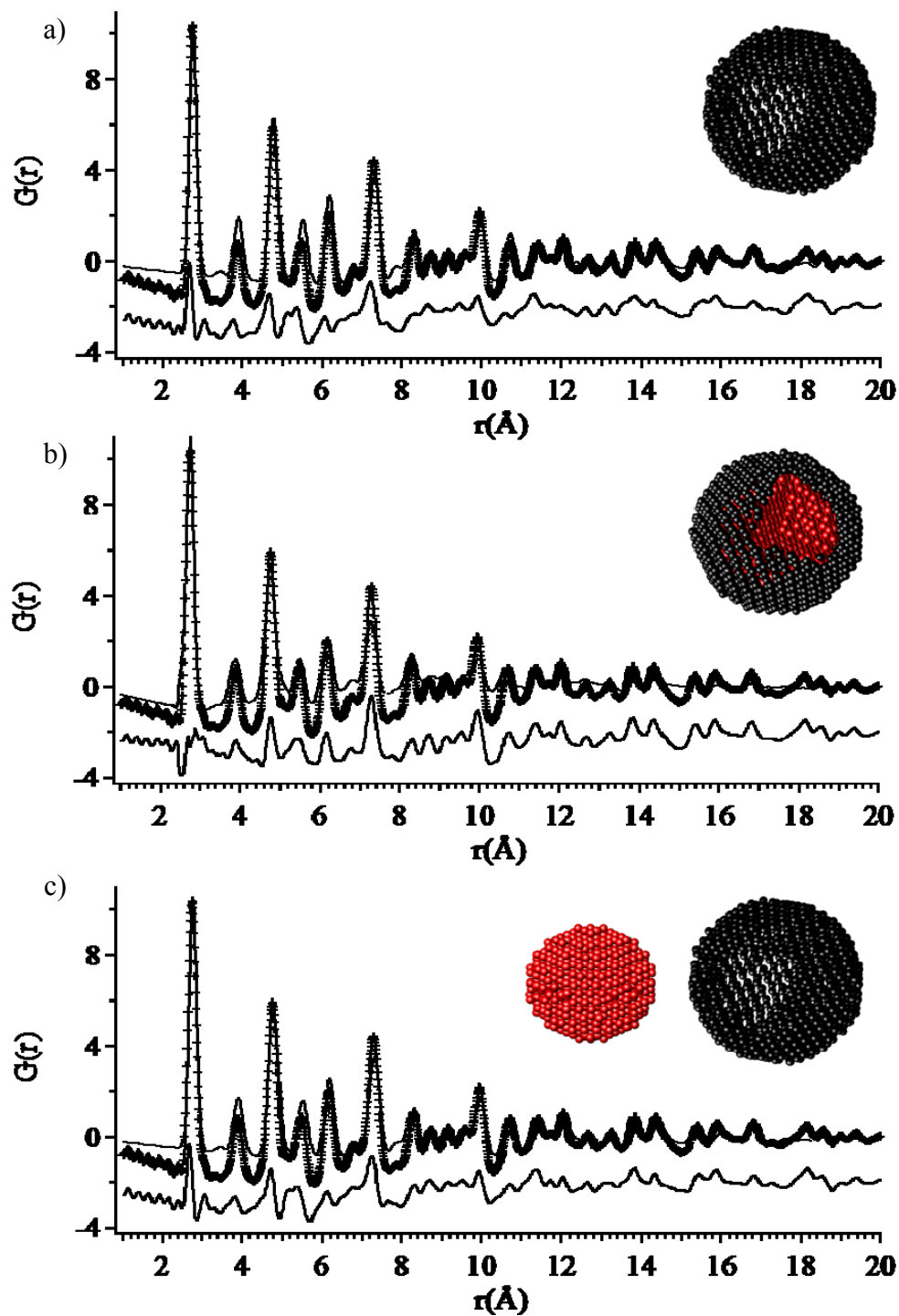


Figure 2.26. PDF refinements of the Ru@Pt core/shell NPs using ATOMS generated model clusters of (a) a 40 Å diameter 1356 atoms Pt-skin, (b) a single-phase 40 Å diameter Ru@Pt with 30 Å diameter Ru core and 2-layers thick Pt shell and (c) a two-phase 40 Å diameter Pt-skin and 30 Å diameter Ru. The experimental data are shown by markers and the fits by solid lines. The residual PDFs are given below each.

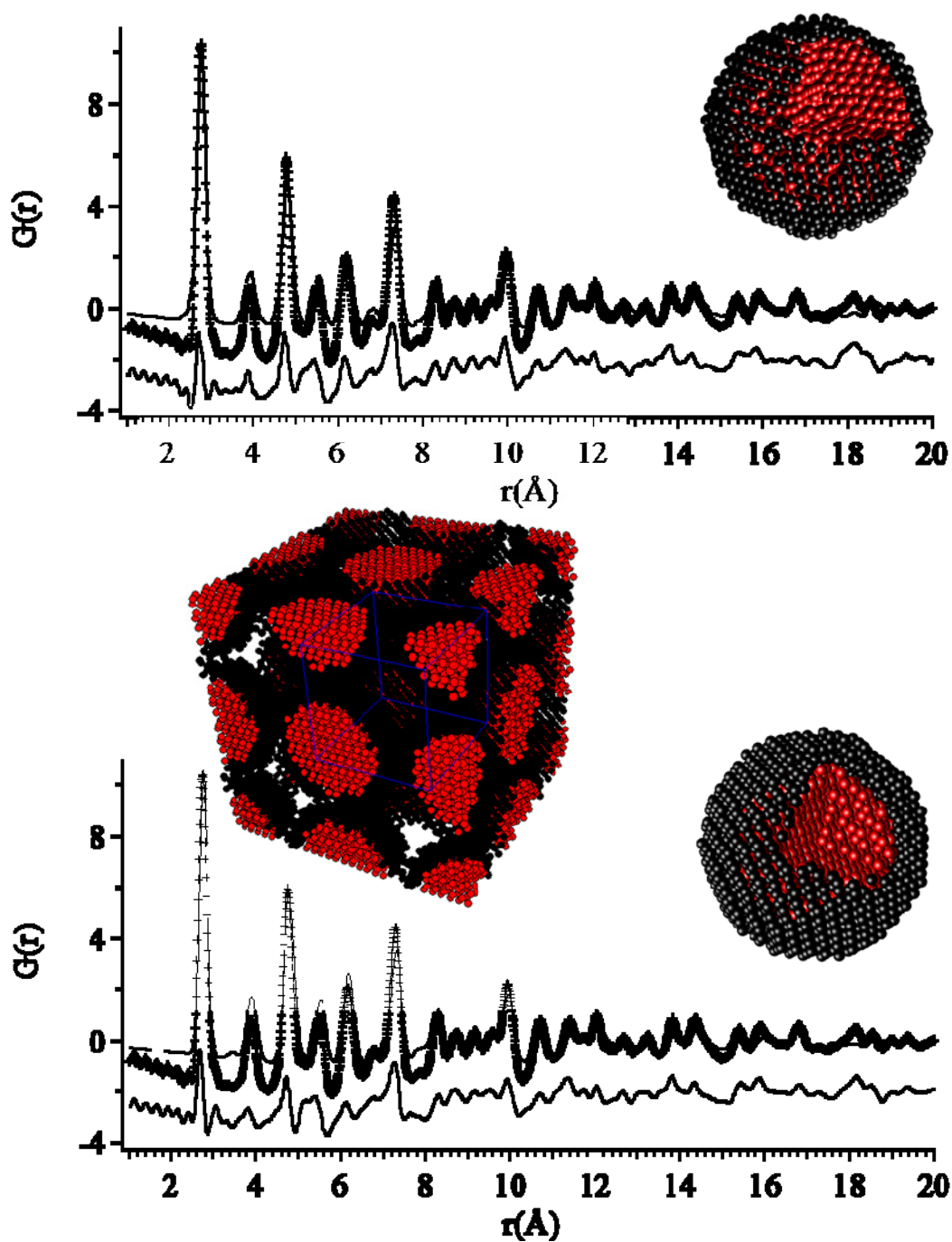


Figure 2.27. PDF refinements of the Ru@Pt NPs using ATOMS generated model clusters of (a) a two-phase 40 Å diameter 1 ML thick Pt-skin and 35 Å Ru, and (b) a two-phase 40 Å diameter 2 ML thick Pt-skin and 30 Å Ru. The experimental data are shown by markers and the fits by solid lines. The residual PDFs are given below each.

2.3.5. Chemical analysis by X-Ray Photoelectron Spectroscopy

X-Ray photoelectron spectra (XPS) binding energies for the Ru@Pt core/shell NPs, Pt₅₀Ru₅₀ alloy NPs, monometallic Pt and Ru NPs as well as Pt wire and Ru powder is tabulated in Table 2.4. XPS for the “as-prepared” Ru:Pt shows a ratio of 58:42, which is again consistent with the precursor composition. The Pt 4f levels show two signals; one for Pt metal (80%) and another for PtO (20%), that are both shifted to higher binding energies relative to the monometallic Pt NPs and the Pt standard (Table 2.4). The Ru XPS data show metallic Ru (67%) and Ru⁴⁺ (33%) components. We attribute the latter to RuO₂. For Ru, the metal and Ru⁴⁺ levels are shifted to lower energy relative to the monometallic Ru NPs. Similarly, the PtRu alloy NPs show a total of 45% Pt by atom, about 80% of which is for Pt metal (Table 2.4). The Ru⁰:Ru⁴⁺ ratio is 63:37. The electronic changes in the core levels of Pt and Ru atoms, as determined by XPS, are also consistent with alloy formation (see Figure 2.15). Chloride was not detected in any of the samples.

Table 2.4. XPS data for the Pt/Ru system

	Ru 3d _{5/2} (eV)		Pt 4f _{7/2} (eV)		Δ Ru 3d _{5/2}		Δ Pt 4f _{7/2}	
	Ru ⁰	Ru ⁴⁺ (RuO ₂)	Pt ⁰	Pt ²⁺ (PtO)				
Pt (wire)	-	-	71.33	72.40	-	-	-0.06	0.10
Ru (powder)	280.28	281.26	-	-	0.21	0.00	-	-
Pt (Nanoparticles)	-	-	71.39	72.50	-	-	-	-
Ru (Nanoparticles)	280.49	281.26	-	-	-	-	-	-
Ru@Pt (NPs)	280.38	281.13	71.68	72.88	0.11	0.13	-0.29	-0.38
PtRu alloy (NPs)	280.29	280.88	71.80	73.17	0.20	0.38	-0.41	-0.67

Electron binding energies of Ru 3d_{5/2} and Pt 4f_{7/2} core levels for bimetallic PtRu alloy, and Ru@Pt core/shell NPs, monometallic Ru, and Pt NPs; and Pt wire, Ru and RuO₂ powders as reference standards (to the left of the table) are shown. The table also shows binding energy shifts for these energy levels relative to Pt and Ru NPs.

2.3.6. Surface probing by CO-sorption

2.3.6.1. Fourier Transformed-Infrared Spectroscopy measurements

To probe the NP surface composition, the as-prepared NPs were dosed with CO in the colloidal suspension and subsequently monitored by FT-IR (Figure 2.28). The IR spectrum of monometallic Pt and Ru NPs is included in Figure 2.28 and clearly shows the distinct Ru-CO (2029 cm^{-1})¹⁸⁷ and Pt-CO (2061 cm^{-1})⁹³ peaks. The IR spectrum of the Ru@Pt NPs shows a single peak centered at 2061 cm^{-1} , which is indicative of a Pt surface. In contrast, the IR spectrum of the PtRu alloy NPs shows two peaks; one at 2035 cm^{-1} and another at 2055 cm^{-1} (Figure 2.28). A homogeneous surface alloy is expected to have a single phonon CO mode intermediate to CO modes of individual Pt and Ru. The observed two-peak feature is probably a competition effect of PVP binding. However, as described previously,^{123,188} the IR-CO probe clearly differentiates surface Ru from surface Pt.

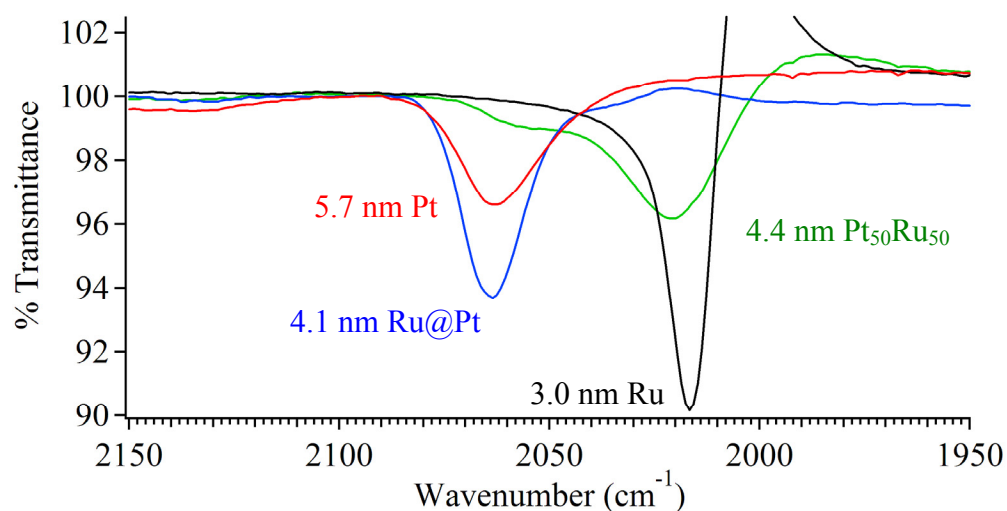


Figure 2.28. FT-IR spectra of CO-saturated colloidal suspensions of monometallic Pt NPs and monometallic Ru NPs, 4.1 nm Ru@Pt core/shell NPs, and 4.4 nm Pt₅₀Ru₅₀ NPs.

The IR spectrum of the PVP-free Ru NPs shows a minor peak at ca. 2060 cm^{-1} as well as the 2030 cm^{-1} peak (Figure 2.29). This peak is attributed to the low-energy surface that preferentially binds to PVP on the PVP-protected NPs. Similarly, the IR spectrum of the PVP-free Pt NPs reveals a sharper peak centered at 2081 cm^{-1} , which is concurrently assigned to the low-energy 111 surface. On the other hand, the PVP-free Ru@Pt core/shell NPs have a single peak for $\nu_{\text{linear}}(\text{CO})$ at 2070 cm^{-1} in their IR spectrum (see Figure 2.29). IR spectroscopy associated with CO probing of NP colloids again reveals the surface characteristics of the proposed core/shell structure compared to the parent monometallic Ru and the related monometallic Pt NPs. Therefore, it is a strong technique to distinguish between different architectures of bimetallic PtRu NPs.

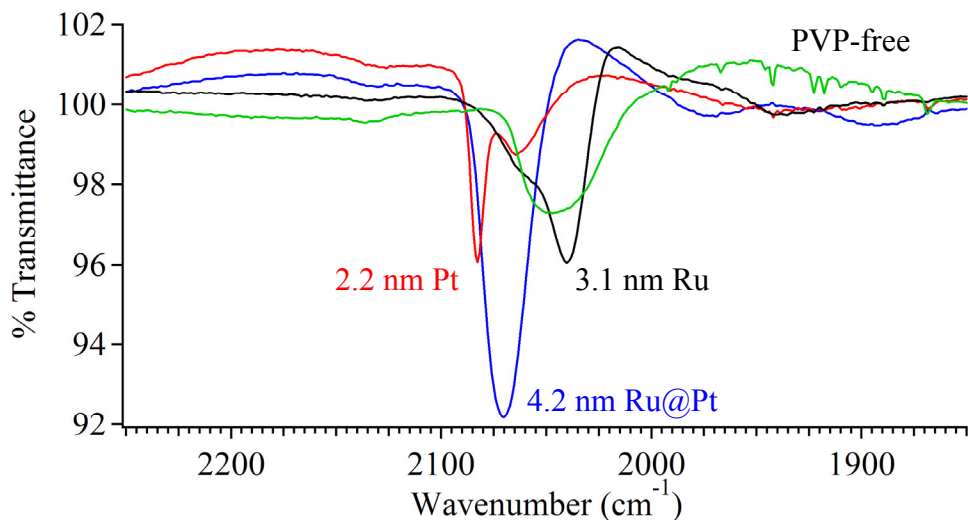


Figure 2.29. FT-IR spectra of CO-saturated colloidal suspensions of PVP-free Ru NPs, PVP-free Pt NPs and PVP-free Ru@Pt NPs in EG.

Next, the IR spectra of CO saturated colloidal suspensions of core/shell NPs have been employed to evaluate Pt shell growth with various layer thicknesses over Ru core NPs. For this, Pt shells corresponding to different molar ratios of Pt to Ru, namely 2:3 1:1 and 2:1 in order of increasing thicknesses, have been monitored using FTIR (Figure 2.30a). The IR spectrum of the Ru@Pt NPs colloids with sub-stoichiometric molar Pt show a major peak at 2055 cm^{-1} which is assigned to $\nu(\text{CO})$ on Pt, slightly red-shifted, and a shoulder at ca. 2030 cm^{-1} which is assigned to the exposed Ru surface (Figure 2.30a blue curve). The IR spectra of the Ru@Pt NPs with Pt:Ru molar ratios of order 1 and higher yield single $\nu(\text{CO})$ on Pt whose exact position shifts blue to 2070 cm^{-1} with increasing shell thickness (Figure 2.30a black curve). As seen in figure 2.30b, the IR spectra of the Ru@Pt NPs synthesized anaerobically with various Pt:Ru molar ratios show similar trends. The NP colloids with sub-stoichiometric molar Pt have two peaks in their CO-probed IR spectrum: a major peak centered at 2060 cm^{-1} and a minor one at ca. 2030 cm^{-1} . There is a correlation of $\nu(\text{CO})$ on Pt observed and thickness of Pt shell for a given Ru core size. The $\nu_{\text{Pt-CO}}$ on 5.7 nm Pt NPs is observed at 2060 cm^{-1} . Therefore, this size correlation is believed to result from combined unit cell distortion and electronic alteration introduced by the pseudo-morphic growth of Pt over Ru.

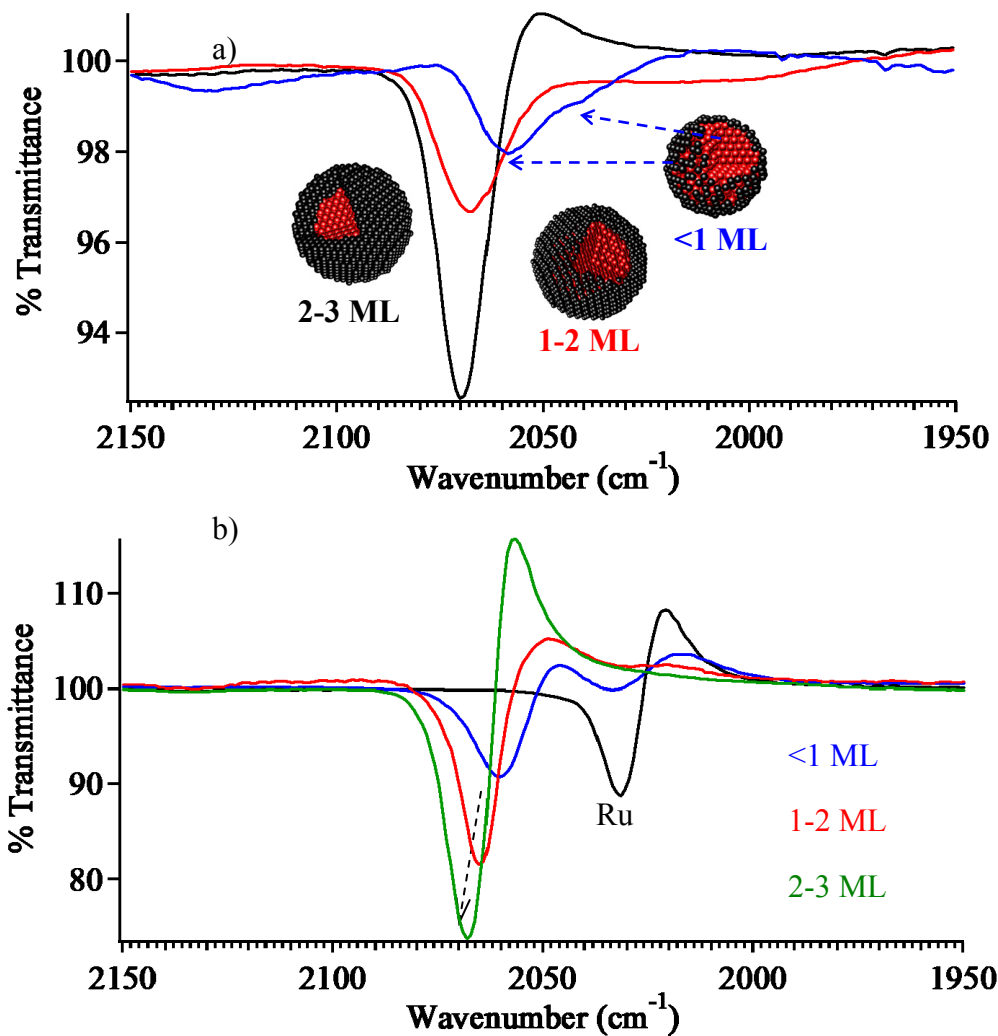


Figure 2.30. FT-IR spectra of CO-saturated colloidal suspensions in EG of the Pt shell series of the 3.0 nm Ru NPs under (a) normal reaction conditions (b) the anaerobic reaction conditions. Pt:Ru compositions are shown in parentheses, and approximate Pt shell thicknesses are given next to them. FT-IR spectrum of CO-saturated colloidal suspension of the anaerobically synthesized Ru NPs is also shown in (b). The progressive spectral shift to higher wavenumbers with the increasing Pt content in (b) is indicated by the arrow.

Finally, the Ru@Pt NPs with various Ru core sizes ranging between ~2.0 and 5.7 nm, and ca. 1 ML thick Pt shells have been evaluated using their IR spectra upon CO probing (Figures 2.31a-c). A general conclusion regarding a size/ $\nu_{\text{Pt-CO}}$ correlation can hardly be drawn from the IR-CO spectra of the Ru@Pt NPs with distinct sizes of Ru cores and ca. 1 ML thick Pt shells. However, the IR-CO spectra of such Ru@Pt NPs observed to date show clustering of $\nu(\text{CO})$ s on Pt in a narrow frequency range of 2060-2066 cm^{-1} as figure 2.31d clearly shows, and thus point out Pt shell formation of 1-2 monolayers.

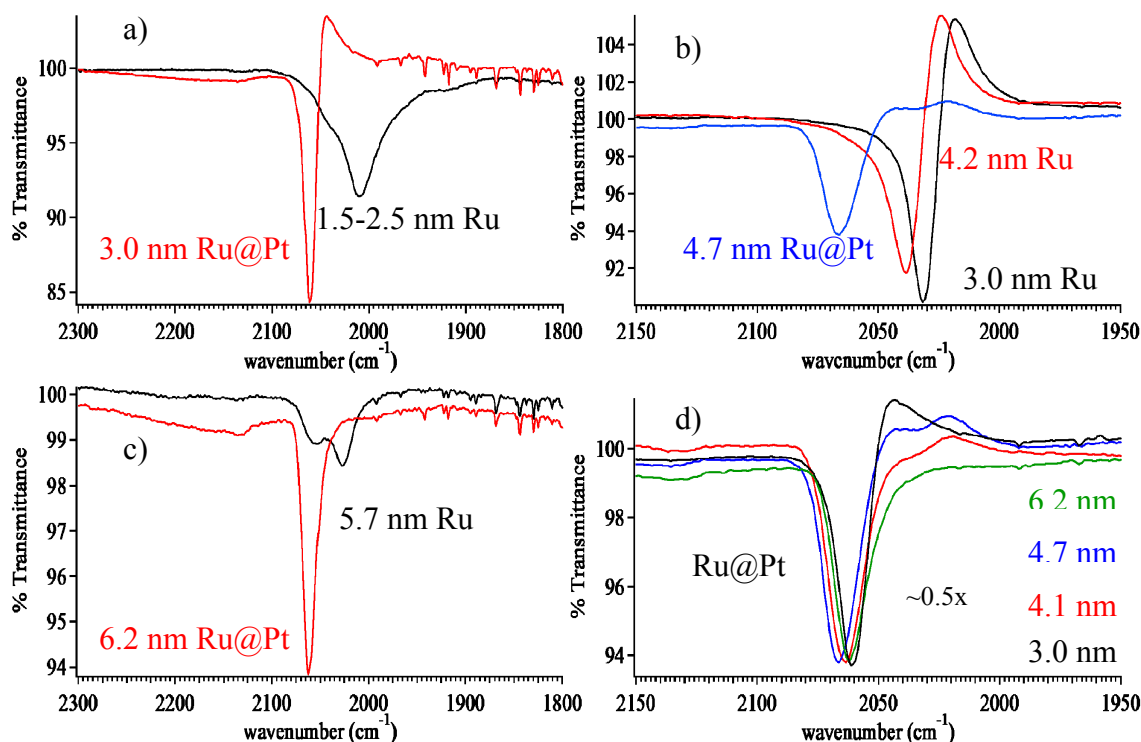


Figure 2.31. FT-IR spectra of CO-saturated colloidal nanoparticles of approximately ML thick Pt shells over (a) 1.5-2.5 nm Ru, (b) sequentially grown 4.2 nm Ru, and (c) 5.7 nm Ru. (d) FT-IR spectra showing $\nu(\text{Pt-CO})$ s on different Ru@Pt core/shell NPs with ca. 1-2 layers thick Pt shells and varying Ru core sizes. FT-IR spectra of CO-saturated colloidal suspensions of the sequentially grown Ru NPs are also shown in (b).

FT-IR spectra of CO-saturated colloids of the $\text{Pt}_x\text{Ru}_{1-x}$ NPs are shown in Figure 2.32. The $\nu(\text{CO})$ s on Pt (or Ru) exhibited progressive shift to higher wavenumbers, towards the $\nu(\text{CO})$ of pure Pt NP colloids, with increasing Pt content, although no such correlation could be deduced for the $\nu(\text{CO})$ of pure Ru NP colloids. A single $\nu(\text{CO})$ was observed on colloidal $\text{Pt}_{80}\text{Ru}_{20}$, $\text{Pt}_{40}\text{Ru}_{60}$ and $\text{Pt}_{34}\text{Ru}_{66}$ at 2053 cm^{-1} , 2013 cm^{-1} and 2008 cm^{-1} , respectively. In contrast, colloidal $\text{Pt}_{66}\text{Ru}_{34}$ and $\text{Pt}_{50}\text{Ru}_{50}$ NPs exhibited two $\nu(\text{CO})$ s in their FT-IR spectra: the strong 2050 cm^{-1} peak and the 2005 cm^{-1} shoulder for the former, and the strong 2021 cm^{-1} peak and the 2055 cm^{-1} shoulder for the latter. Peak linewidths gradually became narrower with increasing Pt composition.

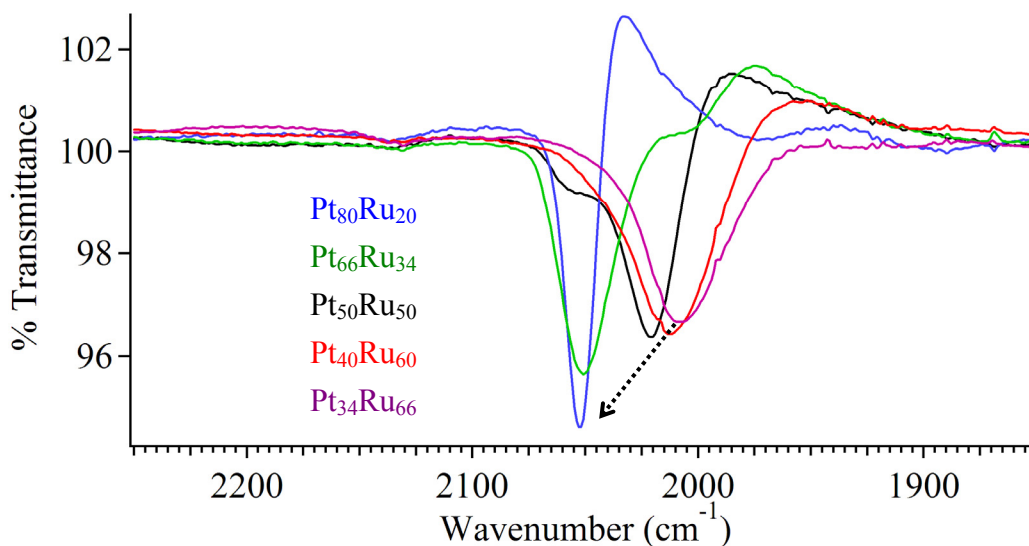


Figure 2.32. FT-IR spectra of CO-saturated colloids of the $\text{Pt}_x\text{Ru}_{1-x}$ ($x=0.33-0.8$) NPs. arrow shows the progressive shift of the $\nu(\text{CO})$ to higher wavenumbers with increasing Pt content.

2.3.6.2. Micro-Raman measurements

The micro-Raman spectra of the PVP-free NPs saturated with CO are shown in Figure 2.33. In addition, Raman analysis of PVP coated NPs leads to the formation of graphite deposits⁵³, which also obscures the M-C region of the spectrum and are not shown. Monometallic Pt NPs give rise to two peaks; namely, a sharp peak at 2098 cm⁻¹ assigned to $\nu(\text{CO})$ on atop Pt sites (Figure 2.33a, top), and a broader 480 cm⁻¹ peak due to $\nu(\text{Pt-C})$ ^{189,190} (Figure 2.33b, top). Similarly, PVP-free Ru NPs give rise to two $\nu(\text{CO})$ features at about 2050 cm⁻¹ and 2140 cm⁻¹ for linearly bound COs on metallic and partially oxidized Ru, respectively. In addition, a very broad 440 cm⁻¹ peak for Ru-C(O) is present¹⁸⁹. The PVP-free Ru@Pt core-shell NPs yield features that are characteristics of Pt surfaces; namely, broadened peaks at 2090 cm⁻¹ and 480 cm⁻¹, which are tentatively assigned to linear $\nu(\text{CO})$ and $\nu(\text{M-C})$ bands, respectively, and are indicative of an electronically altered Pt surfaces (Figures 2.33a and 2.33b, middle).

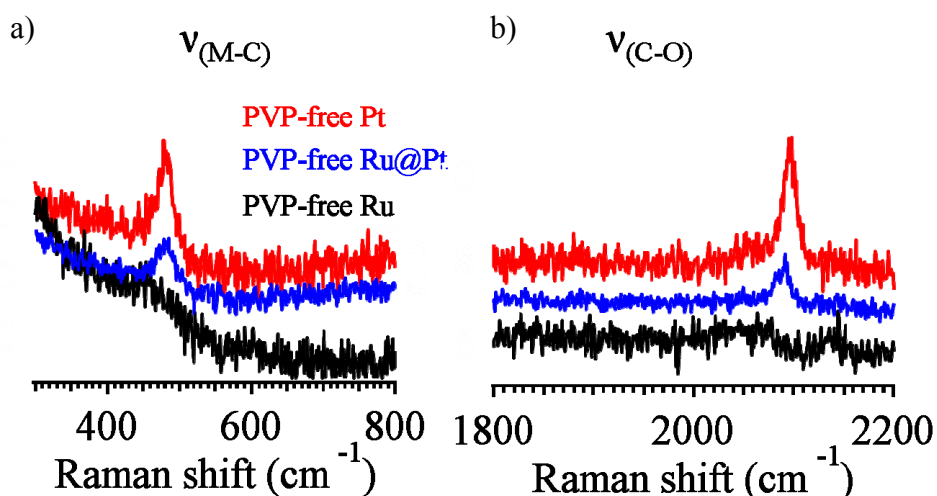


Figure 2.33. Micro-Raman spectra of the PVP-free Pt NPs, PVP-free Ru@Pt NPs and PVP-free Ru NPs (from top to bottom) under flowing 25% vol. CO/air mixture (a) in the $\nu(\text{M-C})$ region and (b) $\nu(\text{C-O})$ region.

The combined TEM, XRD, XPS and IR-CO probe data are all consistent with the core-shell structure for the Ru@Pt NPs and clearly differentiate them from the PtRu alloy NPs. The XRD, EXAFS and XPS studies all suggest an amorphous mixed Ru⁺⁴ / Ru⁰ core that is coated by a Pt shell. Pure Ru NPs show the same characteristics except for higher Ru⁺⁴ / Ru⁰ ratios and slightly higher binding energies.

2.3.7. Catalytic evaluation of the bimetallic Pt/Ru NPs

2.3.7.1. Preferential Oxidation (PROX) of CO

2.3.7.1.1. Experiment

To compare and contrast the activity of the core-shell NPs with that of the alloys and monometallic NPs, we evaluated the PROX reaction (equation 2.2) using H₂ feeds contaminated by 0.2% CO by volume, along with 0.5% O₂. Percents of maximum CO concentrations and percents of maximum H₂O formations are plotted versus temperature in °C in Figure 2.34. The percent of maximum CO concentration is based on the inlet concentration of CO, and the percent of maximum H₂O formation the limiting concentration of O₂. A maximum of 80% H₂O is produced, provided that CO is completely converted to CO₂. The temperature programmed reaction (TPR) data for the core-shell, alloy and monometallic mixture are shown in Figures 2.34. For a given NP catalyst, TPR plots for PROX reaction showing H₂ conversions reveal the temperature window that the nanoparticle surfaces are abundantly freed of CO to carry out the hydrogen chemistry, such that the H₂ light-off temperature can be used as a measure of

PROX reactivity for any NP catalyst. For reference, our pure Pt NP catalysts under these conditions show H₂ oxidation onset (light-off) at 175-180 °C, which is consistent with literature reports.³⁵ In contrast, the PtRu alloy and monometallic mixture catalysts show 83 °C and 79 °C light-off temperatures (2000 ppm CO), respectively (Figure 2.35b). This behavior is consistent with the well-known bifunctional promotional effect in PtRu systems.¹⁹¹ The bulk PtRu alloy and monometallic mixture show complete CO conversion at 95 °C and 105 °C, respectively, for H₂ feeds containing 2000 ppm CO (Figure 35c). Although the synthesis of the Ru@Pt NPs with characteristic structural and spectroscopic features is highly reproducible, the PROX reaction shows deviations at low-temperature kinetic regions. As shown in Figure 2.34a, % concentrations of CO fall in between 65-85% at 35 °C and % formation of H₂O between 0-40% at 35°C.

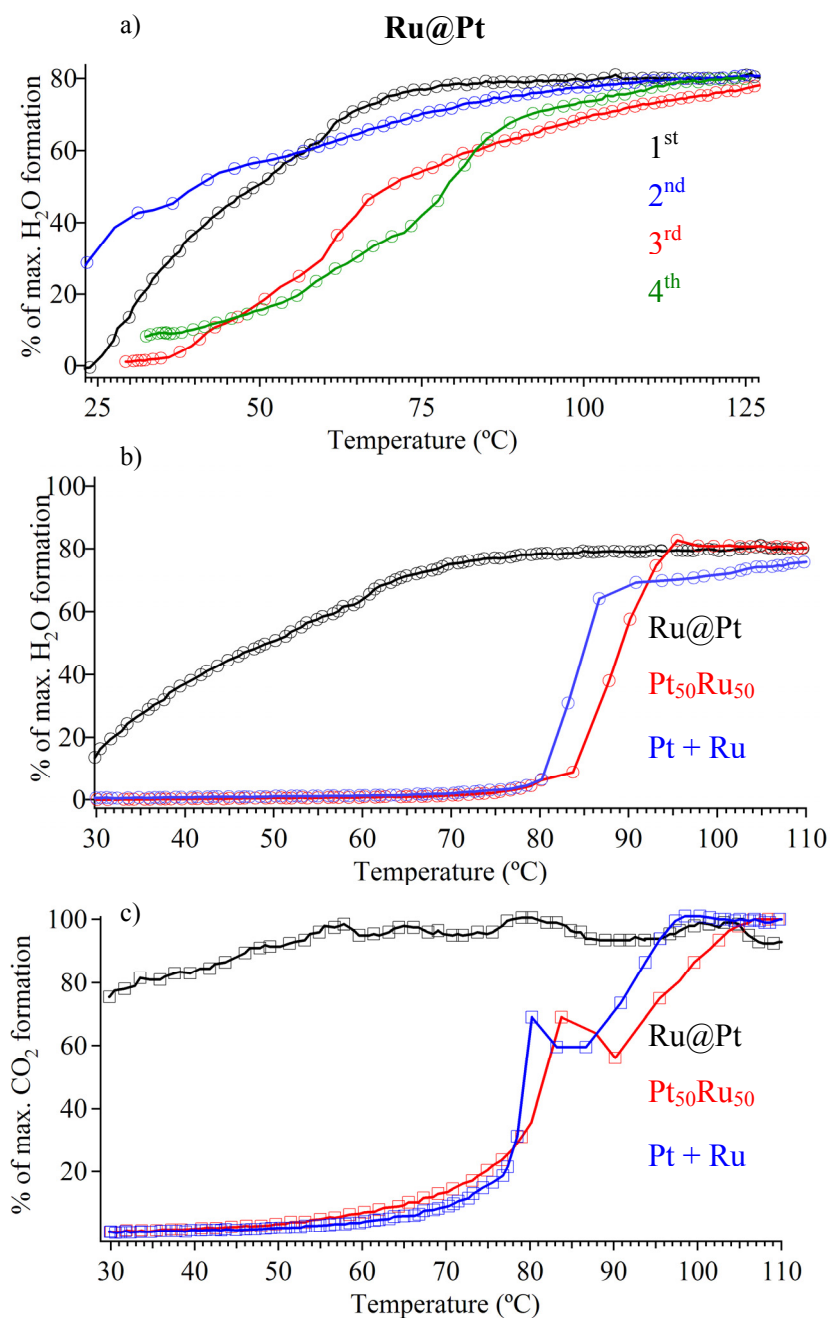


Figure 2.34. TPR plots for the PROX reaction showing H₂O formations 2000 ppm CO level of (a) four different batches of the 4.1 nm Ru@Pt core/shell NP catalysts, and (b) the 4.1 nm Ru@Pt core/shell NP catalyst with the intermediate activity (1st in (a)), the 4.4 nm Pt₅₀Ru₅₀ alloy NP catalyst and the mixtures of monometallic Pt and Ru NPs catalyst. (c) TPR plots for the PROX reaction showing H₂O formations 2000 ppm CO level of the 4.1 nm Ru@Pt core/shell NP catalyst with the intermediate activity, the 4.4 nm Pt₅₀Ru₅₀ alloy NP catalyst and the mixtures of monometallic Pt and Ru NPs catalyst.

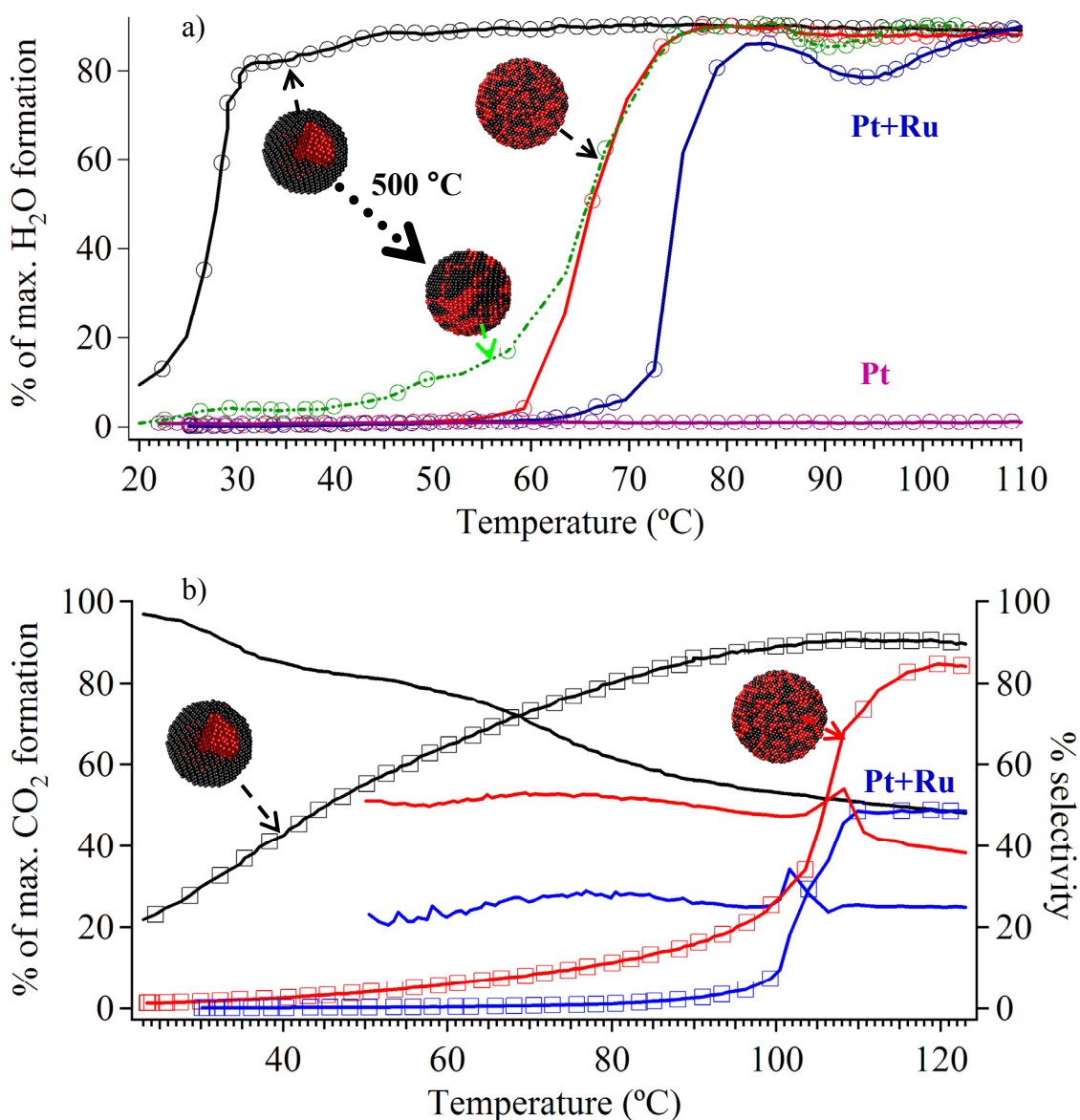


Figure 2.35. TPR plots for the PROX reaction showing (a) H₂O formation at 1000 ppm CO level, and (b) O₂ formation and CO selectivity at 10000 ppm CO level for the as-synthesized core/shell NP catalyst, the alloy NP catalyst and the mixtures of monometallic Pt and Ru NPs catalyst. The gas hourly space velocity is $2.3 \cdot 10^5$ mL/g/h. in (a), and $1.2 \cdot 10^5$ mL/g/h in (b). The gas mixture for the PROX reaction was composed of 0.2% CO, 0.5% O₂, 50% H₂, and balance Ar in (a), and 1% CO, 1% O₂, 50% H₂, and balance Ar in (b). % of maximum O₂ conversion is shown by open triangles and selectivity by lines in (b).

The Ru@Pt core-shell catalysts show the highest activity for all the different architectures studied to date (Figures 2.34 and 2.35). In contrast to the other two bimetallics just described, CO oxidation precedes H₂ oxidation to a greater extent and both occur at much lower temperatures with the core-shell catalyst (*i.e.* it is a more active and more selective PROX catalyst). For the 1000 ppm CO feeds, CO oxidation is completed below 20 °C and H₂ light-off occurs at 22 °C (Figure 2.35a). With 2000 ppm CO, the core-shell catalyst shows 75 % CO conversion by 30 °C with a broad H₂ light-off starting at 25 °C (Figures 2.34b and 2.34c). In contrast, the other bimetallic catalysts show no activity below ~60 °C with H₂ light-offs delayed until temperatures above 75 °C. In 1.0% CO feeds with 1.0% O₂, the Ru@Pt catalyst shows 60% CO conversion with 80% selectivity at 50 °C as compared to <10% conversion and ~50% selectivity for the PtRu alloy and mixed monometallic systems (Figure 2.35b). % of maximum CO₂ formation is based on the inlet concentration of CO, and selectivity, S, is defined by the equation

$$S = N_{\text{CO}} / (N_{\text{CO}} + N_{\text{H}_2\text{O}}) \quad \text{eq. 2.5}$$

While higher selectivities can be found for other Pt catalysts,^{68,192} those systems require reducible oxide supports for oxygen activation and comparable alumina-based catalysts are not as active.^{36,67,193,194} Since no reducible oxide supports were employed in the present system, the origin of enhanced PROX activity for Ru@Pt must be assigned to changes in the electronic structure of the Pt shell.

The Ru@Pt catalyst can be cycled at 200 °C for several hours without loss of activity. Importantly, annealing the Ru@Pt catalyst at 500 °C for 12 hrs induces alloy formation (Figure 2.15) and the resulting catalytic performance then drops to that of the

authentic RuPt alloy (Figure 2.35a). In Figure 2.36, the TPR plots for the PROX reaction at 1000 ppm CO concentration on the $\text{Pt}_x\text{Ru}_{100-x}$ ($x=40-80$) NPs are shown. The alloy NPs exhibit a ‘Volcano’ behavior of PROX activities versus % atomic Pt, which is maximum for the $\text{Pt}_{50}\text{Ru}_{50}$ NPs. Thus, it is a significant finding of this study that the annealed Ru@Pt NPs must have a gradient alloy structure, which is different from the $\text{Pt}_{50}\text{Ru}_{50}$ NPs with identical nominal composition.

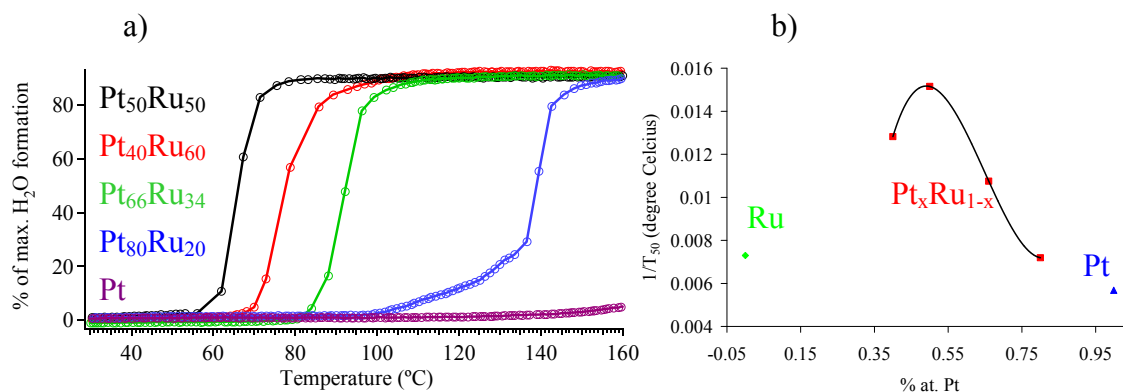


Figure 2.36. (a) TPR plots for the PROX reaction at 1000 ppm CO level on the $\text{Pt}_x\text{Ru}_{100-x}$ ($x=40-80$) alloy NPs, showing the rates of H₂O formation. (b) The temperatures at 50% of H₂O formation in (a) is plotted versus % atomic Pt.

In addition and in agreement with reports on Pt/Al₂O₃ PROX catalysts,^{36,67,193,194} CO oxidation is significantly slower in the absence of H₂ (Figure 2.37), which suggests that the oxidation process is mediated by the presence of H₂. Previous studies have speculated on the origin of this effect but none fully explained this unusual behavior. Furthermore, external H₂O introduced at 3% by volume of Ar feed does not promote CO oxidation until 230 °C in the absence of O₂, so that the water-gas-shift (WGS) reaction is not operative under given reaction conditions. In addition, H₂O reversibly impedes both the PROX reaction (50% H₂) and CO oxidation reaction (0% H₂).

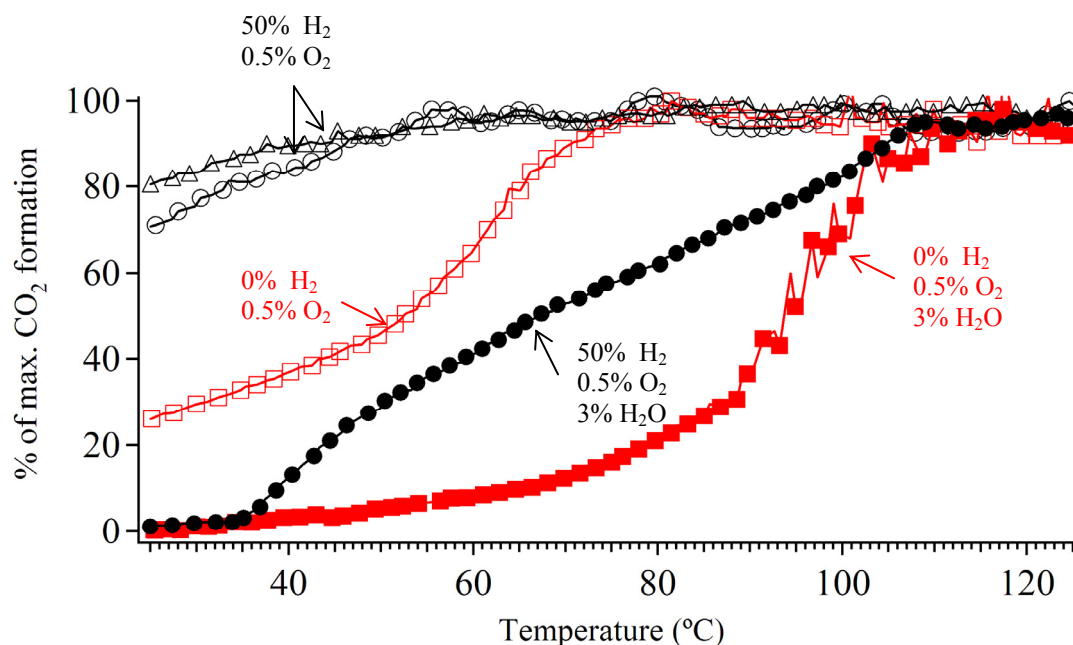


Figure 2.37. TPR plots for the PROX (with 50% H₂) and CO oxidation (with 0% H₂) reactions at 2000 ppm CO level on the Ru@Pt core/shell NPs catalyst showing the effect of humidified gas feeds on the CO₂ formation rates.

In Figure 2.38, % of maximum CO concentrations and H₂O formations are plotted versus temperature for 1% by weight Pt supported catalysts of Ru@Pt NPs with 3.0 nm Ru cores and various Pt shells of 1-2 MLs, submonolayer coverage and 2-3 MLs thick. 4.1 nm Ru@Pt NPs catalyst with 1-2 MLs thick Pt show the highest activity of all different shell thicknesses studied. 4.4 nm Ru@Pt NPs catalyst with 2-3 ML thick Pt shells, on the other hand, exhibit no room temperature activity for CO oxidation and H₂ does not light-off until 130 °C. Thus, electronic/geometric effects are operative for multi-layers of Pt shells over Ru nanoparticle seeds, such that H₂ light-off temperature is still 50 °C below that for monometallic Pt NPs catalyst (Figure 2.38a). Furthermore, 3.7 nm Ru@Pt NPs catalyst with submonolayer coverage of Pt shells exhibit an intermediate

PROX activity, which is also identical to that for the authentic alloy NPs catalyst (Figures 2.34b and 2.34c).

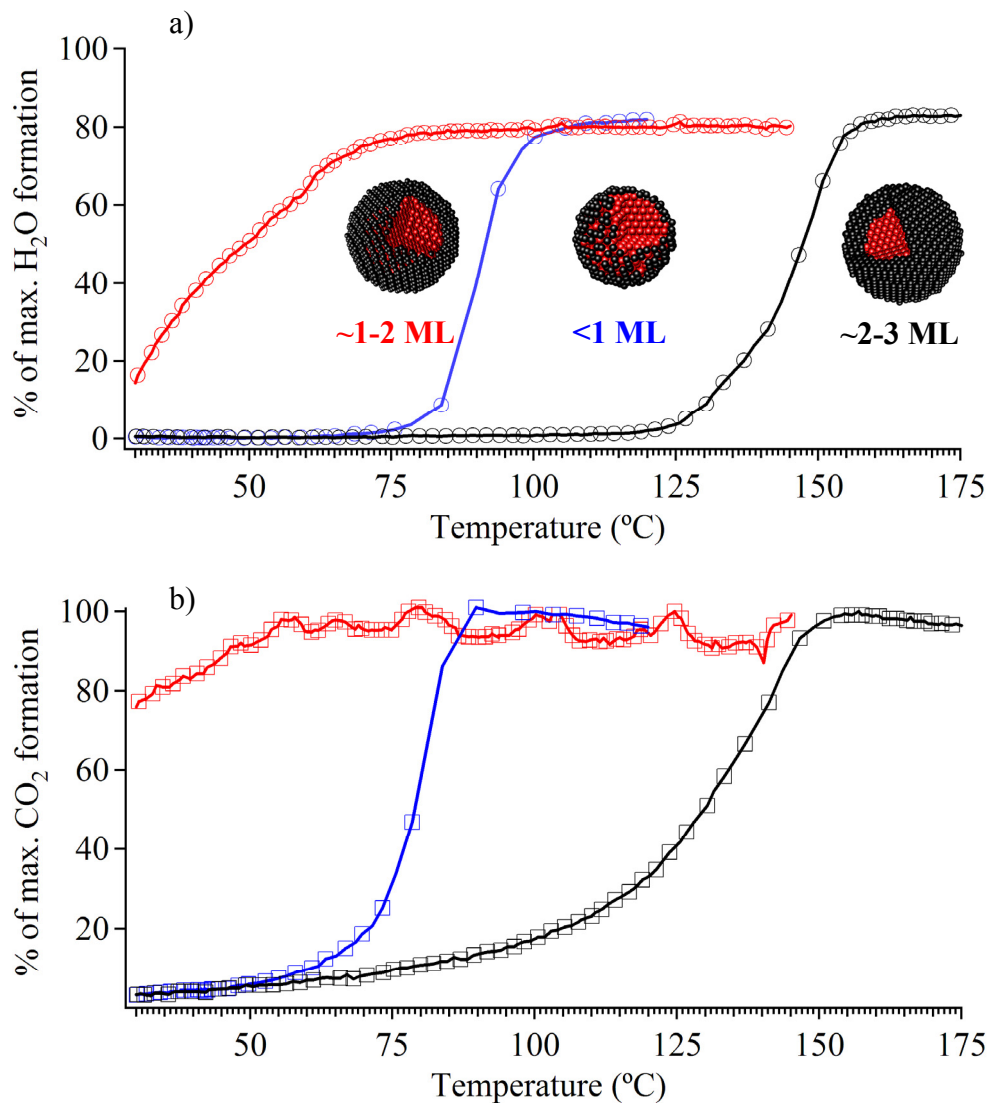


Figure 2.38. TPR plots for the PROX reaction at 2000 ppm CO level showing (a) H₂O and (b) CO₂ formations on the Ru@Pt NPs catalyst with 3.0 nm Ru cores and Pt shells varying between <1 ML and 3 MLs.

Finally, the effect of core sizes for approximately fixed number of Pt monolayers towards catalytic PROX/CO oxidation has been studied (Figure 2.39). For

this purpose, Ru@Pt NPs synthesized at Ru core diameters of 2.0 nm, 3.0 nm, 4.2 nm and 5.7 nm with ca. 1-2 MLs thick Pt shells have been evaluated for the thermal PROX reaction at 2000 ppm of CO. The preliminary results are in favor of a size correlation. The PROX activities increase in the order of

$$4.1 \text{ nm Ru@Pt} \geq 3.0 \text{ nm Ru@Pt} \gg 4.7 \text{ nm Ru@Pt} > 6.2 \text{ nm Ru@Pt}$$

Both 4.1 nm and 3.0 nm Ru@Pt NP catalysts with ca. 1-2 MLs thick Pt shells exhibited room temperature PROX activities (CO oxidation and subsequent H₂ light-off). On the other hand, 4.7 nm and 6.2 nm Ru@Pt NP catalysts exhibit no room temperature CO oxidation (Figure 2.39b)

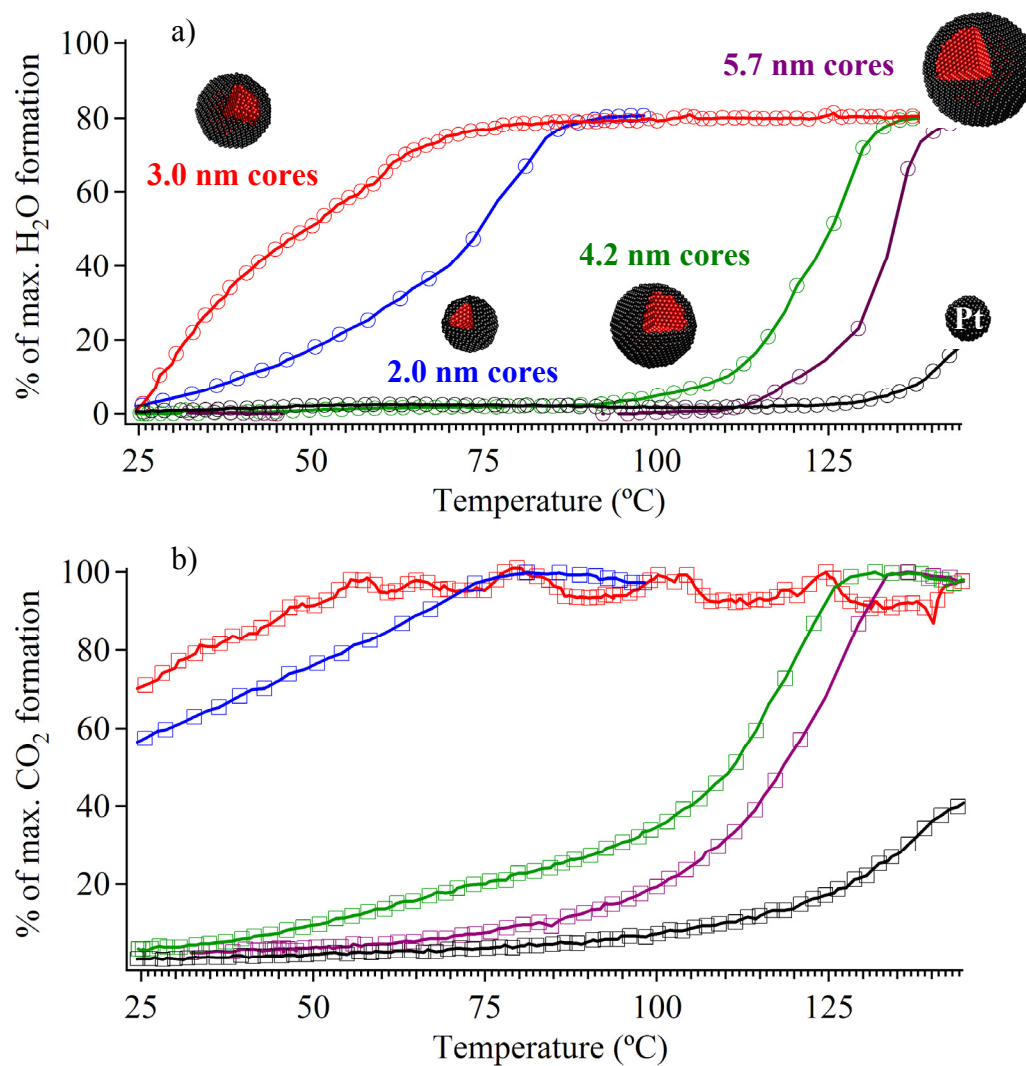


Figure 2.39. TPR plots for the PROX reaction at 2000 ppm CO level showing (a) H₂O and (b) CO₂ formations on the Ru@Pt NPs catalyst with ca. 1-2 MLs thick Pt shells and different Ru core sizes varying between 2.0 nm and 5.7 nm, showing the rates of H₂O formations and CO concentrations. For comparison, the PROX conversions for the 2.0 nm Pt NPs catalyst are also given.

2.3.7.1.2. Density Functional Theory (DFT) calculations

Having established the structure and reactivity of the Ru@Pt NPs with an array of experimental methods, periodic self-consistent DFT calculations was performed

by Prof. Mavrikakis and Dr. Nilekar to elucidate the fundamental reasons behind the unique reactivity of the Ru@Pt core-shell NPs. The Ru@Pt NPs were modeled by a four-layered slab of Ru hcp lattice, with a 2×2 surface unit cell exposing the facet,¹⁴⁰ whereby the top layer of Ru atoms was replaced with Pt atoms (Pt*/Ru(0001)). The binding energies (BE) of reaction intermediates and the activation energy barriers (E_a) for elementary reaction steps characterizing CO and hydrogen oxidation on this surface and on a Pt(111) surface were calculated, to compare the reactivity of Ru@Pt with that of Pt NP's.

The calculated binding energies of various species involved in the proposed reaction mechanism are presented in Table 1. Upon deposition on the Ru(0001) substrate, the Pt monolayer was laterally compressed compared to the lattice constant of pure-Pt bulk. This compression alone would tend to decrease the interaction strength of adsorbates on the Pt surface atoms in Ru@Pt NPs.¹⁰¹ Additionally, the interaction of the Pt-monolayer with the Ru-support atoms caused an additional downshift in the d-band center (ϵ_d) of surface Pt atoms, when compared to the Pt atoms in the top layer of a Pt(111) surface. More specifically, the ϵ_d changed from -2.53 eV for pure Pt(111) to -2.98 eV for the Pt*/Ru(0001) surface, which was also consistent with the observed higher XPS Pt core binding energy in the Ru@Pt NPs relative to the Pt NPs. Down-shifting the d-band center of a surface was shown to decrease the interaction strength of the surface with various adsorbates.¹⁰¹ The binding energies of reactive intermediates for CO+H₂ oxidation on Pt(111) and Pt*/Ru(0001), as listed in Table 1 for a ¼ ML coverage of each species, verified that general trend; Pt*/Ru(0001) binded all adsorbates less strongly than Pt(111). Atomic oxygen (O) and carbon monoxide (CO) showed the largest reduction in

binding energy, by as much as 0.75 and 0.56eV, respectively. In turn, the weaker CO binding on Pt*/Ru(0001) resulted in lower CO saturation coverages for Pt*/Ru(0001), than on Pt(111), for otherwise identical experimental conditions.^{195,196} The calculations for the differential binding energy of CO on a $2\sqrt{3} \times \sqrt{3}$ surface unit cell of both surfaces also showed that at saturation, 2/3 ML of the Pt(111) surface was covered by CO, whereas only 1/2 ML of the Pt*/Ru(0001) surface was covered by CO. Therefore, at high CO concentration environments, Pt*/Ru(0001) would have significantly more CO-free sites to perform catalytic reactions than the CO-saturated Pt(111) surface would have.

Besides the availability of more CO-free surface sites, the energetics of elementary reaction steps on the two surfaces, as probed on the 2×2 unit cell, unless otherwise stated, were drastically different (see Table 2.5 for barriers). For instance, H₂ dissociation on the CO-clean Pt(111) and Pt*/Ru(0001) surfaces was practically spontaneous. However, on the respective CO-saturated surfaces (2/3 ML CO for Pt(111), 1/2 ML CO for Pt*/Ru(0001) , the barrier to H₂ dissociation was significantly higher on Pt(111) than on Pt*/Ru(0001) (by ca. 0.6eV, in the $2\sqrt{3} \times \sqrt{3}$ unit cell). On the basis of these results alone, in the presence of CO, H₂ activation was expected to be much easier on Pt*/Ru(0001) than it is on Pt(111). Similarly, the O+H→OH step, which was energetically the most difficult step in H₂ oxidation towards H₂O formation, had a barrier of 0.85eV on Pt(111), as compared to 0.58eV on Pt*/Ru(0001). This reflected the weaker binding of O and H on Pt*/Ru(0001), leading to more facile bond-making steps. Since both H₂ dissociation and H₂O formation were faster on Pt*/Ru(0001) than on Pt(111), it was expected that Pt*/Ru(0001) would show a lower light-off temperature for H₂O

formation than Pt(111), in complete agreement with the experimental findings (see Figure 2.36).

Then, the CO oxidation mechanism was studied. In the absence of H₂, CO oxidation preceded through the difficult O₂ dissociation step (see Table 2.5). In that case, according to the calculations, not only were O₂(a) and O(a) greatly destabilized on Pt*/Ru(0001) compared to Pt(111), but also the activation energy barrier for O₂ dissociation increased by ca. 0.3eV on Pt*/Ru(0001). Therefore, in the absence of H₂, CO-oxidation would proceed faster on Pt(111), if it were not for CO-poisoning of that surface. However, in the presence of H₂, it was found that a novel H-assisted O₂ dissociation mechanism was quite facile on Pt*/Ru(0001), and was responsible for CO-oxidation at low temperatures. These findings were in good agreement with the experimental observations (see Figure 36) and provided the origin of the proposed H-assisted CO-oxidation process.

Mechanistically, atomic H(a) addition to O₂(a) led to a hydroperoxy intermediate (O₂H(a)) formation, with fairly small barriers on both surfaces (0.33eV and 0.25eV on Pt and Pt*/Ru, respectively). Then, the adsorbed hydroperoxy intermediate (O₂H(a)) decomposed into O(a) and OH(a), again with fairly small barriers (0.16 eV and 0.42eV on Pt and Pt*/Ru, respectively). Subsequently, O(a) addition to CO(a) led to CO₂ formation, with a barrier of 0.79eV on Pt(111), but only ca. half of that (0.41eV) on Pt*/Ru(0001). Again, this substantial difference in the CO(a)+O(a) barriers reflected the considerable destabilization of CO(a) and O(a), 0.57eV and 0.76eV respectively, on Pt*/Ru(0001) versus Pt(111), and agreed well with an earlier single-crystal TPD/TPR study.¹⁹⁷ As a result, CO₂ formation on Ru@Pt NP's showed a light-off temperature

much lower than the respective temperature on Pt NP's. Finally, the fact that $\text{CO(a)} + \text{O(a)} \rightarrow \text{CO}_2$ has a barrier ca. 2/3 of the $\text{O(a)} + \text{H(a)} \rightarrow \text{OH(a)}$ barrier on Pt*/Ru(0001) explained the lower CO_2 formation light-off temperatures compared to the H_2O formation light-off temperatures. It is anticipated that this H_2 -mediated oxygen activation might be relevant for other core-shell nanoparticles and might likely have implications beyond CO oxidation.

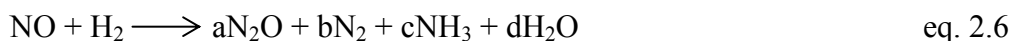
Table 2.5. Calculated PW91 binding energies of various species at 1/4 ML coverage and the activation energy barriers of different elementary steps on Pt(111) and Pt*/Ru(0001).

	Pt(111)	Pt*/Ru(0001)
<i>d-band center of surface Pt atoms, ϵ_d (eV)</i>	-2.53	-2.98
<i>Species</i>	<i>Binding energy, BE (eV)</i>	
O_2	-0.65	-0.26
O	-3.87	-3.11
H	-2.72	-2.42
O_2H	-1.09	-0.95
OH	-2.09	-1.91
CO	-1.82	-1.25
H_2O	-0.27	-0.20
<i>Elementary reactions</i>	<i>Activation energy barrier, E_a (eV)</i>	
$\text{H}_2 + 2^* \rightarrow 2\text{H}^*$	0.00	0.16
$\text{O}_2 + 2^* \rightarrow 2\text{O}^*$	0.77	1.05
$\text{O}_2^* + \text{H}^* \rightarrow \text{O}_2\text{H}^{**}$	0.33	0.25
$\text{O}_2\text{H}^{**} \rightarrow \text{O}^* + \text{OH}^*$	0.16	0.42
$\text{O}^* + \text{H}^* \rightarrow \text{OH}^* + ^*$	0.85	0.58
$\text{OH}^* + \text{H}^* \rightarrow \text{H}_2\text{O}^* + ^*$	0.10	0.15
$\text{CO}^* + \text{O}^* \rightarrow \text{CO}_2^*$	0.79	0.41

For bond-making steps, activation energy barriers are referred to the respective surface-coadsorbed states of the reactants. The d-band center, ϵ_d , is referred to 0 eV for the Fermi level.

2.3.7.2. NO_x Reduction

The 4.1 nm Ru@Pt core/shell and the 4.4 nm Pt₅₀Ru₅₀ alloy NP catalysts were also tested for their catalytic behavior toward NO reduction. NO reduction by H₂ was used as the model reaction for the sake of data analysis. Two catalytic compositions were studied: H₂/NO = 4 (Figure 2.40a and 2.40b) and H₂/NO = 1 (Figure 2.41a and 2.41b). Catalytic reduction of NO_x yields several products:



H₂/NO = 4 condition is known to favor NH₃ formation over N₂ according to the reaction



Figures 2.40 and 2.41 show the % concentration of NO, the % formations of N₂, NH₃, N₂O and NO₂; and the selectivity for N₂. The selectivity is defined as the ratio of the % formation of N₂ to the % concentration of NO. The activity of the Ru@Pt core/shell catalyst reaches 100% around 70 °C as shown in Figure 2.40a for H₂- rich condition. The selectivity toward N₂ is higher than NH₃ at low and high temperature limits and approaches 70% at 375 °C (Figure 2.40a). N₂O is not present at 375 °C (Figure 2.41a). The Pt₅₀Ru₅₀ alloy catalyst, on the other hand, shows a maximum of 40% selectivity under identical conditions (Figure 2.41b).

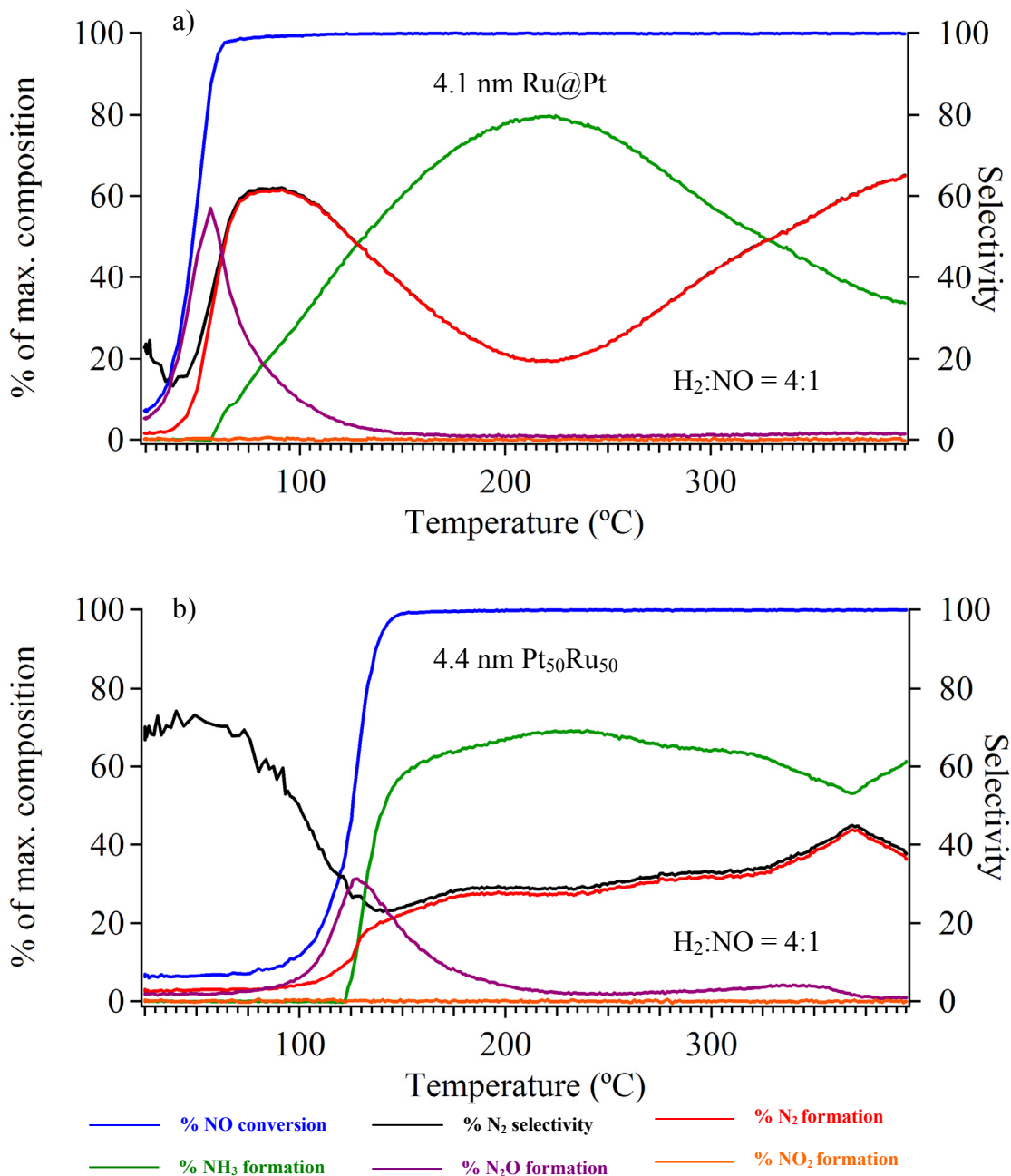


Figure 2.40. TPR plots for NO_x reduction reaction on (a) 4.1 nm Ru@Pt NPs catalyst and (b) 4.4 nm Pt₅₀Ru₅₀ NPs catalyst in NO/H₂ = 4. % N₂ Selectivity is defined as N₂ yield over % NO concentration.

In equimolar composition of H₂ and NO, N₂ is favored over NH₃ according to the reaction:



The activity is 100% at 90 °C, however, drops at intermediate temperatures and rises back at high temperatures (Figure 2.41a). N₂ is the major product at temperatures above 75 °C. The Ru@Pt NPs catalyst reaches ca. 80% selectivity at 90 °C and 99% selectivity at 400 °C. NH₃ and N₂O are the other products at intermediate temperatures (Figure 2.41a). In contrast, the Pt₅₀Ru₅₀ NPs catalyst exhibits 90% selectivity only above ca. 300 °C. The highest selectivity reported under the given conditions is the Cu@Pt catalyst that exhibits 88% selectivity for N₂ production.³⁴ Another catalyst, Pt-SiO₂, shows only 80% selectivity under similar conditions, and furthermore the Pt metal loading is 5% by weight as compared to 1% Pt metal loading for our Ru@Pt NPs catalyst.¹⁹⁸ The results reported here represent a noteworthy improvement in selectivity and activity. In both H₂-rich and H₂-limited conditions, the Ru@Pt core/shell NPs catalyst shows a high activity and an abnormal selectivity toward N₂ formation compared to bimetallic Pt₅₀Ru₅₀ alloy NPs catalyst and the other state-of-the-art NO_x reduction catalysts that were evaluated under milder reaction conditions.

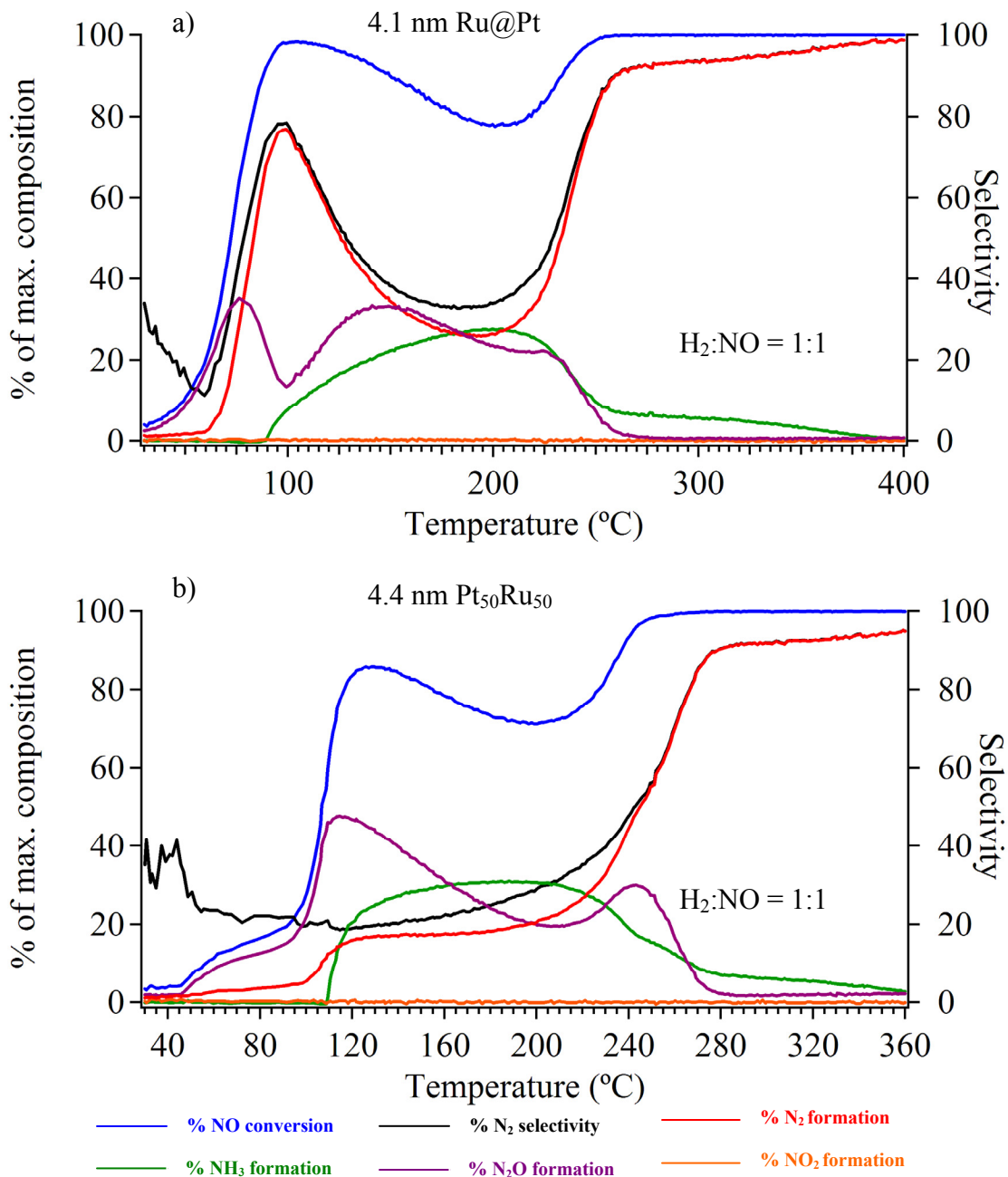
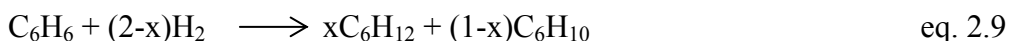


Figure 2.41. TPR plots for NO_x reduction reaction on (a) 4.1 nm Ru@Pt NPs catalyst and (b) 4.4 nm Pt₅₀Ru₅₀ NPs catalyst in NO/H₂ = 1. % N₂ Selectivity is defined as N₂ yield over % NO concentration.

2.3.7.3. Benzene Hydrogenation

Bimetallic Pt/Ru nanoparticle catalysts were finally screened for their surface reactivity in benzene hydrogenation reaction (eq. 2.9). A complete reduction of benzene yields only cyclohexane. On the other hand, a partial reduction reaction produces both cyclohexane and cyclohexene. Turn-over Frequencies (TOFs) for benzene hydrogenation on the bimetallic Ru@Pt core/shell NPs with various core sizes and shell thicknesses, Pt_{1-x}Ru_x alloy NPs, and the monometallic Pt and Ru NPs, as well as, the mixtures of Pt and Ru NPs were calculated, and compared to evaluate their surface reactivity. The surface areas of the catalysts were determined by CO chemisorption via Temperature Programmed Desorption (TPD). TOFs were calculated by simply dividing the specific activity with the surface area. The surface area measurements and the catalysis experiments were performed by Dr. Kunkes, Mr. Tucker, and Ms. Ford from Prof. James Dumas Research Group at the University of Wisconsin-Madison.



Active surface sites, mass-based activities and TOFs ($\mu\text{mol C}_6\text{H}_6 \cdot \text{min}^{-1} \cdot \text{surface metal}^{-1}$) were given in the Table 2.6. First of all, active surface sites measured using CO chemisorption method agreed well with the projected surface areas calculated using TEM particle sizes, such that both could be interchangeably used in determining TOFs. The projected surface areas were calculated assuming average TEM particle sizes, ligand-free surfaces and half-embedding geometry, which described the surface area loss of NPs in contact with the support. To note, the surface areas from the CO chemisorption

measurements were slightly larger than those from the TEM size-projections with the exception of the 4.4 nm Ru@Pt with ca. 2-3 ML thick Pt shells. Strong metal-ligand interaction in the case of the Ru@Pt with ca. 2-3 ML thick Pt shells, which could block the reactive surface sites, might explain the observed chemisorption data.

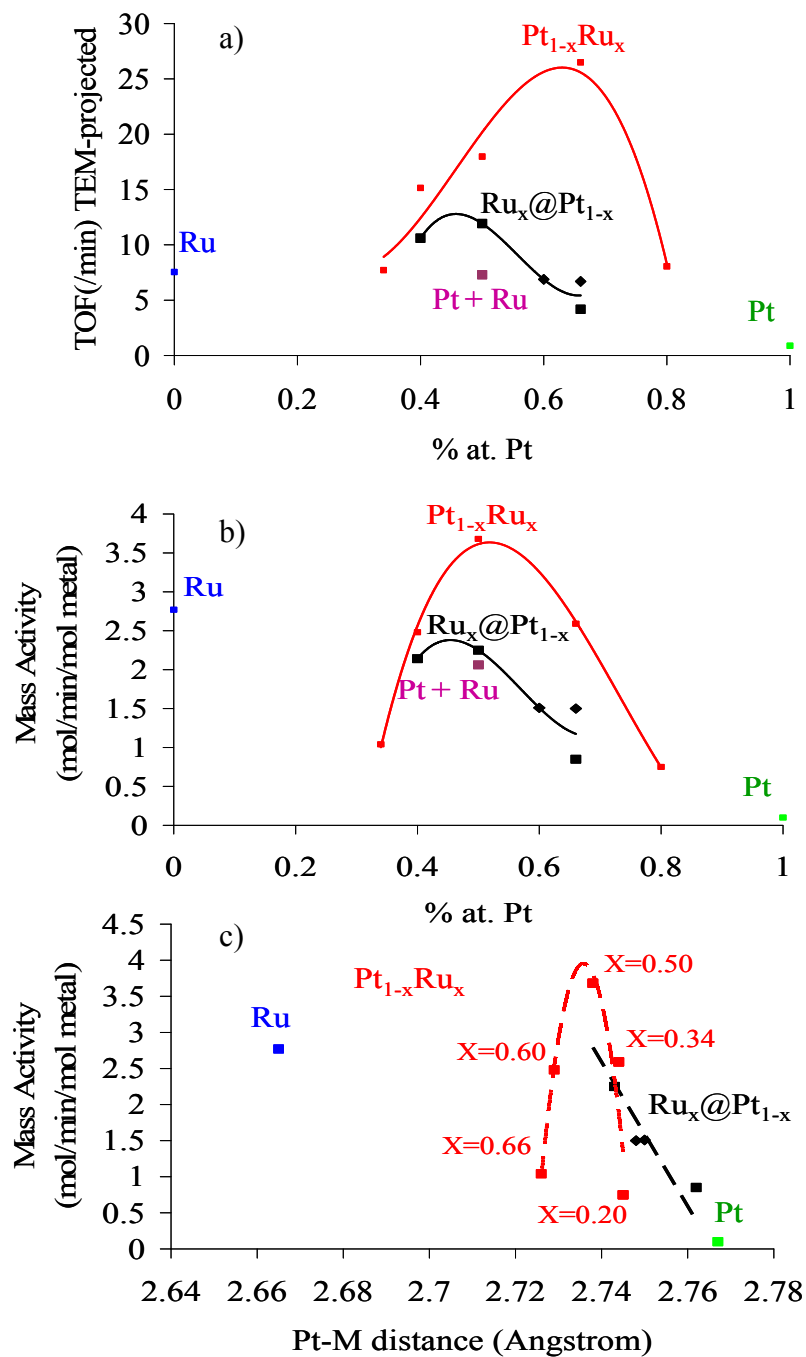


Figure 2.42. Plots of (a) TOFs based on TEM-projected surface areas vs. % atomic Pt, (b) Mass activities vs. % atomic Pt, and (c) Mass activities vs. Pt-M distances for the benzene hydrogenation reaction on the Ru_x@Pt_{1-x}, Pt_{1-x}Ru_x (x=0.2-0.66) NPs catalysts as well as monometallic Pt NPs and monometallic Ru NPs and the mixtures of monometallic NPs catalysts.

The Pt NPs catalyst was not active ($\sim 1 \mu\text{mol C}_6\text{H}_6 \cdot \text{min}^{-1} \cdot \mu\text{mol surface Pt}^{-1}$) toward benzene hydrogenation under the reaction conditions studied. The Ru NPs catalyst, in contrast, showed high activity ($\sim 16 \mu\text{mol C}_6\text{H}_6 \cdot \text{min}^{-1} \cdot \mu\text{mol surface Ru}^{-1}$) in benzene hydrogenation. The mixtures of monometallic Pt and Ru NPs showed a catalytic activity ($14 \mu\text{mol C}_6\text{H}_6 \cdot \text{min}^{-1} \cdot (\mu\text{mol surface Ru} + \text{Pt})^{-1}$) intermediate to those of monometallic Pt NPs and monometallic Ru NPs. The surface reactivity in terms of the TEM size-projected areas and the total mass activities of the Ru@Pt core/shell catalysts were also intermediate to that of Pt and Ru catalysts (Figure 42a). Furthermore, 3.7 nm and 4.1 nm Ru@Pt NPs with <1-layer thick Pt shells and 1-2 layers thick Pt shells, respectively, exhibited similar catalytic activities (ca. $12 \mu\text{mol C}_6\text{H}_6 \cdot \text{min}^{-1} \cdot (\mu\text{mol surface Ru} + \text{Pt})^{-1}$), whereas 4.5 nm core/shell catalyst with 2-3 MLs thick Pt shells performed relatively poor (TOF of $8 \mu\text{mol C}_6\text{H}_6 \cdot \text{min}^{-1} \cdot (\mu\text{mol surface Ru} + \text{Pt})^{-1}$). 3.0 nm and 3.3 nm Ru@Pt NPs with 1-2 layers thick Pt shells also ranked intermediate to others (Figure 42a).

The best benzene hydrogenation catalysts were alloy nanoparticle catalysts with the general formula of $\text{Pt}_x\text{Ru}_{1-x}$ ($x=0.4$ and 0.5). In particular, $\text{Pt}_{50}\text{Ru}_{50}$ NP catalysts showed the second highest TOF ($18 \mu\text{mol C}_6\text{H}_6 \cdot \text{min}^{-1} \cdot (\mu\text{mol surface Ru} + \text{Pt})^{-1}$) and the highest mass activity ($3.68 \mu\text{mol benzene}/\mu\text{mol total metal}/\text{min}$) among those studied (Figures 2.42a and 2.42b, respectively). The % atomic Pt was plotted vs. TOFs in Figure 2.42a and mass activity per gram of catalyst in Figure 2.42b. It was interesting to note that the $\text{Pt}_{1-x}\text{Ru}_x$ NPs and $\text{Ru}_x\text{@Pt}_{1-x}$ NPs independently exhibited polynomial (of order 3) dependence of TOFs and mass activities on % atomic Pt. The envelope functions had similarities to ‘Volcano’¹⁹⁹ plots. TOFs based on the TEM-projected surface areas were

also plotted vs. average Pt-M distances (in Å) in Figure 2.42c. The average Pt-M distances were calculated from the 220 and 311 reflections of the respective X-ray diffraction patterns (see Figure 2.18). It was concluded that the surface reactivity of the bimetallic Pt/Ru NPs correlated with the average metal-metal distance, and thus the benzene hydrogenation on the Pt/Ru system was dependent on the surface structure. The Pt-metal distances for the 4.1 nm Ru@Pt core/shell NPs and the 4.4 nm Pt₅₀Ru₅₀ alloy NPs were taken from the respective EXAFS results. The other data for the Pt-metal distances were calculated from the 111 reflections of the respective XRD patterns, and thus only reflected an estimation of bond distances from average inter-planar spacings. The mass activity (3.6 μmol C₆H₆*min⁻¹(μmol total Ru + Pt)⁻¹) was larger than that of the best benzene hydrogenation catalyst in the literature, 4.8 nm tetrahedral Rh nanoparticles, which exhibited a mass activity of 3.3 μmol C₆H₆*min⁻¹*(μmol total Rh⁻¹) under identical conditions.⁷⁰ The best Ru NPs catalyst under identical reaction conditions reported to have a mass activity of only 0.13 μmol C₆H₆*min⁻¹*(μmol Ru⁻¹). There were also reports of other supported Ru nanoparticles²⁰⁰ and nanoclusters²³ with the mass activities of 18 and 630 μmol C₆H₆*min⁻¹*(μmol Ru⁻¹), respectively, but they were reported under high temperature (110 °C) and/or high H₂ pressures (2.8-8 atm). Origin of the reactivity enhancements is under investigation.

Table 2.6. Benzene hydrogenation data on the Ru_x@Pt_{1-x}, Pt_{1-x}Ru_x, Pt, Ru, and the mixtures of monometallic Pt and Ru NPs catalysts.

	Active Sites (CO chemi.) μmol surface metal / gram catalyst	Active Sites (TEM-proj.) μmol surface metal / gram catalyst	Rate (μmol / gr cat. / min)	TOF(TPD-CO chemisorption) μmol C ₆ H ₆ / μmol surface metal / min	TOF(TEM- projected) μmol C ₆ H ₆ / μmol surface metal / min	Mass activity (μmol C ₆ H ₆ / μmol total metal / min)
Ru*@Pt(1:2)	13.24	18.7	115.7	8.7	6.9	1.50
Ru*@Pt(2:3)	7.98	17.9	128.6	16.1	6.6	1.51
Ru@Pt(1:2)	2.48	15.6	65.0	26.4	4.2	2.25
Ru@Pt(1:1)	14.01	18.9	231.1	16.5	11.9	0.85
Ru@Pt(2:3)	20.78	25.9	274.5	13.2	10.6	2.14
Pt+Ru	22.50	28.9	210.9	9.4	7.3	2.06
Pt ₈₀ Ru ₂₀	3.25	6.0	48.3	14.9	8.1	0.75
Pt ₆₆ Ru ₃₄	6.71	7.6	201.3	30.0	25.5	2.59
Pt ₅₀ Ru ₅₀	15.52	21.0	377.4	24.3	18.0	3.68
Pt ₄₀ Ru ₆₀	16.13	21.0	317.9	19.7	15.1	2.48
Pt ₃₄ Ru ₆₆	14.87	21.0	162.1	10.9	7.7	1.04
Pt	4.87	22.7	5.4	1.1	7.5	0.10
Ru	18.60	6.2	171.2	9.2	0.87	3.33

Data shows active sites as, rate of reaction, turnover frequency (TOF) and mass activity. Active sites were independently calculated by CO chemisorption measurements, and TEM-projected area calculations. Two sets of TOF were separately calculated from the surface areas and rates of reaction.

2.4. Discussions

The 4.1 nm Ru@Pt NPs comprising 1-2 MLs thick Pt shells and 3.0 nm Ru cores was well-characterized by using a combination of techniques. Thin Pt shells, which were evaluated by STEM-EDS line-spectrum, were structurally elucidated by a combination of experiment and simulations using X-ray diffraction and absorption techniques independently. Recently, surface studies of Pt overlayers on Ru(0001) have demonstrated hetero-epitaxial growth of Pt monolayers on Ru.^{99,103} Jacob and co-workers showed that Pt overlayers adapted crystal structures intermediate to those of bulk FCC Pt and HCP Ru up to 3-5 MLs above the substrate. The findings of this study were in favor of the hetero-nucleation and subsequent pseudo-epitaxial growth of thin Pt overlayers on Ru NPs.⁹⁹

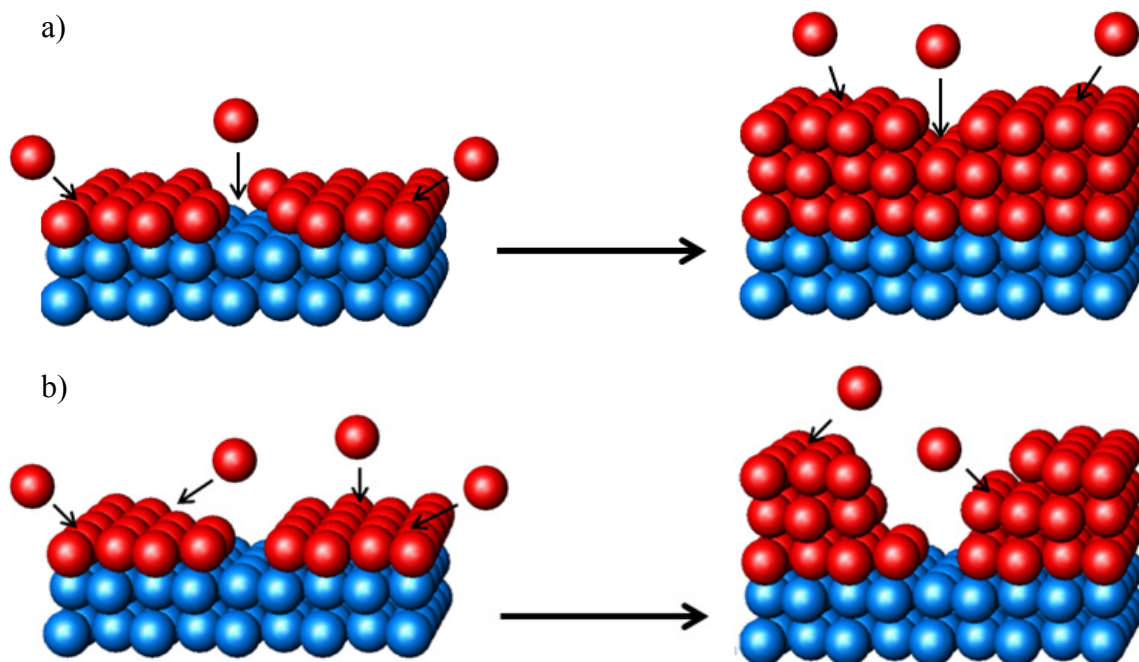
Structural evaluation by powder X-Ray diffraction first showed anomalies associated with thin Pt shells. 200 reflections of nanocrystalline Pt shells were shifted to low angles showing a lattice expansion. On the other hand other reflections were either in-position with those of bulk Pt or shifted to high angles showing lattice contraction. The unit cell was refined by using LeBail fit to 3.897 Å, which in overall points to a lattice contraction. The Debye Function simulations from TEM and EXAFS-derived atom clusters could partially produced the experimental data, but were unable to catch origin of the observed structural anomalies.

In parallel with the surface studies,⁹⁹ thicker Pt shells up to 3 MLs exhibited the same structural anomalies as the thin-shelled Pt overlayers. Interestingly, approximately 1 ML thick Pt shell grown over larger Ru cores (5.7 nm) had 200 reflections shifted to low angles in their XRD pattern. This implies that given the sizes of

core/shell nanoparticles (between 3.0 nm and 6.2 nm), crystal defects and vacancies on Ru NP cores could not accommodate the lattice strain due to the heterogeneous growth of pseudo-morphic Pt (thin) shells. Thus, strain-induced distortion of the Pt lattice led to the structural anomalies in diffraction from Pt thin shells. This was in contrary to the surface study findings for the Pt overlayers on Ru(0001), which suggested a stress-relaxation mechanism to the hetero-epitaxial overlayers through defect and vacancy sites.⁹⁹

Furthermore, EXAFS and PDF data demonstrated rather long range order of FCC Pt shells in accord with the results of XRD experiments for the 4.1 nm Ru@Pt NPs. In contrast, Ru NP cores were highly disordered, and thus showed no closed-packed atomic arrangement and little phase coherence by using EXAFS and PDF modeling. It was suggested by Fan et. al. that heterogeneous growth via a Frank-van der Merwe type mechanism (scheme 2.2a) of host metals whose atomic radius is larger than that of the substrate metal is thermodynamically unfavorable, thus such systems present a non-epitaxial, non-pseudo-morphic, Volmer-Weber type growth mechanism (scheme 2.2b).¹⁰⁰ The core/shell nanoparticles with Ru ($d_{\text{Ru-Ru}}=2.690 \text{ \AA}$)¹²⁰ cores and Pt ($d_{\text{Pt-Pt}}=2.774 \text{ \AA}$)¹²⁰ shells, however, adapted the pseudo-morphic growth employing a Frank van-der Merwe type model. It was also anticipated that the strain-induced disorder of Ru and lattice distortion of Pt at the interface kinetically facilitated the formation of nanoparticles with the core-shell architectures.

Scheme 2.2. Schematics illustration showing (a) Frank van-der Merwe and (b) Volmer-Weber type heterogeneous growth mechanisms.



The catalytic activities of the well-characterized bimetallic Pt/Ru NPs were evaluated in the PROX, de-NO_x and benzene hydrogenation reactions. The PROX reaction is a key reaction to clean H₂ feeds off of CO-contaminant, which is detrimental to cell performances in low-temperature fuel cell applications. High selectivity toward CO oxidation and high reaction activity are desired. Thus, the Ru@Pt NPs with 3.0 nm Ru cores and 1-2 MLs thick Pt shells were found to perform the best among other bimetallic Pt/Ru NPs and monometallic NPs as mixtures or individual. For 1000 ppm CO concentration, to which a typical ZnCu alloy catalyst could reduce the reformat via a water-gas-shift reaction, the Ru@Pt NPs exhibited CO oxidation complete by 20 °C, and subsequent H₂ light-off at 25 °C (Figure 2.35a).

DFT calculations performed by Prof. Mavrikakis and Dr. Nilekar helped elucidating the fundamentals of the unique catalytic behavior of the core/shell NPs. The so-called H₂-assisted CO oxidation mechanism and the low CO saturation coverage were determined to be responsible for the low-temperature CO oxidation behavior. H₂, - starting at low partial pressures, was reported to increase CO oxidation kinetics⁶⁷, but never justified. Introduction of hydroperoxy formation route to O₂ dissociation in the PROX reaction network, which was rationalized by the experiment, led to understanding of this phenomenon. In such a reaction pathway, O₂ formed hydroperoxy intermediate with surface adsorbed atomic H. Dissociation of the hydroperoxy species to give atomic O and molecular OH was followed. Therefore, such a H₂-assisted formation of atomic O occurred with half the energy barrier needed to dissociate O₂ over the Pt overlayers on the Ru. Then, atomic O reacted with CO to form CO₂ at half the energy cost of reaction pathway on pure Pt. Finally, atomic O formed H₂O in a two-step bond making route. Since the rate limiting reaction step exhibited higher activation barrier than that of the bond making reaction between CO and atomic O, H₂O formation was subsequent to CO₂ formation which explained the high selectivity observed. This reaction network was partially supported by the absence of low-temperature CO oxidation in H₂-free feeds for the core/shell NP catalyst (Figure 2.36). Thus, it was demonstrated on the core/shell NPs of bimetallic Pt/Ru system that the architectural control over nanoparticle synthesis may further enhance surface reactivity by circumventing high energy barrier reaction pathways.

A ‘thickness effect’ to the PROX activity was prominent from the study of 2-3 MLs thick Pt shells and Pt shells at sub-monolayer coverages deposited over the 3.0 nm Ru cores (Figure 2.37). The core/shell NPs with thick Pt shells were not as active as the thin-shelled NPs, but did perform better than pure Pt NPs. Furthermore, the core/shell NPs with Pt shells at sub-monolayer coverages performed similar to the Pt₅₀Ru₅₀ alloy NPs. Schlapka et al. reported for the Pt overlayers on Ru(0001) surface that the ‘ligand’ effect induced by the Ru substrate persists up to several monolayers of the Pt overlayer.⁹⁹ It seemed that a ‘size effect’ to the PROX activity was present as the Ru core diameters increased for the fixed thickness of Pt shells (Figure 2.38). The PROX activity dropped drastically with increasing average Ru core sizes, but never reached the limiting level of pure Pt NPs. The Pt_xRu_{1-x} alloys exhibited “volcano”¹⁹⁹ type PROX activity behavior, reaching at a maximum for the Pt₅₀Ru₅₀ alloy. Although the surface compositions could not directly be determined, it was believed that the measured activities were the actual surface reactivities of the Pt_xRu_{1-x} alloy NPs, which correlated with the % atom Ru on the surface.

Finally, the combined effect of strain and electronics on NSA catalysts, which was maximized for approximately monolayer-thick overlayer structures, was isolated.¹⁸² The absence of two kinds of atoms in the NP’s surface excluded possible contributions from the bifunctional mechanism. The unprecedented low CO and H₂ light-off temperatures were demonstrated with experiments on the Ru@Pt NPs and rationalized with a novel H-assisted O₂-dissociation mechanism. Furthermore, the remarkable reactivity improvement observed for the core-shell NPs pointed to a direct connection between model surface science studies on bimetallic single crystals and bimetallic

catalytic NPs. Inorganic synthesis of desired nanoarchitectures, identified as promising catalysts by first-principles, was expected to play a key role in bridging the existing gap between surface science and catalysis.

De-NO_x reaction is of industrial importance because of the pollutant nature of NO_x and their oxidation and reduction products with the exception of N₂, such that higher selectivity toward N₂ is the sole condition that is sought. There are two distinct reaction conditions, namely rich-NO_x¹⁹⁸ and lean-NO_x²⁰¹ reactions. The former is the reduction of NO_x in pure H₂ (as to simulate hydrocarbon fuels); and the latter, in H₂ and O₂ mixtures. The core/shell catalyst tested to date performed poorly toward NO_x reduction under lean-NO_x conditions, probably, because of their enhanced O₂ activation abilities.

For the rich-NO_x reaction, however, the Ru@Pt NPs with 3.0 nm Ru cores and ca. 1-2 MLs thick Pt shells showed the greatest NO_x reduction activity and the highest selectivity toward N₂ under the conditions studied (Figures 2.40a and 2.41a). The core/shell nanoparticles catalyst showed 60% and 80% selectivity for N₂ formation for the H₂-rich and H₂-limited reaction conditions, respectively, at about 100 °C at which the core/shell structure was stable. Besides, the maximum selectivity for N₂ production was reached at elevated temperatures, which peaked to 99% at 400 °C under the H₂-limited conditions.

However, the core/shell structure is thermodynamically not stable, and thus is expected to transform to a gradient alloy in the form of Ru_x@PtRu_{1-x}. Furthermore, experiments indicated that annealing the core/shell nanoparticles at 500 °C in vacuum would transform them into alloys whose X-ray diffraction pattern was identical to that of the authentic Pt₅₀Ru₅₀ alloy (Figure 2.15). Moreover, as shown in Figure 2.35a, the

core/shell NPs catalyst conditioned at 500 °C in vacuum performed in PROX identical to the authentic alloy NPs catalyst. Although such a phase transition occurred in hours (longer than the time interval that the TPR data was collected) and at elevated temperatures (higher than the temperature range that was swept), adsorbate-induced phase segregation might reversibly take place faster than otherwise it would do. Then, almost identical de-NO_x reactivities for the H₂-limited reaction conditions (97±1% at 360 °C) for the alloy and core/shell NPs catalysts could be explained (Figures 2.41a and 2.41b). The highest selectivity for N₂ under the given conditions was reported for the Cu@Pt catalyst that exhibited 93% selectivity for N₂ production.³⁴ On the other hand, the 4.5 nm Pt particles catalyst performed moderately, and thus exhibited only 88% selectivity for N₂ formation.³⁴

Finally, the benzene hydrogenation is a model reaction for chemical storage of H₂. on both weight and volume basis, benzene provides a high storage density for H₂. Furthermore, there is an increasing demand for hydrogenation catalysts to meet new regulations that put limits to the content of aromatics in hydrocarbon fuels.^{69,202} The Pt_xRu_{1-x} alloy NPs, in general, showed high surface reactivity (TOF) for hydrogenation of benzene at 1 atm H₂ and room temperature, which was challenging to achieve high reaction activities. Furthermore, the surface reactivities and the mass-based activities indicated ‘Volcano’¹⁹⁹ type behavior with % Pt content (Figure 2.42). As opposed to PROX and De-NO_x reaction studies, the alloy NPs exhibited higher TOF and mass-activity than the core/shell NPs with identical elemental compositions. Regardless of the particle architecture, ‘Volcano’ type correlation of mass-activities (and TOFs) and inter-planar spacings as determined from X-ray diffraction data was noteworthy, and indicated

that high surface reactivity was at least partially favored by geometrical effects (Figure 42c). In regard to the effects of surface morphology and particle geometry in heterogeneous catalysis, there is an ongoing debate on the ‘structure sensitive’¹⁰⁴ nature of the benzene hydrogenation reaction. Some factions suggested that the activity scales with exposed metal surface, thus the benzene hydrogenation is ‘structure insensitive’.²⁰² More recent studies on morphologically-controlled Pt NPs showed that nano-crystalline Pt cubes with 100 only surface formed exclusively cyclohexane, but cuboctahedral Pt NPs with mixtures of 111 and 100 surfaces formed both cyclohexane and cyclohexene, thus revealed ‘structure sensitive’ nature of the benzene hydrogenation reaction.⁸⁰ The results presented in this study were in favor of a combination of ligand and geometric effects in surface reactivity for hydrogenation of benzene, and thus indirectly supported structure sensitivity of the reaction.

In addition to its stabilizing role in NP synthesis, PVP can also be used as a size- and shape-controlling agent.²⁰³ The size control effect of PVP on Pt NPs is evident from a comparison of 2.2 nm PVP-free Pt particles and 5.7 nm PVP-stabilized Pt particles. On the other hand, the PVP-free monometallic Ru and PVP-free Ru@Pt core/shell NPs exhibited almost identical average particle sizes as their PVP-stabilized counterparts. Moreover, no change on particle morphologies was prominent from the TEM analysis.

PVP is known to bind weakly to NP surface.²⁰³ Thus, it is anticipated that PVP blocks surface active-sites and hinders heterogeneous reactions such as PROX, de-NO_x and benzene hydrogenation. It was found on the bimetallic Pt/Ru NP catalyst that the as-prepared catalyst exhibited similar catalytic behaviors as the PROX-conditioned (isothermal at 200 °C for 2 h) catalysts for PROX reaction. Although the resulting PROX

reactivity of the PROX-conditioned core/shell NP catalyst slightly increased with respect to the as-prepared one, room temperature CO oxidation behavior was always present. Furthermore, the PVP-free core/shell NP catalyst performed much poorer than the PVP-stabilized one for PROX reaction due to particle agglomeration.

For benzene hydrogenation reaction, the pre-conditioned NP catalysts exhibited negligibly small catalytic activities. The reported catalytic activities could only be measured after conditioning the catalysts under air (or PROX) feeds (isothermal at 200 °C for 5 h). Thus, it was anticipated that PVP shell coating around nanoparticles hindered diffusion, adsorption and/or reaction of moderate-sized molecules such as benzene, but did not significantly influence those of small molecules such as H₂, O₂, CO and NO_x. Thermally- and/or adsorbate-induced phase segregation and/or surface restructuring of the bimetallic nanoparticles have potentials to influence the nanoparticle architecture.¹⁰⁹ Thus, the resulting catalytic properties may show variations due to catalyst stability. In general, PROX reaction conditions given in this study had no significant effect on the catalytic properties. Potential thermal and adsorbate effects on the nanoparticle architectures of the bimetallic Pt/Ru system (and others) are currently under investigation and beyond the scope of this thesis.

Chapter 3

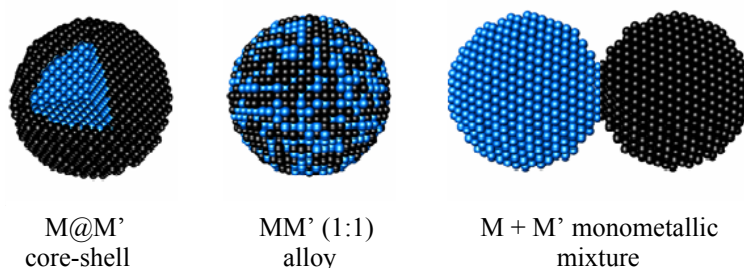
Synthesis and characterization of nano-structured Rh-Pt bimetallic particles for PROX reaction

3.1. Introduction

Rodriguez, Goodman and others^{89,99,130} have performed detailed studies of metal thin film overlayers deposited on bulk metallic surfaces. The studies were designed to probe the electronic structures and the nature of metal-metal bonding between the metal overlayers and the metallic substrates. The results showed that work functions of metallic films were altered from their bulk values due to the structural and electronic effects of the underlying metal host. Through a combination of thermal desorption studies and photoelectron experiments, the studies documented significant intermetallic electron transfers between overlayer and substrate metals having different d-band electronic populations. In general, it was shown that electron density was transferred from those metals with filled d-states to those with less filled d-states. These findings differ from the electronic interactions in bulk intermetallics and alloys where electronegativity considerations dictate the magnitude and direction of electron transfer. More recent studies^{99,102,103,127-129} have shown that lowering the energy of the metal overlayer's d-band center has a significant impact on the interactions of the metal overlayer with adsorbate molecules on the surface. The resulting changes in activation energies and bond enthalpies of adsorbates have dramatic effects on the catalytic activities. For example, Mavrikakis *et al.* have shown^{8,9} that hydrogen bond enthalpies

on Pt monolayers were reduced by as much as 0.4 eV depending on the substrate, which makes them far more active for hydrogenation than bulk Pt. In a study of Pt overlayers on Ru(0001) hosts, Jakob and co-workers elegantly showed how the structural and electronic influences of the host could be experimentally differentiated.⁹⁹ They showed that the electronic influence of the host Ru metal on the Pt overlayer was maximized with single monolayer films but quickly disappeared after 3 or more monolayers of coverage. In contrast, the structural influences of the substrate persisted to greater overlayer thickness due to long-range pseudomorphic growth.³

Scheme 3.1. Schematic illustration of various bimetallic particle architectures.



Translation of these results from bulk monolayer surface structures to nanoparticles (NPs) with monolayer shells on metallic cores (*i.e.* M@M' core-shell NPs, see drawing in Scheme 3.1) is not completely obvious. For example, how will deviations from bulk band structures and finite electronic states affect charge transfer between the core and shell metals? How will the surface strain of the shell of a core-shell NP compare to that of a bulk thin film overlayer grown pseudomorphically on a faceted substrate? Mavrikakis and co-workers have developed remarkably accurate “Near Surface Alloy” theoretical models for describing trends in activity, adsorbate binding and

mechanistic pathways on various core-shell structures.⁹⁰ However, several approximations must be made in order to perform such detailed analysis on these large, complicated systems. The approximations, such as perfectly faceted substrates and uniform interfaces between core and shell metal layers, may cause complications in modeling non-uniform, multifaceted core-shell NPs made from solution. It is clear that additional comparative experimental investigations of core-shell and alloy NP systems are needed to unravel the underlying structural and electronic principles governing the activities of bimetallic nanoparticles and help refine modeling studies.

While some bimetallic NP catalysts show expected and somewhat systematic changes, other systems are less predictable and have surprising activities. For example, CO oxidation catalyzed by Pt_{1-x}Rh_x alloy NPs show activities intermediate to those of the Pt and Rh NP end members.²⁰⁴ In contrast, the preferential oxidation of CO in hydrogen (PROX) activities of the Pt_{1-x}Ru_x NPs are much better than those of the Pt and Ru end members due to synergistic effects of the alloy surfaces. Moreover, the Ru@Pt core-shell NPs are far superior to the Pt_{1-x}Ru_x alloy NPs and monometallic mixtures.¹⁷⁶ To experimentally probe the importance of architecture in bimetallic NP systems, we have embarked on a systematic evaluation of bimetallic particles in different architectural configurations; namely, core-shell, alloy and mixed monometallic NPs (see scheme 3.1).

In this chapter, the full synthetic, spectroscopic and structural characterization of Rh@Pt core-shell NPs with different core sizes and shell thicknesses – with and without surfactant stabilizers will be presented. In addition, the preliminary catalysis studies show that the Rh@Pt core-shell NPs are superior to the alloy and monometallic mixtures for PROX applications.

3.2. Experimental

3.2.1. Materials

All reactions were carried out under N₂ atmosphere using standard Schlenk line on a Fisher Scientific Isotherm hot plate stirrer with a temperature control unit using a Teflon coated K-type thermocouple. Chemicals, PtCl₂ (Engelhard, Pt 73.09%), Pt(acac)₂ (Strem, 98%, acac=acetylacetonate), Rh(NO₃)₃·2H₂O (Alfa Aesar, 99.9% pure, Rh 31.1%), RhCl₃ (Engelhard, Rh 39.46%), Rh₂(CO)₄Cl₂ (Fluka, >97%), polyvinylpyrrolidone (Aldrich, typical M_w=55000), ethylene glycol (VWR, H₂O >0.02%), acetone (Pharmco Aaper, HPLC-UV Grade), ethanol (Pharmco Aaper, 200 proof) and γ-Al₂O₃ (Alfa Aesar, 99.97% metal basis) were purchase and used as received.

3.2.2. Sample characterization of the proposed nanostructures

The colloidal suspensions described below were diluted with acetone and centrifuged at 6000 rpm using a Hermle Z 300. The supernatants were clear. The precipitates were washed with acetone and acetone-ethanol mixture upon sonication using a Fisher Scientific FS30H sonicator bath. The cycles of dilution by acetone-ethanol mixtures, sonication and centrifugation were repeated 4-5 times. The precipitates were dried in open air prior to characterization.

3.2.2.1. Powder X-ray Diffraction

A Bruker C2 Discover (Parallel Beam) General Area Diffraction Detection (GADDS) system was used for powder diffraction detection. The monochromatic Cu K α radiation source that was biased at 40 mV and 40 mA was employed along with Bruker ACS Hi-Star detector. The diffraction patterns were acquired between 33-90° by integrating four frames with 14° 2 θ per frame. The samples were oscillated in the xy-axis to homogenize the diffracting grains.

3.2.2.2. Debye Function Simulations

Powder diffraction patterns were simulated using the DISCUS software package.¹ The ATOMS program was used to generate the spherical core/shell nanoclusters of desired Rh core sizes and Pt shell thicknesses. Fractional atom coordinates in a P₁ cubic lattice of 100 Å cell size were simulated using Debye function with no symmetry constraints.

Model clusters are generated using ATOMS software package. First, FCC Rh and Pt unit cells are created in GSAS with the lattice parameters from JC-PDS files and the fractional coordinates of a FCC unit cell. The .gsas file for Pt cell is read from ATOMS, and single unit cell is expanded to a spherical nanocluster of desired particle diameter. The generated atomic coordinates are opened in EXCEL to calculate the atomic distances. Atoms with distances that are equal to and smaller than the diameter of the corresponding Rh cluster are deleted. The remaining atoms that constitute the Pt skin are saved as a .pdb file. Finally, the two, namely Rh core cluster and Pt skin cluster, are

opened in the same EXCEL sheet. The fractional coordinates are generated from the atomic coordinates for a 100 Å cell. The atom labels, the fractional coordinates, and the thermal parameters with user-defined values of 0.01 Å⁻² for both Rh and Pt atoms are saved as a 5-column DISCUS .stru file. The unit cell is defined as 100 Å, and the spacegroup as P₁. The .stru file is read in DISCUS. The powder diffractions are simulated using ‘powder’ subroutine with built-in ‘Debye’ function in DISCUS. Periodic diffractions from the model clusters are also evaluated. It has been found that diffraction from a ML thick Pt nanoshell is plausible, and thus Debye Function Analysis of the model clusters gives a qualitative picture of the synthesized core/shell structures.

3.2.2.3. Fourier Transformed-Infrared Spectroscopy

For the IR-CO probe experiments, the colloidal solutions of the desired nanoparticle architectures were bubbled with CO using a stainless steel needle submerged in the solution at a flow rate between 20 and 40 sccm for ca. 20 minutes. A 100 µL aliquot of CO saturated colloidal solution was filled in a liquid IR cell and monitored in a Nexus 870 FT-IR spectrometer. The liquid IR cell consisted of a 0.5 mm Teflon spacer sandwiched between two rectangular-shaped CaF₂ windows. The colloidal solution prior to CO bubbling was used for the background spectra.

3.2.2.4. Micro-Raman Spectroscopy

A Renishaw Raman Microscope was employed to measure the micro-Raman spectra of CO saturated nanoparticles. The nanoparticle powders were dispersed on glass

slides and then sealed in a gas-tight Linkam temperature control stage. A 632.8 nm He:Ne or 488 nm Ar ion laser was focused on the particles through 0.5 mm quartz window using Leica N plan L50x/0.50 objective lens. The backscattered light was monitored with a resolution of 20 exposures per second between 300 and 2400 cm^{-1} . The particles were dosed with CO, CO/air or CO/Argon mixtures for about 20 minutes. The spectra were recorded under flowing gas streams.

3.2.2.5. Transmission Electron Microscopy

TEM samples were prepared directly from the reaction solutions by diluting 20 μL of colloids to ~ 2 mL with deionized water. 3 μL of such mixtures were drop-cast and dried on continuous carbon film-deposited copper grids. A JEM 2100 LaB6 TEM operating at 200 kV was used for both low and high resolution imaging.

3.2.2.6. Scanning Transmission Electron Microscopy-Energy Dispersive Spectroscopy

A Jeol 2100F Field Emission Transmission Electron Microscope (FE-TEM) equipped with an Inca Energy Dispersive Spectrometer (EDS) was used for line and point spectrum of nanoparticles. The FE-TEM was operated at 200 kV and in the scanning mode.

3.2.3. Catalytic evaluation for PROX reaction

Catalysis runs were carried out using 105 mg of catalyst charges in all cases. A standard fixed bed flow-through reactor was employed and has been described elsewhere^{95,98,176}. An inlet velocity for gases of 0.21 m/s, and a total flow rate of 400 NmL/min was employed. The gas hourly space velocity (GHSV) was calculated to be $2.3 \times 10^5 \text{ mL} \cdot \text{g}^{-1} \cdot \text{h}^{-1}$ with a corresponding residence time about 35 milliseconds. The gas mixture for the PROX reaction was composed of 0.2% CO (99.5% pure, Al tank), 0.5% O₂ (99.999% pure), 50% H₂ (99.999% pure), and balance Ar (99.999% pure). The catalysts were reduced in 50% H₂-Ar mixture at 200°C prior to catalysis. The temperature was set to 200°C and the heating ramp is 1.8 °C/min. The gases were introduced to the reactor using carefully calibrated mass flow controllers. The gas products were monitored online using a Prima δB mass spectrometer.

3.2.4. Synthesis of bimetallic Rh-Pt NPs with various architectures

2.7. nm Rh NPs.

Method 1. In a typical synthesis, 33.0 mg of Rh(NO₃)₃·2H₂O were dissolved in 20 mL of ethylene glycol (EG) in a 50 mL 3-neck round bottom flask along with 28.0 mg of PVP₅₅₀₀₀. The Rh³⁺ precursor salt was loaded in a dry box; all other transfers were done on a Schlenk line under N₂ atmospheres. The mixture was heated to ~80°C and kept isothermal 10-15 min. to dissolve the contents of the reaction mixture. The light brown solution was brought to boil in EG and refluxed for *ca.* 90 min. in flowing N₂ with

vigorous stirring. The solution turned black and colloidal at about 110 °C. The reaction was quenched over ice. The colloids are stable for months without any precipitation.

Method 2. In a typical reaction, 53.3 mg of RhCl_3 and 56.0 mg of PVP_{55000} were dissolved in 10 mL of EG in a 50 mL 2-neck round bottom flask at 80°C in flowing N_2 . In a separate 100 mL 3-neck flask, 30 mL of EG was heated to 100°C in flowing N_2 . Approx. 40 mg of granular NaBH_4 were then added into hot EG and the mixture heated to ~150°C. The 80 °C RhCl_3 solution was then syringed into the 150 °C NaBH_4 solution. The resulting mixture instantly turned black colloidal and was refluxed for about 90 min. in flowing N_2 . The reaction was quenched on ice. Rh NPs colloids are stable for months without any precipitation.

5.7 nm Pt NPs. In a typical synthesis, 54.0 mg of PtCl_2 and 55.0 mg of PVP_{55000} in 40 ml of EG were refluxed for 1 h. To prepare the physical mixture, the monometallic colloidal suspensions of Pt and Rh NPs were mixed and stirred overnight.

3.3 nm and 3.9 nm Rh NPs. Typically, 20.3 mg of RhCl_3 were dissolved in 8 mL of Rh NP colloidal suspension (see Method 1 above) and diluted to 16 mL with EG. The mixture was heated to 80°C in flowing N_2 to fully dissolve the RhCl_3 . The mixture was then heated to 130°C and aged for 4.5 hours at 130±2°C. The reaction was quenched by immersing the flask in an ice bath yielding 3.3 nm Rh NPs. Larger 3.9 nm Rh NPs were synthesized as described above, except 41.0 mg of RhCl_3 were dissolved in 16 mL of EG, mixed with 8 mL of Rh colloidal suspension (Method 1) and the mixture was aged at 130±2°C for 4 hours.

2.2 nm PVP-free Rh NPs. 49.0 mg of $\text{Rh}(\text{NO}_3)_3 \cdot 2\text{H}_2\text{O}$ and 15.4 mg of $\text{Rh}_2(\text{CO})_4\text{Cl}_2$ were transferred into a 50 mL 2-neck round bottom flask in a dry box. The

precursor salts were dissolved in 22.5 mL of EG on a Schlenk line under positive N₂ pressure. The solution was slowly brought to a boil and aged over 90 min. with vigorous stirring. The reaction was quenched over ice. Some degree of aggregation/precipitation occurred after the reaction was quenched, but the colloidal suspension was restored with stirring.

2.2 nm PVP-free Pt NPs. 126.1 mg of H₂PtCl₆ were dissolved in 22 mL of EG. The yellow solution was slowly ramped to 130°C, aged for 90 min to give a give a black colloidal suspension. The colloidal suspension of Pt NPs was aged for an additional 30 min. at 180 °C and was then quenched in an ice bath. The colloids were not stable in suspension and precipitated after 2 h at room temperature.

3.2.4.1. Synthesis of Rh@Pt core/shell NPs with various core sizes and shell thicknesses

3.2 nm Rh@Pt NPs with 1 ML thick Pt shells. In a typical synthesis, 14.0 mg of PtCl₂ were dissolved in 10 mL of 2.7 nm Rh NP colloidal suspension and charged with an additional 10 mL of EG. The mixture was stirred at ~60°C to dissolve the PtCl₂. The solution was brought to 130°C with a temperature ramp of ~2°C/min and aged for 4 h. The reaction was quenched over ice. The Rh@Pt nanoparticle colloids were not stable in solution, and precipitated after 24 hours.

3.5 nm Rh@Pt NPs with 2 ML thick Pt shells. The same synthetic protocols were employed as the synthesis of 3.2 nm Rh@Pt NPs, with the exception that 28.1 mg PtCl₂ was used. The colloids were not stable in suspension and precipitated overnight.

5.1 nm Rh@Pt NPs with 2 ML thick Pt shells. In a typical reaction, 47.1 mg of PtCl₂ were dissolved in 10 mL of EG. 10 mL of 3.9 nm Rh NP colloidal suspension was then added under flowing N₂ atmosphere at room temperature. The mixture was heated to 80°C to ensure dissolution of the PtCl₂. The temperature was then ramped to 130 °C at a ramping rate of ~1 °C/min. The mixture was aged at 130±3°C for 4.5 hour and then quenched to room temperature in an ice bath.

4.4 nm Rh@Pt NPs with 1 ML thick Pt shells. 17.7 mg of PtCl₂ were dissolved in 10 mL of EG. 10 mL of 3.9 nm Rh NPs suspension were added. Finally, the mixture was ramped to 130°C with a heating rate of 1-2 °C/min and aged for 4 hours. The colloidal suspension was quenched in an ice bath.

4.3 nm Rh@Pt NPs with 2 ML thick Pt shells. 27.8 mg of PtCl₂ were dissolved in 10 mL of EG and 10 mL of 3.3 nm Rh NPs suspension were added as described above. Pt was deposited at 130°C. The colloidal suspension was quenched in an ice bath after 4 h. of aging.

2.7 nm PVP-free Rh@Pt NPs with ca. 1 ML thick Pt shells. The same procedures were used as described above, except the 2.2 nm PVP-free Rh colloids were used, the deposition temperature was 130°C, and the deposition time was 2 h. A slow temperature ramp of ~1 °C/min was employed for the Pt deposition. The PVP-free colloids were stable for only short periods of time and precipitate over 2 hours unless stirred.

3.2.4.2. Synthesis of PVP free Rh@Pt core/shell NPs

2.7 nm PVP-free Rh@Pt NPs with ca. 1 ML thick Pt shells. The same procedures were used as described above, except the 2.2 nm PVP-free Rh colloids were used, the deposition temperature was 130°C, and the deposition time was 2 h. A slow temperature ramp of ~1 °C/min was employed for the Pt deposition. The PVP-free colloids were stable for only short periods of time and precipitate over 2 hours unless stirred.

3.3 nm PVP-free Rh@Pt NPs with ca. 2 ML thick Pt shells. The same as the synthesis of 2.7 nm PVP-free Rh@Pt NPs, with the exception that 28.1 mg PtCl₂ was dissolved in EG and PVP-free Rh NPs suspension. The colloids were precipitated in 2 hours unless stirred.

3.2.4.3. Synthesis of Pt_xRh_{1-x} (x=0,1)

Pt₅₀Rh₅₀ alloy NPs. 40.0 mg of Pt(acac)₂ and 19.6 mg of Rh₂(CO)₄Cl₂ salts were dissolved in 20 mL of EG along with 55.0 mg of PVP₅₅₀₀₀. The temperature was ramped to a boil in less than 10 min. The solution turned black colloidal at about 170°C. The colloidal suspension was refluxed for about 2 h and quenched over ice.

3.2.5. Preparation of γ -Al₂O₃ supported catalysts

The catalysts were prepared by adding γ -Al₂O₃ to colloidal suspensions of nanoparticles, and drying the slurry under vacuum. Typically, 10 mL of Rh(~2.7 nm)@Pt (~1 ML) nanoparticle colloidal suspension and 973 mg γ -Al₂O₃ were mixed overnight

and vacuum dried at temperatures over 100°C while vigorously stirring the mixture. Such composition yielded a 1% by weight Pt alumina-supported catalyst. The catalyst was washed with acetone several times with an equi-volume mixture of acetone and ethanol, and then baked at 60°C overnight.

3.3. Results

3.3.1. Synthesis of Rh@Pt core/shell and Pt_xRh_{1-x} alloys NPs with or without PVP

In this study, monometallic NPs of Rh and Pt were prepared by modifications of known polyol methods.⁵⁸ The Rh NPs were used directly in catalytic evaluations and were also used as the core “seeds” in the preparation of Rh@Pt core-shell particles. Uniform 2.7 nm Rh NPs were prepared by reducing Rh(NO₃)₃·2H₂O in ethylene glycol in the presence of PVP stabilizers. Changing the temperature and / or the PVP : Rh ratio did not significantly affect the resulting NP sizes or size distributions. A second method for making 2.7 nm Rh NPs from RhCl₃ was also employed to make catalysts and seeds for subsequent growth studies. While both methods gave NPs that were structurally and spectroscopically identical, the RhCl₃ method produced superior catalysts. Chloride or other impurities were not detected by EDS in any of the Rh NPs. To prepare larger Rh NPs, a sequential growth method was employed in which additional Rh layers were deposited over preformed Rh seeds at temperatures that did not favor self-nucleation. The procedure is similar to that described by Somorjai and Tilley but with different precursors and less PVP.^{205,206} The less oxidizing RhCl₃ precursor was used for the

sequential growth step. By controlling the stoichiometry, uniform Rh NPs of 3.3 nm or 3.9 nm were prepared. Representative TEM images and particle size histograms are found in Figures 3.1.

Pt shells were deposited on the Rh seeds to generate Rh@Pt core-shell NPs by using a PtCl₂ precursor and similar seeded growth techniques.²⁰⁷ To achieve a desired shell thickness, the PtCl₂ concentrations were adjusted to accommodate the size of the Rh core particles. The stoichiometric ratios were calculated by employing a modified form of Schmid's Magic Number algorithm for icosahedral clusters and the density of the FCC metal (see Chapter 2, Table 2.1).^{92,110-112} The Pt shells were also deposited at under-nucleation temperatures to avoid self-nucleation of monometallic Pt NPs. Aging the colloidal solutions up to 3-4 hours was required to guarantee clear/colorless supernatants with no PtCl₂ deposits. Rh@Pt NPs were selectively prepared from 2.7, 3.3 and 3.9 nm Rh cores with ~1 and ~ 2 ML Pt shells. Representative TEM images and particle size histograms are found in Figures 3.1. The size evolutions of the core-shell particles are in agreement with the calculated shell thicknesses and thus agree well with expectations based on the Schmid model. While CO probe experiments show that the core Rh particles are completely encapsulated by the Pt shells (see below), the monolayer coverages described here will certainly have variations from particle-to-particle due to core size dispersity and are only intended to represent mean values. After Pt deposition, the colloids persisted for ca. 24 hours and then began to agglomerate and deposit on the bottom of the flask.

Pt_{1-x}Rh_x alloy NPs were prepared by co-reduction of Pt(acac)₂ and Rh₂(CO)₄Cl₂ in EG solutions with PVP stabilizers.^{204,208,209} It was empirically found that

these precursors gave the most homogeneous alloy structures and avoided monometallic particle contaminates and the graded alloy formation produced from other methods. TEM analysis shows 4.9 nm particles but show some shape anisotropy (see Figure 3.3).

PVP-free samples of Rh and Rh@Pt NPs were also prepared using different precursors and slightly different protocols. The resulting particles had mean sizes and size distributions similar the PVP analogs but the particles agglomerated (see Figure 3.2) and the colloids persisted for short time periods (*ca.* 1-2 hours) before deposition as expected.

The NPs described above have been fully characterized by a combination of TEM, single particle EDS, EDS line scans, XRD analysis, FT-IR and micro-Raman CO probe experiments and catalytic evaluation. These experiments are described below.

3.3.2. Size, shape and distribution by Transition Electron Microscopy

Rh NPs exhibit a mean particle diameter of 2.7 nm with narrow size distribution, as shown in Figure 3.1a and 3.1c. Particles are nano-crystalline, and show inter-planar spacing of 111 Rh (Figure 3.1b). Sequentially-grown Rh NPs with two times the molar Rh³⁺ monomer as the metallic Rh show 3.3 nm particle diameters in average (Figure 3.2a and 3.2c). Particles are nano-crystalline, and exhibit predominantly 111 Rh surfaces (Figure 3.2b). Similarly, Rh NPs which are sequentially grown from 2.7 nm Rh NP seeds and five times the elemental Rh as the metallic Rh in the colloidal suspension, are 3.9 nm in diameter in average, and expose mostly polycrystalline Rh surfaces (Figure 3.3).

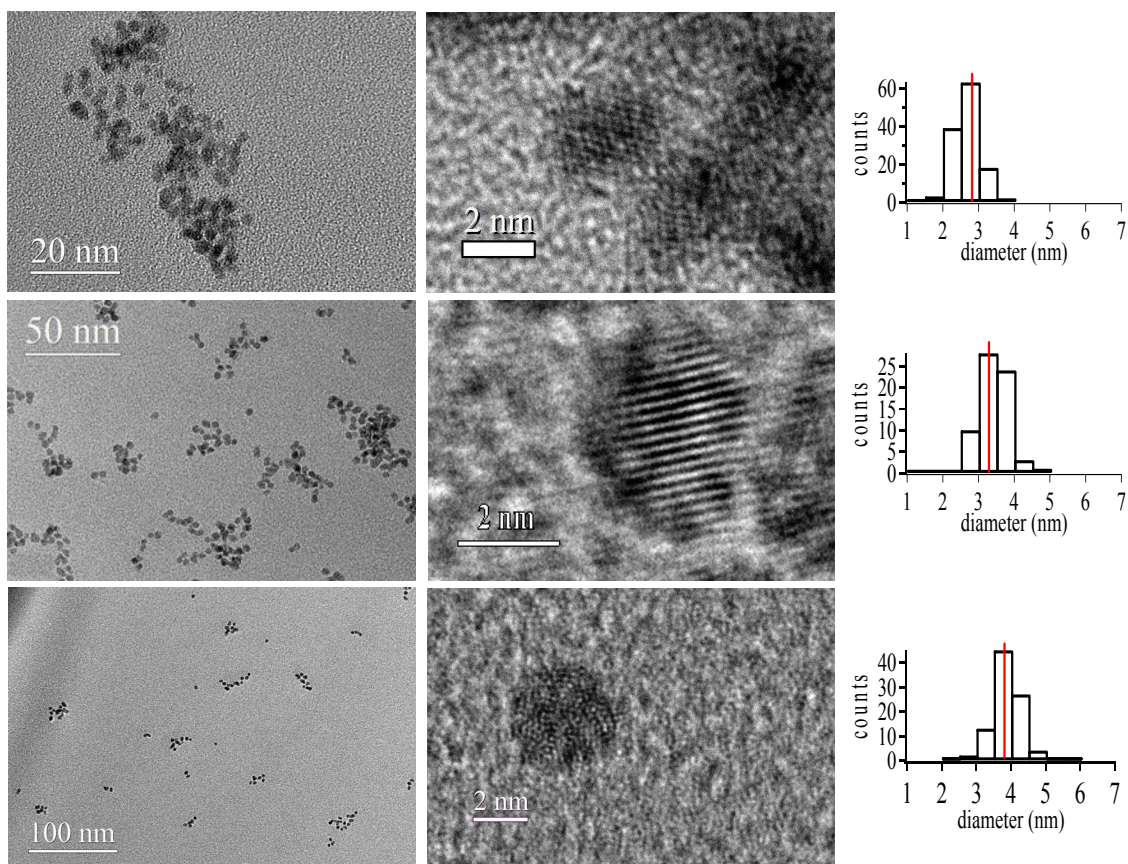


Figure 3.1. TEM images of (a) 2.7 nm Rh, (d) 3.3 nm sequentially-grown Rh, and (g) 3.9 nm sequentially-grown Rh particles. (b, e and h) HR-TEM images and (c, f and i) particle size histograms of the particles shown in (a, d and g), respectively.

Rh@Pt NPs with 2.7 nm Rh cores and equi-molar Pt and Rh exhibit a mean particle size of 3.2 nm, and thus have ca. 1 ML thick Pt shells, which is in accord with Schmid's model. Figure 3.2d shows 3.5 nm Rh@Pt particles with 2.7 nm Rh cores and ca. 1-2 MLs thick Pt shells. Nanocrystalline particles exhibit a broader size distribution than those with 1 ML thick Pt shells (Figure 3.2f), and are multiply twinned (Figure 3.2e). Rh@Pt NPs with 3.3 nm sequentially-grown Rh cores and Pt:Rh ratio of 4:3 are 4.3 nm in diameter in average (Figure 3.2g and 3.2i). Particles are predicted to have ca. 2 ML thick Pt shells based on Schmid's model. Moreover, particles are nano-crystalline

and exhibit multiple twinning (Figure 3.2h). Sequentially-grown 3.9 nm Rh NPs are employed to grow Pt shells of ca. 1 ML and ca. 2 ML thicknesses. Figures 3.2j and 3.2m show 4.4 nm and 5.1 nm Rh@Pt NPs, respectively, in order of increasing Pt:Rh ratio. Particles are multiply twinned. In addition, 5.1 nm Rh@Pt particles exhibits 111 twinning (Figure 3.2o).

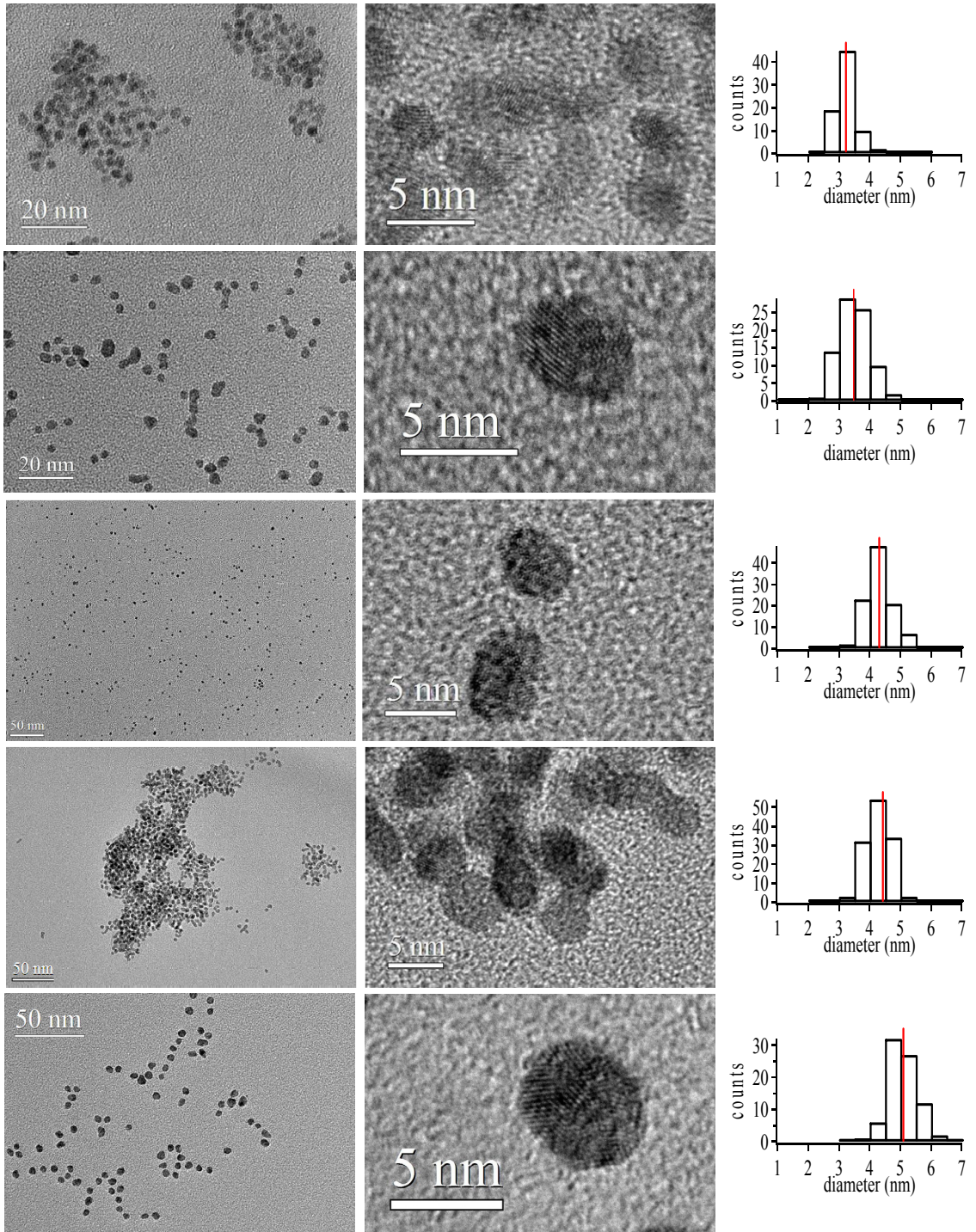


Figure 3.2. Representative TEM images of (a) 3.2 nm Rh@Pt NPs with 2.7 nm Rh cores and ca. 1 ML thick Pt shells, (d) 3.5 nm Rh@Pt NPs with 2.7 nm Rh cores and ca. 1-2 layers thick Pt shells, (g) 4.3 nm Rh@Pt NPs with 3.3 nm Rh cores and ca. 2 ML thick Pt shells, (j) 4.4 nm Rh@Pt NPs with 3.9 nm Rh cores and ca. 1 ML thick Pt shells and (m) 5.1 nm Rh@Pt NPs with 3.9 nm Rh cores and ca. 2 ML thick Pt shells. (b, e, h, k and n) HR-TEM images and (c, f, i, l and o) particle size histograms of the particles shown in (a, d, g, j and m), respectively.

Pt₅₀Rh₅₀ alloy NPs exhibits a mean particle diameter of 4.9 nm (Figure 3.3a and 3.3d). Nanoparticles are mostly spherical, but unisotropic particles with aspect ratios of 1-2 also exist. Relatively broad size distribution is apparent from Figure 3.3d, owing to shape unistropy and distribution. Figure 3.3b shows a Pt₅₀Rh₅₀ single-crystal and Figure 3.3c, its Fast Fourier Transform.

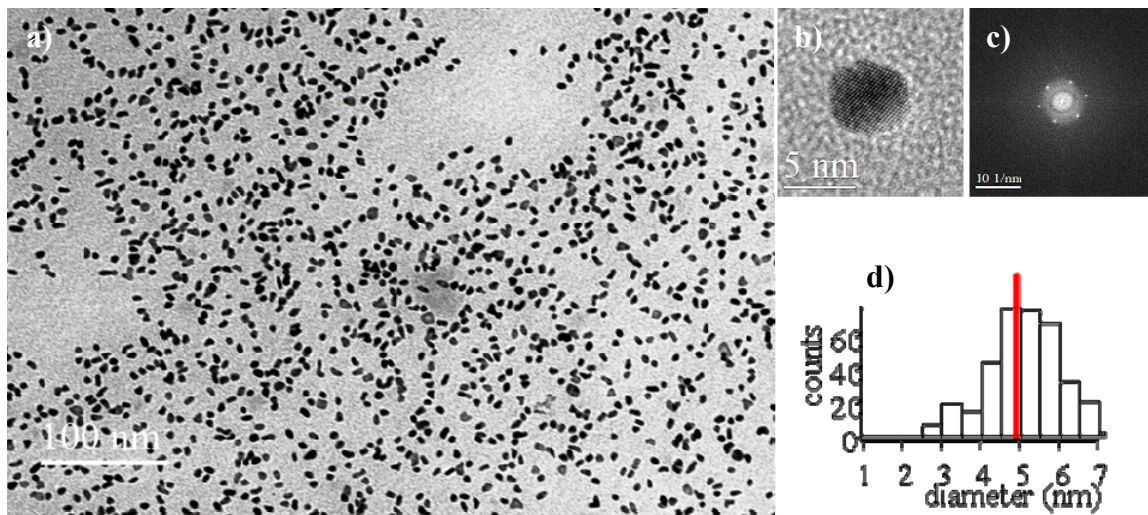


Figure 3.3. (a) TEM and (b) HR-TEM images, (c) FFT and (d) particle size histogram of Pt₅₀Rh₅₀ NPs.

PVP-free Rh NPs exhibits 2.2 nm particle diameters in average and thus smaller by ca. 1 ML than those synthesized in the presence of PVP according to Schmid's shell model (Figure 3.4a and 3.4c). PVP-free Rh@Pt NPs with Pt:Rh ratio of 1:1 show a mean particle size of 2.7 nm (3.4d and 3.4f) and those with 2:1 elemental ratio, 3.3 nm (Figures 3.4g and 3.4i). PVP-free particles are nano-crystalline, similar to their PVP-protected counterparts and therefore exhibit very narrow size distributions.

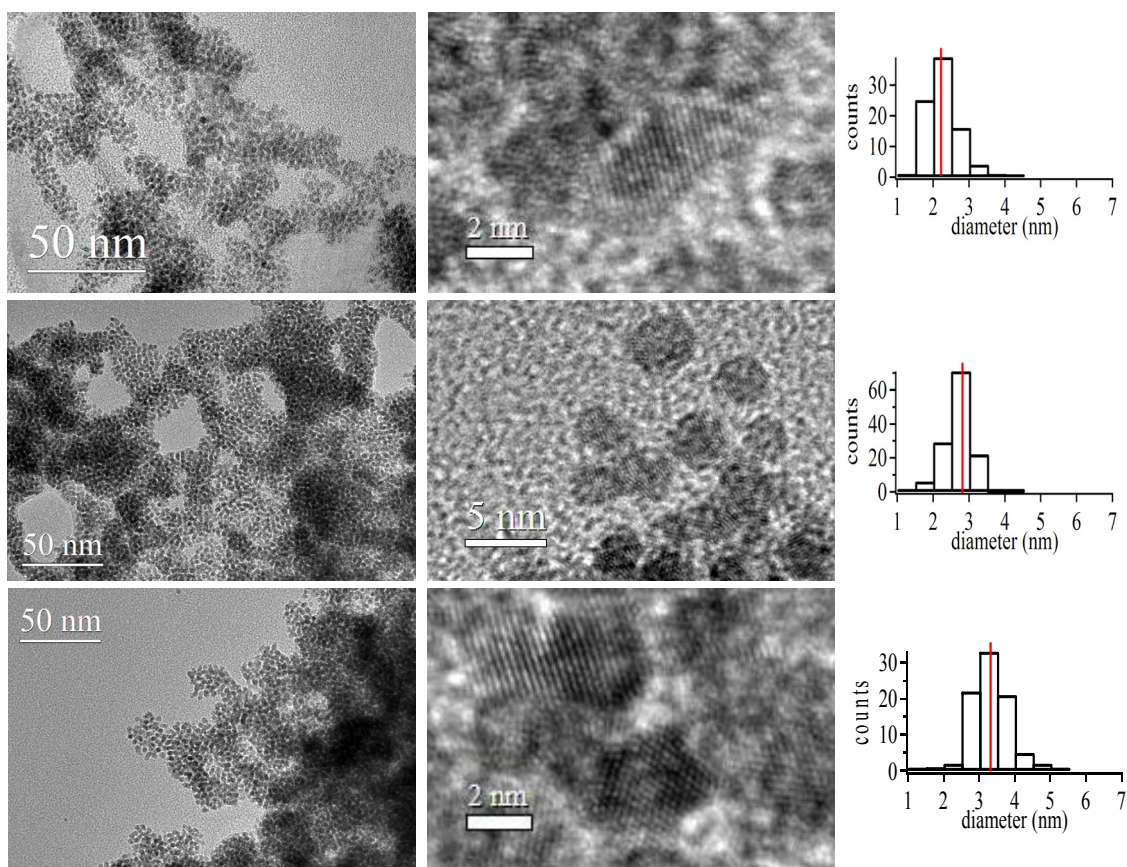


Figure 3.4. Representative TEM images of (a) 2.2 nm PVP-free Rh NPs, (d) PVP-free 2.7 nm Rh@Pt NPs comprising 2.2 nm Rh cores and ca. 1 ML thick Pt shells, and (g) PVP-free 3.3 nm Rh@Pt NPs comprising 2.2 nm Rh cores and ca. 2 ML thick Pt shells. High resolution images and particle size histograms of the particles in a, d and g are shown directly next to each figure.

3.3.3. Composition and architecture by Scanning Transition Electron

Microscopy

The composition and architecture (core-shell vs. alloy) of individual NPs were evaluated using a 1.5 nm EDS probe in a JEOL 2100 FE TEM operating in the STEM mode. Multiple single-particle EDS analysis of core-shell and alloy NPs from various syntheses confirmed that all particles are bimetallic in nature and stray monometallic particles were not observed in any of the samples. STEM-EDS line scans were recorded from 5.1 nm Rh@Pt NPs containing 2 ML Pt shells (Figure 3.5a). The data clearly show the Pt M line with a bimodal Pt distribution that reaches a maximum at the edge of the particle (*i.e.* the shell) whereas the Rh L line shows maximum Rh concentration at the center of the particle. STEM-EDS point spectra acquired from different regions of a distinct nanoparticle show the highest atomic % Pt at the edge with more atomic % Rh at the center (Figure 3.6), which is consistent with the EDS line scan. In contrast, the Pt₅₀Rh₅₀ alloy NPs show single Gaussian distributions of X-rays across the particle for both elements as expected from the random arrangement of atoms (Figure 3.5b). Definitive EDS line scan spectra could not be obtained for the 3-4.5 nm Rh@Pt NPs due to limitations of the 1.5 nm probe size. However, correlations of XRD and CO probe experiments (see below) show that the smaller core-shell particles have the same structure.

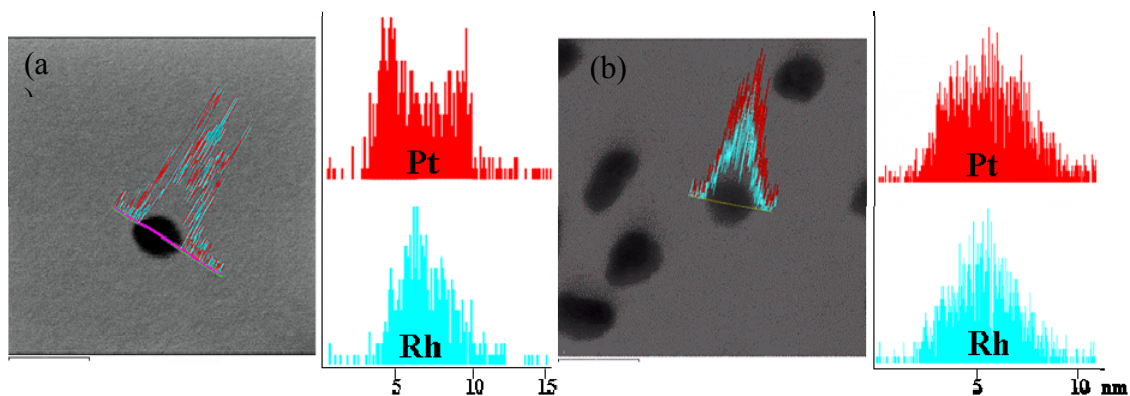


Figure 3.5. Representative STEM-EDS line spectra of (a) a 5.1 nm Rh@Pt NP with 3.9 nm Rh core and 2 ML Pt shell, and (b) a 5 nm Pt₅₀Rh₅₀ alloy nanoparticle. Relative atomic % composition (vertical axis) of Pt (red) and Rh (blue) are plotted against the line scan probe position (horizontal axis) and are given next to STEM images. A 1.5 nm probe was used to trace 10 - 15 nm scans across each particle. The particle center is at ~ 6.5 nm in (a) and ~ 5.5 nm in (b).

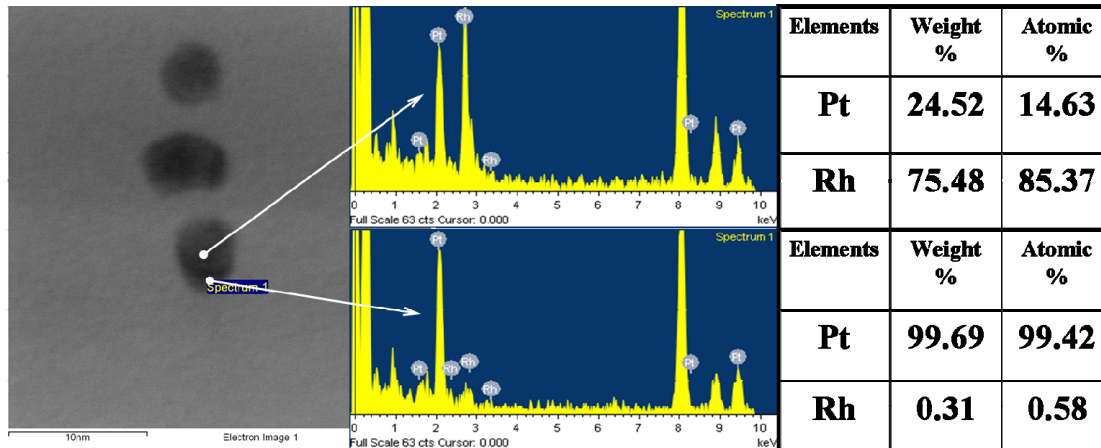


Figure 3.6. A representative STEM-EDS point analysis of a 5 nm Rh@Pt core/shell nanoparticle with ~2 ML thick Pt shells, showing two spectra: one from the center of the particle (top), and another from the edge (bottom).

3.3.4. Surface-adsorbed CO probing by FT-IR

To evaluate the surface structures of the various NPs, we employed CO-probe experiments^{93,123,124} as a qualitative tool to differentiate Pt from Rh on the surface of the particles. CO is a well-known and long-studied molecular probe, and is particularly convenient to monitor by FT-IR and micro-Raman spectroscopy. The core/shell architecture with only one type of surface atom can qualitatively be distinguished from other bimetallic architectures; namely, alloys and physical mixtures, which have both elements on the NP surface. CO saturated colloidal Rh suspensions give rise to two features in their FT-IR spectra. The strong broad peak at about 2030 cm^{-1} is assigned to CO in the atop position, and the lower intensity band at 1940 cm^{-1} to bridging CO on Rh (see Figure 3.7). PVP-free Rh NPs have the identical spectra (Figure 3.8). Sequentially-grown 3.3 nm Rh colloids exhibit a blue-shifted spectrum by $\sim 5\text{-}10 \text{ cm}^{-1}$ of the $\nu_{\text{atop}}(\text{CO})$ and $\nu_{\text{bridge}}(\text{CO})$ compared to that of the parent Rh NP colloids. Furthermore, sequentially-grown 3.9 nm Rh NP colloids show similar blue-shifts in their CO-probed IR spectrum. Additionally, a distinct $\nu_{\text{bridge}}(\text{CO})$ peak at lower wavenumbers than that on the parent Rh NP colloids is apparent. Gem dicarbonyl modes were not observed in colloidal 2.7 nm Rh particles.²¹⁰⁻²¹² As the Rh cores increased in size, gem carbonyls with symmetrical stretch at 2000 cm^{-1} and asymmetrical stretch at 2080 cm^{-1} became detectable. For 3.9 nm Rh NP colloids, both modes of gem carbonyls are prominent in the spectrum, as shown in Figure 3.9a.

The CO-probe technique has been used to spectroscopically monitor the formation of the Pt shell in the synthesis of the Rh@Pt NPs. The colloidal solutions were sampled at various times in the reaction, saturated with CO and evaluated by FT-IR

(Figure 3.7a). The $\nu(\text{CO})$ bands associated with the Rh NPs decrease in intensity as the terminal and bridging CO bands associated with CO sorbed to Pt surfaces emerge. After 4 hours of reaction, CO bands associated with exposed Rh surfaces have disappeared and only Pt-CO modes are observed. Assuming that the incomplete Pt shell exists as small islands on the Rh core at short reaction times, the FT-IR data suggest that the sorbed CO on the two surfaces are not strongly coupled and give rise to separate $\nu(\text{CO})$ modes. This observation is in contrast to spectra for the $\text{Pt}_{50}\text{Rh}_{50}$ alloy NP colloids that show a single, atop $\nu(\text{CO})$ peak that is intermediate to those on monometallic Pt and Rh (Figure 3.7b). Importantly, the core-shell architecture is conveniently distinguished from both the alloy and monometallic rhodium phases by FT-IR CO probe experiments.

As the Rh cores increase in size and / or thicker Pt shells are deposited, the Rh@Pt atop mode is blue shifted from 2061 to 2075 cm^{-1} (Figure 3.9b) but is always distinct from the alloy atop $\nu(\text{CO})$ mode, which appears at 2055-2058 cm^{-1} . As such, the IR experiments provide a connection between small particles, for which TEM line scans are not possible, and the larger particles where line scans clearly distinguish the core-shell architecture from the alloy. The blue shift of the atop mode may be due to differential faceting of the Pt shell as the particles become larger or lateral effects associated with altered equilibrium CO coverages. Interestingly, the FT-IR spectra for the PVP-free Rh@Pt core-shell NPs are virtually identical to those of PVP protected particles (Figure 3.8) suggesting that PVP does not significantly affect the equilibrium CO coverage or the electronic structure of the surface.

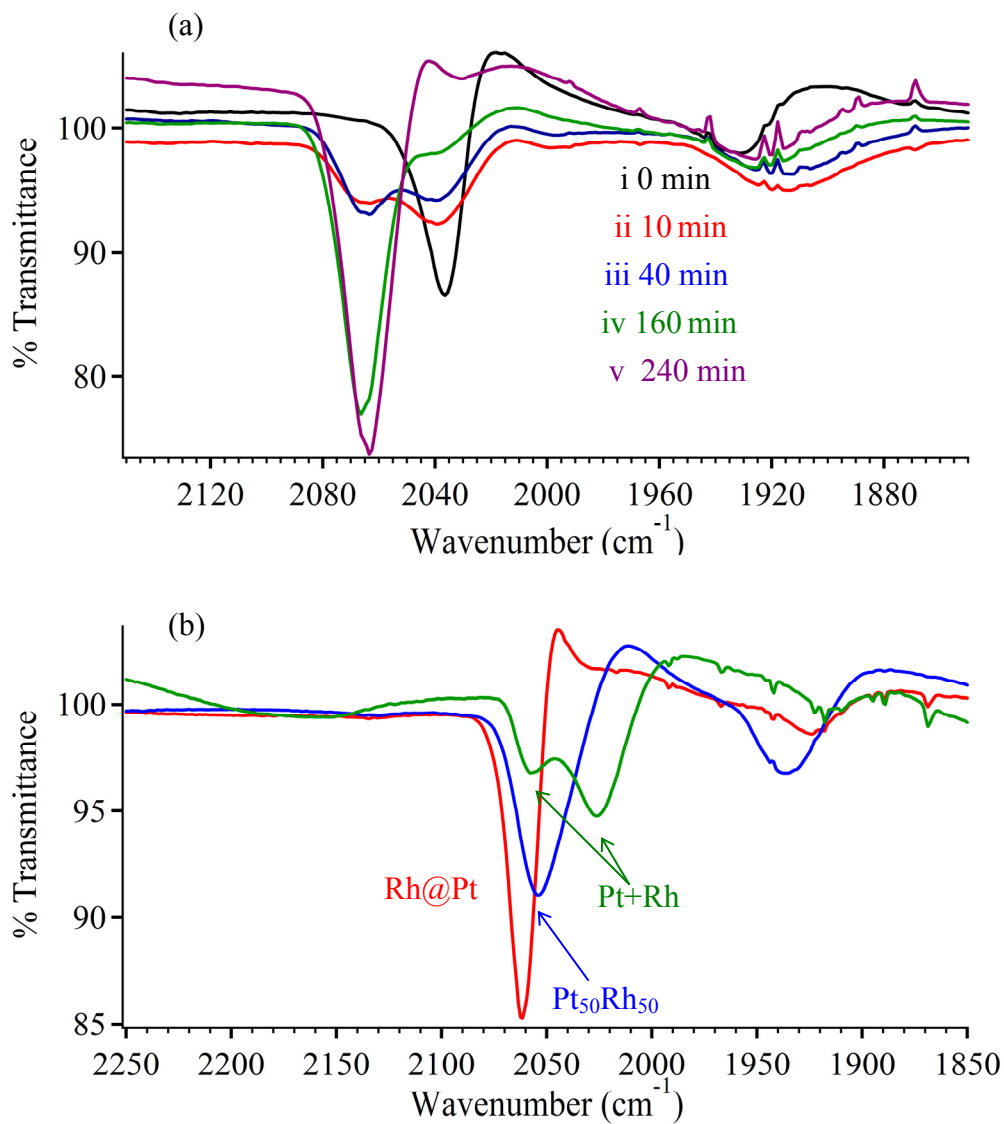


Figure 3.7. (a) The *ex-situ* FT-IR spectra of CO-saturated colloidal suspensions sampled as a function of time during the synthesis of the Rh@Pt NPs. The stacked plots show (i) parent Rh core NPs at 0 min, (ii) Rh@Pt NPs in 10th min, (iii) in 40th min, (iv) in 160th min, (v) and 240th min. (b) FT-IR spectra of CO saturated colloidal suspensions comparing core-shell (red), 50:50 alloy (blue) and a mixture of monometallic Rh and Pt nanoparticles (green).

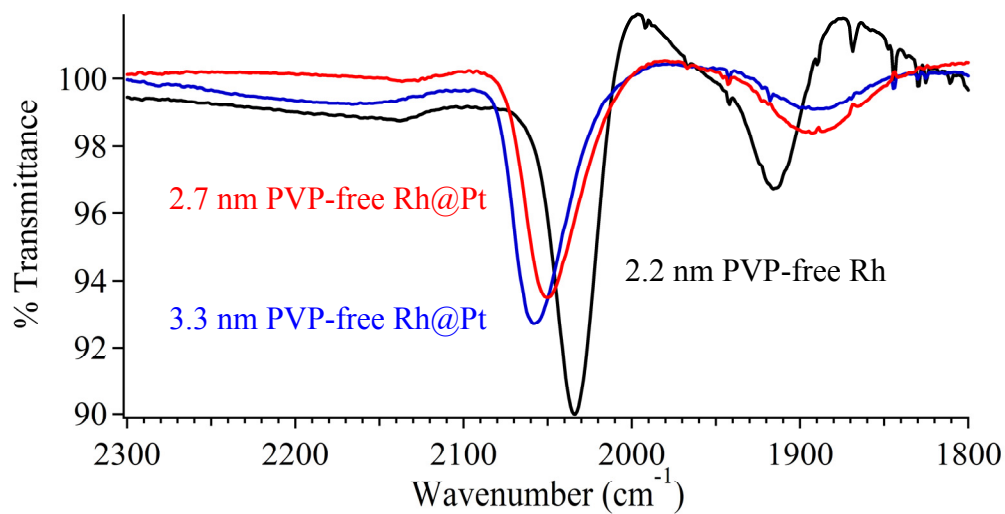


Figure 3.8. FT-IR spectra of CO-saturated colloids of PVP-free Rh NPs, PVP-free Rh@Pt NPs with ca. 1 ML thick Pt shells and PVP-free Rh@Pt NPs with ca. ca. 2 ML thick Pt shells.

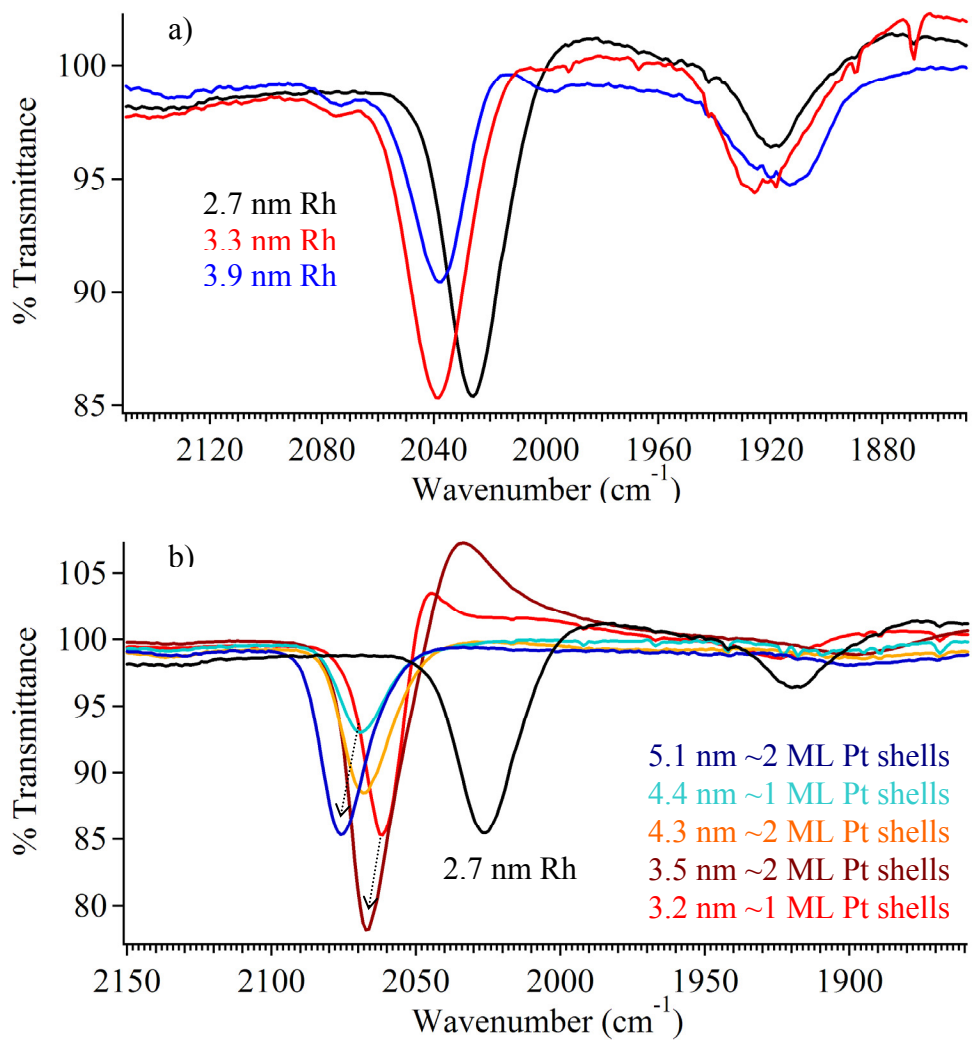


Figure 3.9. FT-IR spectra of CO-saturated colloids of (a) Rh NPs of different sizes and (b) Rh@Pt NPs comprising different core sizes and shell thicknesses.

3.3.5. Micro Raman for surface probing

Micro-Raman spectra of Rh@Pt, Rh and Pt NPs saturated with CO are shown in Figure 3.10. Raman analyses of PVP-coated NPs were not extensively studied due to the formation of PVP-derived graphite-like deposits³⁷ that diminish CO signal intensities and obscure the M-C regions of the spectrum. The Raman data described below were collected from PVP-free samples under flowing CO atmospheres. Maximum peak intensities were observed with 2.5 : 1 air-to-CO gas mixtures but the peak positions were the same in pure CO. Peaks in both regions of the spectrum disappeared when the CO atmospheres were removed. Monometallic Pt NPs give rise to two peaks; namely, a sharp peak at 2095 cm⁻¹ assigned to $\nu(\text{CO})$ on atop Pt sites, and a broader 480 cm⁻¹ peak due to the $\nu(\text{Pt-C})$ mode (Figure 3.10). Similarly, Rh NPs give rise to two $\nu(\text{CO})$ features at 2060 cm⁻¹ and ~1920 cm⁻¹ for linear atop CO and bridging CO, respectively. In addition, a very broad 440 cm⁻¹ peak for the $\nu(\text{Rh-C})$ mode is present. The Rh@Pt core-shell NPs yield features that are characteristics of Pt surfaces; namely, broadened peaks at 2090 cm⁻¹ and 480 cm⁻¹, which are assigned to linear $\nu(\text{CO})$ and $\nu(\text{M-C})$ bands, respectively, and may be indicative of electronically altered Pt surfaces.

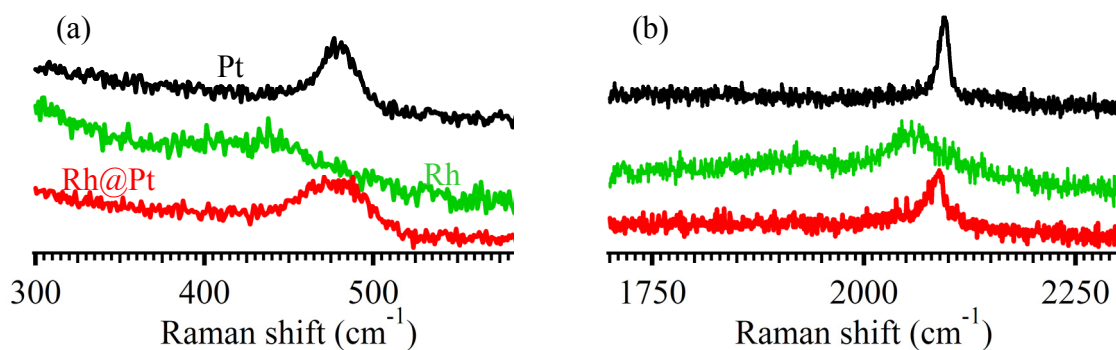


Figure 3.10. 633 nm micro-Raman spectra of CO-saturated PVP-free NPs showing (a) the $\nu(\text{M-C})$ region ($\text{M} = \text{Pt}, \text{Rh}$), and (b) the $\nu(\text{CO})$ region. The data were recorded for 2.2 nm Pt NPs (black), 2.2 nm Rh NPs (green), and 2.7 nm Rh@Pt NPs (red) in 2.5 : 1 air-to-CO gas mixtures.

3.3.6. Structure by XRD

Powder X-ray diffraction analysis (XRD) coupled with Debye Function (DF) simulations provides an effective means of differentiating alloys from core-shell NPs and for monitoring shell growth in multilayer particles. Powder diffraction profiles of as-made 2.7 nm Rh NPs exhibit strong broad 111 reflections centered *ca.* 41° (Figure 3.11a). The 200 reflection and other high angle peaks are weak, but metallic Rh is evident. Figure 3.11a shows that crystallinity increases with increasing size of the Rh NPs, however the peaks remain broad and denote disorder. The core-shell and alloy NPs of identical composition and similar size are easily differentiated by their XRD patterns (Figure 3.11b).

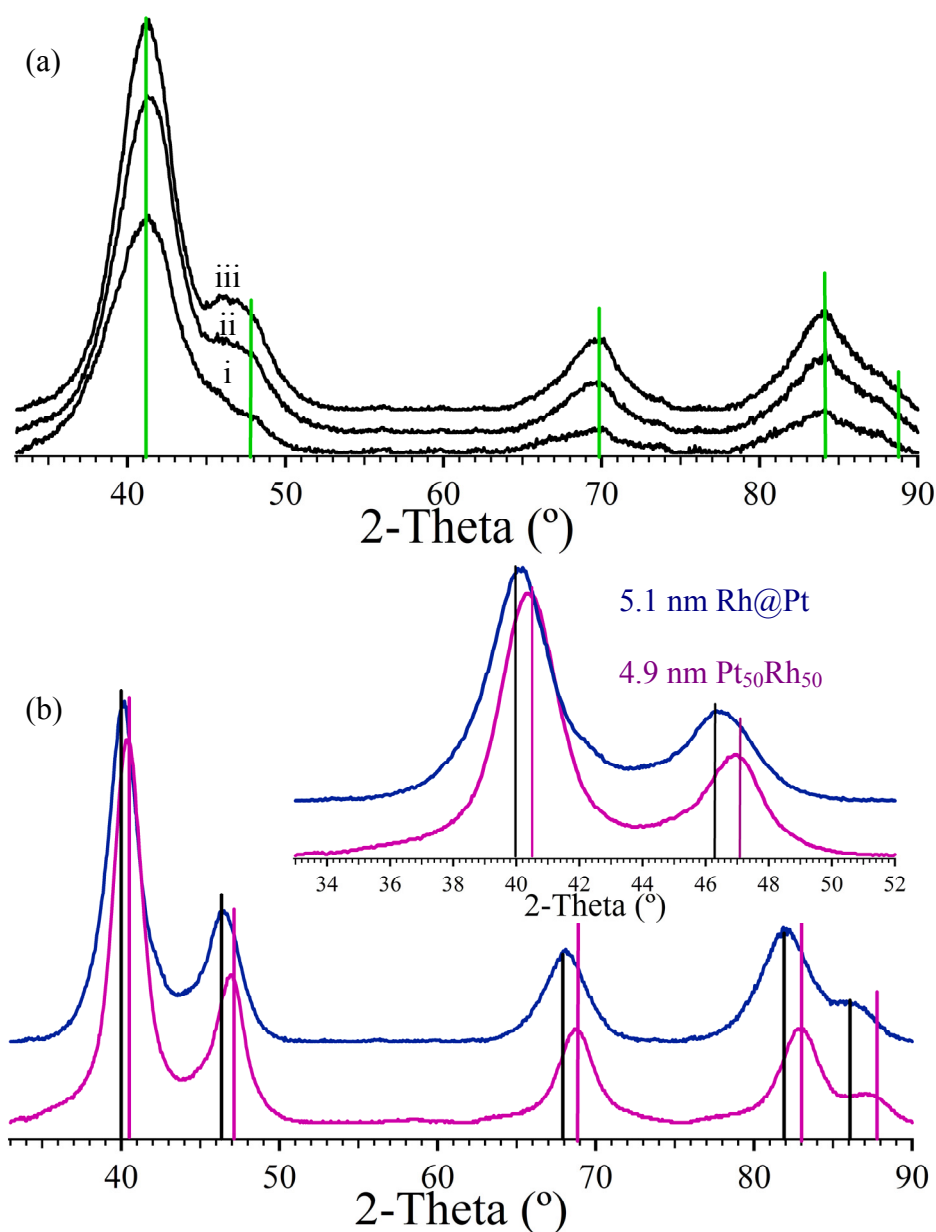


Figure 3.11. XRD profiles comparing (a) Rh NPs via polyol reduction of $\text{Rh}(\text{NO}_3)_3 \cdot 2\text{H}_2\text{O}$ to give, (i) 2.7 nm as-synthesized Rh NPs, (ii) 3.3 nm Rh NPs and (iii) 3.9 nm Rh NPs grown from sequential deposition. (b) XRD profiles of Rh@Pt core-shell (blue pattern) and Pt₅₀Rh₅₀ alloy (purple pattern) NPs of similar particle diameters. The inset shows an enlargement of the 111 and 200 reflections. JC-PDS lines for Pt (black), Rh (green), and Pt₅₀Rh₅₀ alloy (purple) are also shown.

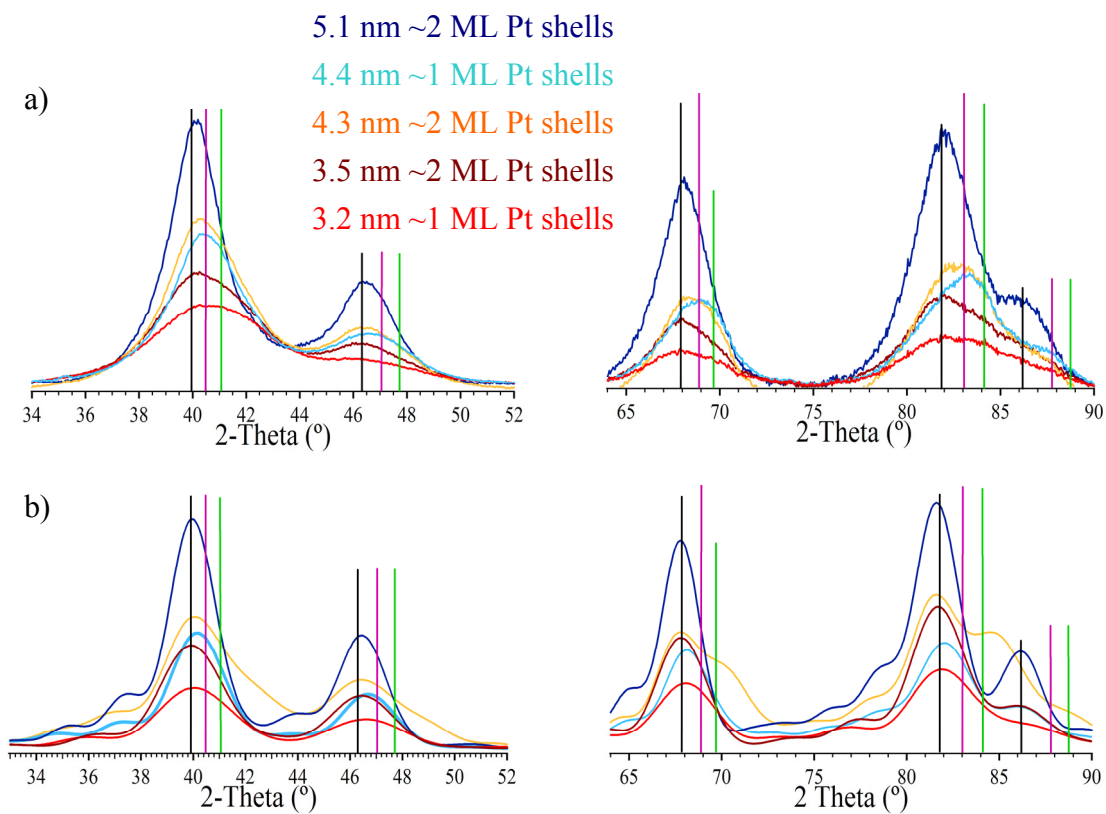


Figure 3.12. (a) XRD profiles and (b) DF simulations of Rh@Pt NPs of various core diameters and shell thicknesses. Red - 2.7 nm Rh core, 1 ML Pt shell; Reddish brown – 2.7 nm Rh core, 2 ML thick Pt shell; Light blue – 3.9 nm Rh core, 1 ML Pt shell; Orange – 3.3 nm Rh core, 2 ML Pt shell; Dark blue – 3.9 nm Rh core, 2 ML Pt shell. JC-PDS peak positions for Pt (black), 1:1 RhPt alloy (purple) and Rh (green) are also presented.

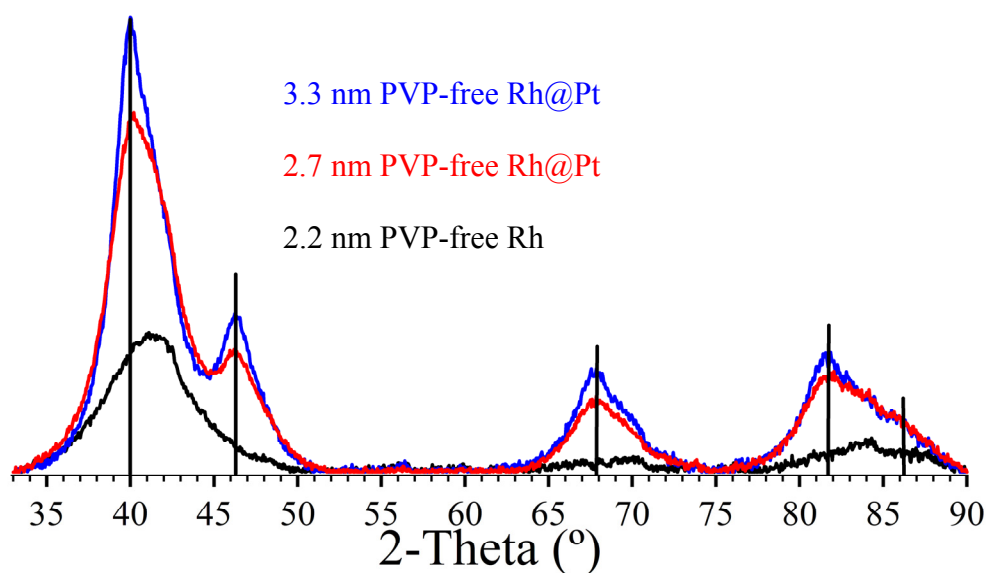


Figure 3.13. XRD profiles of PVP-free 2.2 nm Rh particles and PVP-free Rh@Pt NPs comprising 2.2 nm Rh cores and various shell thicknesses.

XRD analyses of core-shell particles are hindered by similarities of the FCC unit cells of the two metals (Pt, $a = 3.916 \text{ \AA}$; Rh, $a = 3.814 \text{ \AA}$). However, discernible shifts in peak positions in both experimental and simulated diffraction patterns provide non-intuitive insight into the diffraction behavior of core-shell bimetallic NP structures. In particular, that data show that (1) the diffraction patterns are dominated by the thin (1-3 ML) Pt shells, (2) shifts in the XRD profiles can be accurately described through DF modeling and (3) DF / XRD analysis can be used to evaluate changes in shell thicknesses in particles having the same core size. These findings are described below.

The Rh@Pt NPs all show a single 111 FCC peak centered at *ca.* 40° for which distinct Pt and Rh phases cannot be discerned due to the inherent broadness of the diffraction patterns (Figure 3.12a). While the peak positions of the Rh@Pt core-shell particles are dominated by Pt diffraction, the peaks shift towards Rh peak positions as the

mass % Rh increases. For example, as the Rh cores become larger with Pt shells of the same size, the diffraction peaks shift towards those of bulk Rh. Likewise, as the Pt shell thickness is increased on Rh cores of the same size, the diffraction peaks shift further toward those of bulk Pt. In certain cases, such as the 4.4 nm Rh@Pt NPs comprising 3.9 nm Rh cores and 1 ML thick Pt shells, the XRD patterns approach the peak positions of the bulk Pt₅₀Rh₅₀ alloy phase (see light blue profile in Figure 3.12a). However, this shift does not result from Pt₅₀Rh₅₀ alloy formation but instead is a consequence of mass averaged diffraction effects associated with the core-shell structure. The IR CO-probe data for these 4.4 nm Rh@Pt particles clearly shows a pure Pt surface and are inconsistent with alloy formation (see Figure 3.9). To further illustrate this point, Debye Function (DF) simulations were performed of model core-shell systems generated from idealized spherical particles of FCC metals with the desired core and shell configurations.²¹³⁻²¹⁵ Details of the models are given in the experimental. The simulated powder diffraction patterns were calculated from non-distorted model particles using the Debye function in the DISCUS software package.¹ The simulations are shown in Figure 3.12b and qualitatively show systematic peak shifts toward higher angles as the core size increases and/or the shell thickness decreases. For example, two Rh@Pt NPs with 3.9 nm Rh cores are shown in Figure 3.12. Those particles with 2ML Pt shells (dark blue) show diffraction peaks that are almost perfectly aligned with bulk Pt whereas those with 1ML Pt shells (light blue) are noticeably shifted toward Rh peak positions in both the simulated and observed XRD patterns. The *quantitative* differences in peak positions most likely result from lattice distortions (primarily in the shell) associated with the pseudo-epitaxial growth of thin Pt shells on the particle cores.

As in other core-shell and alloy NP systems, multiple analytical methods are required to fully characterize and differentiate the different architectural configurations. While STEM-EDS line scans shown in Figure 3.5 clearly differentiate the 5.1 nm Rh@Pt core-shell NPs from the 4.9 nm Pt₅₀Rh₅₀ alloy NPs, the smaller catalytically relevant NPs cannot be evaluated through line scans due to limitations of the probe size. However, the micro Raman data and comparisons of IR-CO probe experiments and XRD data show that the small particles have the same core-shell architectures as the larger particles evaluated in Figure 3.11. Moreover, the activities of the core-shell and alloy particles are distinguished in the catalytic evaluations described below.

3.3.7. Catalytic Evaluation of supported Pt/Rh bimetallic catalysts in PROX/CO oxidation

To compare and contrast the activity of the core-shell NPs with that of the alloys and monometallic NPs, we evaluated the PROX reaction (preferential oxidation of CO in H₂) using H₂ feeds contaminated by 0.2% CO by volume, along with 0.5% O₂. The Pt-Rh catalysts were supported on γ -Al₂O₃ and each were loaded with 1.0 wt. % Pt and equimolar Pt:Rh ratios. The reactions were conducted in a fixed-bed, flow-through reactor, and catalytic activity was monitored by way of temperature programmed reactions (TPR) measuring the evolution of H₂O and CO₂. The results are shown in Figure 3.13. The maximum CO₂ formation (100 % in Figure 3.13) is based on the 0.2% inlet CO concentration. The maximum H₂O formation was calculated from the limiting reactant O₂, so that 100% H₂O formation would result in conversion of all O₂ to water.

Using the gas mixtures described above, complete conversion of CO to CO₂ followed by hydrogen oxidation with the remaining O₂ would result in an 80% H₂O formation.

The TPR data for the core-shell Rh@Pt NPs with ca. 1 ML thick Pt shells, Pt₅₀Rh₅₀ alloy NPs and monometallic mixtures of Pt and Rh NPs are shown in Figure 3.13. In general, CO oxidation significantly precedes H₂ oxidation for the core-shell and alloy catalysts, which gives rise to high PROX selectivities at relatively low temperatures. For the 4 different batches of Rh@Pt catalysts, the temperature for complete CO conversion varied from 60 °C to 90 °C with H₂ light-off varying from 35 °C and 60 °C (see Figure 3.14). In contrast, CO and H₂ oxidation occur almost simultaneously for the monometallic mixture, which gives very poor PROX selectivities along with low activities. For reference, our pure Pt NP catalysts under these conditions show CO and H₂ oxidation onsets (light-off) at 155-160°C and 175-180 °C, respectively, which is consistent with literature reports.³⁵ While the monometallic mixture of Rh + Pt shows somewhat better PROX activity (160 °C complete CO oxidation) than that of pure Pt (190 °C complete CO oxidation), it is far less active than the Pt₅₀Rh₅₀ alloy (105 °C complete CO oxidation) or Rh@Pt core-shell (70 °C complete CO oxidation) catalysts under identical conditions and loadings (Figure 3.13). In particular, the best Rh@Pt core-shell NP catalyst shows complete CO oxidation by 40 °C and a subsequent H₂ oxidation that is complete by 80 °C with exceedingly high PROX selectivity at room temperature (see Figure 3.14). However, a representative catalyst with activity that is intermediate in the 4 independent batches tested is shown in Figure 3.14 for comparison.

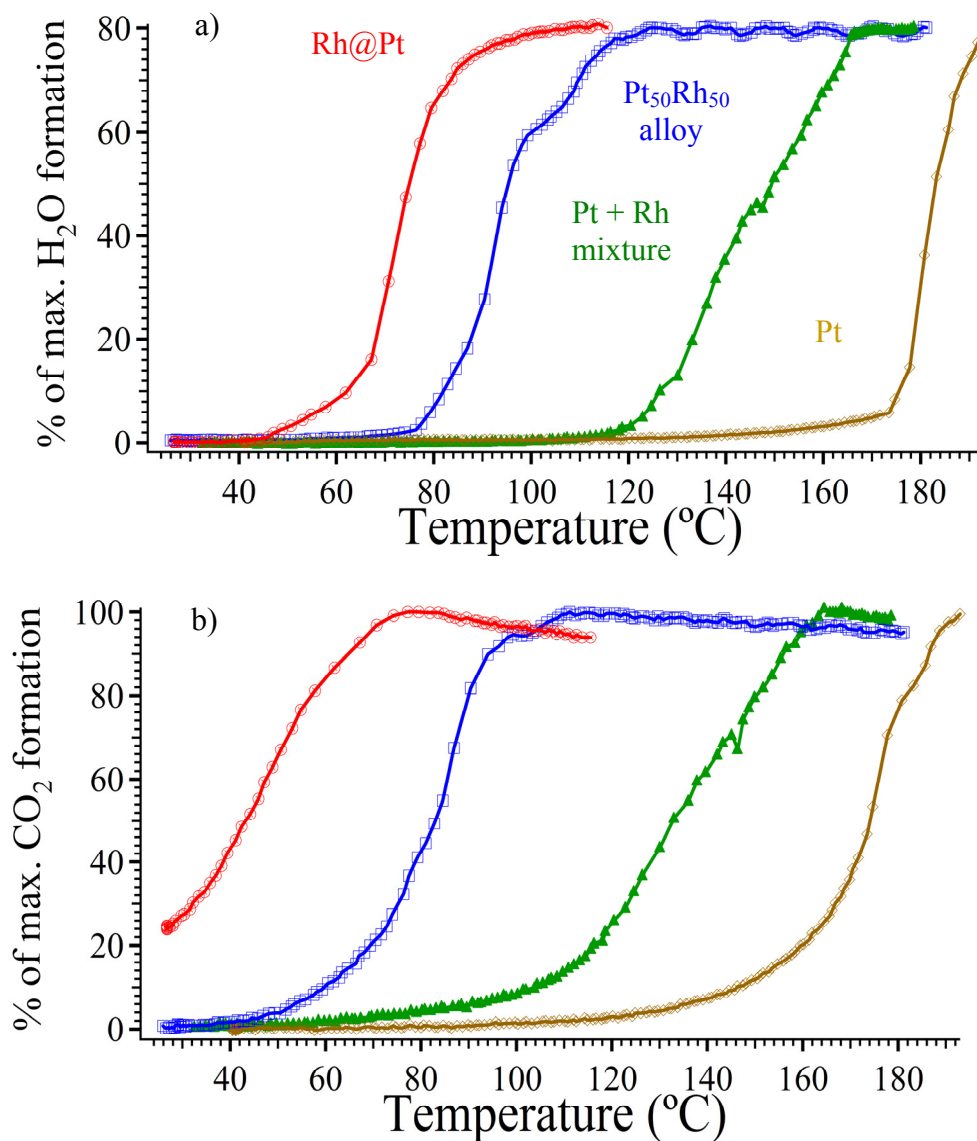


Figure 3.14. TPR plots showing (a) H₂O formation, and (b) CO₂ formation for monometallic Pt NPs, monometallic mixtures of Pt NPs and 2.7 nm Rh particles, 4.9 nm Pt₅₀Rh₅₀ alloy NPs and 3.2 nm Rh@Pt NPs for H₂ streams contaminated with 2000 ppm CO. Percent of maximum H₂O formation was calculated from the limiting reactant, O₂, and % of maximum CO₂ formation is relative to the CO inlet concentration. See the text for details.

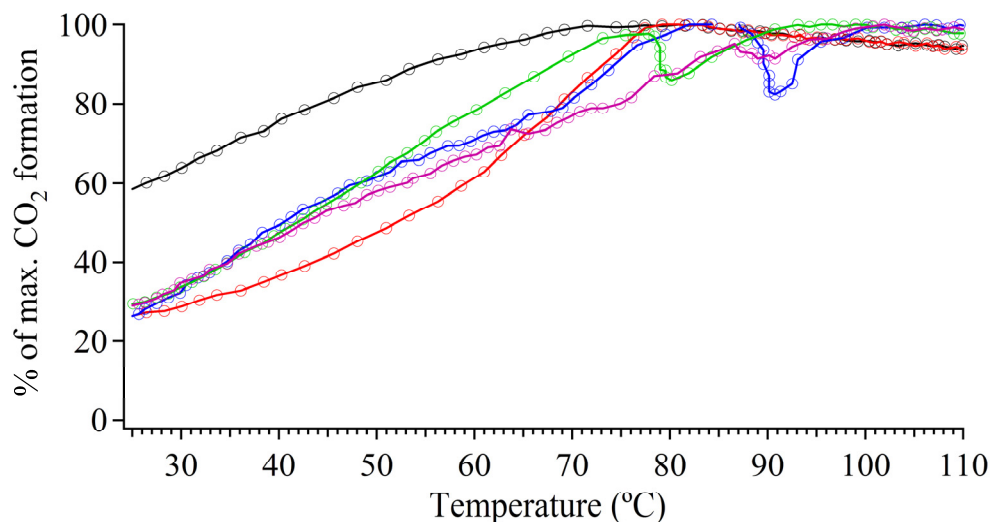


Figure 3.15. TPR plots showing CO₂ formation for 5 different supported catalysts from 4 different Rh@Pt NPs batches of colloids. The blue and green catalysts were prepared from the same colloid preparation. The red plot is the one presented in Figure 3.7 of the text.

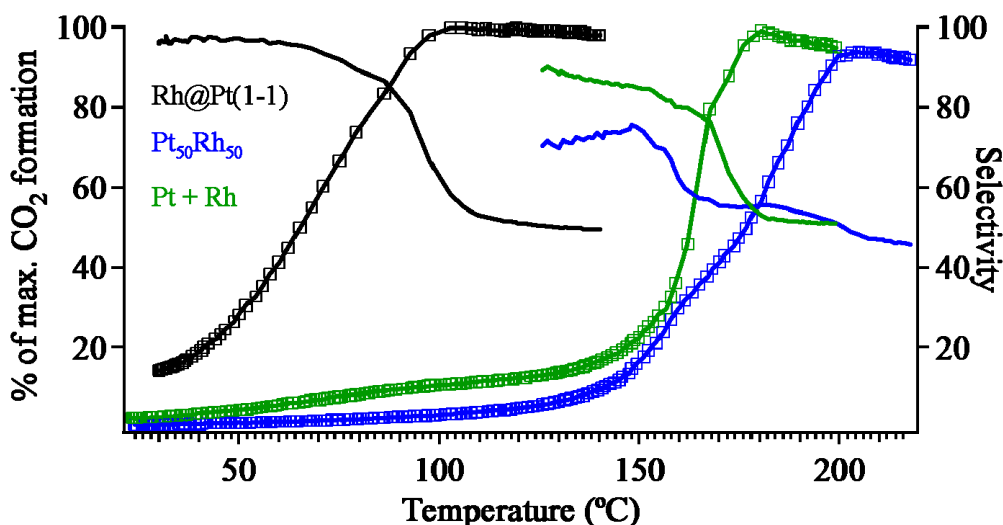


Figure 3.16. TPR plots showing % maximum CO₂ formation (connected dots) in PROX reactions for the three different Rh-Pt catalysts described in the text. The PROX feed is composed of 1% CO, 1% O₂, 50% H₂ and an Ar balance. The solid lines denote the corresponding PROX selectivity, defined as $[\chi_{\text{CO}_2}/(\chi_{\text{CO}_2} + \chi_{\text{H}_2\text{O}})] \times 100$ where χ_{CO_2} is the fraction of O₂ used to convert CO to CO₂ and $\chi_{\text{H}_2\text{O}}$ is the fraction of O₂ used to convert H₂ to H₂O. CO₂ and H₂O were used to calculate selectivities due to their superior sensitivity to mass spectrometric detection relative to O₂ and CO.

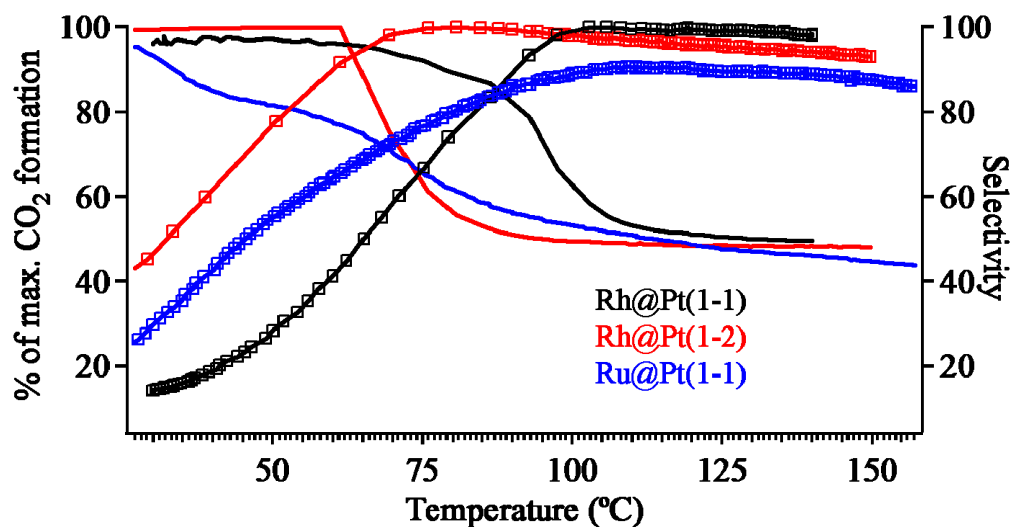


Figure 3.17. TPR plots showing % CO₂ conversions (connected dots) in PROX reactions for the three Rh@Pt and Ru@Pt catalysts described in the text. The PROX feed is composed of 1% CO, 1% O₂, 50% H₂ and an Ar balance. The solid lines denote the corresponding PROX selectivity, defined as $[\chi_{\text{CO}_2}/(\chi_{\text{CO}_2} + \chi_{\text{H}_2\text{O}})] \times 100$ where χ_{CO_2} is the fraction of O₂ used to convert CO to CO₂ and $\chi_{\text{H}_2\text{O}}$ is the fraction of O₂ used to convert H₂ to H₂O. CO₂ and H₂O were used to calculate selectivities due to their superior sensitivity to mass spectrometric detection relative to O₂ and CO.

3.4. Discussion

Through the use of various precursors and protocols, PtRh bimetallic nanoparticles with different architectures (*i.e.* core-shell, alloy and mixtures of monometallic NP) can be prepared selectively. Combinations of analytical techniques are required to identify and characterize the different configurations; especially for small bimetallics where EDS line scans are not feasible. The complete architectural series of Rh and Pt bimetallic NPs represents the third such complete series along with the PtAu^{95,98} and PtRu¹⁷⁶ systems. While the sizes, compositions and projected surface areas of the NPs within these three series are quite similar, the catalytic activities are markedly different. For both the PtRu and PtRh bimetallic systems, the core-shell particles were most active for PROX, followed by the alloys, the mixture of monometallic NPs and finally the pure Pt NPs. The enhancements in activities are directly related to the changes in architectural configurations, which either alter the electronic structures of the surface metals and / or facilitate alternate reaction mechanisms relative to pure Pt. However, the changes in activities for the different Rh-Pt architectures are less dramatic than the Ru-Pt systems¹⁷⁶ but the PROX selectivities are better (see Table 3.1). Mavrikakis has shown^{8,9} that core-shell particles containing Pt shells on Rh and Ru cores have lower equilibrium CO coverages and lower Pt-H bond enthalpies relative to pure Pt, which explains the enhancements in CO and H₂ oxidation kinetics. These differences in substrate binding are correlated with shifts in the Pt d-band center due to charge transfer between the Pt shell and the core metals. The situation is directly analogous to the thin film studies of Goodman and Campbell¹²⁷⁻¹²⁹ in which electron transfer between metal overlayers and their metallic hosts altered the metal-metal interactions and surface

electronic structures. The authors noted that the electronic charge transfer in the overlayer structures differed from that in the bulk alloys, suggesting that the Rh-Pt electronic interactions in Rh@Pt NPs and RhPt alloy NPs may also be different. In addition to possible difference in electronic structure, the alloy NPs also have two types of surface atoms and can therefore promote alternate mechanisms of reaction in which different atoms catalyze different steps (*e.g.* the bifunctional mechanism).^{48,216}

A comparison of the PROX activities and selectivities for a 1% CO, 1% O₂ and 50% H₂ feed of the different Rh-Pt catalysts and the Ru@Pt catalyst¹¹ is given in Table 3.1 and Figure 3.17. While the activities of the Rh@Pt NPs towards PROX are better than the RhPt alloy, the differences are not as dramatic as the Ru/Pt system.¹¹ Although it is clear that the Pt-Rh bimetallic particles have a clear synergistic effect for PROX activity, the enhancement of the core-shell structure is far less pronounced in the present case. However, the presence of room temperature CO oxidation in all of the Rh@Pt systems tested and the lack of such activity for the alloys clearly demarcates the differences in the architectures.

Table 3.1. Comparative PROX selectivities^a for the different Rh-Pt and the Ru@Pt core/shell^b catalysts.

1% CO 1% O ₂	T _{50±5} (O ₂) ^c °C	Selectivity ^d @T _{50±5}	T _{50±5} (CO) ^e °C	Selectivity ^d @T _{50±5}	T _{comp±0.1} (O ₂) ^f °C	Selectivity ^d @T _{comp±1}
Ru@Pt (1:1)	66±4	74±3	51±5	81±1	178±3	40.4±0.4
Rh@Pt (1:1)	79±4	90±3	68±2	94±2	136±1	49.7±0.1
Rh@Pt (1:2)	44±6	99.8±0.1	39±10	99.6±0.2	122±1	48.6±0.1
Pt + Rh	163	76	163	76	192±7	47.0±0.5
Pt ₅₀ Rh ₅₀	174±6	55.2±0.4	172±4	55.8±0.6	215±3	46.2±0.3

^a PROX feed is composed of 1% CO, 1% O₂, 50% H₂ and an Ar balance. ^b See Chapter 1.

^c Temperature of 50±5% O₂ consumption. ^d Selectivity is defined as $[\chi_{\text{CO}_2}/(\chi_{\text{CO}_2}+\chi_{\text{H}_2\text{O}})] \times 100$ where χ_{CO_2} is the fraction of O₂ used to convert CO to CO₂ and $\chi_{\text{H}_2\text{O}}$ is the fraction of O₂ used to convert H₂ to H₂O. ^e Temperature of 50±5% CO concentrations. ^f Temperature of complete (99.9±0.1%) O₂ consumption. ^g Temperatures and selectivities were estimated due to abrupt light off (see Figures 3.16 and 3.17 for TPR data).

Finally, it is important to note that PVP-free NPs of various architectures are easily accessible by the methods described herein, however, the stability of the colloids is limited and the resulting particles show significant agglomeration (see Figure 3.3). While the FT-IR CO probe data of the PVP-protected and PVP-free NPs are virtually identical, the Raman signals of the CO-saturated PVP-free NPs are significantly more intense. The lack of graphitic deposits associated with PVP degradation⁵³ may explain the gain in

intensity of the latter. Catalytically, the PVP-free particles did not perform as well as the PVP-protected materials due to agglomeration.

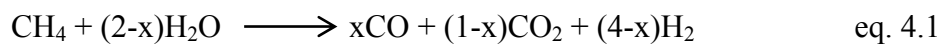
Chapter 4

Synthesis and characterization of other M@Pt (M=Ir, Pd and Au) and Ru@M' (M'=Pd and Rh) core/shell NPs and their distinguishing PROX properties

4.1. Introduction

It has been a long-time research effort to achieve “catalysis by design”^{90,217} on architecturally controlled nanostructures. There are reports on combinatorial searches for multi-purpose catalysts on nanoparticles of binary and ternary alloys of transition metals.²¹⁸ However, it is not practical to do similar combinatorial studies on architecturally sophisticated structures such as core/shell NPs of ML thick shells. A promising approach for designing new catalysts and/or improving existing ones is to combine fundamental surface science studies, NP synthesis methodologies and first principle theoretical predictions. DFT calculations provide the basic tools to analyze reaction mechanisms.^{21,217,219,220} Therefore, NSA theory implemented for periodic slab calculations can be a starting point for NPs of core/shell structure with ca. 1-2 MLs thick shells. As stated in theory, NSAs are overlayers at 1 ML coverage of one metal type over multiple layers of a different host metal.^{90,151} Core/shell structures with 1-2 MLs thick shells are synthetic counterparts to NSAs (see Chapter 2). Thus, NSA theory can first be tested on core/shell NP systems for some catalytic reactions of industrial/scientific importance, and then extended to other structural systems of synthetic relevance. Thus NSA theory can be the foundation for modeling nano-structured core/shell architectures.

Preferential oxidation of CO in H₂-rich feeds (PROX) is a fundamental reaction of industrial and scientific focus.^{35-37,43,67,68,122} CO is known to strongly bind to metal surface, and inhibit surface-catalyzed reactions such as H₂ oxidation, which otherwise has no/little energy barrier at room temperature.⁴³ Pure H₂ being used in PEMFC possesses no problems on Pt-derived electrodes.⁴³ However, it has been studied that surface poisoning from CO-contaminated H₂ feeds is detrimental in terms of overall fuel cell performance.^{42,43,77,78} Industrially, H₂ is produced via the well-known steam reforming process (equation 4.1), which can be described as partial oxidation of hydrocarbons, which also produces about 2% by volume CO.²⁸ CO concentrations can be reduced down to 150-300 ppm level via water-gas-shift reaction (equation 4.2),^{29,30} wherein CO is preferentially oxidized to CO₂ by H₂O. The PROX reaction comes into play after CO-contaminated H₂-rich feed is admitted to the fuel cell. An alternative to the PROX reaction is the CO tolerant H₂ activation reaction, which is also of the closest relevance to core/shell architectures. PROX and CO tolerant H₂ oxidation catalysts fundamentally follow two distinct reaction schemes (see equations 4.3 and 4.4). In principle, both mechanisms help in improving cell performances in PEMFCs. A PROX catalyst with 100% selectivity for CO should complete CO oxidation preferentially below 80 °C, the typical operating temperature of PEMFC,^{38,78} so that subsequent H₂ electro-oxidation can take place. 100% CO-tolerant catalysts, on the other hand, should be able to do the electro-oxidation of H₂ irrespective of the level of CO contamination with no or little loss of cell performance.



$$x = 0.001-0.02$$



$$y = 1.5 \cdot 10^{-5} - 3.0 \cdot 10^{-5}$$

The choice of bimetallic (multi-component) system is of fundamental importance, and primarily determines whether partial or complete PROX behavior, or CO-tolerance will be observed. Transition metals, particularly platinum group metals (PGMs), including Pt,^{63,64,163} Pd,¹⁶⁶ Au,²²¹ Ir,⁷⁵ Rh^{60,205,206,222,223} and Ru,¹⁶⁴ are robust under synthetic conditions that are characteristic of wet chemical reaction routes. Compared to more oxyphilic first group and early TMs, PGMs have certain synthetic advantages; positive reduction potentials of PGMs allows one to use mild reducing solvents such as ethylene glycol, which in turn allows one to control and tune Bulk and surface properties such as size,^{60,221,224} oxidation state,²¹² particle shape^{51,61,164,205} and surface geometry.^{52,63,64,225}

To our perspectives and understandings of heterogeneous catalysis, the choice of nanoparticle architecture is as fundamental as the choice of metal types to be employed. Bimetallic particle architectures those are relevant to catalysis in a synthetic point of view are core/shell,^{34,88,100,105,108,113,115,226} hetero-aggregates,^{95,227} alloys,^{116,170,209,212,228} and physical mixtures of monometallic particles. The first three of the above mentioned architectures may exhibit various different structures. For example, core/shell particles may have an overlayer structure or sandwich structure,⁹¹ and alloys may have a cluster-in-cluster or homogenous random structures. Each structure has

unique physical, chemical and catalytic properties and thus is equivalently important in PROX reaction and other heterogeneous reactions. However, the core/shell architecture with the overlayer structure possesses the highest level of importance to our perception of heterogeneous catalysis, particularly PROX, because it is free of complex surface make-up of alloys and hetero-aggregates, but still exhibits a unique form of surface structure via substrate effects.^{101,102,229,230}

Furthermore, the synthesis of such structures would help us understand thermodynamics of formation of bimetallic nanoparticles. Thus, the gap between microscale and nanoscale chemical and physical properties of bimetallic particles could be bridged.¹⁷⁶ Synthetic limitations to one or more of such bimetallic structures are dictated by the interplay between thermodynamics of mixing two (or more) metals and kinetic barriers of reaction conditions. Each and every bimetallic catalyst can thus synthetically be prepared by changing the reaction conditions and/or synthetic approach. Finally, stability of the synthesized particle is the sole factor determining the merit of applicability to industrial processes. Stability against thermal aging^{34,176} and/or heat/adsorbate-induced re-structuring^{34,90,106} is the final target, but could only be understood after establishing the fundamentals of particle properties in the nanoscale. Hence, systematic studies on architecturally controlled bimetallic nanoparticles play a key role. The next generation catalysts to be fabricated via a ‘catalysis by design’ approach strongly depend on the new generic models that are to be built upon findings of such studies.

In this chapter, bimetallic M@Pt (M=Ir, Pd and Au) and Ru@M (M=Pt and Rh) overlayer nanostructures, and trimetallic M@Pd (M=Ru@Pt and Ir@Pt) sandwiched

core/shell structures will be discussed in terms of their PROX surface reactivities. All the nanoparticles were synthesized in ethylene glycol with PVP as a protecting agent. The M@Pt NPs were prepared with approximately 1 ML thick Pt shells, analogues to the Ru@Pt (1:1) NPs with 3.0 nm Ru cores in Chapter 2 and the Rh@Pt (1:1) NPs with 2.7 nm Rh cores in Chapter 3. The Ru@M NPs were separately prepared in 1-2 MLs and 2-3 MLs thick M shells. The well-characterized NP catalysts were screened using the Temperature-Programmed Reaction (TPR), and evaluated for the PROX reaction under various conditions. The TPR results for the M@Pt (M=Ru and Rh) NPs catalysts are also included in the plots, and are compared to the present core/shell NP catalysts. DFT calculations performed by Prof. Mavriakakis and Dr. Nilekar are briefly described and discussed in context with the experimental results.

4.2. Experimental

4.2.1. Materials

All reactions were carried out under N₂ atmosphere using standard Schlenk line on a Fisher Scientific Isotherm hot plate stirrer with a temperature control unit using a Teflon coated K-type thermocouple. Chemicals, PtCl₂ (Engelhard, Pt 73.09%), H₂PtCl₆.6H₂O (Mallinckrodt, 37.50% Pt), Rh(acac)₃ (Aldrich, 97% pure, Rh 25.70%), RhCl₃ (Engelhard, Rh 39.46%), PdCl₂ (Engelhard, Pd 60%), IrCl₃ (Engelhard, Ir 52.70%), HAuCl₄ (Aldrich, 99.999% pure, Au 57.84% Au), NaBH₄ (Aldrich, 98% pure, granular), polyvinylpyrrolidone (Aldrich, typical M_w=55000), ethylene glycol (VWR, H₂O >0.02%), acetone (Pharmco Aaper, HPLC-UV Grade), ethanol (Pharmco Aaper,

200 proof) and γ -Al₂O₃ (Alfa Aesar, 99.97% metal basis) were purchase and used as received.

4.2.2. Sample Characterization

(See Chapters 2 and 3 for the details of sample characterization)

4.2.3. Density Functional Theory (DFT) calculations

Periodic, self-consistent DFT calculations are carried out using DACAPO,^{177,178} a total-energy code by Prof. Manos Mavrikakis and Dr. Anand Nilekar at the University of Wisconsin. The metal surfaces are modeled using four-layer slabs, with at least five equivalent layers of vacuum separating periodic images of metal slabs in the z-direction of the unit cell. To determine CO-saturation coverages, and H₂ activation energy barriers in the presence of CO on all surfaces, a ($2\sqrt{3} \times \sqrt{3}$) surface unit cell is employed. To calculate binding energies of various intermediates and the activation energy barriers for elementary steps in the PROX reaction network, a (2×2) unit cell is used. Adsorption is allowed on only one of the two exposed surfaces of each slab, and the electrostatic potential is adjusted accordingly.¹⁷⁹ All degrees of freedom for the top two layers of the slab and for all adsorbate atoms are relaxed.

The Pt*/M surfaces are modeled by a single layer of platinum atoms placed on top of three-layer slabs of Au(111), Pd(111), Ir(111), Rh(111), or Ru(0001). Accordingly, the Pt-overlayer adopts the lattice constant of the respective substrate. The equilibrium PW91 lattice constants for bulk metals are calculated to be 4.18 Å (Au), 4.00

Å (Pt), 3.99 Å (Pd), 3.86 Å (Ir), 3.85 Å (Rh), and 2.74 Å (Ru), in good agreement with the experimental values (4.08 Å (Au), 3.92 Å (Pt), 3.89 Å (Pd), 3.84 Å (Ir), 3.80 Å (Rh), and 2.70 Å (Ru)). For the Ru hcp lattice, a value of $c/a = 1.582$ is used.

Binding energies (BE's) are calculated as follows: $BE = E_{ads} - E_{clean} - E_{gas}$, where E_{ads} , E_{clean} and E_{gas} are the total energies of the slab with the adsorbate on it, the metal slab without adsorbed species, and the adsorbed species in the gas phase, respectively. The differential binding energy (BE_{diff}) for CO is defined as the energy change for the reaction: $(nCO(a) + surface + CO(g) \rightarrow (n+1) CO(a) + surface)$; the highest CO coverage for which the differential binding energy of CO is still negative defines the CO-saturation coverage on the respective surface. Zero-point energy corrections are small, and are not included in this analysis.

4.2.4. Synthesis of M@Pt (M=Ir, Pd and Au) and Ru@M (M=Pd and Rh) core/shell NPs

4.2.4.1. Synthesis of Ir@Pt NPs

2.0 nm Ir NPs. In a typical reaction, 144.6 mg $IrCl_3$ (0.4 mmol Ir) and 57.1 mg PVP₅₅₀₀₀ were dissolved in 12 mL EG in a 50 mL 2-neck round bottom flask at about 80°C in flowing N_2 . In a 100 mL 3-neck flask, 30 mL EG was brought to 100°C in flowing N_2 . Next, ~40 mg granular $NaBH_4$ was added into hot EG. Temperature was set to 200°C, and then Ir^{3+} solution was injected into $NaBH_4$ solution. The resultant colloidal suspension was black. Below reflux temperature, 500 μ L of 0.02 M NaBr solution in EG was admitted to the reaction flask. The colloidal suspension was refluxed for about 90

min. in flowing N₂. The reaction was quenched on ice. Ir NPs colloids are stable for months without any precipitation.

2.5 nm Ir@Pt (4:5) NPs. Typically, 67.4 mg PtCl₂ (0.25 mmol Pt) was dissolved in 18 mL EG at room temperature in a 50 mL 3-neck round bottom flask. The flask was evacuated and purged with N₂ several minutes. The cycle of vacuuming and N₂-flushing was repeated several times. Then, 18 mL of Ir NPs suspension was air-less transferred using a gas-tight syringe into Pt²⁺ solution at room temperature. Temperature was first ramped to 80 °C to dissolve Pt²⁺ salt precursor. From there, two methods were reproducibly employed.

Method 1. The suspension was quickly ramped to 140 °C with a ramping rate of 2-3 °C/min. Then, temperature was slowly brought to 160 °C with a heating rate of 0.5-1 °C/min. Temperature was held isothermally at 160 ±2 °C for 1.5 hours. The reaction was quenched in an ice bath. The colloids are stable for weeks.

Method 2. The Ir/Pt suspension was slowly heated to 100 °C with a temperature ramping of 1°C/min. The colloids were aged at 100 ±1 °C for 4 hours. The reaction was quenched in an ice bath. The colloids are stable for weeks.

Sub-2.0 nm PVP-free Ir NPs. 18.4 mg IrCl₃ was added in a 50 mL 3-neck flask with 15 mL EG. Having the flask evacuated and N₂-purged several times, temperature was ramped to 100 °C and kept isothermal for 60 min. Next, it was ramped to 130 °C. Color slowly turned dark and colloidal within 30 min. Finally, the colloidal suspension was aged at 130 ±3 °C for 30 min before the reaction was stopped. The colloids are not stable and precipitate within an hour if not stirred.

Ir@Pt (1:1) NPs. The procedure was as described for 2.5 nm Ir@Pt(4:5) NPs, except 27.6 mg PtCl₂ was dissolved in 9 mL EG and 9 mL of Ir NPs suspension. The mixture was heated / aged as described in Method 1.

Ir@Pt (1:2) NPs. 56.0 mg PtCl₂, 9 mL EG and 9 mL of Ir NPs suspension were reacted as described for 2.5 nm Ir@Pt(4:5) NPs and Method 1.

2.5 nm PVP-free Ir@Pt (3:4) NP. 26.0 mg H₂PtCl₆.6H₂O was admitted into 15 mL of PVP-free Ir NPs under flowing N₂ (positive pressure). Temperature was ramped to 100 °C with ca. 1-2 °C/min. the Ir/Pt suspension was aged at 100 ±2 °C for 2 hour. The reaction was then stopped. The colloids have short shelf-lives, and precipitate within an hour if not stirred.

3.0 nm Ir@Pt@Pd (4:5:5) NPs. In a 100 mL 3-neck round bottom flask, 22.0 mg PdCl₂ was dissolved in 18 mL EG at room temperature. The flask was evacuated and purged with N₂ several minutes. The cycle of vacuuming and N₂-flushing was repeated several times. Then, 18 mL of Ir@Pt NPs suspension (Method 1) was air-less transferred into Pd²⁺ solution at room temperature. Temperature was first ramped to 80 °C and held isothermal for 1 hour to dissolve Pd²⁺ salt precursor, and then brought to 100 °C with a ramping rate of 0.5-1 °C/min. the colloids were aged at 100 ±2 °C for 2 hours. The reaction was stopped. The colloids are stable for days.

4.2.4.2. Synthesis of Pd@Pt NPs

4.0 nm Pd NPs. In a typical reaction, 72.4 mg PdCl₂ (0.4 mmol Pd) and 56.0 mg PVP₅₅₀₀₀ were dissolved in 10 mL EG in a 50 mL 2-neck round bottom flask at about 80°C in flowing N₂. In a 50 mL 3-neck flask, 10 mL EG was brought to 70°C in flowing

N₂. Next, 500 μL of 0.02 M NaBr solution in EG and ~20 mg granular NaBH₄ was admitted into hot EG. Temperature was set to 200 °C, and finally Pd²⁺ solution was injected into NaBH₄ solution at 70 °C. Solution instantly turned black colloidal. The colloidal suspension was refluxed for about 120 min. in flowing N₂. The reaction was quenched on ice. Pd NPs colloids are stable for days without any precipitation.

4.5 nm Pd@Pt (2:1) NPs. Typically, 27.0 mg PtCl₂ was dissolved in 5 mL EG at room temperature in a 50 mL 3-neck round bottom flask. Following several cycles of vacuuming and N₂-purging, 10 mL of 4.0 nm Pd colloidal suspension was injected in under flowing N₂. Temperature was first ramped to 80 °C to dissolve Pt²⁺ salt precursor, and then to 120 °C with a ramping rate of 1-2 °C/min. Pd/Pt suspension was kept isothermal at 120 ±2 °C for 120 min. The reaction was then stopped. The colloids are stable for 1 day.

5.0 nm Pd@Pt(1:1) NPs. The protocol was described above. Differently, PtCl₂ was dissolved in 15 mL EG, and only 5 mL of Pd NPs suspension was admitted to Pt²⁺ solution.

4.2.4.3. Synthesis of Au@Pt NPs

5.0 nm Au NPs. Typically, 33.4 mg HAuCl₄ (0.1 mmol Au) and 27.0 mg PVP₅₅₀₀₀ was dissolved in 30 mL EG at room temperature in a 100 mL 3-neck flask. The flask was evacuated and backfilled with N₂ several times. Then, temperature was ramped to 60 °C and stabilized at 60 ±1°C. In a separate 25 mL 2-neck flask, 20 mg NaBH₄ was dissolved in 10 mL EG. Then, the freshly prepared NaBH₄ solution was admitted dropwise into the Au³⁺ solution at 60 °C. Yellow solution turned dark purple and colloidal. The colloidal

suspension was aged for 120 min. the reaction was then stopped. The colloids were centrifuged with 20% vol. ethanol in acetone and redispersed in 40 mL EG upon sonication. The redispersed colloids are stable in suspension weeks.

8.0 nm Au@Pt (2:3) NPs. In a typical synthesis, 11.1 mg PtCl₂ was dissolved in 10 mL EG at room temperature in a 50 mL 3-neck flask. Having the flask evacuated and N₂-purged, 10 mL of Au NPs suspension was injected. Temperature was first ramped to 60 °C and then slowly brought to 130 °C with a ramping rate of 2-3 °C/min. the Au/Pt suspension was aged at 130 ±3 °C for 3 hours. The reaction was then quenched in ac ice bath.

6.0 nm Au@Pt (2:1) NPs. Synthesis was the same as described above, except that only 3.4 mg (0.3x) PtCl₂ was used.

2.5 nm Au NP. Synthesis of the 2.0 nm Au particles was the same as described synthesis of 5.0 nm particles, except that 80 mg (4x) NaBH₄ was used.

3.4 nm Au@Pt (2:3) NPs. Synthesis of 2.5 nm Au@Pt particles followed the same protocol as that of 6.0-8.0 nm particles, except that the Au/Pt suspension was heated to 100 °C with a temperature ramp of 1-2 °C/min.

4.2.4.4. Synthesis of Ru@Pd NPs

3.0 nm Ru NPs. Synthesis was described in chapter 2.

4.5 nm Ru@Pd (1:1) NPs. 15 mg PdCl₂ (0.8 mmol Pd) and 12 mg PVP₅₅₀₀₀ was dissolved in 16 mL EG in a 100 mL 3-neck flask. Following several cycles of vacuuming and N₂-backfilling, 16 mL of Ru NPs suspension was transferred into the flask using a gastight syringe. Temperature was brought to 100 °C and kept isothermal for 2 hours. The Ru/Pd suspension was ramped to first 120 °C with a ramping rate of 0.5-1 °C/min,

and then boiling EG temperature with a rate of 1-2 °C/min. The colloidal suspension was refluxed for 1.5 hours. The reaction was then stopped.

5.0 nm Ru@Pd (1:2) NPs. Typically, 17.6 mg PdCl₂ (0.1 mmol Pd) was dissolved in 15 mL EG in a 50 mL 3-neck flask. The flask was evacuated and N₂ flushed several times before 10 mL of Ru NPs suspension was admitted using a gastight syringe. The Ru/Pd suspension was aged at 80 °C for 30 min, and then ramped to 130 °C with a temperature ramp of 0.5-1 °C/min. The colloidal suspension was aged at 130 ±3 °C for 4 hours. The reaction was then stopped. The colloids are stable for a day.

4.8 nm Ru@Pt@Pd (3:2:5) NPs. Typically, 17.0 mg PdCl₂ and 14.0 mg PVP₅₅₀₀₀ was dissolved in 16 mL of Ru@Pt (3:2) NP colloids (Chapter 2) at room temperature under N₂ atmosphere. The colloidal suspension was quickly brought to 130 °C. From there, temperature was slowly ramped to 170 °C with a rate of 0.5-1 °C/min, and finally brought to ~200 °C with a fast temperature ramp. The reaction went on at reflux for 90 min. and quenched in an ice bath. A small precipitation occurred at the bottom of the vial after stirring stopped. In general, the NP colloids were stable in the suspension for months.

4.2.4.5. Synthesis of Ru@Rh NPs

3.9 nm Ru@Rh (1:1) NPs. Typically, 20.4 mg Rh(acac)₃ (0.05 mmol Rh) was dissolved in 10 mL EG at room temperature in a 50 mL 3-neck flask. Having the flask evacuated and N₂-flushed several times, 10 mL of Ru NPs suspension was air-less transferred into the reaction flask using a gas-tight syringe. The Ru/Rh suspension was first heated to 80 °C to dissolve the Rh³⁺ salt precursor. Then, a two-step temperature ramping was employed to bring the Ru/Rh suspension to refluxing EG. First, temperature was quickly

ramped to 130 °C. Next, the temperature was ramped to 170 °C slowly at a ramping rate of 0.5-1 °C/min. Finally, the suspension was quickly brought to boiling EG temperature at which it was aged for 60 min. the reaction was then quenched in an ice bath. The colloids are stable for weeks without any precipitation.

4.3 nm Ru@Rh (1:2) NPs.

Method 1. The same as described above, except that 41 mg Rh(acac)₃ (0.1 mmol Rh) was used and the Ru/Rh suspension was aged for 120 min.

Method 2. In a 100 mL 3-neck flask, 52.0 mg RhCl₃ (0.2 mmol Rh) and 14 mg PVP₅₅₀₀₀ was dissolved in 20 mL EG. The flask was evacuated and N₂-flushed several times, then 20 mL of Ru NPs suspension was injected using a gastight syringe. To dissolve the Rh³⁺ salt precursor, temperature was brought to 80 °C and held there for 30 min. Temperature was then ramped to boiling EG temperature with a ramping rate of ca. 1 °C/min. The Ru/Rh suspension was aged at reflux for 90 min.

4.2.4.6. Preparation of γ -Al₂O₃ supported catalysts

The M@Pt (M=Ru, Rh, Ir, Pd and Au) NPs catalysts were prepared by adding γ -Al₂O₃ to colloidal suspensions of nanoparticles, and drying the slurry under vacuum. The metal loadings were normalized by weight with respect to Pt. Typically, 10 mL of Ir@Pt(4:5) (~1 ML) nanoparticle colloidal suspension and 1287 mg γ -Al₂O₃ were mixed overnight and vacuum dried at temperatures about 100°C while vigorously stirring the mixture. Such composition yielded a 1% by weight Pt alumina-supported catalyst. The catalyst was washed with acetone several times and with an equi-volume mixture of acetone and ethanol twice and then baked at 60°C overnight.

The Ru@M (M=Rh and Pd) NPs catalysts were also supported in γ -Al₂O₃, but the metal loadings were normalized by weight with respect to M to yield mass equivalent of equi-molar Pt. Typically, 10 mL of Ru@Rh(1:1) (~1 ML) nanoparticle colloidal suspension and 480 mg γ -Al₂O₃ were mixed overnight and vacuum dried at temperatures about 100 °C. Such composition yielded a 0.52% by weight alumina-supported catalyst. The catalyst was washed and dried as described above.

4.3. Results

4.3.1. Synthesis of M@Pt (M=Ir, Pd and Au) core/shell NPs

Ir NPs were synthesized via an injection of a hot IrCl₃ solution into a NaBH₄ solution in EG at 150°C to give 2.0 nm spherical Ir NPs. Pt was deposited of ca. 1-2 MLs in EG at 130 °C. Therefore, Pt deposition proceeded mostly via a heterogeneous nucleation and growth mechanism. PVP-free Ir NPs, in contrast, could be synthesized via a modified EG reduction reaction. The synthetic procedure for Pt deposition over PVP-free Ir NP seeds was similar to the one with PVP, except deposition temperature was 100 °C.

Pd NPs from NaBH₄ reduction in EG (ca. 4.0 nm) show smaller mean sizes than regular EG reduction (ca. 6.0 nm). Pt was sequentially grown at 120 °C.

Au NPs were also synthesized via a modified NaBH₄ reduction reaction in EG. The order of addition was reversed; freshly prepared NaBH₄ solution in EG was injected into HAuCl₄-PVP solution in EG at 60 °C. The Au³⁺ concentration was decreased by 4-fold relative to the other monometallic NP syntheses. The inverse

addition of Au^{3+} solution into NaBH_4 solution was observed to cause over-10 nm twinned (some with 5-fold axis) particles. Larger mean sizes (ca. 50 nm) also resulted from elevated temperatures of aging the colloids and higher metal concentrations. The size of sub-10 nm Au NPs could be controlled and tuned by adjusting the concentration of NaBH_4 solution. For example, 0.1 M NaBH_4 in EG resulted in ca. 5.0 nm Au NPs, and 0.4 M NaBH_4 in EG resulted in ca. 2.5 nm Au NPs. Before Pt deposition, Au NP colloids were washed to remove residual boron contaminants. Au NPs were redispersed in EG and added to the PtCl_2 solution in EG. Uniform spherical particles with Pt coatings were obtained when deposition temperature was below 100 °C. Depositions at 130 °C resulted in mixtures of Au-Pt hetero-aggregates, dimers, spheres and short aspect ratio wires;⁹⁵ at above 150 °C, exclusively worm-like wires with alternating Au and Pt fragments were obtained. Pt growth over 5.0 nm Au NP seeds, on the other hand, was carried out at 130 °C. 8.0 nm Au@Pt NPs could be obtained with high yields under given conditions.

4.3.2. Synthesis of Ru@M (M=Pd and Rh) core/shell NPs

Ru NPs were synthesized from $\text{Ru}(\text{acac})_3$ in EG via poly-ol reduction as described above. Rh was deposited over Ru NP seeds from either RhCl_3 or $\text{Rh}(\text{acac})_3$ precursors with similar yields and efficiencies. As in case of Ru@Pt NPs, Rh was deposited in various shell thicknesses of 1-3 layers at reflux conditions. To avoid self-nucleation of Rh, a 3-step ramping of temperature between 80 °C and 200 °C was employed. In contrast to Rh, Pd growth over Ru NPs was trivial. Pd deposition at boiling EG temperature with an elemental ratio of 1:1 yielded NPs with a broad size distribution (4.5 ± 2.0 nm). Besides thermodynamically controlled favorable Pd-Pd bonding could not

be completely overcome even at boiling EG temperature, resulting in monometallic Pd NPs in small percentages by number. The synthesis of uniform Ru@Pd NPs with homogeneous elemental compositions required 2-fold excess Pd (66% mole), which yielded ca. 2-3 MLs thick Pd shells at deposition temperatures of 130 °C or below. However, the better PROX performances were obtained for catalysts that were prepared from those non-uniform Ru@Pd NPs with nominal Ru:Pd compositions of 1:1 (see below).

4.3.3. Size and size distribution analysis by TEM

TEM particle sizes were evaluated for the M@Pt and Ru@M NPs before and after deposition of the respective shell metals. All the bimetallic/trimetallic systems showed increases of the average particle diameters compared to those of the core metals. In general, particle size distributions were uniform and produced a single Gaussian distribution. Furthermore, relative increases in particle sizes were consistent with Schmid's cluster models, and thus supported the core/shell structures. TEM size evaluations would be discussed below in more detail.

Ir NPs have 2.0 nm mean size, and are very close to being monodisperse (Figure 4.1a and 4.1c). The particles exhibit 111 facets exposed with inter-planar spacings of 0.210 nm (Figure 4.1b). Ir@Pt NPs with a nominal Pt:Ir ratio of 5:4 show a narrow size distribution with a mean diameter of 2.5 nm (Figures 4.1d and 4.1f). Particles are nano-crystalline, and show both hexagonal (ABAB.. ordering) and face centered cubic (ABCA.. ordering) packing of atoms (see Figure 4.1h and FFT in 4.1i). PVP-free synthesis of Ir@Pt yields somewhat smaller nanoparticles (ca. 2.0 nm) than those with

PVP (ca. 2.5 nm). The average particle size is 2.0 nm with a narrower distribution (2.0 ± 1.0 nm) than PVP-protected Ir@Pt NPs (2.5 ± 1.5 nm) (Figure 4.2a). Particles are nanocrystalline, and mostly exhibit 111 spacing of cubic (FCC) lattice (Figure 4.2b). Sequentially grown Ir@Pt@Pd NPs with Ir@Pt NPs seeds exhibit 3.0 nm diameters with a broad size distribution, 3.0 ± 2.0 nm (Figure 4.2d and 4.2f).

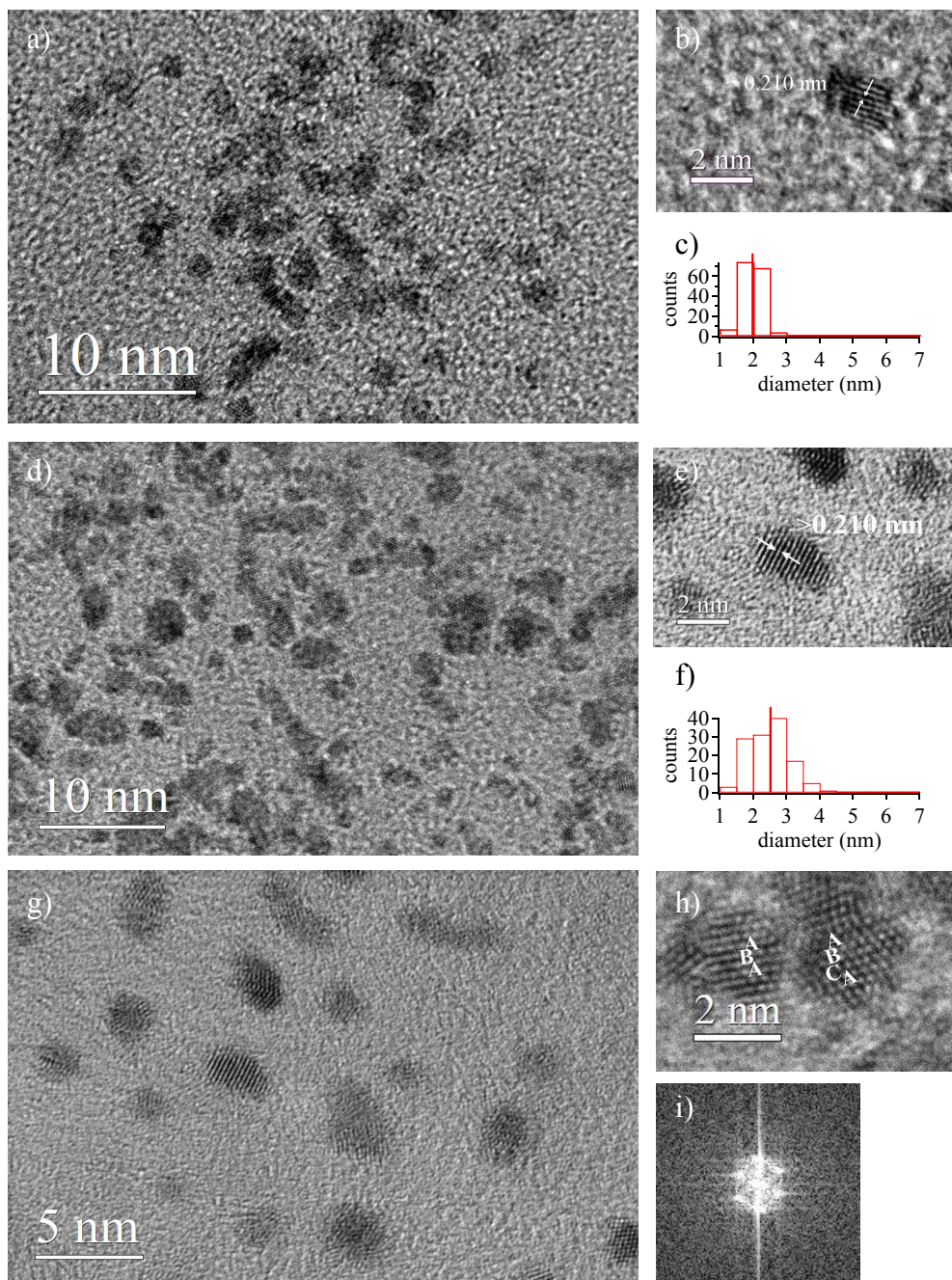


Figure 4.1. TEM images of (a) Ir NPs, and (d) Ir@Pt (4:5) NPs. HR-TEM images of (b) Ir NPs, and (e, g and h) Ir@Pt NPs. 111 planes with inter-planar spacing of 0.210 Å for an iridium nanoparticle are shown in (b). 111 planes of a Ir@Pt nanoparticle is also shown in (e). (h) HR-TEM showing a Ir@Pt NP with the hexagonal packing, and another Ir@Pt NP with the face center cubic packing. FFT of the Ir@Pt nanoparticle with the FCC packing is given in (i). Particle size histograms of the Ir NPs and Ir@Pt NPs are shown in (c) and (f), respectively.

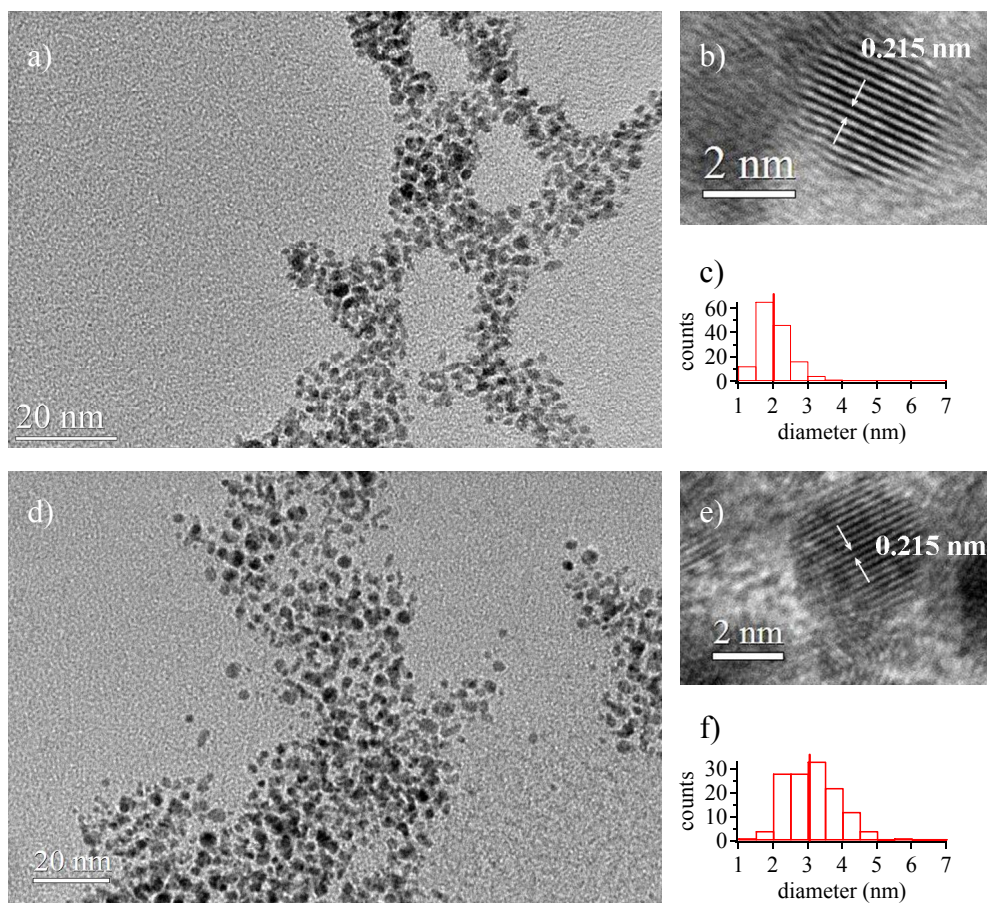


Figure 4.2. TEM images of (a) PVP-free Ir@Pt NPs, and (d) PVP-protected Ir@Pt@Pd NPs. HR-TEM images of (b) PVP-free Ir@Pt NPs, and (e) PVP-protected Ir@Pt@Pd NPs. 111 planes with inter-planar spacing of 0.215 nm for both PVP-free Ir@Pt and Ir@Pt@Pd nanoparticles are also shown in (b) and (e), respectively. Particle size histograms are given in (c) and (f).

A 3.0 nm Ru NP host with sequentially grown Pd in 1:1 elemental ratio show a final particle diameter of 4.5 nm in average (Figures 4.3a and 4.3c). The size increase corresponds to 2-3 MLs of Pd shells, which is larger than the observed mean size of the Ru@Pt NPs (4.1 nm) with the identical elemental ratio of Ru:M (M=Pt and Pd). 2-fold excess Pd (66% mole) deposited at 130 °C yields particles with 5.0 nm diameter in average and a narrower size distribution, 5.0 ± 1.5 nm (Figures 4.3d and 4.3f). Likewise, the Schmid model systematically underestimates the size of Ru@Pd NPs. Oxide formation at the interface of Ru and Pd may account for the size gap between the calculated and observed NPs (see Appendix for the Micro-Raman analysis of oxide formation in the Ru@Pd NPs). The particles are nanocrystalline and multiply twinned (Figures 4.3b and 4.3e). The nano-crystalline Ru@Pt@Pd particles upon Pd nucleation at 1-2 monolayer coverage over 3.7 nm Ru@Pt particles (see Chapter 2) yields an average particle diameter of 4.8 nm with narrow size distribution (Figure 4.3g-i).

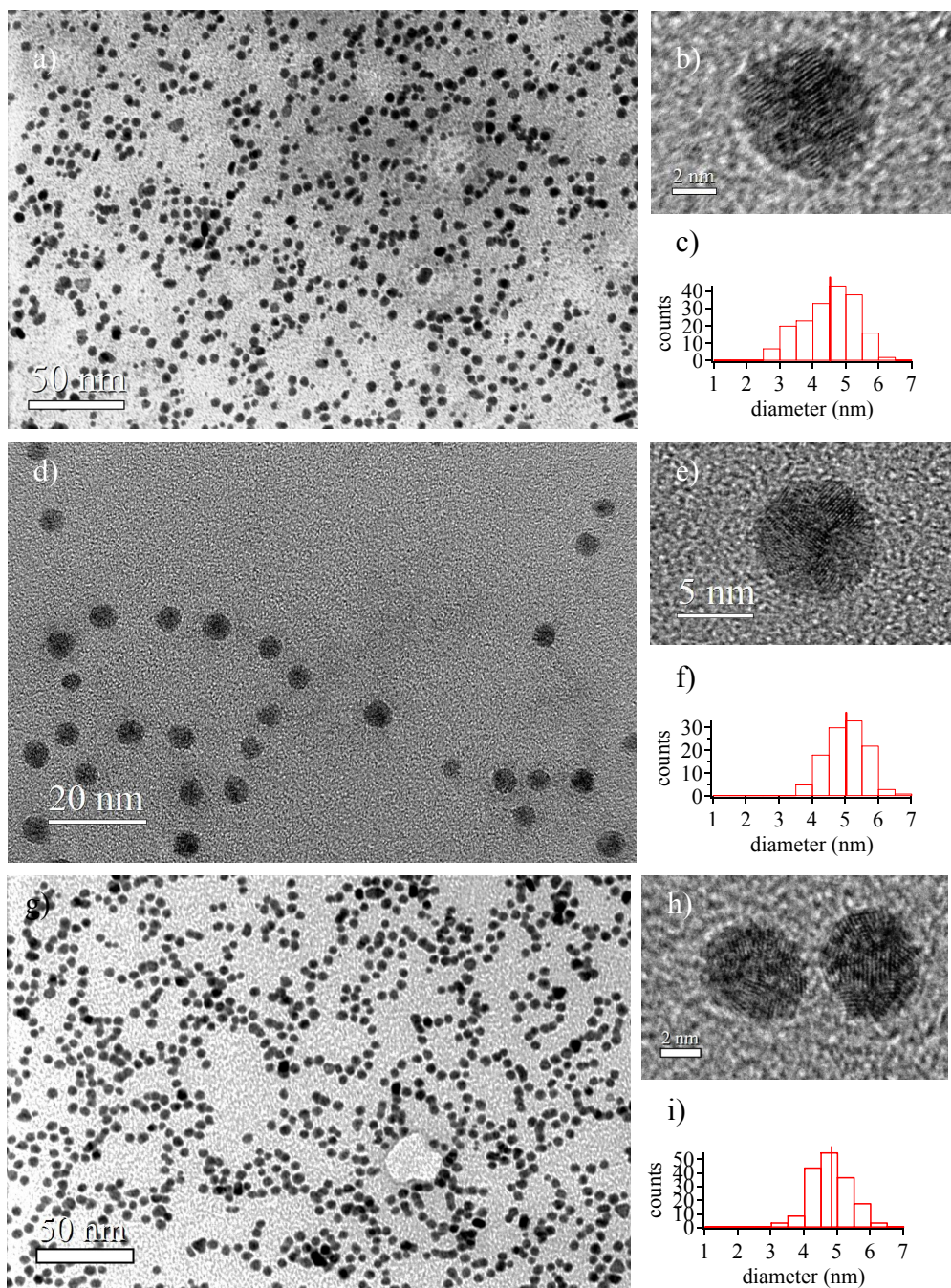


Figure 4.3. TEM images of (a) Ru@Pd (1:1) NPs with ca. 1-2 MLs thick Pd shells (d) Ru@Pd (1:2) NPs with ca. 2-3 MLs thick Pd shells (g) Ru@Pt@Pd (3:2:5) NPs with sandwiched Pt shells at sub-monolayer coverage and Pd shells of 1-2 MLs thick. (c, f and i) HR-TEM images, and (b, e and h) particle size histograms of NPs shown in (a, d and g), respectively.

4.3.4. Composition and architecture by Scanning Transition Electron

Microscopy

The composition and architecture (core-shell vs. alloy) were evaluated using a 1.5 nm EDS probe in a JEOL 2100 FE TEM operating in the STEM mode. Multiple single-particle EDS analysis of core-shell and alloy NPs from various syntheses confirmed that all particles are bimetallic in nature with no stray monometallic particles observed in any of the samples. Furthermore, line spectra acquired across the randomly selected single particles revealed the core shell structuring.

The STEM-EDS line scans were recorded from 7.8 nm Au@Pt NPs with 6.0 nm Au cores and ~3 ML Pt shells (figure 4.4a) clearly show the Pt L line with a bimodal Pt distribution that reaches a maximum at the edge of the particle (i.e. the shell) whereas the Au L line shows maximum Au concentration at the center of the particle. In Figure 4.4, a representative EDS line spectrum of a ~10 nm Au@Pt nanoparticle is shown. The particle center of gravity lies at ca. 15 nm of the line spectrum, which shows a maximum of X-ray counts for the Au M line, and minima for the Pt M line. STEM-EDS line and point spectra of the 3.4 nm Au@Pt NPs are shown in the Appendix.

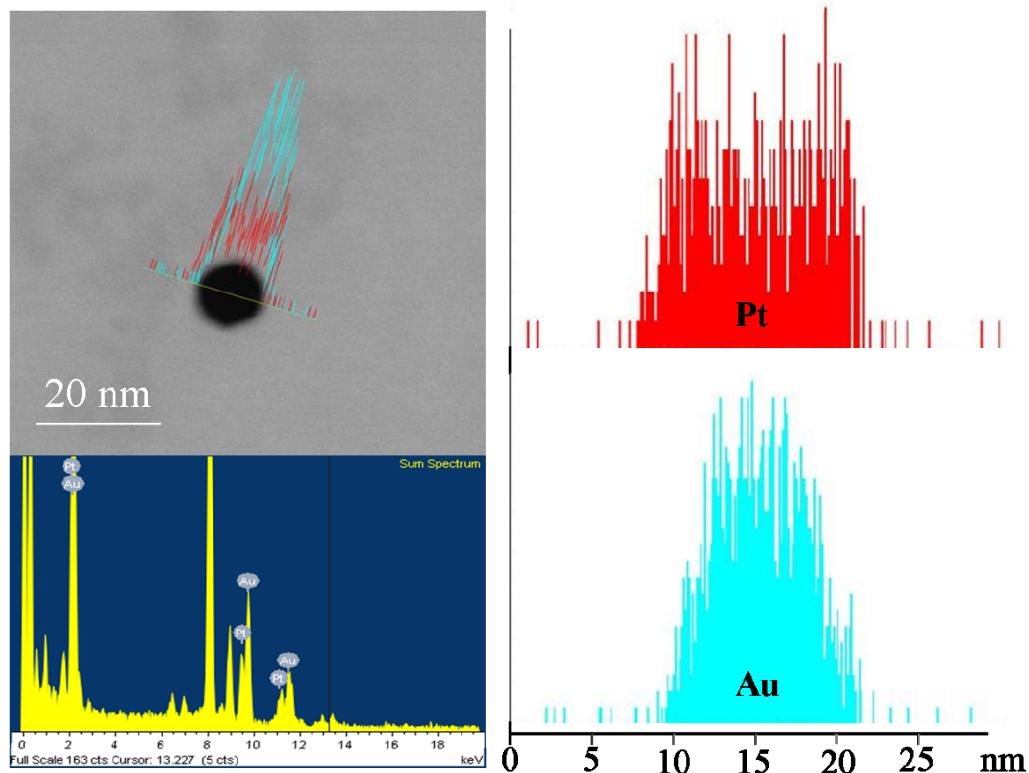


Figure 4.4. Representative STEM-EDS line spectra of a ~ 8.0 nm Au@Pt NP with ~ 6.0 nm Au core and 3-4 layers thick Pt shells. Relative atomic % composition (vertical axis) of Au (blue) and Pt (red) are plotted against the line scan probe position (horizontal axis) and are given next to STEM image. A 1.5 nm probe was used to trace 15 – 20 nm scans across each particle. The particle center is at ~ 15 . Representative EDS spectrum is given below STEM image.

The 5.0 nm Ru@Pd particles with ca. 2-3 MLs thick Pt shells were analyzed by STEM-EDS in the scanning mode using the 1.5 nm probe. Due to the probe size, the 4.5 nm Ru@Pd particles with ca. 1-2 MLs thick Pd shells could not be investigated. Owing to the thickness effect, the spatial resolutions of shell spectra were still poor compared to those of core spectrum, shown in Figure 4.5. The 4.8 nm Ru@Pt@Pd particles were also scanned under 1.5 nm probe size of STEM-EDS. A representative ~ 5 nm particle exhibited the bi-modal distribution of Pt L X-rays, reaching maxima at the

particle edges, the broad diffuse distribution of Pd L X-rays and the narrow compact distribution of Ru L X-rays, reaching a maximum at the center (Figure 4.6). STEM-EDS point spectra of the tri-metallic nanoparticles also showed the Pd-rich outermost edge (Figure 4.7a, spectrum 1) and the Pt-rich outer-core edge (Figure 4.7a, spectrum 2), and the Ru-rich core (Figure 7b). Representative line-spectrum of a 4.3 nm Ru@Rh particle comprising of 2-3 MLs thick Rh shells is shown in the Appendix (Figure A4.6).

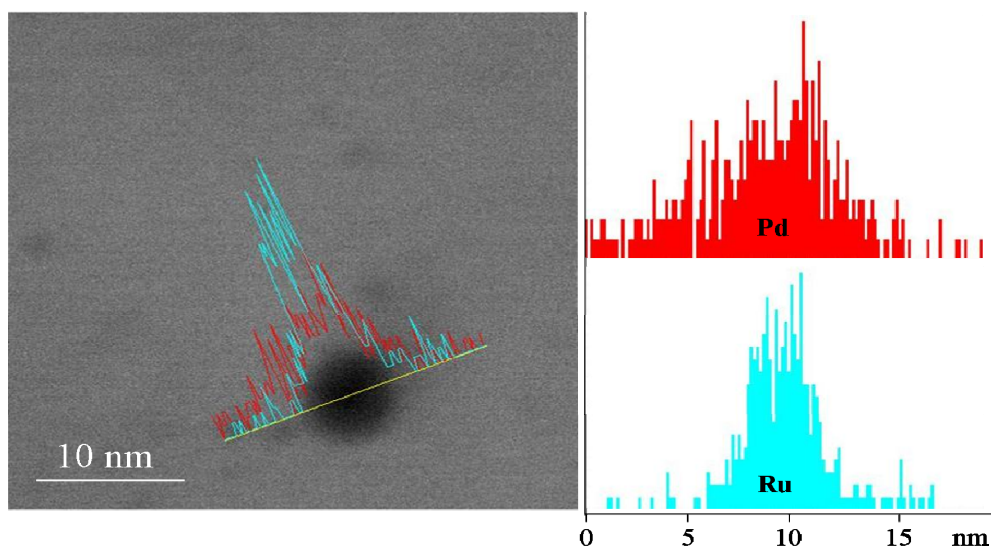


Figure 4.5. Representative STEM-EDS line spectra of a 5.0 nm Ru@Pd NP comprising of a 3.0 nm Ru core and ca. 2-3 layers thick Pd shells. Relative atomic % composition (vertical axis) of Ru (blue) and Pd (red) are plotted against the line scan probe position (horizontal axis) and are given next to STEM images. A 1.5 nm probe was used to trace 15 – 20 nm scans across each particle. The particle center is at ~ 9 nm in (b).

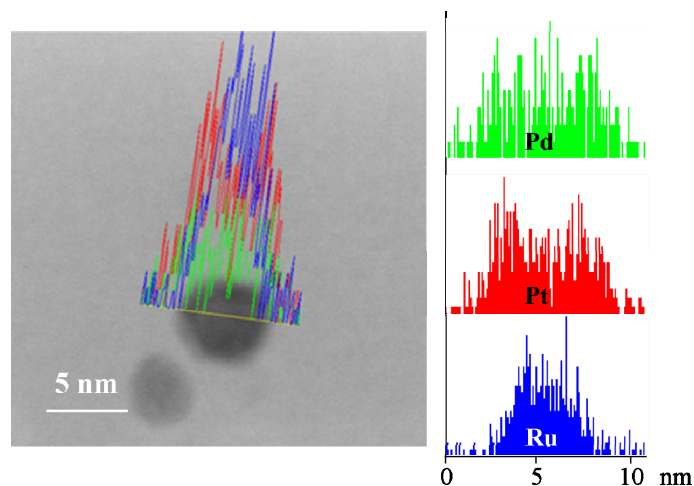


Figure 4.6. Representative STEM-EDS line spectra of a 4.8 nm Ru@Pt@Pd particle with 3.0 nm Ru core, sandwiched Pt shells at sub-monolayer coverage and 1-2 MLs thick Pd shells. Relative atomic % composition (vertical axis) of Ru (blue), Pt (red) and Pd (green) are plotted against the line scan probe position (horizontal axis) and are given next to STEM images. A 1.5 nm probe was used to trace ~11 nm scans across the particle. The particle center is at ~ 6 nm.

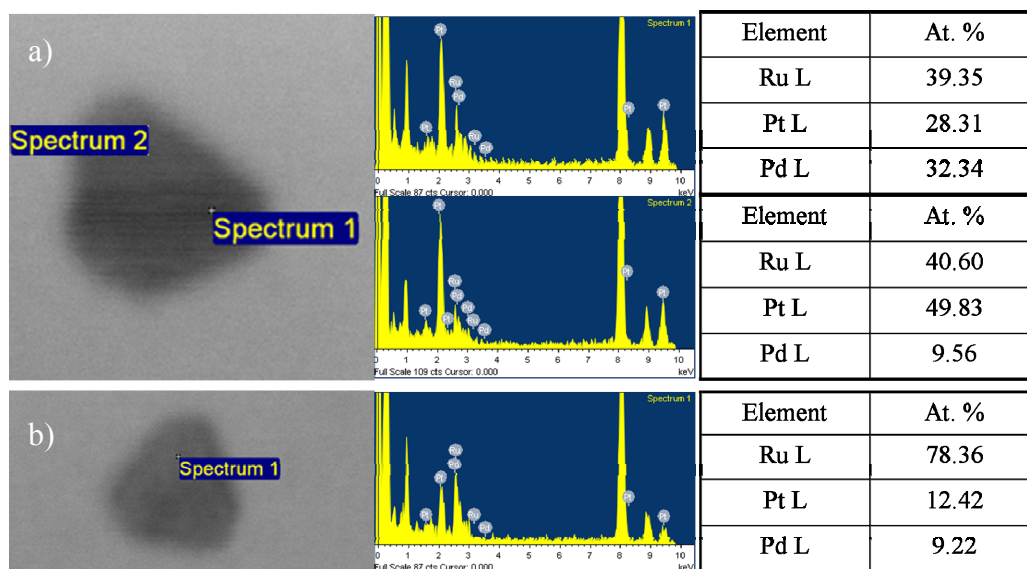


Figure 4.7. STEM-EDS point analysis of two randomly chosen Ru@Pt@Pd NPs, showing (a) edge spectrum and (b) core spectrum. EDS spectra are shown next to each STEM image along with the table, showing the % compositions from the spectra.

4.3.5. Structural evaluation by XRD

As-synthesized monometallic Ir NPs are poorly crystalline. The X-ray diffraction pattern is distinct from the bulk Ir, and possibly reveals phase transition to hexagonal closed pack (HCP) lattice. However, TEM images show the presence of NPs with 111 lattice spacing of FCC Ir. We believe that both FCC and HCP arrangement of atoms co-exist in the powder. Furthermore, the observation of hexagonal arrangement of atoms for the Ir@Pt NPs supports this hypothesis. The X-ray diffraction patterns for increasing molar presence of Pt are given in Figure 4.8a in successive plots. They reveal all, but 200 reflections of FCC Pt, shifting to the bulk Pt with increasing ratio of Pt to Ir. For all the compositions of Ir:Pt studied, 200 diffractions are in line with that of the bulk Pt, and thus do not undergo the composition-dependent peak shifts. This phenomenon is similar to that observed for Ru@Pt NPs with thin Pt shells, and thus attributed to the strain-induced distortion of the FCC Pt lattice. Pt shells must then be pseudo-morphically grown over Ir NP seeds. PVP-free Ir NPs are similarly poorly crystalline, but show more structural deviations from the bulk Ir. PVP-free Ir@Pt NPs also shows the same structural anomalies as the PVP-protected ones, as revealed by their X-Ray diffraction pattern (Figure 4.8b).

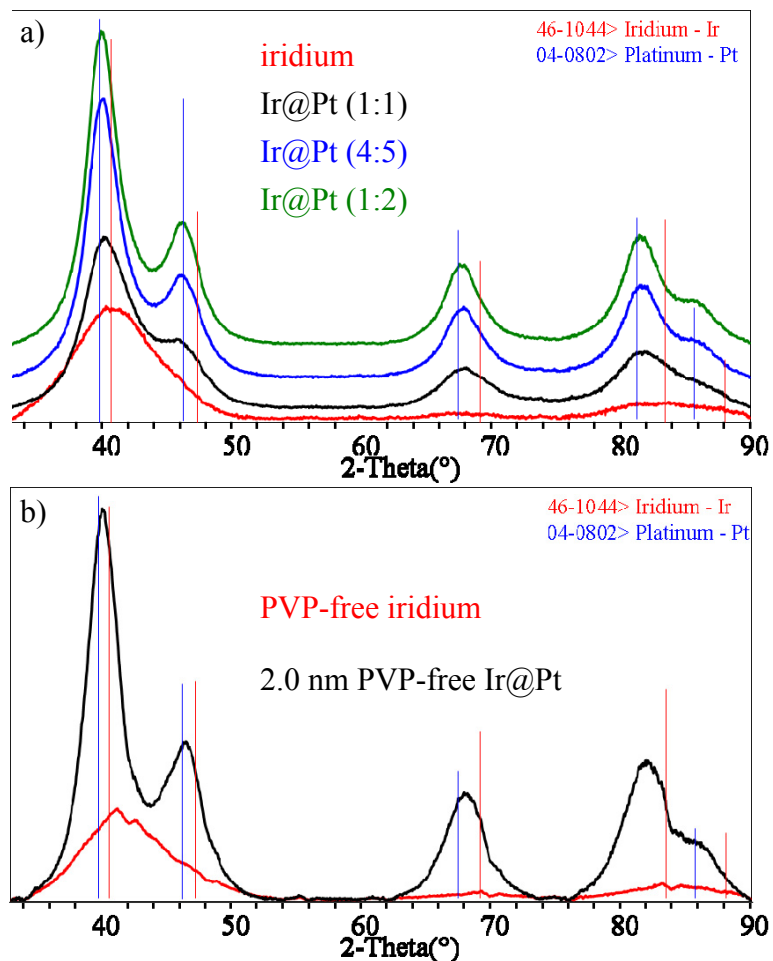


Figure 4.8. Powder XRD patterns of (a) PVP-protected 2.0 nm Ir particles and their Pt shell series, and (b) PVP-free Ir NPs and 2.5 nm Ir@Pt (3:4) particles. JC-PDS lines for Pt (blue) and Ir (red) are also presented.

Because the lattice constants of FCC Pt and Pd are virtually identical ($a_{\text{Pt}} = 3.916 \text{ \AA}$ and $a_{\text{Pd}} = 3.897 \text{ \AA}$) XRD analysis is not a useful tool to distinguish core/shell from alloy NPs. However, CO-probe studies are very informative regarding surface compositions, and thus will be discussed in the following sections.

The 3.4 nm Au@Pt particles were shown to have the core/shell architecture as revealed by a combination of XRD and STEM-EDS analysis. Pt growth over the

preformed 2.5 nm Au seeds begins as soon as the reaction is heated, as studied by XRD. Powder X-ray diffraction of a centrifuged and dried aliquot of the reaction mixture reveals the FCC Pt phase along with the FCC Au phase and unreacted PtCl₂. After one hour at 100 °C, the diffraction from the Pt shell becomes more prominent, and thus PtCl₂ reflections are less intense. Only after 3 hours at 100 °C, PtCl₂ reflections disappear, and FCC Pt and FCC Au can be distinguished in the X-ray pattern (Figure 4.9). The progressive narrowing of the Pt linewidths with time, -as well as decreasing PtCl₂, reveals that Pt growth is from solution, and thus follows slow kinetics. XRD clearly rules out the formation of bimetallic NPs with the alloy structures. However, XRD does not distinguish between self-nucleation and hetero-nucleation of the Pt, such that the diffraction pattern can be originated from the NPs with the core/shell structures and/or the mixtures of monometallic NPs. STEM-EDS line spectrum and multiple point spectra clearly shows the formation of bimetallic NPs with the core/shell architecture, complementing the XRD studies (see Appendix for STEM-EDS line and point analysis of the 3.4 nm Au@Pt particles).

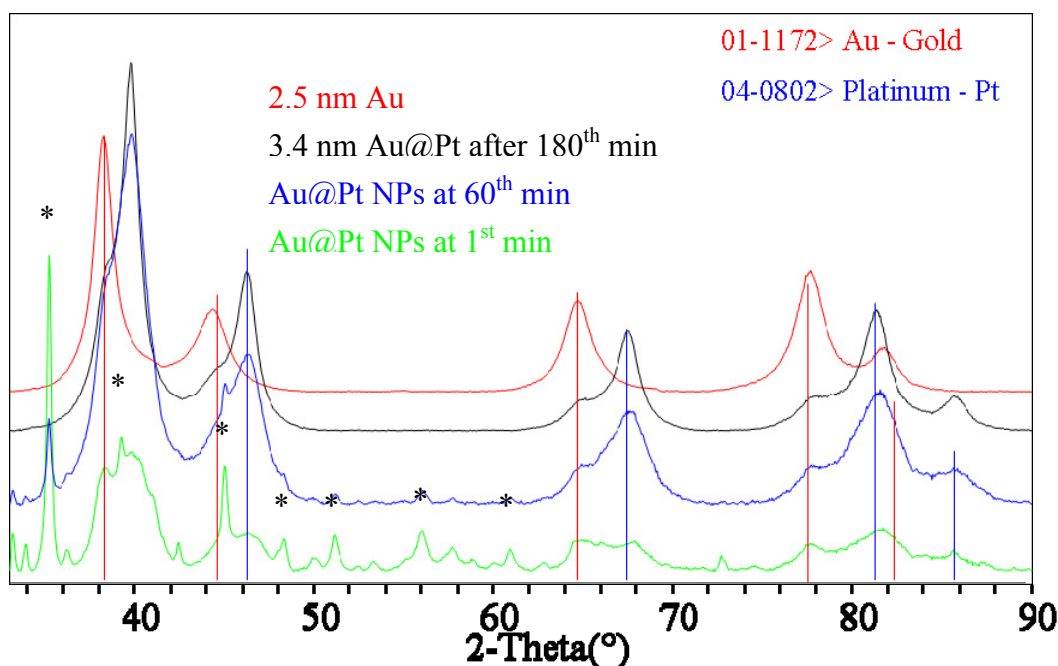


Figure 4.9. Transient powder XRD patterns of nano-crystalline Au@Pt particles collected ex-situ at 1st min, 60th min and 180th min of Pt growth reaction at 100 °C compared to powder diffraction pattern of 2.5 nm Au NPs. * show the major reflections of (unreacted) PtCl₂. JC-PDS lines for Pt (blue) and Au (red) are also presented.

Similar to the Ru@Pt NPs, XRD revealed diffraction anomalies related to the thin shell formation in the nanocrystalline Ru@M (M=Rh and Pd) systems. Ru NPs diffract weakly, however, the metallic HCP structure is clearly evident from EXAFS and XANES analysis. Rh NPs have poorly crystalline FCC unit cell of bulk Rh. Therefore, Ru@Rh NPs show a mixed structural make-up. In contrast to high angle peaks (>60 °2θ) which are almost lined-up with FCC Rh (and also with HCP Ru), low angle reflections of Rh 111 and 200 can not be discerned from XRD patterns (Figure 4.10a). Instead, the 111 diffraction shifts to that of the bulk Rh with increasing molar ratio of Rh to Ru. The 200 diffraction, however, seems to be static and grows in intensity with the Rh content.

Similarly, X-Ray diffraction patterns of Ru@Pd NPs with various elemental ratios of Pd and Ru has been evaluated, and found structural anomalies associated with growth of thin Pd shells (Figure 4.10b). X-ray diffraction from the Ru@Pd NPs reveals the presence of a nanocrystalline Pd co-phase, which is pseudo-morphic to the Ru phase. Furthermore, the peaks shifts to the FCC Pd peak positions with increasing Pd content for the 5.0 nm Ru@Pd NPs with 2-3 MLs thick Pd shells. Moreover, FCC Pd reflections increase in intensity with increasing Pd content of the nanoparticles, such that Pd 200 reflection which is weak for the 4.5 nm Ru@Pd particles with ca. 1-2 MLs thick Pd shells become prominent for the 5.0 nm Ru@Pd particles with 2-3 MLs thick Pd shells. As revealed by TEM, XRD also shows the presence of monometallic Pd NPs in low number (~5%) and large volume (ca. 7-times the volume of the 4.5 nm Ru@Pd particles with 1-2 ML thick Pd shells, given the 6.0 nm mean size of monometallic Pd via EG reduction reaction) densities. The XRD co-pattern with the sharp peaks has been attributed to nanocrystalline Pd NPs (with high diffracting volumes, but small number densities) observed in TEM images (Figure 4.3a).

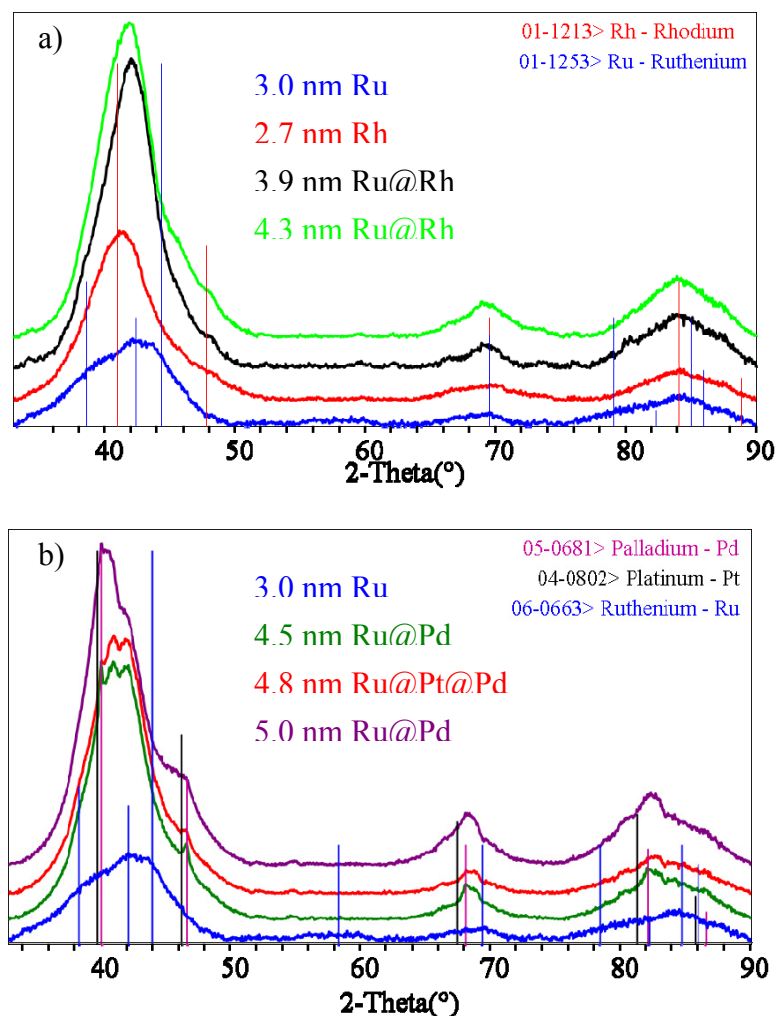


Figure 4.10. Powder XRD patterns of (a) Ru@Rh NPs with the 3.0 nm Ru cores and varying Rh shell thicknesses compared to those of monometallic 2.7 nm Rh NPs and 3.0 nm Ru nanoparticle seeds, and (b) Ru@Pd NPs with the 3.0 nm Ru cores and varying Pd shell thicknesses compared to that of 3.0 nm Ru particle seeds and the 4.8 nm Ru@Pt@Pd NPs. JC-PDS lines for Pt (black), Ru (blue), Rh (red) and Pd (purple) are also presented.

4.3.6. Surface-adsorbed CO probing by FT-IR

A CO probe study of the 2.5 nm Ir@Pt particles has revealed an electronically and geometrically altered Pt surface. CO saturated colloids of 2.0 nm Ir particles show a single broad $\nu(\text{CO})$ at 2040 cm^{-1} for atop CO on Ir.²³¹ The Ir@Pt NPs with sub-monolayer coverages of Pt, as calculated from the starting Pt:Ir elemental ratio of 1, show a single symmetric $\nu(\text{CO})$ at 2050 cm^{-1} which is intermediate to $\nu(\text{CO})$ on Pt and $\nu(\text{CO})$ on Ir. Furthermore, FT-IR spectra of CO-saturated colloids of the Ir@Pt NPs indicated blue-shift of $\nu_{\text{atop}}(\text{CO})$ s away from $\nu_{\text{atop}}(\text{CO})$ on Ir with increasing Pt content. Higher Pt:Ir molar ratios of <2 gives a single narrow $\nu(\text{CO})$ at ca. 2060 cm^{-1} which is almost characteristic $\nu(\text{CO})$ on Pt for M@Pt NPs (M=Ru, Rh) with thin Pt shells (Figure 4.11a). Thus, the 2.5 nm Ir@Pt NP colloids exhibited $\nu_{\text{atop}}(\text{CO})$ on Pt at 2059 cm^{-1} , $\sim 5\text{ cm}^{-1}$ red-shifted from $\nu_{\text{atop}}(\text{CO})$ on monometallic Pt NP colloids (Figure 4.11a). In overall, the $\nu_{\text{atop}}(\text{CO})$, as well as the X-ray diffraction pattern, of the 2.5 nm Ir@Pt particles revealed an electronically and geometrically altered Pt surface.

Further evidence for the core/shell structuring with electronically-altered Pt shells comes from the 2.0 nm PVP-free Ir@Pt particles with ca. 1 ML thick Pt shells (Figure 4.11b). A single symmetric $\nu_{\text{atop}}(\text{CO})$ centered at 2073 cm^{-1} has been observed for the 2.0 nm PVP-free, which is virtually distinct from those of the 2.2 nm PVP-free Pt particles and the parent Ir NPs. The blue-shift by ca. 10 cm^{-1} relative to the PVP-protected Ir@Pt NPs is believed to be a combination of size,¹⁶⁸ coverage and lateral effects.^{93,167} The $\nu_{\text{bridge}}(\text{CO})$ of Ir centered at ca. 1970 cm^{-1} was attributed to the size effects,¹⁶⁸ and thus was absent for the PVP-free Ir@Pt NPs (Figure 4.11b).

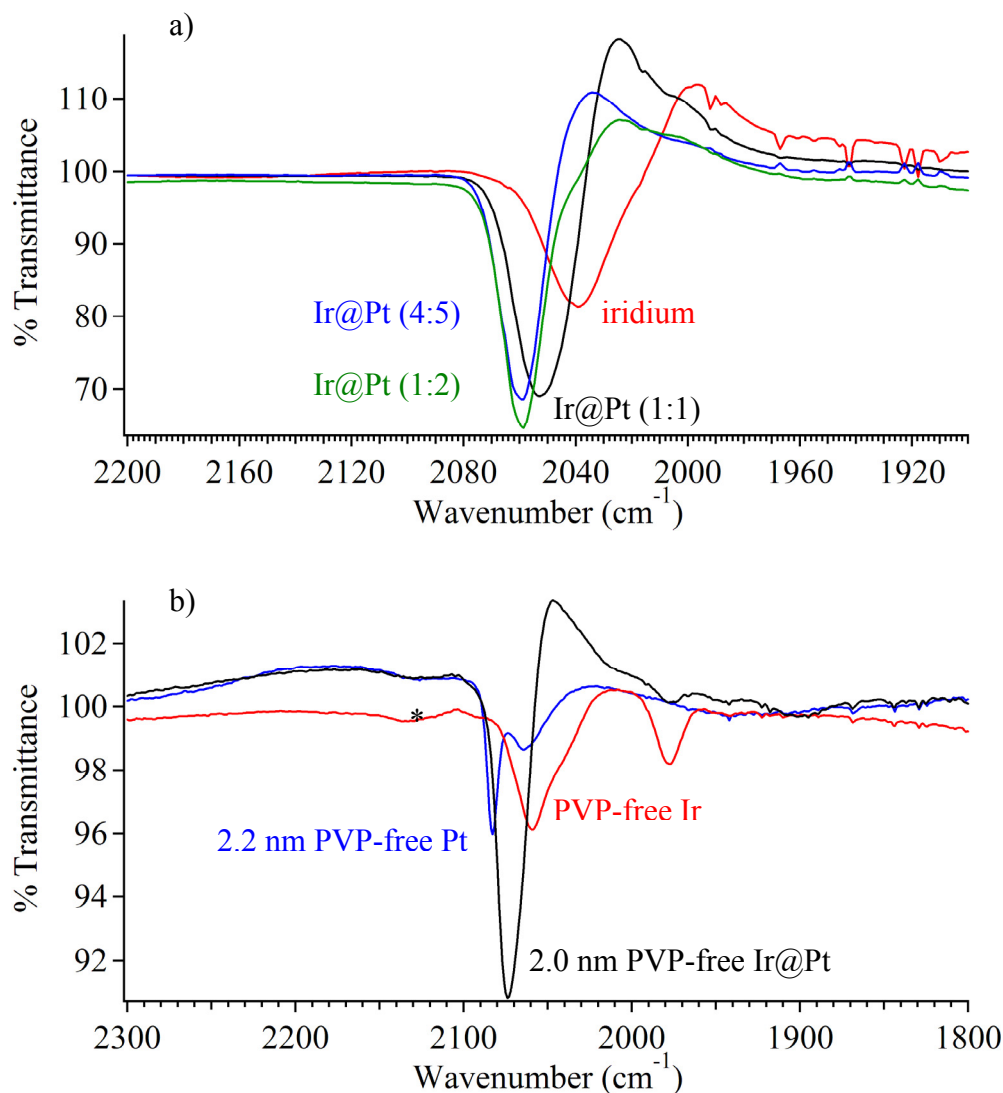


Figure 4.11. FT-IR spectra of CO-saturated colloids of (a) 2.0 nm PVP-protected Ir particles and Ir@Pt NPs of varying Ir:Pt ratios: 1:1, 2:3 and 1:2; and (b) PVP-free Ir NPs, 2.2 nm PVP-free Pt and 2.5 nm PVP-free Ir@Pt particles. Asterisks show free-CO in the colloidal suspension.

As shown in Figure 4.11a, $\nu(\text{CO})$ on monometallic Pd NPs have a broad diversity of both linear and bridging modes of CO binding. Large Pd NPs from the direct EG reduction reaction give rise to a single atop $\nu(\text{CO})$ ^{93,232,233} on Pd at 2050 cm⁻¹ and a single bridging $\nu(\text{CO})$ on Pd⁹³ at 1950 cm⁻¹. Pd NPs from the NaBH₄ reduction reaction

show a blue-shift of atop $\nu(\text{CO})$ on Pd to 2060 cm^{-1} . Besides the 1950 cm^{-1} peak, there is another $\nu_{\text{bridge}}(\text{CO})$ on Pd at 1930 cm^{-1} . After etching the Pd NPs with NaBr, the 2050 cm^{-1} peak for $\nu_{\text{atop}}(\text{CO})$ on Pd appears back along with the 2060 cm^{-1} peak. Thus, a single sharp peak grows at 2050 cm^{-1} for $\nu_{\text{bridge}}(\text{CO})$ on Pd. Hence all the evidence points to the presence of both 111 and 100 surface sites on monometallic Pd NPs before and after NaBr treatment. The 2050 cm^{-1} and 1950 cm^{-1} peaks are tentatively assigned to atop and bridging $\nu(\text{CO})$ s on the edge and terrace surface sites of Pd NPs,^{232,233} and thus the 2060 cm^{-1} and 1930 cm^{-1} peaks are assigned to the atop and bridging $\nu(\text{CO})$ s emerged due to corner and defect sites on Pd NP surfaces.^{232,233} After Pt deposition at monolayer coverage, a single strong peak shows up at 2060 cm^{-1} along with a broad weak feature at 1900 cm^{-1} . The former is attributed to $\nu_{\text{atop}}(\text{CO})$ on Pt and the latter to bridging $\nu(\text{CO})$ on the electronically altered Pt surface sites (Figure 4.11a). To demonstrate the sensitivity of FT-IR monitoring of adsorbed CO on Pt and Pd surfaces, Pt and Pd have been successively deposited over Pd NPs. Pd@Pt@Pd NPs with monolayer thick Pt shells sandwiched between Pd cores and monolayer thick Pd shells show $\nu(\text{CO})$ s that are characteristic of Pd 111 surface sites. Characteristic $\nu(\text{CO})$ peaks for atop and bridging COs on electronically altered Pt surface sites can be fully restored after 1-2 monolayers of Pt is deposited over the Pd@Pt@Pd NP cores (Figure 4.11b).

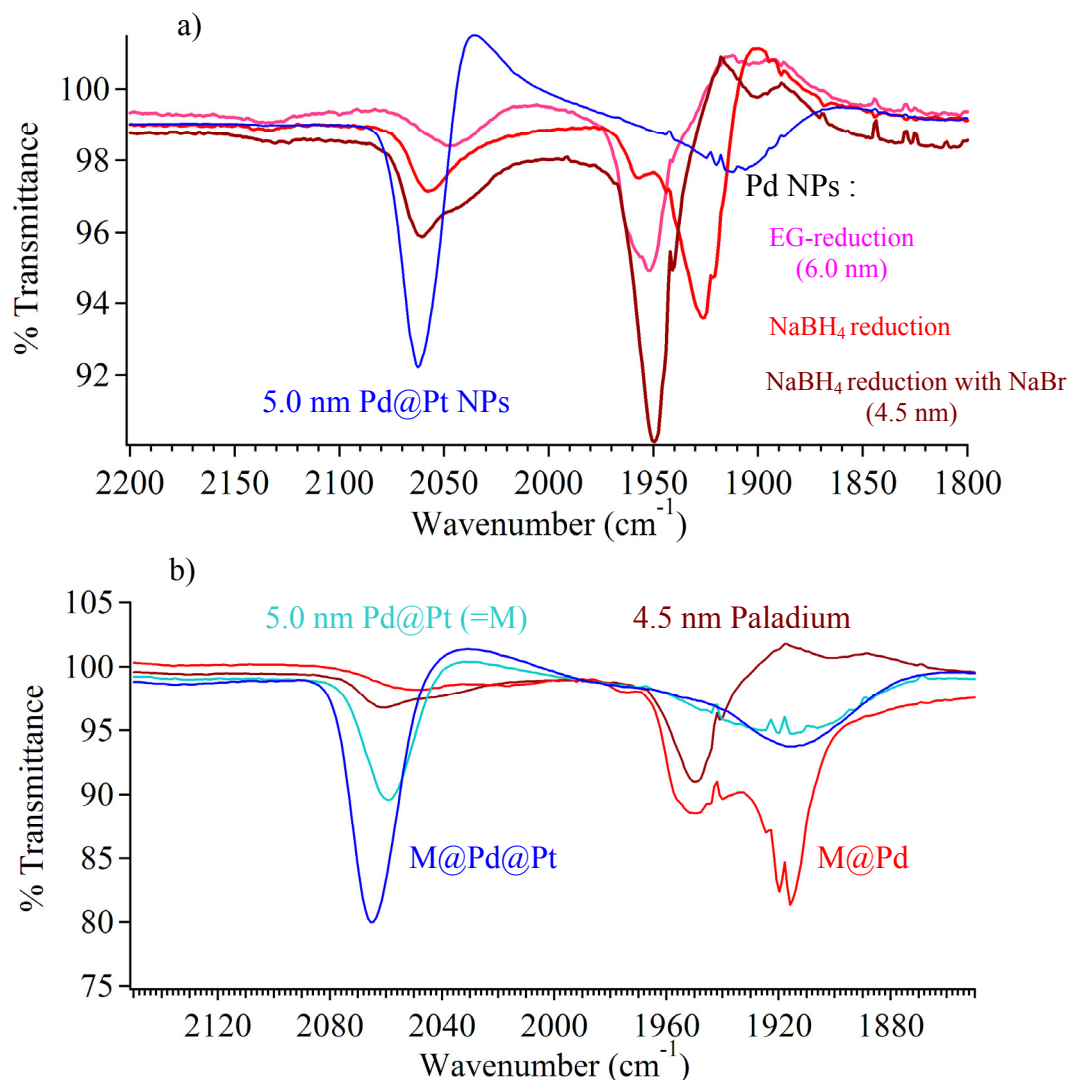


Figure 4.11. FT-IR spectra of CO-saturated colloids of (a) EG-reduced Pd NPs, NaBH₄-reduced Pd NPs, 4.0 nm NaBH₄-reduced Pd particles after NaBr treatment and 4.5 nm Pd@Pt core/shell particles with 4.0 nm Pd cores and ca. 1 ML thick Pt shells; and (b) bimetallic Pd/Pt NPs with alternating Pt and Pd layers at ca. 1 ML coverage, namely Pd@Pt, Pd@Pt@Pd, and Pd@Pt@Pd@Pt core/shell NPs.

The tri-metallic Ir@Pt@Pd NPs with monolayer thick Pt shells sandwiched between Ir cores and ca. 1-2 MLs thick Pd shells have been characterized by FT-IR spectroscopy of CO saturated colloids. A single sharp peak at 2060 cm⁻¹ for Ir@Pt NPs is replaced by a broader and weaker peak at 2050 cm⁻¹ for linearly-bound CO on Pd surface

sites upon Pd deposition. Thus, another peak at 1950 cm^{-1} is assigned to bridging CO on two Pd surface sites. For control, further deposition onto the Ir@Pt NP cores from a Pt^{2+} salt precursor has been evaluated. It has been found that $\nu_{\text{atop}}(\text{CO})$ on Pt further blue-shifts to 2065 cm^{-1} with no apparent bridging $\nu(\text{CO})$ upon growth of more Pt shells, as expected (Figure 4.12).

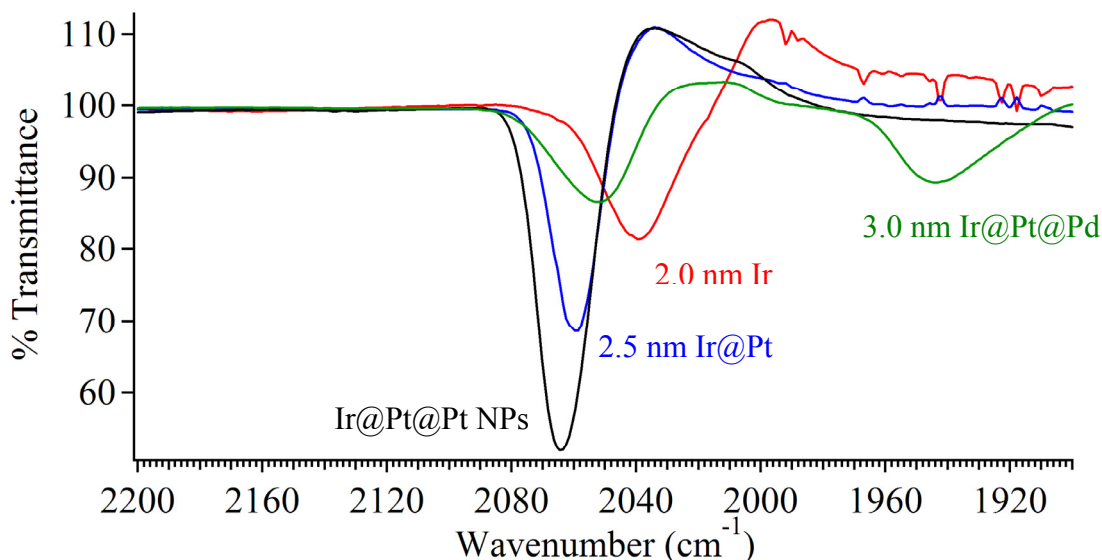


Figure 4.12. FT-IR spectra of CO-saturated colloids of 2.0 nm Ir particles, 2.5 nm Ir@Pt particles, 3.0 nm Ir@Pt@Pd NPs with 2.5 nm Ir@Pt cores and ca. 1 ML thick Pd shells, and 3.0 nm Ir@Pt NPs after two-step Pt growth.

Ru@M (M=Rh and Pd) NPs have also been characterized using FT-IR spectroscopy of the CO-saturated NP colloids. CO-probed surface analysis of the Ru@M NP systems demonstrated their core/shell architecture with Ru trapped in the core and electronically/geometrically-altered shells. Ru NPs show a single sharp peak for atop $\nu(\text{CO})$ at $2020\text{--}2035\text{ cm}^{-1}$ range. Similarly, $\nu_{\text{atop}}(\text{CO})$ of Rh NPs fall in almost the same range. In contrast, Rh NPs also show $\nu_{\text{bridge}}(\text{CO})$ at 1920 cm^{-1} , which is absent for Ru

NPs. FT-IR spectra of CO-saturated colloids of the Ru@Rh NPs exhibited ca. 10 cm^{-1} blue-shift of the $\nu_{\text{atop}}(\text{CO})$ and ca. 20 cm^{-1} blue-shift of the $\nu_{\text{bridge}}(\text{CO})$ with respect to those of the 2.7 nm Rh colloids. The $\nu_{\text{atop}}(\text{CO})$ s were also blue-shifted by ca. 5 cm^{-1} compared to that of the 3.0 nm Ru colloids (Figure 4.13a). These results were in favor of an electronically modified Rh surface. The 4.3 nm Ru@Rh NP colloids further exhibited a higher $I_{\text{bridge}}(\text{CO}) / I_{\text{atop}}(\text{CO})$ ratio which could be attributed to a geometrically different Rh surface than monometallic Rh surface and thus complementary to the XRD. Moreover, Atop $\nu(\text{CO})$ modes are strong and have narrow linewidths; bridging $\nu(\text{CO})$ modes exhibit increasing peak intensity with increasing Rh:Ru elemental ratio.

For the Ru/Pd system, CO probe studies were in favor of the formation of core/shell NPs with structurally-altered Pd shells, which were analogues to the Ru@Pt NPs (Chapter 2) and the Ru@Rh NPs (see above). As shown in Figure 4.13b, Ru@Pd NPs show characteristic $\nu(\text{CO})$ s for atop and bridging CO on Pd. However, the peak positions are shifted blue by ca. 10 cm^{-1} for the $\nu_{\text{atop}}(\text{CO})$ and ca. 5 cm^{-1} for the $\nu_{\text{bridge}}(\text{CO})$. Similarly, it was observed for the $\text{Ru}_x\text{@Pd}_{1-x}$ NPs that the $\nu_{\text{atop}}(\text{CO})$ s were blue-shifted accompanied by a loss in intensity and the $I_{\text{atop}}(\text{CO}) / I_{\text{atop}}(\text{CO})$ ratio was greatly diminished relative to the 4.0 nm Pd NPs (Figure 4.13b). It was believed that the decreasing ratio of edge sites to face sites associated with hetero-nucleation and subsequent growth of Pd was responsible for it.¹⁶⁸

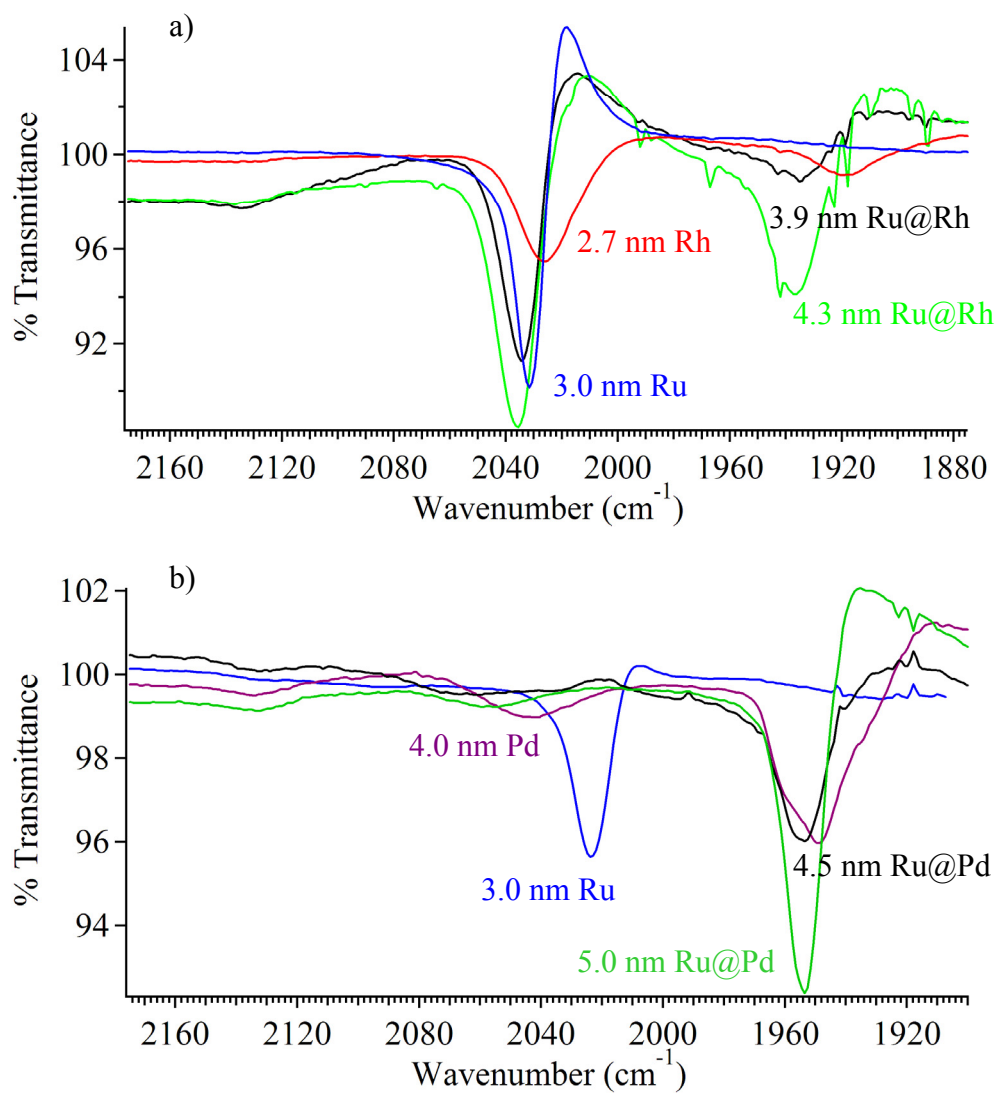


Figure 4.13. FT-IR spectra of CO-saturated colloids of (a) 3.0 nm Ru particles, 2.7 nm Rh particles, 3.9 nm Ru@Rh particles with ca. 1-2 MLs thick Rh shells, and 4.3 nm Ru@Rh particles with ca. 2-3 MLs thick Rh shells; and (b) 3.0 nm Ru particles, 4.0 nm Pd particles, 4.5 nm Ru@Pd particles with ca. 1-2 layers thick Pd shells, and 5.0 nm Ru@Pd particles with ca. 2-3 MLs thick Pd shells 4.0 nm Pd particles.

Finally, the tri-metallic Ru@Pt@Pd NPs with Pt shells of sub-monolayer coverage sandwiched between Ru core and 1-2 monolayers thick Pd shells have been evaluated by monitoring growth of successive layers with CO probe FT-IR (Figure 4.14).

The 2:1 stoichiometry of the elements in Ru@Pt NPs provides a partial coating of Ru NP cores, as calculated using Schmid's model. The $\nu(\text{CO})$ peak at 2023 cm^{-1} shifts blue to 2040 cm^{-1} with intensity loss and linewidth broadening. Accordingly, the $\nu(\text{CO})$ on Pt appears at 2065 cm^{-1} . Pd was used in a 1:1 elemental ratio with respect to total Ru and Pt loading to provide 1-2 MLs thick Pd shells. Strong $\nu(\text{CO})$ on Ru and $\nu(\text{CO})$ on Pt disappear in favor of a weak $\nu_{\text{atop}}(\text{CO})$ on Pd at 2050 cm^{-1} and a strong $\nu_{\text{bridge}}(\text{CO})$ on Pd at 1950 cm^{-1} . For comparison, Ru deposition with the same relative elemental ratio as Pd restores Ru-CO only peak at 2030 cm^{-1} .

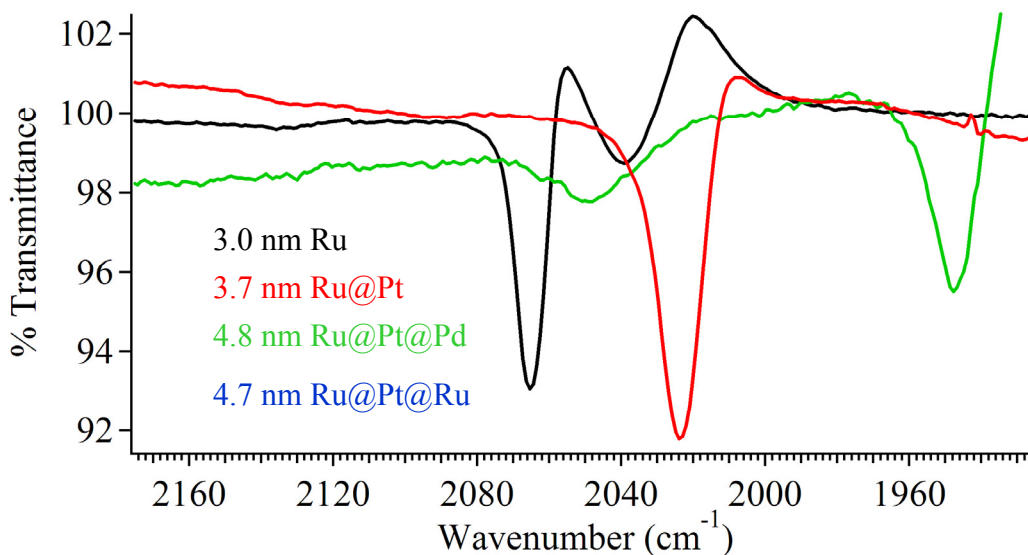


Figure 4.14. FT-IR spectra of CO-saturated colloids of 3.0 nm Rh particles, 3.7 nm Ru@Pt particles with submonolayer coverage of Pt, 4.8 nm Ru@Pt@Pd NPs with ca. 1-2 MLs thick Pd shells. For control, FT-IR spectrum of CO-saturated colloids of Ru@Pt@Ru NPs with 3.7 nm Ru@Pt cores and ca. 1-2 MLs thick Ru shells is also shown.

4.3.6. Micro Raman for structure analysis and surface probing

Micro-Raman has been used to characterize CO saturated surfaces of PVP-free Ir@Pt NPs. PVP-free Pt NPs show the $\nu(\text{Pt-C})$ at ca. 480 cm^{-1} and the Pt-CO peak at 2095 cm^{-1} as discussed in Chapters 2 and 3. PVP-free Ir NPs show a very strong $\nu(\text{Ir-C})$ peak at 539 cm^{-1} and a weaker Ir-CO peak at 2075 cm^{-1} . PVP-free Ir@Pt NPs, on the other hand, exhibit very weak $\nu(\text{M-C})$ at ca. 480 cm^{-1} (Figure 4.15a) and a weak $\nu(\text{CO})$ peak at ca. 2085 cm^{-1} (Figure 4.15b), which are tentatively attributed to CO adsorption on electronically altered Pt surface sites.

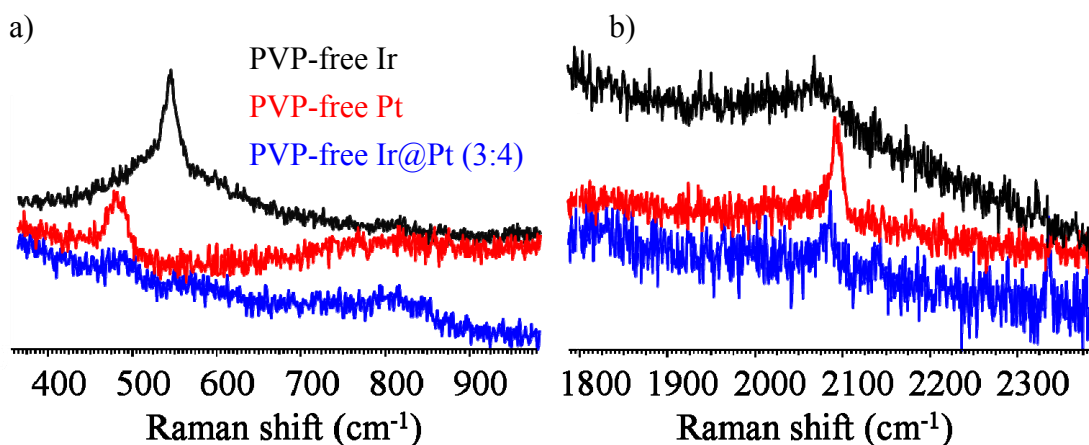


Figure 4.15. Micro-Raman spectra of PVP-free Ir, PVP-free Pt and PVP-free Ir@Pt (3:4) NPs in the (a) M-C stretch region and (b) C-O stretch region.

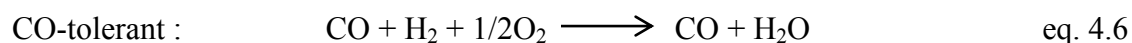
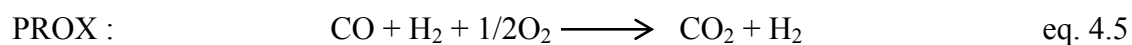
4.3.7. Catalytic Evaluation of supported M@Pt NP catalysts in PROX/CO oxidation

4.3.7.1. M@Pt NPs (M=Ru, Rh, Ir, Pd, Au)

The catalytic activity of M@Pt (M=Ru, Rh, Ir, Pd and Au) core/shell NPs with approximately 1 ML thick Pt shells toward PROX reaction was evaluated under various reaction conditions. M@Pt nanoparticle catalysts supported in γ -Al₂O₃ by 1% weight Pt were first screened at a PROX feed composed of 1000 ppm CO, 5000 ppm O₂, 50% H₂ and 49.7% Ar. Because the core/shell nanoparticles of ca. 1 ML thick Pt shells (and similar particle sizes) were normalized by Pt content, the total surface area of any catalyst charge was approximately equal. For example, the 2.5 nm Ir@Pt particles, 1.0% by weight Pt supported in γ -Al₂O₃, had a TEM-projected surface area of ca. $1.5 * 10^3$ m² and a number density of ca. $2.0 * 10^{20}$ nanoparticles per gram of the catalyst. Similarly, the 5.0 nm Pd@Pt particles, 1.0% by weight Pt supported in γ -Al₂O₃, had a TEM-projected surface area of ca. $1.4 * 10^{20}$ m² and a number density of ca. $0.4 * 10^{20}$ nanoparticles per gram of the catalyst. As such, the observed trends in PROX activity and selectivity would directly reflect the surface reactivity.

For 1000 ppm CO, the PROX activities decreased in the order of Ru@Pt > Rh@Pt > Ir@Pt > Pd@Pt > Au@Pt > Pt. Furthermore, all but the Au@Pt catalyst showed H₂ activation subsequent to CO oxidation (Figure 4.16). For the Au@Pt NPs catalyst, however, H₂ and CO oxidations occurred simultaneously (Figure 4.18). For 2000 ppm CO, the trends in PROX activities were retained with minor differences (Figure 4.17). The PROX activities followed the order Ru@Pt > Rh@Pt \approx Ir@Pt >

Pd@Pt > Au@Pt > Pt. The most noticeable difference from the 1000 ppm CO case was the M@Pt core/shell NPs with Rh and Ir NP cores performed comparable, but poorer than the Ru@Pt NPs, as shown in Figure 4.17. Secondly, the Au@Pt NPs catalyst exhibited only partial CO oxidation at complete O₂ consumption. CO-tolerant behavior (see equations 4.5 and 4.6) of the Au@Pt NPs became apparent, however, their low temperature CO and H₂ oxidation capability made them better H₂ activation catalyst in the presence of CO than monometallic Pt NPs.



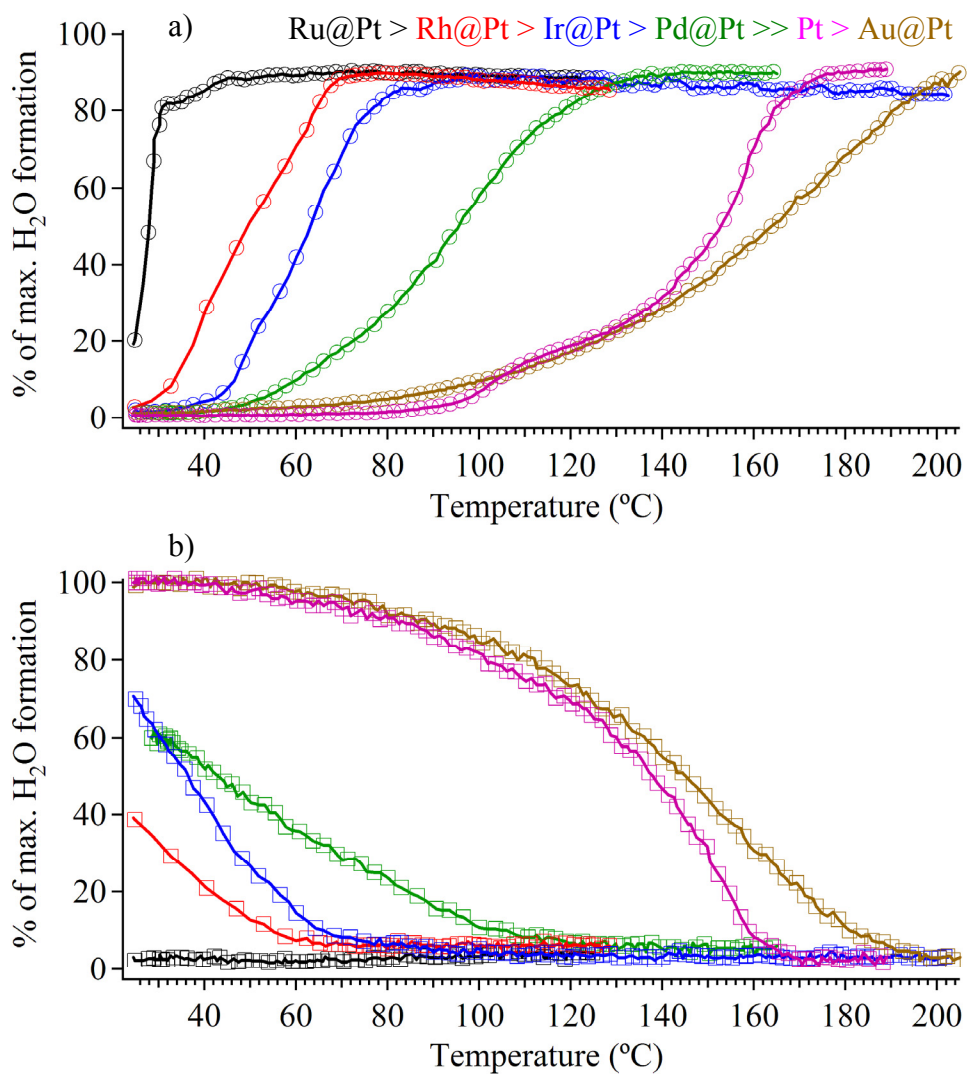


Figure 4.16. TPR plots for the PROX reaction showing (a) H₂O formations and (b) CO concentrations at 1000 ppm CO level of the M@Pt (M=Ru, Rh, Ir, Pd and Au) core/shell NPs with ca. 1 ML thick Pt shells and the 2.5 nm Pt particle catalysts. The gas hourly space velocity is 2.3×10^5 mL/g/h. The gas mixture for the PROX reaction was composed of 0.1% CO, 0.5% O₂, 50% H₂, and balance Ar.

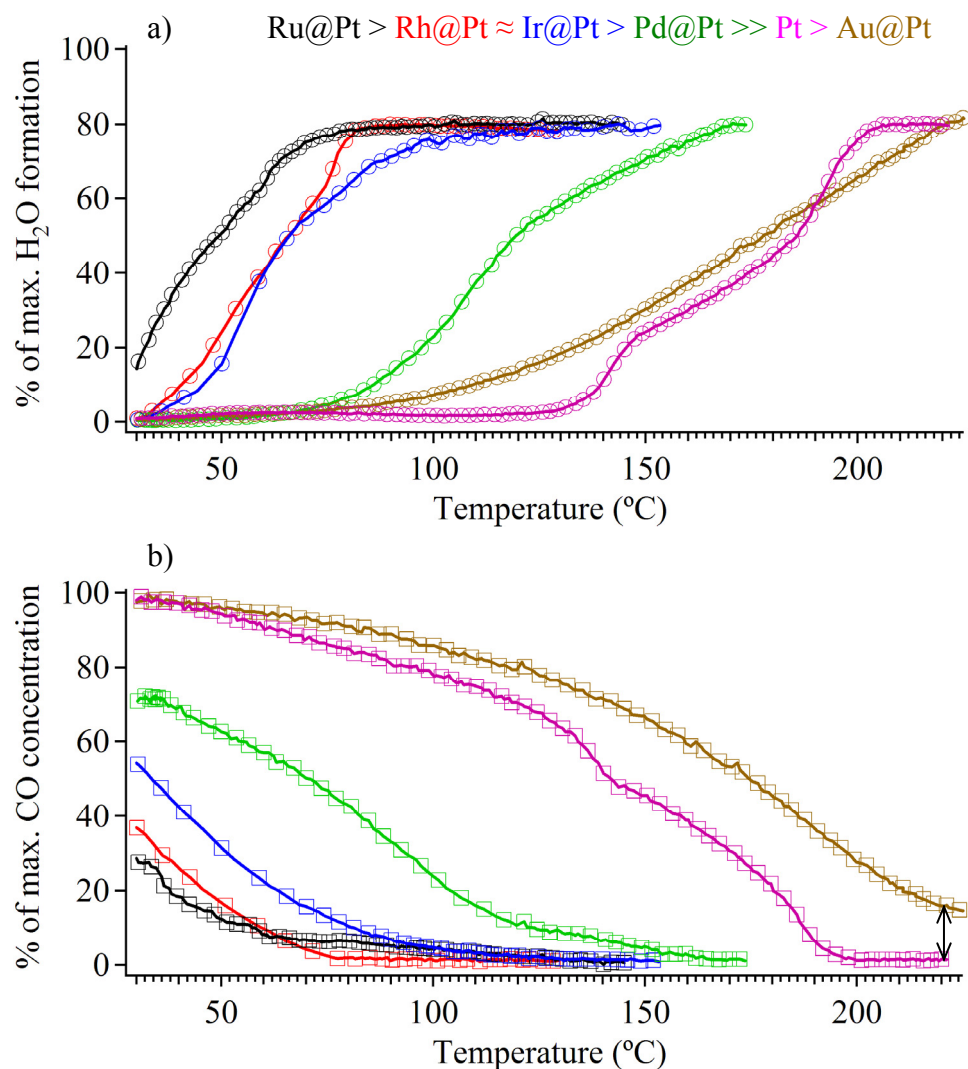


Figure 4.17. TPR plots for the PROX reaction showing (a) H₂O formations and (b) CO concentration at 2000 ppm CO level of the M@Pt (M=Ru, Rh, Ir, Pd and Au) core/shell NPs with ca. 1 ML thick Pt shells and the 2.5 nm Pt particle catalysts. The gas hourly space velocity is 2.3×10^5 mL/g/h. The gas mixture for the PROX reaction was composed of 0.2% CO, 0.5% O₂, 50% H₂, and balance Ar. Arrow shows % of unreacted CO.

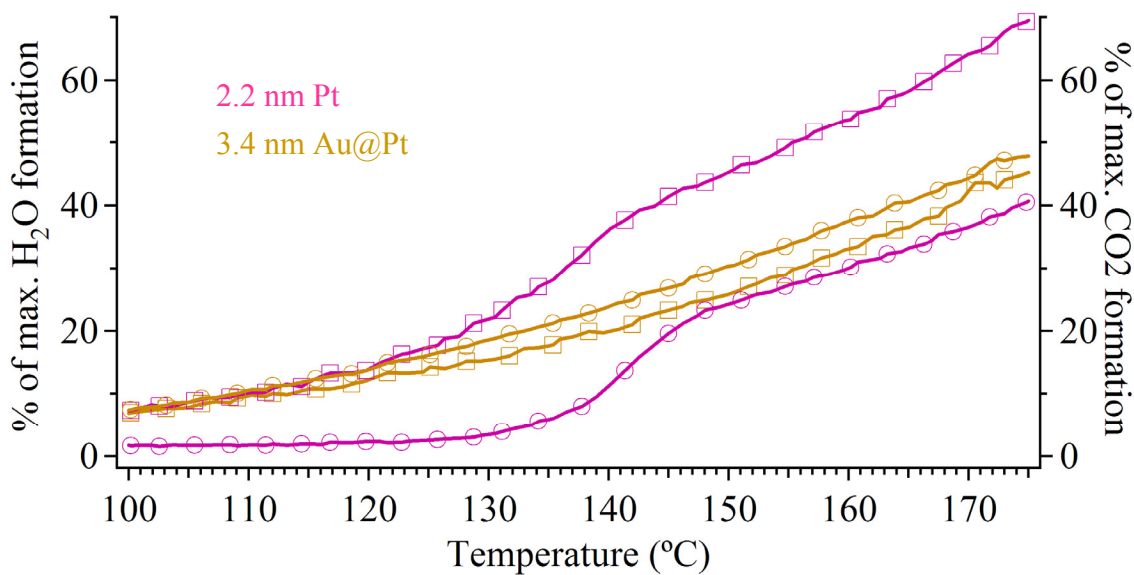


Figure 4.18. TPR plots for the PROX reaction showing CO₂ (open triangles) and H₂O (open circles) formations at 2000 ppm CO level of the 3.4 nm core/shell Au@Pt and 2.2 nm monometallic Pt catalysts.

Finally, the Ir@Pt NPs with ca. 1 ML thick Pt shells outperformed the Rh@Pt and Ru@Pt NPs with ca.1 ML thick Pt shells at 10000 ppm (1.0%) CO level (Figure 4.19). Moreover, the Rh@Pt catalyst performed better than the Ru@Pt catalyst. CO selectivity ranged between >90% at low temperatures for partial O₂ conversions and >55% at high temperatures for complete O₂ conversions. The Au@Pt NPs with ca. 1 ML thick Pt shells exhibited the lowest activity among all studied under given temperature and CO partial pressure. As shown in Figure 4.19, CO selectivity for the PROX reaction on the Au@Pt catalyst never exceeded 60%, and went below 40% at high temperatures (>150 °C) and intermediate O₂ conversions. Although the Au@Pt catalyst exhibited higher CO conversion rates than the Pt catalyst at kinetically controlled region at low temperatures (Figure 4.19), the distinct thermo-chemistry of PROX reaction on the

electronically/geometrically-altered Au@Pt surface resulted in its unique CO-tolerant behavior (see DFT section below).

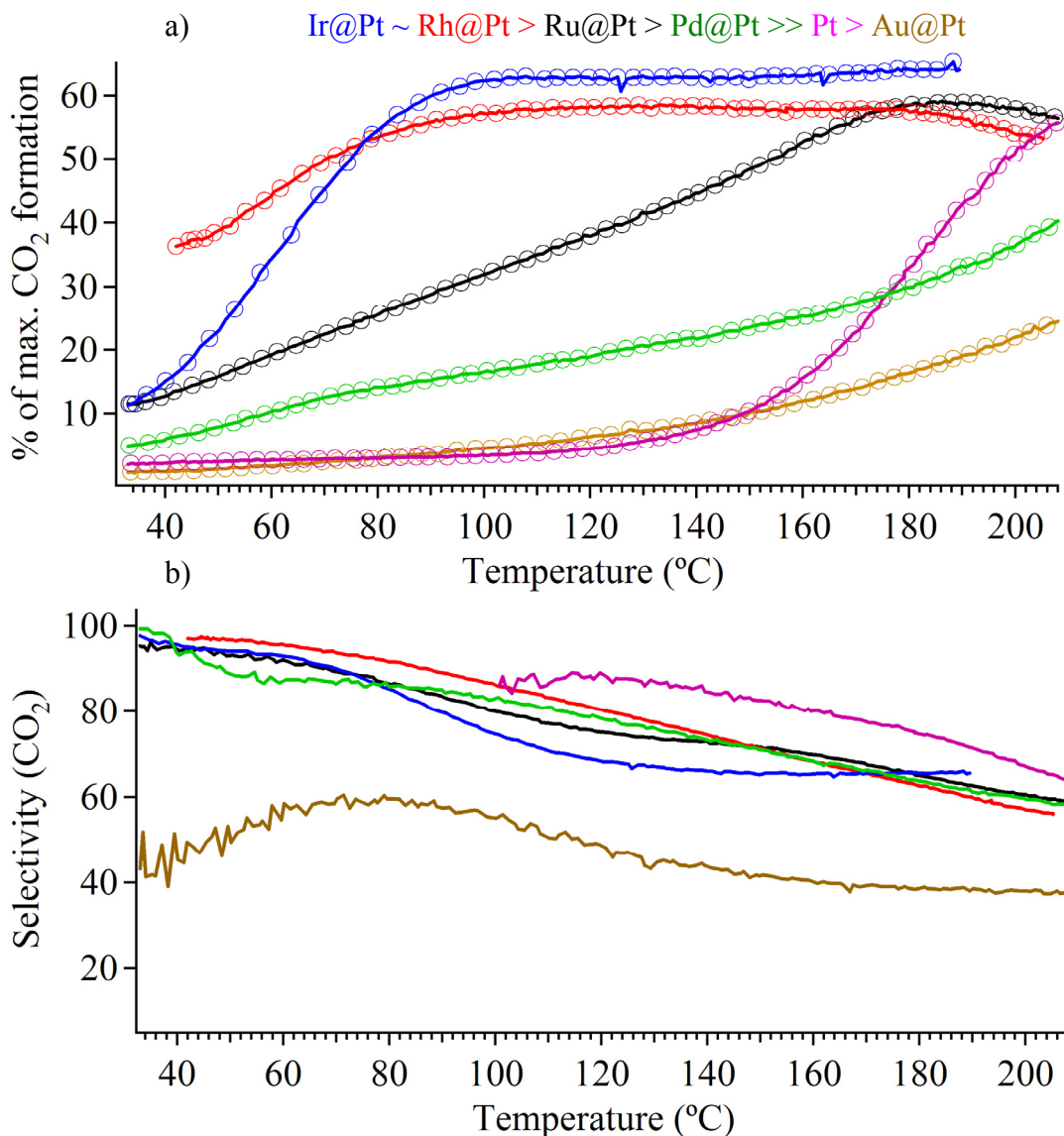


Figure 4.19. TPR plots for the PROX reaction showing (a) CO₂ formation and (b) selectivity for CO₂ formation at 10000 ppm CO level of the M@Pt (M=Ru, Rh, Ir and Au) core/shell NPs with ca. 1 ML thick Pt shells and the 2.5 nm Pt particle catalysts. The gas hourly space velocity is 2.3×10^5 mL/g/h. The gas mixture for the PROX reaction was composed of 1.0% CO, 0.5% O₂, 50% H₂, and balance Ar. CO selectivity is defined as $100 \times (\chi_{\text{CO}_2} / (\chi_{\text{CO}_2} + \chi_{\text{H}_2\text{O}}))$.

4.3.7.2. Ru@M NPs (M=Pt, Rh and Pd)

The PROX reaction was also used to evaluate the catalytic activity of Ru@M (M=Pt, Pd and Rh) core/shell NPs. The Ru@M (1:2) NP catalysts with ca. 2-3 MLs thick M shells were prepared 1.0 % M by weight in γ -Al₂O₃. The Ru@M (1:1) (M=Pt and Rh) NP catalysts with ca. 1-2 monolayer thick M shells were 0.52 and 0.53% M, respectively, by weight supported in γ -Al₂O₃. The Ru@Pt (1:1) NP catalyst with ca. 1-2 MLs thick Pt shells were also prepared 1.0% Pt by weight. Having that the supported core/shell NPs were normalized by weight of the shell-metals, they had comparable total surface areas per gram of any catalyst charge, except the Ru@Pt (1:2) NP catalyst which had approximately half the total surface area as the others. For 2000 ppm CO concentration, the Ru@M (1:1) NPs (M=Pt, Pd and Rh) with ca. 1-2 MLs thick M shells showed increasing PROX activities in the order of Ru@Pt (1:1) >> Ru@Pd (1:1) > Ru@Rh (1:1). Furthermore, the Ru@Pd (1:1) NP catalyst exhibited partial CO oxidation (>90%) at complete O₂ conversion (Figure 4.20). The same activity order was also observed for the Ru@M (1:2) (M=Pt, Pd and Rh) series of NP catalysts only with minor differences. The Ru@Pt (1:2) NPs performed better (Figure 4.21). The Ru@M (1:2) (M=Pt and Rh) NPs exhibited identical performances with partial CO oxidations (~60% at maximum).

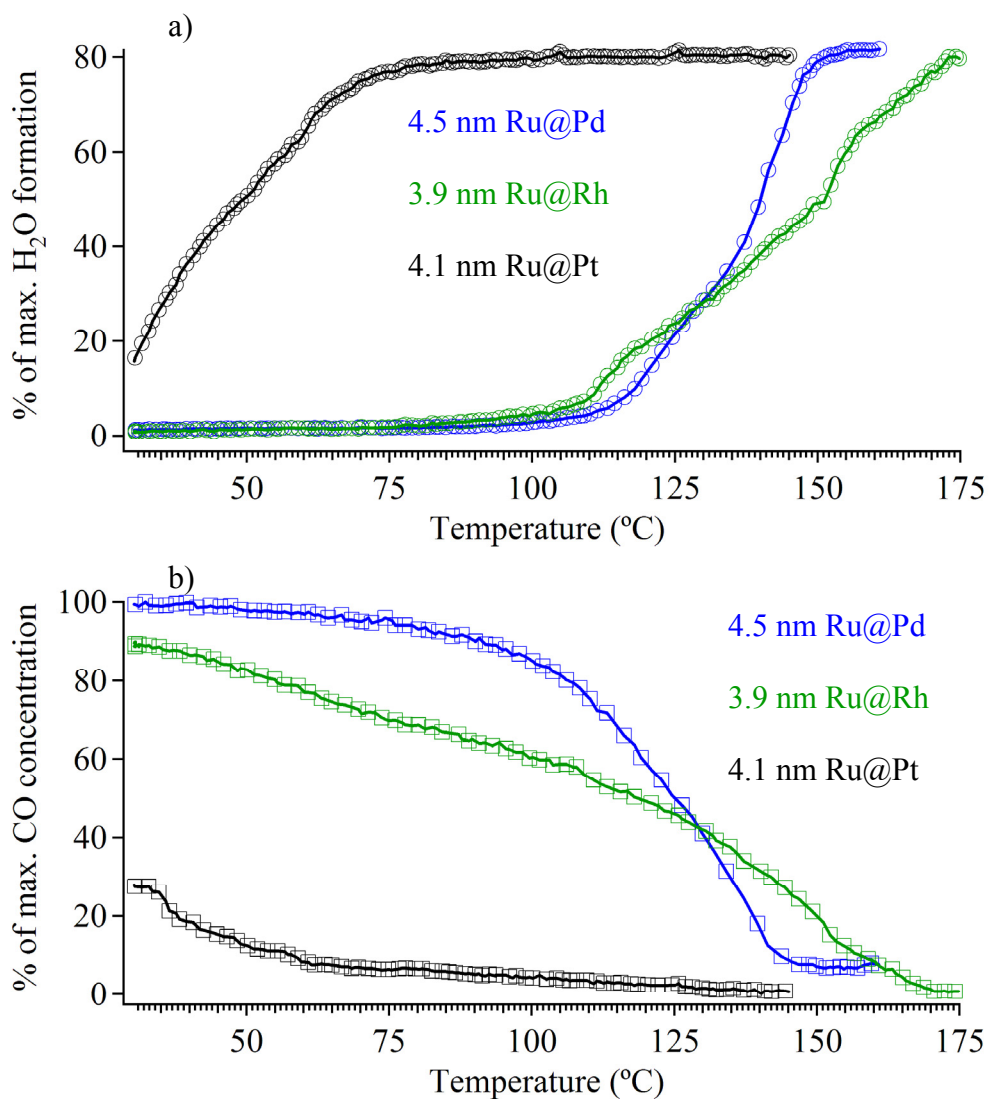


Figure 4.20. TPR plots for the PROX reaction showing (a) H₂O formations and (b) CO concentration at 2000 ppm CO level of the Ru@M (1:1) (M=Pt, Pd and Rh) core/shell NPs with ca. 1-2 MLs thick M shells. The gas hourly space velocity is 2.3×10^5 mL/g/h. The gas mixture for the PROX reaction was composed of 0.2% CO, 0.5% O₂, 50% H₂, and balance Ar.

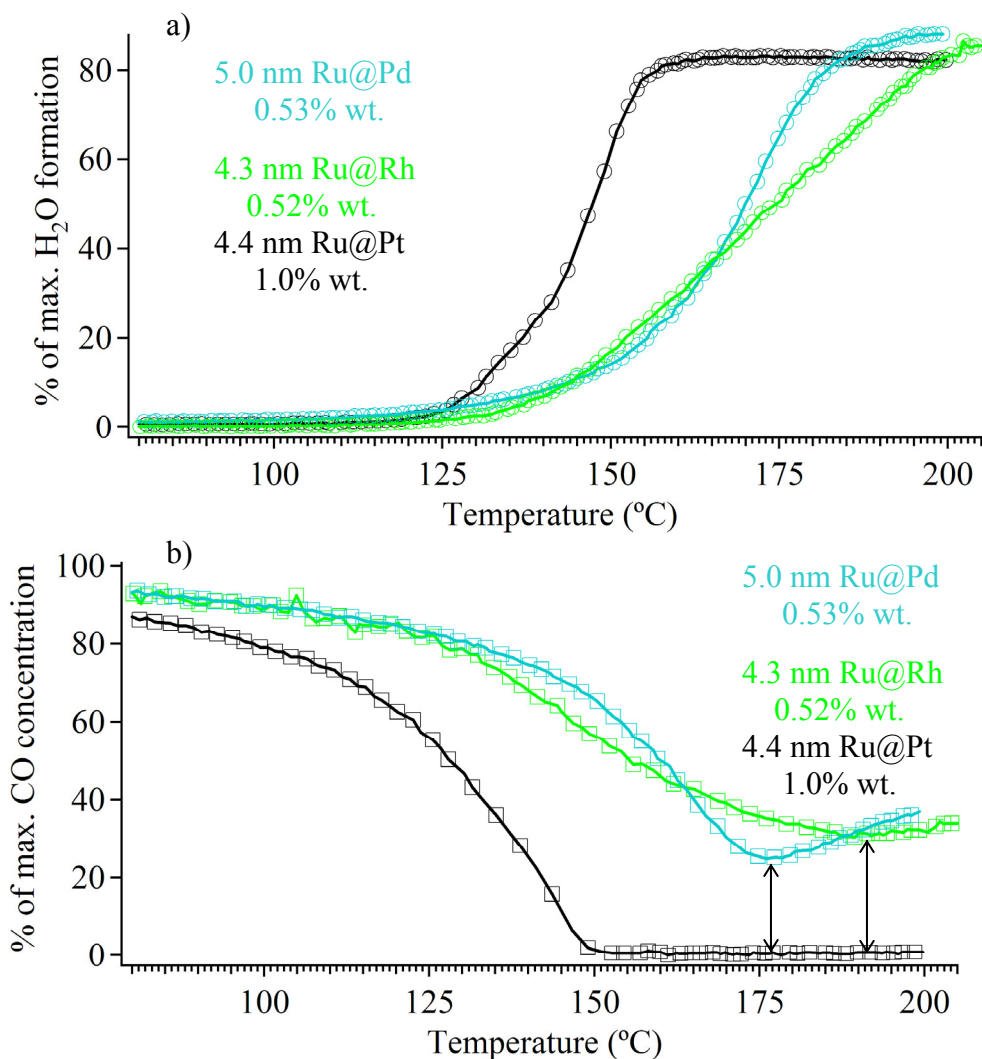


Figure 4.21. TPR plots for the PROX reaction showing (a) H₂O formations and (b) CO concentrations at 2000 ppm CO level of the Ru@M (1:2) (M=Pt, Pd and Rh) core/shell NPs with ca. 2-3 MLs thick M shells. The gas hourly space velocity is 2.3×10^5 mL/g/h. The gas mixture for the PROX reaction was composed of 0.2% CO, 0.5% O₂, 50% H₂, and balance Ar. Arrows show % of unreacted CO.

CO selectivity and PROX activity of the Ru@M NPs (M=Pt, Pd and Rh) were determined using H₂ feeds contaminated with 1.0% CO and stoichiometric concentrations of O₂. The Ru@Pt (1:1) NPs were the most active toward PROX reaction under the conditions studied. As shown in Figure 4.22a, the Ru@Rh (1:1) NPs exhibited

the highest selectivity toward CO oxidation (>60%), and the Ru@Pd (1:1) NPs the lowest selectivity (<40%). Figure 4.22b showed the CO selectivity and PROX activity of the $\text{Ru}_x\text{@M}_{1-x}$ (M=Pd and Rh; $x=0.33$ and 0.5) NP catalysts. The improved CO selectivity of the Ru@Rh (1:1) NPs with ca. 1-2 MLs thick Rh shells dropped drastically for the Ru@Rh (1:2) NPs with ca 2-3 MLs thick Rh shells. Similarly, the PROX activity was lower for the thick layers of Rh on Ru than the thinly shelled Ru@Rh NPs (Figure 4.22b). Since the number of surface atoms was normalized with respect to Rh, the PROX reactivity differences across the $\text{Ru}_x\text{@Rh}_{1-x}$ series NP catalysts were attributed to the substrate effects. Similar trends could be tracked on the $\text{Ru}_x\text{@Pd}_{1-x}$ series of NP catalysts, except that the differences were not as significant (Figure 4.22b).

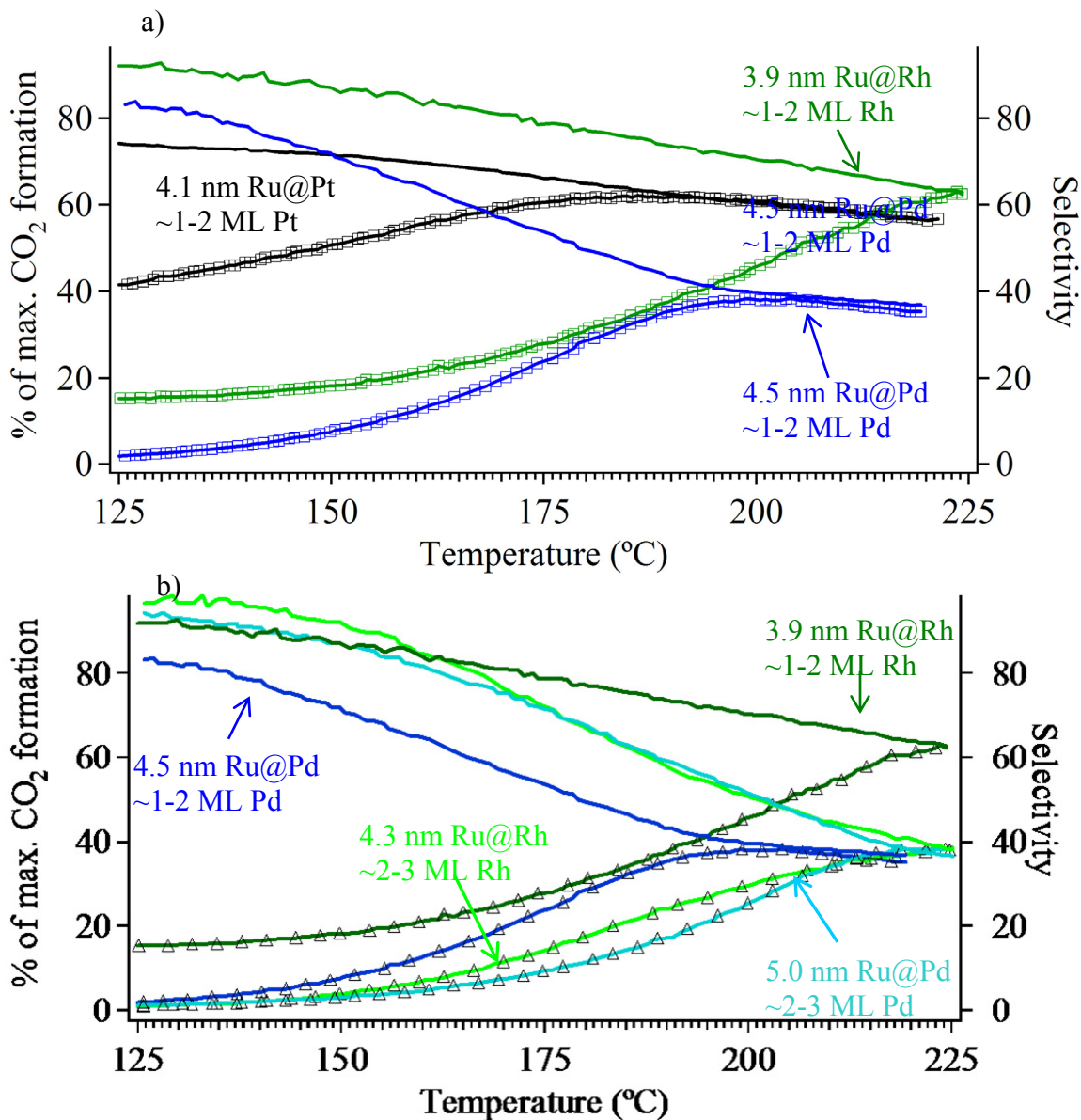


Figure 4.22. TPR plots for the PROX reaction showing CO₂ formations and CO selectivities at 10000 ppm CO level of (a) the Ru@M (1:1) (M=Pt, Pd and Rh) core/shell NPs with ca. 1-2 layers thick Pt shells catalysts, and (b) the Ru_x@M_{1-x} (M=Pd and Rh; x=0.33 and 0.5) core/shell NPs catalysts. The gas hourly space velocity is 2.3×10^5 mL/g/h. The gas mixture for the PROX reaction was composed of 1.0% CO, 0.5% O₂, 50% H₂, and balance Ar. CO selectivity is defined as $100 \times (\chi_{\text{CO}_2} / (\chi_{\text{CO}_2} + \chi_{\text{H}_2\text{O}}))$. % of maximum CO₂ formation is shown by open squares, and % selectivities by lines.

Finally, the $\text{Ru}_x\text{@Pt}_{1-x}$ NPs ($x=0.5$ and 0.33) were compared to the 3.0 nm Ru particles catalyst (1.0% Ru by weight) and the 2.7 nm Rh particle catalyst (1.0% Rh by weight). It was observed that the Ru@Pt (1:1) NPs with ca. 1-2 MLs thick Rh shells exhibited PROX activity intermediate to those of monometallic Ru and monometallic Rh NPs (Figure 4.23). In contrast, the Ru@Rh (1:2) NPs with ca. 2-3 MLs thick Rh shells performed poorer than the end members. Moreover, they exhibited a CO tolerant behavior with only a fraction of CO (~60%) oxidized to CO_2 . The CO-tolerant behavior was a unique property because neither the Ru NPs nor the Rh NPs exhibited CO tolerance under O_2 -rich CO- contaminated H_2 feeds. The catalytic properties of the Rh atoms were altered by the substrate to give a modified surface reactivity at 2 ML coverage. The true nature of the catalytic changes could be of electronic (or geometric) and thus require more systematic studies.

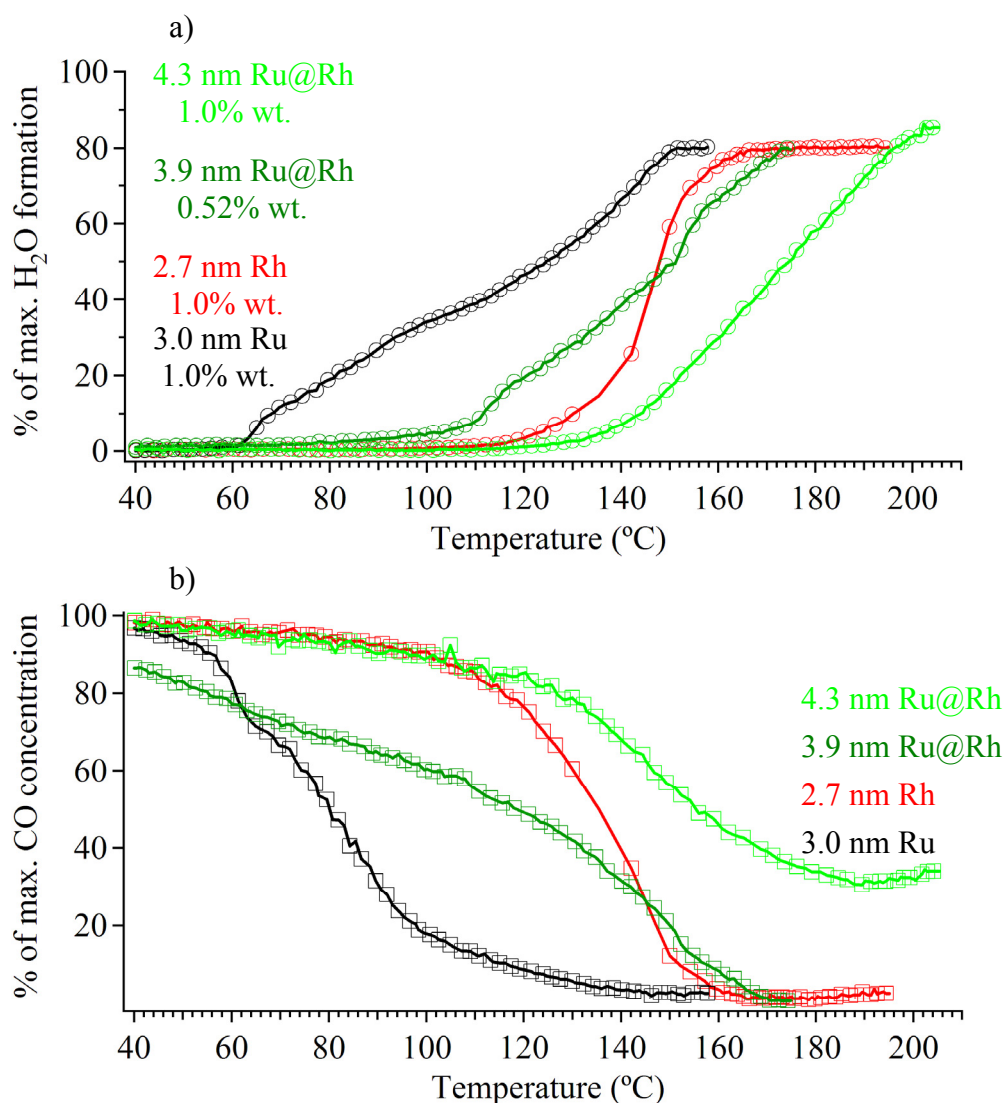


Figure 4.23. TPR plots for the PROX reaction showing (a) H₂O formations and (b) CO concentrations at 2000 ppm CO level of the Ru_x@Rh_{1-x} (x=0.33 and 0.5) NPs, 2.7 nm Rh particles and 3.0 nm Ru particles catalysts. The gas mixture for the PROX reaction was composed of 0.2% CO, 0.5% O₂, 50% H₂, and balance Ar.

4.3.7.3. M@Pt@Pd NPs (M=Ru and Ir)

The catalytic activity and CO selectivity of PROX reaction was shown to be tunable on the well-characterized tri-metallic core-shell structures with sandwiched Pt

and ca. 1 ML thick Pd shells of Pt group elements. The Ru/Pt/Pd system was studied in PROX reaction under 2000 ppm CO-contaminated H₂ feeds. The 4.8 nm Ru@Pt@Pd particles were synthesized via nucleation of Pd over the preformed 3.7 nm Ru@Pt particles, so that the Ru@Pt NPs were included in Figure 4.24 as well as the 4.5 nm Ru@Pd particles with ca. 1-2 MLs thick Pd shells and 5.0 nm Ru@Pd particles with ca. 2-3 MLs thick Pd shells. The Ru@Pt@Pd NPs were supported in γ -Al₂O₃ 0.55% Pd by weight and the Ru@Pt NPs 1.0% Pt by weight, so that all the core/shell structures regardless of their composition and overall particle size had approximately the same projected surface area. The Ru@Pt NPs had the lowest H₂ activation temperature catalyst, subsequent to CO oxidation light-off, and thus showed the highest activity toward PROX reaction (Figure 4.24). The Ru_x@Rh_{1-x} NP catalysts performed relatively poor with partial CO oxidation at temperature of complete O₂ oxidation. The Ru@Pt@Pd NPs with Pt shells at sub-monolayer coverage sandwiched in between 3.0 nm Ru cores and Pd shells of 1-2 MLs thick exhibited PROX activity and selectivity intermediate to those of the Ru_x@Pd_{1-x} NPs with Pd shells of ca. 1-2 MLs thick (x=0.5) and of ca. 2-3 MLs thick (x=0.33).

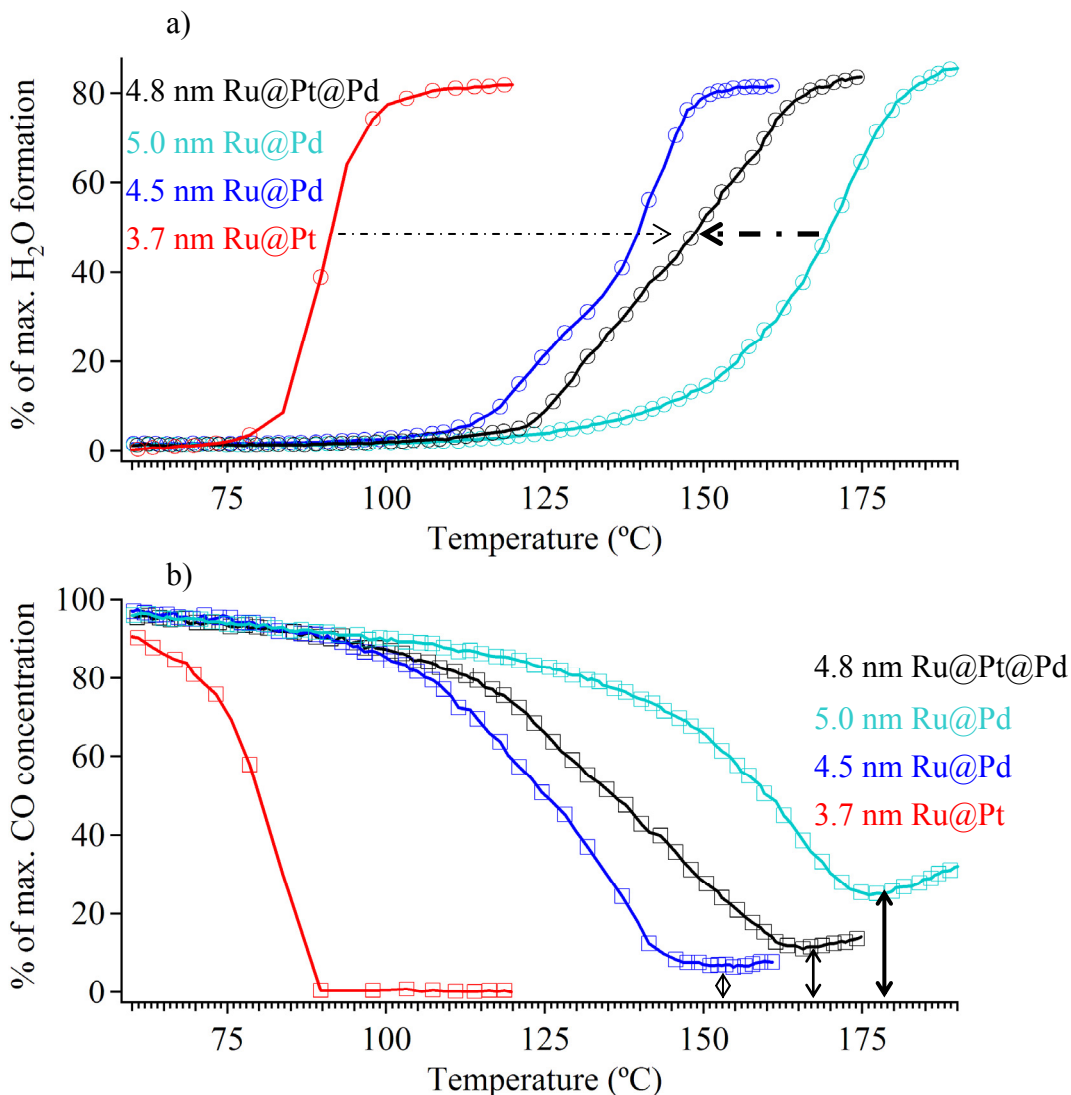


Figure 4.24. TPR plots for the PROX reaction showing (a) H₂O formations and (b) CO concentrations at 2000 ppm CO level of the 4.4 nm Ru@Pd@Pt core/shell1/shell2 particles, Ru_x@Rh_{1-x} (x=0.33 and 0.5) NPs, and 3.7 nm Ru@Pt particles catalysts. The gas mixture for the PROX reaction was composed of 0.2% CO, 0.5% O₂, 50% H₂, and balance Ar.

Finally, the 3.0 nm Ir@Pt@Pd particles with 2.5 nm Ir@Pt particle cores and ca. 1 ML thick Pd shells were evaluated in PROX reaction, and compared to the parent Ir@Pt NPs and the 4.5 nm Ru@Pd particles. The catalyst loading was normalized to those of the bimetallic systems to give the same projected surface area. The 4.5 nm

Ru@Pd particles with ca. 1-2 MLs thick Pd shells exhibited the highest PROX activity among the other core/shell NPs with Pd surface atoms (see Figure 4.25). In general, core/shell NPs with the Pd shells exhibited lower surface reactivities than those with the Pt shells of similar thicknesses. As seen in Figure 4.25 for 2000 ppm CO level, the Ir@Pt@Pd NPs with ca. 1 ML thick Pd shells performed with little loss of PROX activity compared to the parent bimetallic particles with Pt-only surface atoms (see Figure 4.12 in FT-IR section). In contrast, the Ru@Pd NPs with ca. 1-2 MLs thick Pd shells exhibited poor performance, -ca. 2 orders of magnitude lower reaction kinetics than the Ir@Pt@Pd NPs, under identical reaction conditions (Figure 4.25). For 1.0% CO level, the trimetallic NPs with Pd-only surface atoms showed ~40% CO concentration with ~90% selectivity at about 80 °C. CO selectivity dropped to ~55% at 130 °C at which point PROX reaction was over. However, the Ru@Pd NPs with the same number of Pd surface atoms did not ignite CO oxidation until 140 °C, subsequent to H₂ activation. In contrast to the tri-metallic system with Pd-only surface, CO selectivity dropped quickly below 40% for the bimetallic system with Pd-only surface. Thus, the 3.0 nm Ir@Pt@Pd particles exhibited a better PROX character than the CO-tolerant 4.5 nm Ru@Pd particles of similar projected surface-Pd. The $\nu_{\text{atop}}(\text{CO})$ peak intensity relative to that of the $\nu_{\text{bridge}}(\text{CO})$ on the Ir@Pt@Pd NP colloids (Figure 4.12) was greatly enhanced compared to those on the monometallic Pd (Figure 4.11a), and the core/shell Ru@Pd (Figure 4.13b) and Ru@Pt@Pd (Figure 4.14) NP colloids. Along with the spectral shifts in peak positions, these intensity changes are resulted from the altered electronic/geometric structure of the Ir@Pt@Pd NPs relative to the other NPs with Pd-only surfaces. Thus, the

substrate effect may account for the enhanced surface reactivity of the Ir@Pt@Pd NPs toward the PROX reaction.

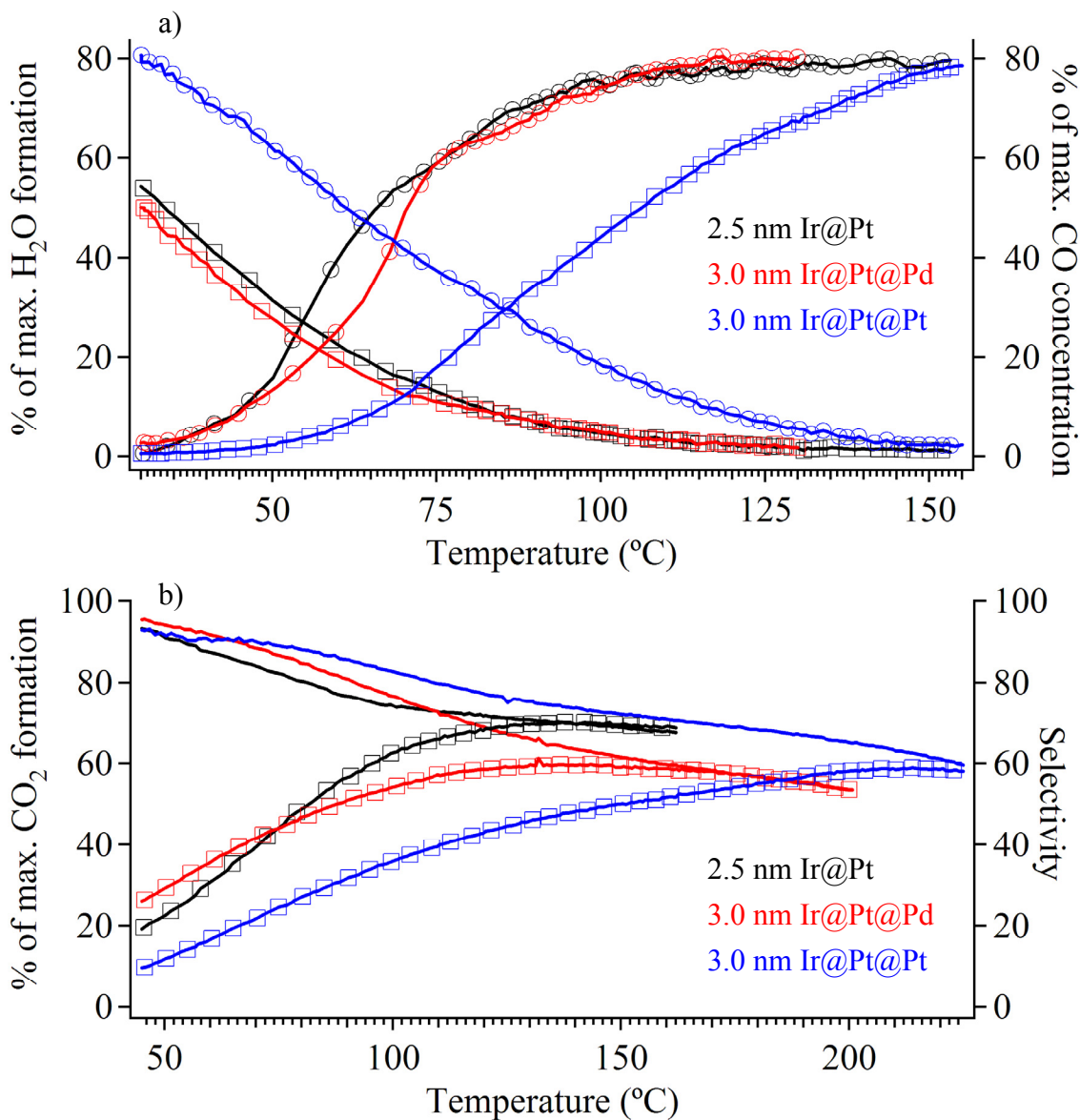


Figure 2.25. TPR plots for the PROX reaction showing (a) H₂O formations and CO concentrations at 2000 ppm CO level and (b) CO₂ formation and selectivity at 1.0% CO and 0.5% O₂ for the 3.0 nm Ir@Pt@Pd core/shell1/shell2 particles, 3.0 nm Ir@Pt@Pt core/shell particles, and 2.5 nm Ir@Pt particles catalysts. The gas hourly space velocity is 2.3×10^5 mL/g/h.

4.3.8. Density Functional Theory (DFT) Calculations

DFT calculations were employed first to study the adsorption energetic of CO as a function of its surface coverage, and to estimate the CO saturation coverage on the closest-packed facet of these NSA model surfaces, and then to analyze the thermochemistry and kinetics of H₂ dissociation (H₂ → 2H*) on these model surfaces as a function of CO coverage. DFT calculations were performed at the University of Wisconsin-Madison by Prof. Mavrikakis and Dr. Nilekar.

The Pt*/M surfaces which were analogues to the M@Pt core/shell NPs were modeled by a single layer of platinum atoms placed on top of three-layer slabs of Au(111), Pd(111), Ir(111), Rh(111), or Ru(0001). Binding energies (BE's) were calculated as follows: $BE = E_{ads} - E_{clean} - E_{gas}$, where E_{ads} , E_{clean} and E_{gas} are the total energies of the slab with the adsorbate on it, the metal slab without adsorbed species, and the adsorbed species in the gas phase, respectively. The differential binding energy (BE_{diff}) for CO was defined as the energy change for the reaction: $(nCO(a) + surface + CO(g) \rightarrow (n+1) CO(a) + surface)$; the highest CO coverage for which the differential binding energy of CO was still negative defines the CO-saturation coverage on the respective surface.

The differential binding energies (BE_{diff}) of CO on the six Pt-containing surfaces were plotted as a function of CO coverage in Figure 4.26 along with the optimized geometries for CO on Pt(111), at $\theta_{CO} = 1/6, 1/3, 1/2$ and $2/3$ ML. With increasing CO coverage the BE_{diff} decreases for all surfaces, reflecting a weaker binding because of surface atom sharing and because of adsorbate-adsorbate repulsion.

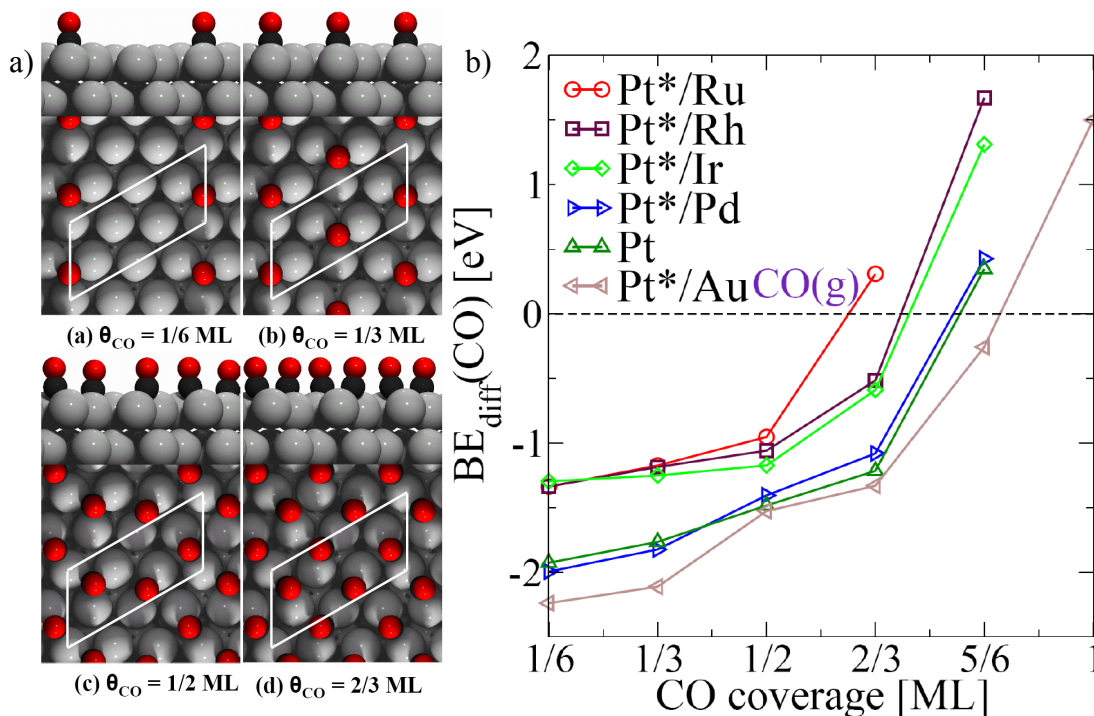


Figure 4.26. (a) Cross-section and a-top views of the optimized geometries of CO adsorbed on Pt(111) at various coverages. Red, black and gray spheres represent O, C and Pt atoms, respectively. As a guide to the eye the unit cell drawn with white lines. (b) Differential binding energy for CO as a function of CO coverage on various Pt*/M model (111) or (0001) surfaces. A positive differential BE indicates that the respective state is not stable on the surface.

At all CO coverages, a Pt monolayer on Ru(0001), Rh(111) and Ir(111) exhibited considerably weaker CO binding as compared to Pt(111), because of both the ligand effect and the compressive strain introduced in the Pt overlayer by the respective substrate. For example, since $BE_{\text{diff}}(\theta_{\text{CO}}=2/3 \text{ ML})$ was positive on Pt*/Ru, the corresponding $\theta_{\text{CO}}^{\text{sat}}$ for this surface was 1/2 ML (Figure 4.26). Among the surfaces studied here, only Pt*/Au showed a higher BE_{diff} for CO at all coverages when compared to Pt, yielding a $\theta_{\text{CO}}^{\text{sat}} = 5/6 \text{ ML}$. This was partly because of the expansive strain induced to the Pt overlayer by the Au substrate. Differences in CO saturation coverage and the

$BE_{\text{diff}}(\text{CO})$ on various surfaces should relate to the relative difficulty in CO removal via oxidation and to the availability of free surface sites for catalytic events. In particular: (i) the lower the CO-saturation coverage the more free sites for catalytic events would exist on the surface, and (ii) the weaker the binding of CO on a surface, the easier to oxidize it to CO_2 on that surface.

The activation energy barrier (E_a) and heat of reaction (ΔH) as a function of the CO coverage were plotted in Figure 4.27. These data clearly showed that the heat of reaction, $E(2^*\text{H}(\text{a})) - E(\text{H}_2(\text{a}))$, uniformly decreased with increasing CO coverage on all surfaces (Figure 4.27a). Since the initial state for this reaction, $\text{H}_2(\text{a})$, bonded very weakly, if at all, on all surfaces, the change in heat of reaction reflected the change in binding of atomic hydrogen in the presence of CO. As shown in Figure 4.27a, the activation energy for H_2 dissociation increased with CO coverage for all surfaces studied. For instance, H_2 dissociation remained spontaneous ($E_a = 0$ eV) on Pt(111) for $\theta_{\text{CO}} = 0$, $1/6$ and $1/3$ ML. However, E_a increased to 0.31 and 1.4 eV for $\theta_{\text{CO}} = 1/2$ and $2/3$ ML, respectively. Therefore, apart from the site-blocking effect introduced because of high CO coverage, the Pt surface also became considerably less reactive: the barrier for H_2 dissociation on the CO-saturated Pt(111) surface was 1.4eV. The effect of CO coverage on E_a for H_2 dissociation on other surfaces follows a similar trend. Among all surfaces studied, Pt*/Ru(0001) had the lowest CO-saturation coverage ($1/2$ ML) and required the lowest E_a (0.85 eV), to activate H_2 , which was almost half of that for H_2 dissociation on the CO-saturated Pt(111) surface. For Pt*/Au, the most stretched surface, the exothermicity of the reaction was retained at all CO coverages, except at the CO saturation coverage ($5/6$ ML). For Pt*/Pd and Pt, the reaction became endothermic at the

CO-saturation coverage (2/3 ML). The reaction became endothermic at lower CO coverages ($\geq 1/2$ ML) for Pt*/Ru, Pt*/Rh and Pt*/Ir, all binding adsorbates more weakly (Figure 4.27b).

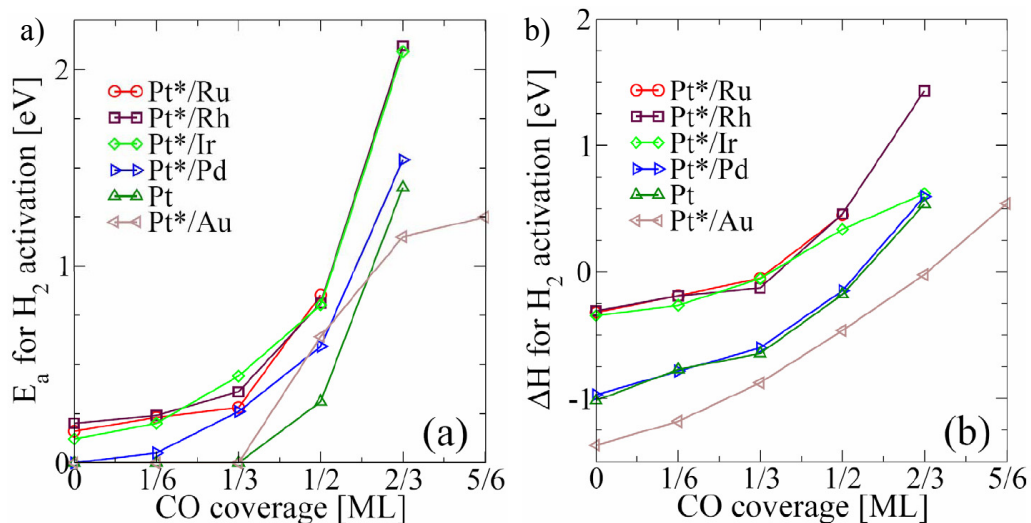
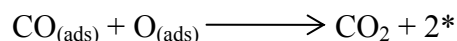
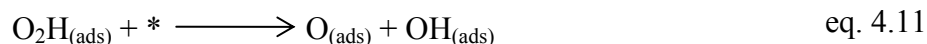
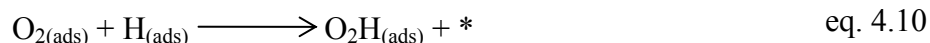


Figure 4.27. (a) the activation energy barrier (E_a) and (b) heat of reaction (ΔH) for H₂ dissociation as a function of CO coverage on Pt*/M and Pt(111) on a four-layered slab in a ($\sqrt{3} \times 2\sqrt{3}$) surface unit cell.

The strength of CO binding on a surface, which determined the CO saturation coverage, and the activation energy for H₂ dissociation, were both important factors determining the relative reactivity of these surfaces. For a surface with higher CO binding energy, it was necessary to increase the reaction temperature to higher levels for removing some CO from the surface, so that empty sites could be generated for the adsorption/activation of other PROX reactants. As shown above, surfaces with increased CO binding required higher activation energy barriers and thus higher reaction temperatures for elementary steps to proceed. From Figure 4.27, one could suggest the following: (i) Pt*/Ru would be the most reactive one, since it had the lowest CO-

saturation coverage (1/2 ML), (ii) Pt*/Au would be the least reactive one, as it showed the highest CO-saturation coverage (5/6 ML), (iii) All other surfaces had a 2/3 ML CO-saturation coverage. To estimate their relative PROX activity, one could draw a vertical line in Figure 4.25 at any CO coverage above 1/2ML, the saturation coverage for Pt*/Ru. On such a line, one could rank-order the surfaces on the basis of differential binding of CO, as follows: Pt < Pt*/Pd < Pt*/Ir < Pt*/Rh, with Pt and Pt*/Rh showing the strongest and weakest CO binding respectively. Although differences between a few bimetallics in Figure 4.26 were small, one could still attempt to derive some qualitative reactivity trends. More specifically, it looked as if the relative PROX reactivity of these six surfaces follows the trend: Pt*/Ru > Pt*/Rh > Pt*/Ir > Pt*/Pd > Pt > Pt*/Au. As shown above, this relative PROX activity order was verified when the corresponding M@Pt nanoparticle catalysts were tested experimentally for PROX (see Figure 4.16). Although there were a number of prior experimental studies demonstrating the effect of CO coverage on various reactions.^{39,40,44,67,234}

To explain the relative PROX reactivity of various M@Pt NPs, the detailed reaction mechanism was elucidated. In particular, the following elementary reaction steps were accounted for:



where * denoted a surface site.

Apart from the elementary steps in the traditionally accepted PROX mechanism,^{67,217} equations 4.10 and 4.11 were included, which included the formation of a hydroperoxy (O_2H) intermediate via hydrogenation of O_2 and its dissociation into O^* and OH^* . The motivation for including these two additional steps came from our experimental observation that CO oxidation rates on the Ru@Pt NPs were higher in presence of H_2 than in its absence. The thermodynamics and kinetics of all the above elementary steps was investigated on all six Pt*/M model surfaces with a (2×2) surface unit cell. Simple inspection of the above reaction network suggested that the PROX activity and selectivity of a surface would depend on its ability to: (1) generate surface O through either the direct or H-mediated O_2 dissociation (equation: 4.8, or 4.10 with 4.11, respectively), (2) remove CO through its oxidation (equation 4.13) and (3) remove the remaining surface O through H_2O elimination (equations: 4.9 with 4.13, and 4.11 with 4.12).

The binding energies of all relevant species in the PROX reaction network on all six surfaces were plotted in Figure 4.27a. Hydroxyl (OH^*), hydroperoxy (O_2H^*) and molecular oxygen (O_2^*) all showed smaller variations in their binding energies from one surface to the next. As discussed earlier (see Figure 4.27), the binding energy of CO showed significant variation on the six surfaces. Accordingly, these variations reflected modifications in the electronic structure of the Pt-overlayer induced by the supporting metal surface through strain and the ligand effects.^{90,151,235}

The activation energies of bond-breaking/making PROX elementary steps (equations 4.3-4.7) were shown in Figure 4.27b. The direct O₂ dissociation step (equation 4.8) had the highest activation energy on Pt*/Ru, Pt*/Rh and Pt*/Ir with a barrier greater than 1 eV, which decreased progressively on Pt*/Pd, Pt and Pt*/Au. Therefore, in the absence of H₂, CO oxidation proceeded via this difficult O₂ dissociation step on all surfaces and resulted in lower reaction rates on Pt*/Ru, Pt*/Rh and Pt*/Ir, as compared to those on Pt*/Pd, Pt and Pt*/Pd. However, in the presence of H₂, the H-mediated O₂ dissociation mechanism (equations 4.10 and 4.11) was very easy on all surfaces. On all six surfaces and for the latter mechanism, atomic H* addition to O₂* led to the formation of a hydroperoxy intermediate (O₂H*) with small barriers ($E_a < 0.35$ eV). Then, the hydroperoxy intermediate (O₂H*) decomposed into O* and OH*, again with fairly small barriers on all surfaces ($E_a < 0.42$ eV). Therefore, in H₂-rich PROX reaction environments, surface O* was primarily generated through the H-assisted O₂ dissociation mechanism. Importantly, this suggestion could also explain the experimentally observed enhancement of CO oxidation rates induced by the presence of H₂.⁶⁷

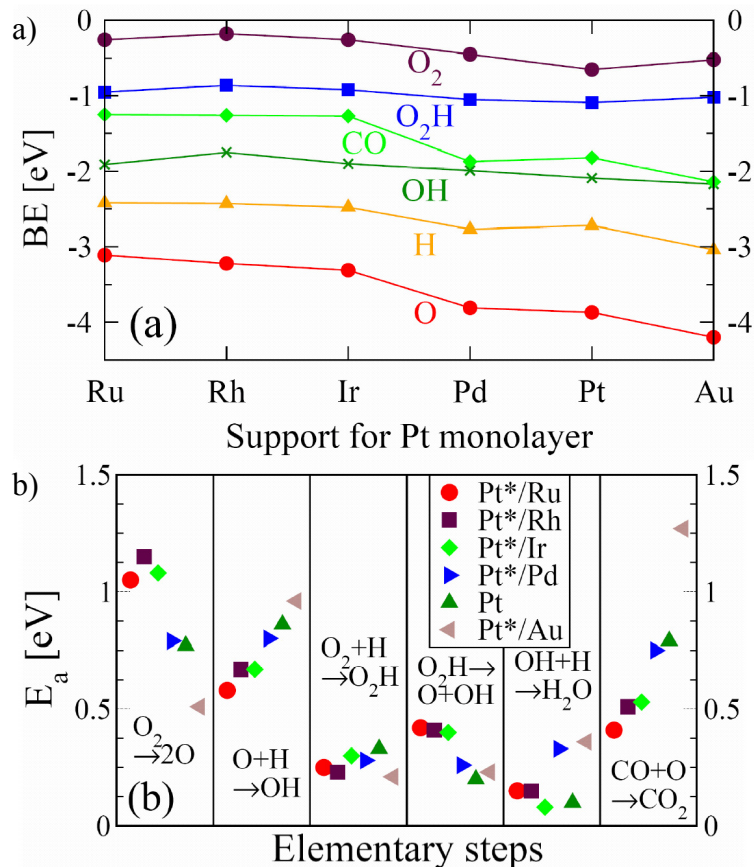


Figure 4.28. (a) Binding energy (BE) of different reaction intermediates and (b) the activation energy (E_a) for different PROX elementary steps on Pt*/M and Pt(111) on four-layer slabs with a (2 x 2) surface unit cell.

Overall, since direct O₂ dissociation could be circumvented through the H-mediated O₂ activation on all surfaces, CO oxidation and OH formation were energetically the most difficult steps on all six surfaces. The relative energetics of these two steps dictated both their relative activity and selectivity for PROX. The barrier for the more difficult of these two steps increased in the following order: Pt*/Ru < Pt*/Rh < Pt*/Ir < Pt*/Pd < Pt < Pt*/Au, and should accordingly affect the PROX activity of these surfaces. This relative activity order was in excellent agreement with the experimentally observed trends for the light-off temperature (Figures 4.16 and 4.17), where complete CO-oxidation had been achieved. Figure 4.29 clearly shows a correlation between the

DFT-derived activation energies for the rate limiting CO oxidation step (equation 4.13) and the experimentally observed temperatures of 50% CO₂ formation at 2000 ppm CO level. Furthermore, on all these surfaces, with the exception of Pt*/Au, CO oxidation had a smaller barrier than OH formation $O^*+H^* \rightarrow OH^*$, resulting in higher selectivity for CO rather than hydrogen oxidation.

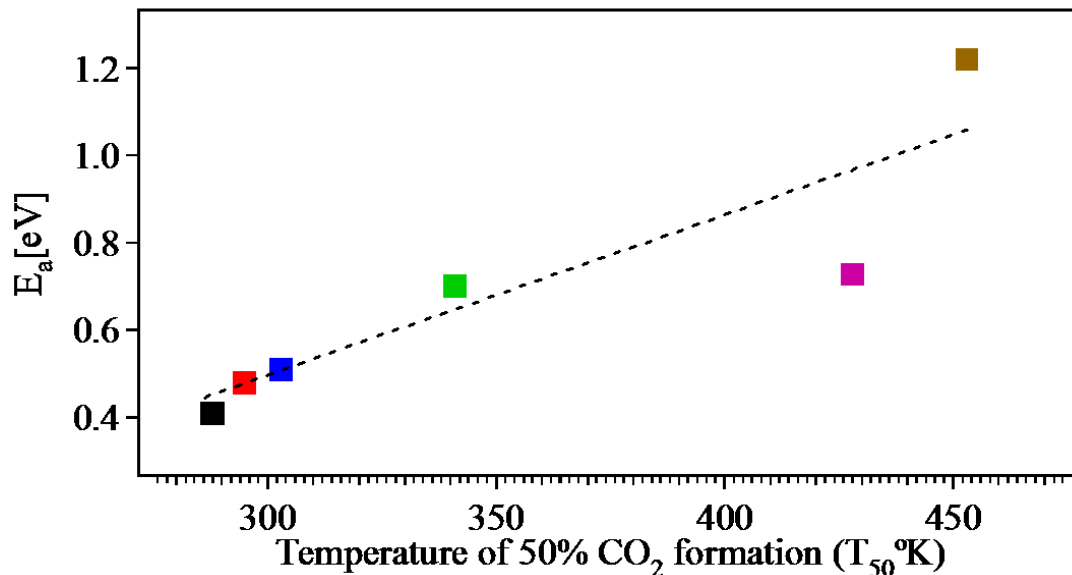
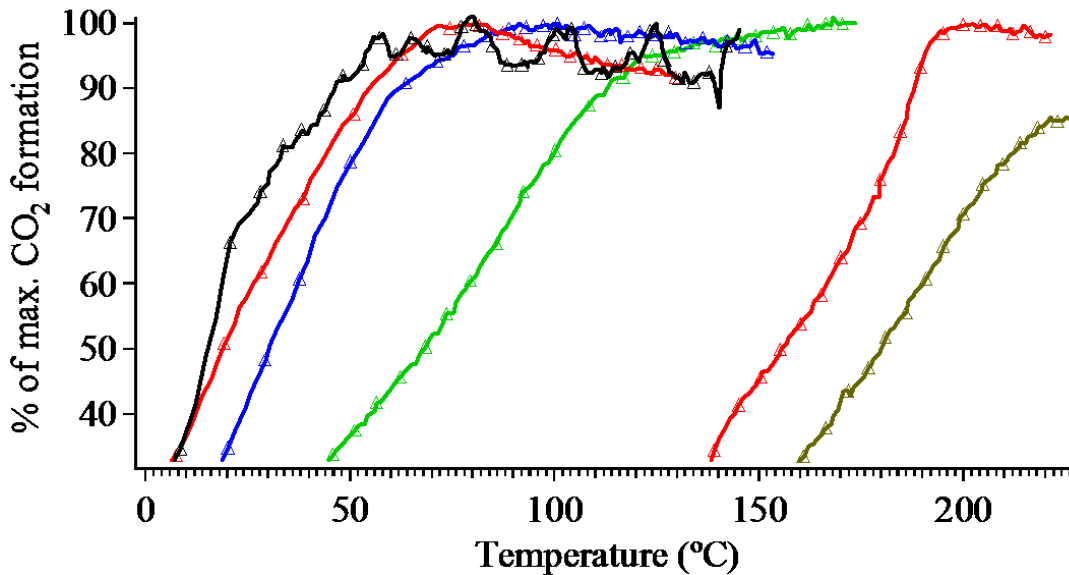


Figure 4.29. (a) TPR plots for the PROX reaction showing CO₂ formations at 2000 ppm CO level on the core/shell M@Pt (M=Ru, Rh, Ir, Pd and Au) and monometallic Pt NPs. (b) The activation energies, E_as, for the rate limiting reaction step of CO oxidation on the Pt*/M NSAs and Pt(111) are plotted against temperatures of 50% CO₂ formation on the core/shell M@Pt and monometallic Pt NPs (M=Ru, Rh, Ir, Pd and Au).

4.4. Discussions

The core/shell Ru@M (M=Ru, Rh and Pd) NPs at varying M shell thicknesses and M@Pt (M=Ru, Rh, Ir, Pd and Au) NPs with ca. 1 ML thick Pt shells were synthesized using polyol method. NPs were characterized in powders using XRD and Micro-Raman and in colloidal suspension using FT-IR CO probing, TEM size evaluation and STEM-EDS linescans and point analyses.

An interesting finding of this study is the observation of electronically/geometrically-altered Pt shell structures of the M@Pt NP systems (M=Ru, Rh, Ir, Pd and Au). The red-shifted $\nu_{\text{atop}}(\text{CO})$ of Pt shells relative to monometallic Pt (Figure 4.11a), as well as the X-ray diffraction pattern with systematic peak shifts to high angles (Figure 4.8a), of the 2.5 nm Ir@Pt particles revealed an electronically and geometrically altered Pt surface. Furthermore, the Micro-Raman spectra in the $\nu(\text{M-C})$ region as well as $\nu(\text{CO})$ region of the 2.0 nm PVP-free Ir@Pt particles (Figure 4.15) clearly point out to the formation of electronically/geometrically-altered Pt shells.

For the Ru@M NP systems (M=Rh and Pd), both structural and spectroscopic results were in favor of the formation of core/shell NPs with structurally-altered shells, which was analogous to the Ru@Pt NPs (Chapter 2). The X-ray diffraction patterns were pseudo-FCC, and thus favored shells Rh (or Pd) pseudo-morphic to Ru NP cores. $^{99}\text{FT-IR}$ spectra of CO-saturated colloids of the Ru@Rh NPs exhibited ca. 10 cm^{-1} blue-shift of the $\nu_{\text{atop}}(\text{CO})$ and ca. 20 cm^{-1} blue-shift of the $\nu_{\text{bridge}}(\text{CO})$ of Rh with respect to those of the 2.7 nm Rh colloids. The $\nu_{\text{atop,Rh}}(\text{CO})$ s were also blue-shifted by ca. 5 cm^{-1} compared to that of the 3.0 nm Ru colloids (Figure 4.13a). These results were in favor of an electronically modified Rh surface. The 4.3 nm Ru@Rh NP colloids with ca. 2-3 MLs

thick Rh shells further exhibited a lower $I_{\text{atop}}(\text{CO}) / I_{\text{bridge}}(\text{CO})$ ratio than that of the 3.0 nm Ru@Rh colloids with ca. 1-2 ML thick shells, which could be attributed to a geometrically different Rh surface, and thus complementary to the XRD. Similarly, it was observed for the Ru_x@Pd_{1-x} NPs that the $\nu_{\text{atop}}(\text{CO})$ s were blue-shifted accompanied by a loss in intensity and the $I_{\text{atop}}(\text{CO}) / I_{\text{bridge}}(\text{CO})$ ratio was greatly diminished relative to the 4.0 nm Pd NPs (Figure 4.13b). It was believed that the decreasing ratio of edge sites to face sites associated with hetero-nucleation and subsequent growth of Pd was responsible for it.¹⁶⁸ This phenomenon is believed to have further implications in the PROX reaction and will be discussed in detail below.

The structural anomalies associated with thin Pt shell formation for the Ir@Pt NP and the Ru@M NPs (M=Rh and Pd) are another important finding of this chapter, and thus are in parallel with those represented in this thesis for the Ru@Pt NPs and others reported by Schlapka et al. for the Pt overlayers on Ru(0001) substrates.⁹⁹ A lattice mismatch between the bulk crystals of the core and shell metal would create a strain at the core/shell interface. Furthermore, the lattice strain could induce the observed structural anomalies. The Ir@Pt and Ru@M NPs exhibit medium lattice mismatches (>2.0%) with positive signs (i.e. the shell metals had larger bulk crystals than the core metals), with the exception of the Ru@Rh NPs, which had a lattice mismatch of only 0.5% with negative sign (i.e. Ru had a slightly larger bulk crystal than Rh). Thus, no correlation with the sign and/or magnitude of the lattice mismatch could be drawn. Moreover, a disorder in the host Ru NP (and possibly Ir NP) cores as revealed by an EXAFS analysis in Chapter 2 would affect the nucleation and growth of the Pt (or Rh, or Pd) shells, and thus introduce a structurally-modified metal overlayer.

The particle morphology of the Pd@Pt NPs was clearly different from that of the parent Pd NPs. Thus, the Pd@Pt NPs present an example of the non-conformal heterogeneous growth, which is markedly different from the other M@Pt core/shell NPs (M=Ru, Rh and Ir) (see Figure A4.1 in the Appendix). Upon deposition of Pt at ca. 1 ML coverage, a single strong $\nu_{\text{atop}}(\text{CO})$ at 2060 cm^{-1} and a weak, broad $\nu_{\text{bridge}}(\text{CO})$ for the modified Pt surface were observed (Figure 4.11), which was also consistent with the studies of Toshima and co-workers on the related 2.9 nm Pd@Pt NP colloids.⁹³

Similar to the Pd@Pt NP system, TEM showed changes in particle morphology for the 3.4 nm Au@Pt particles (see Figure A4.3 in the Appendix). The deposition reaction of Pt was carried out at low temperatures, such that it was governed by kinetic factors, which could explain the shape anisotropy associated with the Pt growth (see the experimental section). Other Au@Pt NPs with various morphologies were reported. Synthetically-relevant polyol reduction reaction employed within a delayed nucleation strategy was demonstrated to yield 4.5 nm nanocrystals of mostly core/shell architectures, and thus, exhibited conformal Pt overlayers.¹²⁶ On the other hand, aqueous synthesis employing a sequential-deposition strategy was independently reported by Fan et al.¹⁰⁰ and Du et al.²³⁶ to synthesize Pt-decorated Au NPs. It was also suggested by Fan et al. that Pt overlayers pseudo-morphic to Au core could not be made owing to the large lattice mismatch (ca. 4.1%) between the two. The results of this study did not support such a growth model. It was demonstrated that conformal Pt overlayers could be grown over Au NP seeds regardless of the core diameters. Moreover, slow growth kinetics was shown to be involved in size-dependent shape-anisotropy of the Au@Pt NPs (Figure 4.8).

Having the formation of bimetallic Pt/M nanoparticles with the well-defined core/shell structures established, experimentally observed surface reactivity of the respective nanoparticle catalysts could be evaluated with fewer complications. It was found that the M@Pt NPs exhibited an increasing activity trend at low CO partial pressures (0.1-0.2%) with M to the upper-left of the periodic table: the Ru@Pt NPs showing the highest activity toward PROX activity and the Au@Pt NPs, the lowest among those studied (Figures 4.16 and 4.17). The temperatures of 50±5% O₂ conversions and the selectivities for CO₂ formation at 50±5% O₂ conversion for PROX reaction at 1.0% CO and 0.5% O₂ on the M@Pt core/shell NPs and 2.2 nm Pt particles are shown in Table 4.1. At high CO partial pressures (1.0%), the trend for the PROX activities inverted for the Ru@Pt and Ir@Pt NPs: the Ir@Pt NPs became more active in PROX than the Rh@Pt NPs and the Ru@Pt NPs, less active. The core/shell NPs, with the exception of Au@Pt NPs, showed comparable PROX selectivities. The Au@Pt NPs, in contrast, exhibited a CO tolerant behavior, which was developed at low CO partial pressures, and reached a maximum at 1.0% CO concentration (Figure 4.19).

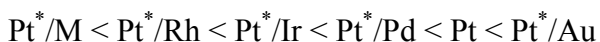
Table 4.1. Comparative PROX selectivities^a for the M@Pt^b core/shell and monometallic Pt NP catalysts.

	$T_{50\pm 5\%}(\text{O}_2)$ ^c	S (CO) @ $T_{50\pm 5\%}$ ^d
4.1 nm Ru@Pt	121±9	75.0±1.5
3.2 nm Rh@Pt	84±8	90.5±2.2
2.5 nm Ir@Pt	75±3	87.4±1.7
4.5 nm Pd@Pt	182±8	63.0±2.0
3.4 nm Au@Pt	163±8	39.8±0.7
2.2 nm Pt	182±3	74.5±1.0

^a PROX feed is composed of 1% CO, 0.5% O₂, 50% H₂ and an Ar balance. ^b M=Ru, Rh, Ir Pd and Au. ^c Temperature of 50±5% O₂ conversion. ^d Selectivity is defined as $[\chi_{\text{CO}_2}/(\chi_{\text{CO}_2}+\chi_{\text{H}_2\text{O}})] \times 100$ where χ_{CO_2} is the fraction of O₂ used to convert CO to CO₂ and $\chi_{\text{H}_2\text{O}}$ is the fraction of O₂ used to convert H₂ to H₂O (see Figures 4.19 for TPR data).

It was shown by using DFT calculations on the Pt*/M surfaces, to which the M@Pt core/shell NPs were the synthetic counterparts, that the PROX activities of the respective surfaces would follow the same trends as were experimentally observed at low CO partial pressures. It was explained on the basis of the calculated equilibrium CO coverages and the corresponding barriers to H₂ activation that the PROX reaction strongly correlated to the availability of CO-free surface sites at any time. Thus, the

Pt*/M surfaces with the lowest CO saturation coverage would exhibit the highest PROX activity. The Pt*/M surfaces ranked as:



in order of increasing CO saturation coverages. Furthermore, H₂ activation energies of CO-saturated Pt*/M NSAs followed the same trend. Although the CO coverages could not be determined experimentally on the M@Pt NPs, the experimentally observed PROX activities at low CO partial pressures (0.1-0.2%) perfectly correlated with the calculated activation energies for the rate limiting CO oxidation step (Figure 4.29).

DFT calculations also shed light on the CO tolerant behavior, as well as the low PROX activity observed for the Au@Pt NPs (Figures 4.16-4.19). Theoretically determined higher CO saturation coverage and accordingly decreased surface availability on the Pt*/Au(111) NSA than pure Pt(111) would account for the reduced PROX activity of the Au@Pt NPs. To understand the lowered PROX selectivity, however, the reaction mechanism should be tracked to the thermo-chemistry governing the relative easiness of the respective reaction steps. , CO oxidation step was highly de-stabilized on the Au@Pt NPs, such that it was energetically less favorable than the highest of the two step H₂O formation. Although CO site blocking was the reaction limiting, as soon as the surface was freed of CO by desorption and/or oxidative removal, atomic O and H could react to form H₂O. This piece of information was experimentally traced by the observation that H₂ activation was simultaneous to CO oxidation (Figure 4.18).

In contrast, the PROX reaction proceeded >80% selective toward CO oxidation over the M@Pt NPs (M=Ru, Rh and Ir) at kinetically-controlled region at low temperatures (Figure 4.19). This was theoretically shown on the Pt*/M NSAs (M=Ru, Rh

and Ir) via a circumvention of the high energy direct O₂ dissociation step (equation 4.8) by the energetically more favorable H₂-assisted O₂ dissociation step (equation 4.10), which was experimentally justified on the Ru@Pt NP system in Chapter 2.

Given the particle diameters increasing in the order of Ir@Pt (2.5 nm) < Rh@Pt (3.2 nm) < Ru@Pt (4.1 nm), reversal of the PROX activities at high CO partial pressures (i.e. 1.0% CO) could be attributed to the increased frequency of edge and corner sites relative to face sites. However, the 3.0 nm Ru@Pt particles with ca. 1-2 MLs thick Pt shells were found to perform poorer than the 4.1 nm particles in PROX (see Chapter 2). Thus, size, by itself, could not account for the observed trend at 1.0% CO concentration. Moreover, the presence of nanocrystals with the more energetic HCP structure might at least partially contribute the better PROX performances at high CO partial pressures of the Ir@Pt NPs catalyst. Thus, relative abundance of more energetic surface sites, still, could not be ruled out. This point requires further systematic studies and is currently under investigation.

Next, the thickness effect on the PROX activity and selectivity for the Ru@M (M=Pt, Pd and Rh) NPs was shown. For that, NPs at different shell thicknesses were synthesized and evaluated for PROX reaction. In Table 4.2, the temperatures of 50±5% O₂ conversions and the selectivities for CO₂ formation at 50±5% O₂ conversion for PROX reaction at 1.0% CO and 0.5% O₂ on the Ru@M core/shell NPs are shown for comparison. It was found on the Ru@Pt and Ru@Pd NP systems that the only detectable influence of varying the shell thickness was on the PROX performances, which became poorer with increasing the shell thicknesses beyond 2-3 MLs as suggested by Goodman and co-workers for other relevant surface overlayer structures.¹³⁰ The Ru@Rh NP system

exhibited PROX activities intermediate to those of the end members at 1-2 MLs thickness of Rh shells, but performed poorer than both the 3.0 nm Ru core particles and the 2.7 nm Rh particles at 2-3 MLs coverage of Rh. Moreover, the particles developed a CO-tolerant behavior which resembled that of the Ru@Pd and Au@Pt NPs. This phenomenon could be partly explained by a certain combination of strain and ligand effects, but also strongly suggested the size effects on surface reactivity to be taken into consideration.

Table 4.2. Comparative PROX selectivities^a for the Ru@M^b core/shell NP catalysts.

	$T_{50\pm 5\%}(\text{O}_2)$ ^c	S (CO) @ $T_{50\pm 5\%}$ ^d
4.1 nm Ru@Pt	121±9	75.0±1.5
3.9 nm Ru@Rh	182±5	76.6±1.8
4.5 nm Ru@Pd	173±3	54.9±1.8
4.3 nm Ru@Rh	191±3	57.1±2.6
5.0 nm Ru@Pd	195±3	55.7±2.4

^a PROX feed is composed of 1% CO, 0.5% O₂, 50% H₂ and an Ar balance. ^b M=Pt, Rh and Pd. ^c Temperature of 50±5% O₂ conversion. ^d Selectivity is defined as $[\chi_{\text{CO}_2}/(\chi_{\text{CO}_2}+\chi_{\text{H}_2\text{O}})] \times 100$ where χ_{CO_2} is the fraction of O₂ used to convert CO to CO₂ and $\chi_{\text{H}_2\text{O}}$ is the fraction of O₂ used to convert H₂ to H₂O (see Figures 4.19 for TPR data).

Finally, the surface reactivity of well-characterized tri-metallic nanoparticles with the core/shell architecture was shown to be tunable by composition and structure. The Ru@Pt@Pd NPs with sandwiched layer of Pt at sub-monolayer coverage and 1-2

MLs thick Pd shells exhibited drastic loss of reactivity compared to the parent Ru/Pt surface, but also showed reactivity intermediate to those of other Pd surfaces with varying shell thicknesses and Ru-only cores (see Figure 4.23). For the Ir@Pt@Pd NPs with ca. 1 ML thick Pt shells, a sandwiched layer of Pt at ca. monolayer coverage enhanced both activity and selectivity at low temperatures toward PROX reaction of the Pd surface at ca. monolayer coverage (Figure 4.24b). Although direct comparisons could not be made between different M@Pd (M=Ru@Pt and Ir@Pt) NPs, because of different particle sizes (4.8 nm vs. 3.0 nm) and compositions of the ca. 2 MLs thick shells (sub-monolayer thick Pt plus ca. 1-2 MLs thick Pd versus ca. 1 ML of each Pt and Pd), Pd surface reactivity was also shown to be tunable in a broad TPR temperature window with high sensitivity.

Chapter 5

Conclusion

Bimetallic composites of transition group metals are under investigation of many research communities. Metal overlayers that could be heterogeneously deposited over single crystal metal surfaces were studied first.¹³⁰ The findings of these surface science studies put forward the fundamentals of substrate effect. The electronic structure of overlayer metal atoms was shown to be significantly altered by the host via charge transfer. The growth mechanism of the overlayers, in addition to geometric effects, may change chemical properties of the surface. Furthermore, surface-adsorbate binding properties of the geometrically and/or electronically-altered metal atoms were also modified, which opened up new possibilities in catalysis.

A d-band center shift relative to Fermi level can be introduced geometrically by lattice compression or expansion. The catalytic enhancements for these materials has been explained on theoretical grounds by way of near surface alloys NSAs.⁹⁰ Thus, the ‘catalysis by design’ strategy (theory guided materials design) comes into play for fabrication of next generation novel catalysts. However, even the most fundamental synthetic approaches are still empirically determined such that Edisonian trial-and-error strategy is the best method that synthetic chemist have in their disposal. Given the difficulty in evaluating the optimal synthetic conditions, the ‘catalysis by design’ strategy will accelerate the progress in the research of novel catalysts. Thus, synthetic chemists can focus on synthesis to develop new methods and/or to improve already existing ones.

Translation of the surface science and theoretical studies to catalytically relevant nanoparticles is not well-understood. Size- and shape/morphology-controlled monometallic nanoparticles were heavily investigated, but catalytically they offered little. Bimetallic nanoparticles with alloy architectures have been known and applied to heterogeneous catalysis for decades. Surface bi-functionality and randomness of atomic packing are factors that complicate a thorough evaluation of their surface reactivities. Core/shell nanoparticle architectures, on the other hand, can be seen as the synthetic counterpart to NSAs, so that it may serve as a starting point to test the NSA theory on catalytically relevant nanocomposites.

This study focused on the architecturally-controlled core/shell nanoparticles of platinum group metals with the general formulas $M@Pt$ ($M=Ru, Rh, Ir, Pd$ and Au) and the $Ru@M$ ($M=Rh$ and Pd). The enhanced catalytic activities of these well-defined structures toward various heterogeneous reactions of industrial and scientific importance such as PROX, de- NO_x and benzene hydrogenation reactions were shown, in which electronically-altered metal overlayers could be evaluated. Therefore, this study bridged for the first time the long existing experimental gap with the surface science and theoretical studies.

5.1. ‘Catalysis by design’ strategy for improved catalytic properties

Fabrication of nanocomposite catalysts with predictable catalytic properties is in the heart of the ‘catalysis by design’ approach. Bimetallic nanoparticles with the core/shell architectures are the synthetic counterparts to NSAs, and therefore serve as a robust system to understand the NSA theory⁹⁰ on experimental grounds. Furthermore, the

Ru@M (M=Ru, Rh, Ir, Pd and Au) NPs were synthetically isolated and shown to have electronically/geometrically-altered structures as predicted by NSA theory.

It was shown for the first time on an architecturally-controlled bimetallic nanoparticle system that the improved catalytic properties could be achieved via a modified reaction network; the so-called H₂-assisted CO oxidation mechanism. H₂-mediated enhancement of PROX activities was first reported on monometallic Pt nanoparticles a decade ago,⁶⁷ but its origin has remained unknown. H₂-assisted room temperature CO oxidation was first observed on the Ru@Pt core/shell NPs and its mechanism, surface peroxy formation, was identified. It was also shown that the core/shell architecture was superior in catalyzing PROX reaction than any other bimetallic architecture studied to date, namely alloys and mixtures of the end members.

Other core/shell NPs with Pt shells such as Ir@Pt NPs and Rh@Pt NPs were synthetically isolated and demonstrated to have extraordinary PROX activities comparable and even superior to that of the Ru@Pt NPs under certain conditions. Some other M@Pt core/shell NPs, i.e. the Pd@Pt NPs, exhibited no room temperature CO oxidation behavior however they still performed better than pure Pt NPs. As such, H₂-assisted CO oxidation mechanism on the Au@Pt NPs did not effectively function to remove CO, but led to a CO-tolerant Pt surface. Thus, it was demonstrated that enhanced catalytic activity and desired product selectivity of electronically-altered metal overlayers (i.e. nanocomposite shells) can be achieved by engineering the host metal (i.e. nanoparticle cores).

The NSA theory predicted the surface reactivity trends observed for the Ru@M core/shell NPs, and justified it by addressing a novel reaction mechanism. These

findings are of fundamental importance to heterogeneous catalysis, and are expected to lead ‘catalysis by design’ strategy to new horizons.

5.2. Architecturally-controlled Pt-free bimetallic NP catalysts

A primary goal of the catalyst community is to synthesize catalytically active and air-stable Pt-free NP catalysts. Achieving this goal will require understanding on structurally and chemically well-established PGM systems the most fundamental catalytic reactions. Thus, earth abundant cheap minerals can be utilized in replacement of scarce and expensive PGMs. The preliminary studies presented in this thesis employed strictly platinum group metal (PGM) cores and shells because of synthetic concerns. PGMs can be synthesized in various sizes, shapes and morphologies with tunable physical, chemical and catalytic properties. Reaction parameters such as temperature, time, metal and surfactant concentrations can reproducibly be modified to achieve desired particle properties. Nanoparticle architecture can also be controlled. The next step towards Pt-free nanoparticle catalysts/electro-catalysts is to reduce or eliminate the Pt content by using 1st row TMs such as Fe, Ni and Cu in the core. Kinetically-stabilized Cu@Pt core/shell NPs catalyst was synthetically prepared and successfully applied to catalytic de-NO_x reaction.³⁴ The findings of this study put forward the fundamentals of such an approach by taking a step up to structural and catalytic evaluation of the core/shell nanoparticle series of PGMs toward various heterogeneous reactions such as PROX, de-NO₂ and benzene hydrogenation.

5.3. Structure-reactivity correlations in heterogeneous catalysis

In this study, chemical and physical properties of the bimetallic nanoparticle catalysts were shown to have profound catalytic influences on various heterogeneous reactions such as PROX, de-NO_x and benzene hydrogenation. For example, surface reactivity of the bimetallic Pt/Ru nanoparticle system for benzene hydrogenation reaction was shown to be structure-dependent. The nature of surface reactivity is usually dictated by the electronic and crystal structure of catalyst metal(s) and the actual thermochemistry governing the heterogeneous reaction mechanism.

The complex structural and crystallographic make-up of core/shell nanoparticles was shown to be responsible for the extraordinary catalytic activity of nanoparticles with the core/shell architecture. A combination of tools and techniques were necessary to analyze with atomic precision the local structure of core/shell nanoparticles. Structurally sophisticated nanoparticle architectures, i.e. core/shell nanoparticles are the most demanding in terms of evaluation of such particle properties. Characterization of such bimetallic phases is of fundamental importance, however full structural analysis set a major drawback because of nanocrystalline nature of particles. There are recent reports on the synthesis and characterization of architecturally and morphologically-controlled Au@Pt,¹⁰⁸ Pd@Pt¹⁰⁵ and Au@Pd¹⁰⁰ core/shell NPs comprising of multiple monolayers of shells. STEM-EDS and TEM have been widely used to characterize large bimetallic nanocrystals with thick shells. As such, TEM-derived techniques are not successful in distinguishing thin metal shells from the cores. Thus, characterization of such bimetallic phases requires use of techniques other than those that are conventionally employed. For example, the Ru@Pt NPs with 1-2 ML thick

Pt shells was shown to have structural anomalies related to the strain-induced lattice distortion of FCC Pt shells and disordered Ru cores by a complementary study using XRD, EXAFS and PDF. An incommensurate distorted shell structure pseudomorphically grown on non-closely-packed Ru cores was one of the findings of this study, which was shown to have unprecedented catalytic results in PROX reaction.

Particle parameters such as local atomic arrangement and crystal structure, and structural deviations from the ideal thermodynamic phases may have profound influences on the reactivity of heterogeneous catalysts. For example, the Rh@Pt NPs with ca. 1-2 MLs thick Pt shells exhibited the core/shell architecture, which was inherently different from that for the Ru@Pt NPs of similar core sizes and shell thicknesses. The reason behind this was anticipated to be the distinct bulk crystal structures of the core metals, namely Rh (FCC) and Ru (HCP), although the lattice mismatch between bulk crystals of Pt and Ru was comparable in magnitude and sign to the lattice mismatch between bulk crystal of Pt and Rh. This phenomenon might have further implications in catalysis beyond the catalytic predictions of the DFT calculations, because of the basic geometric assumptions made by the theory. Having these assumptions put aside, what would be the effect of substrate in heterogeneous catalysis on purely electronic grounds? What would be the relative contributions of 'ligand' effect and geometric effect? As such, the architectural-control over the bimetallic phase of interest would not be sufficient to address such questions.

The ultimate control over crystal structure and local arrangement and coordination of metal atoms were also sought. Thus, the electronic and geometric contributions to the substrate effect could be well-understood. For example, Rh and Ir

crystallize in FCC close-packed structure in bulk. On the other hand, the preliminary results presented in this study suggest nanocrystals of Rh and Ir may also crystallize in HCP close-packed structure and/or structures intermediate to FCC and HCP at very small size regimes. Given the geometrically small difference between HCP and FCC crystals, one can be kinetically-stabilized against the other, and furthermore the wet chemical synthesis of metal nanoparticles provides the basic techniques to achieve such metastable phases. Once the phase-controlled synthesis of such isoelectronic structures is achieved, the theory can be put on a further test to understand the 'ligand' only effect on heterogeneous catalysis. At the moment, there is no satisfactory explanation for the implications of geometric-only effect in heterogeneous reaction mechanism and surface reactivity, provided that bulk crystals for the substrate and hetero-epitaxial overlayers are assumed by the theory. Overall, this study put forward the most fundamental aspects of nanoparticle catalyst design, synthesis and characterization, and is intended to be put to further advancement beyond its preliminary findings.

Appendix

Chapter 4

Pd NPs synthesized in EG via NaBH_4 reduction are ca. 6.0 nm. Etching with catalytic amounts of NaBr focuses particle size to ca. 4.0 nm (Figures A4.1a-c). Pd@Pt NPs show 4.5 nm diameters in average (Figure A4.1d and A4.1f). Particles are mostly (>80% by number) cubic in shape with 100 facets (Figure A4.1e). There also co-exists with the cubes, larger spheroids (ca. 6.0 nm) less than 10% by number.

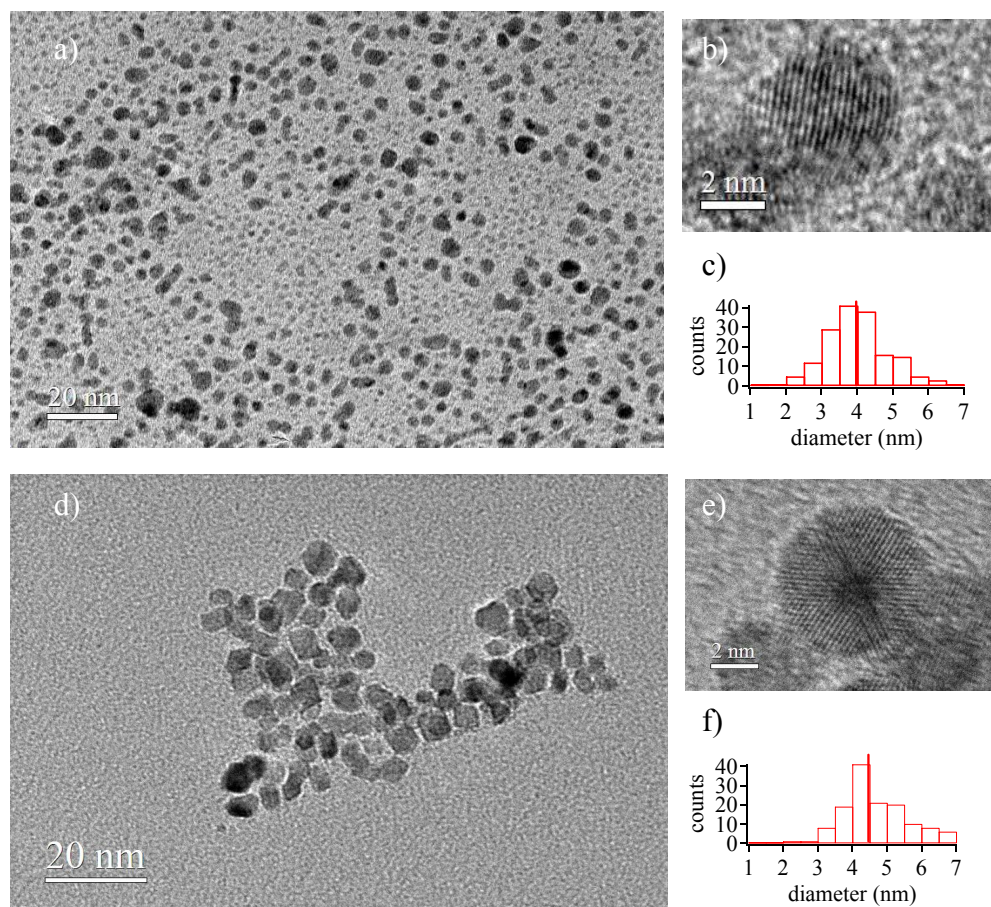


Figure A4.1. TEM images of (a) Pd NPs, and (d) Pd@Pt NPs. HR-TEM images of (b) Pd NPs, and (e) cubic Pd@Pt NPs. Particle size histograms of (a) and (d) are shown in (c) and (f), respectively.

Ru@Rh NPs with a nominal Ru:Rh ratio of 1:1 have 3.9 nm diameter in average (Figures A4.2a and A4.2c), and those with 1:2 molar ratio have 4.3 nm diameter in average (Figures A4.2d and A4.2f). Mean particle sizes above are in parallel with the Ru@Pt NPs of identical compositions, and thus agree with the Schmid model. Particles are nano-crystalline and multiply-twinned (Figures A4.2b and A4.2e).

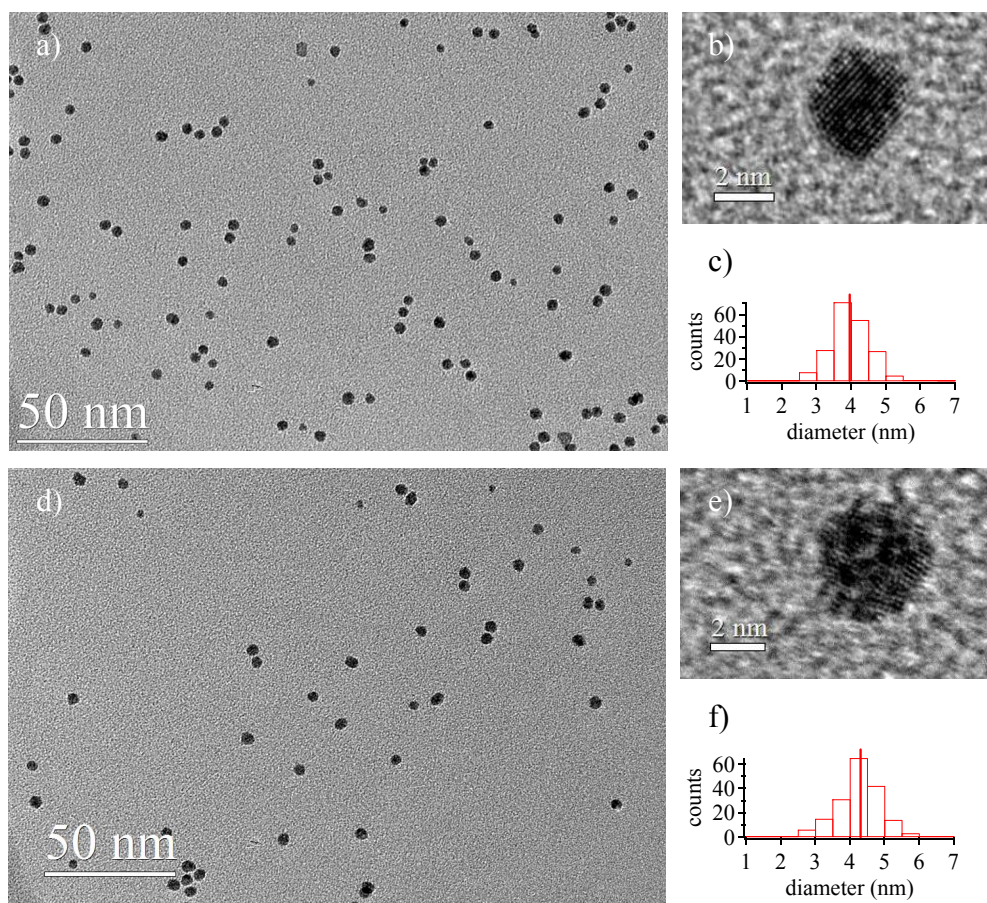


Figure A4.2. TEM images of Ru@Rh NPs with nominal Rh:Ru ratios of (a) 1:1, and (d) 2:1. HR-TEM images of Ru@Rh NPs with nominal Rh:Ru ratios of (b) 1:1, and (e) 2:1. Particle size histograms of (a) and (d) are also shown in (c) and (f), respectively.

Au NPs have a mean particle size of 6.0 nm and exhibit a narrow size distribution. Most particles exist in non-spherical shapes such as cubes and non-uniform polygons (see Figures A4.3a and A4.3c). Au@Pt NPs from the 6.0 nm Au nanoparticle seeds and two-times molar Pt as Au have 7.8 nm average diameter, and exhibit a broader size distribution. Particles are mostly spherical (see Figures A4.3d and A4.3f). Au NPs synthesized from excess NaBH₄ are 2.5 nm in average, and monodisperse in size (Figures A4.3g and A4.3i). Most particles are spherical, but some cuboctahedra also exists in the colloidal suspension (Figures A4.3h). Au@Pt NPs from the 2.5 nm Au nanoparticle seeds show a mean particle size of 3.4 nm, and size uniformity (Figures A4.3j-l). Particles are mostly spherical (>75%), but anisotropic particles also exist with aspect ratios of about 2 (Figure A4.3g).

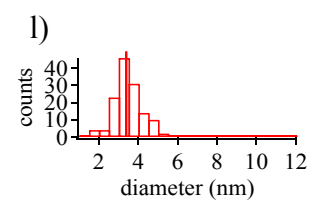
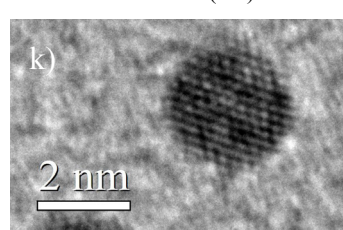
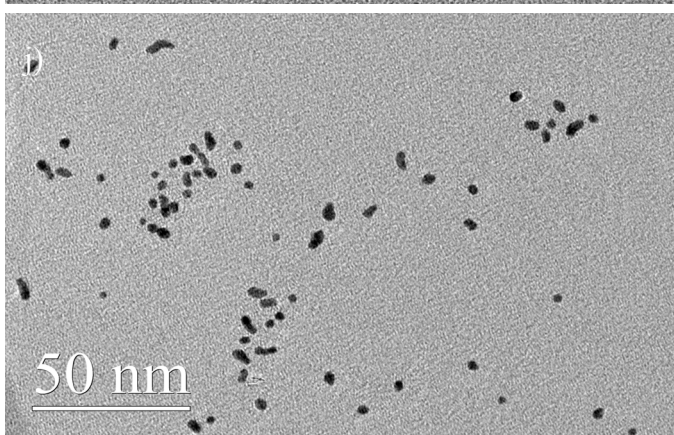
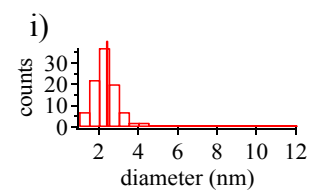
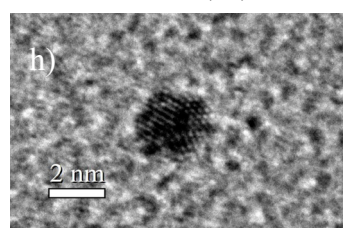
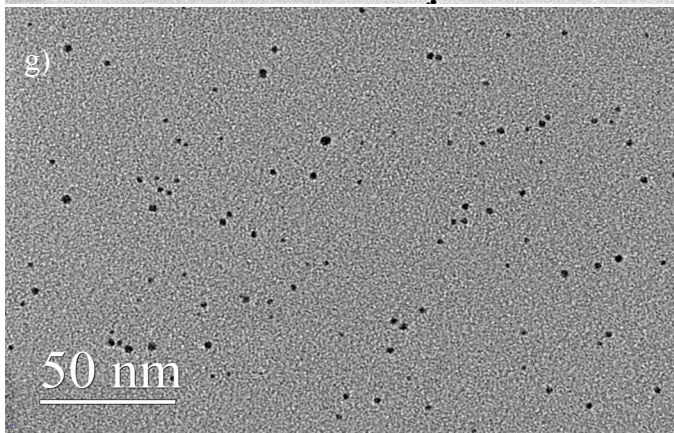
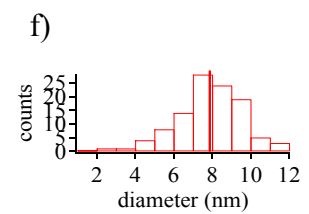
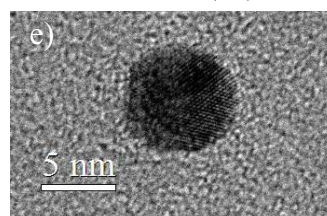
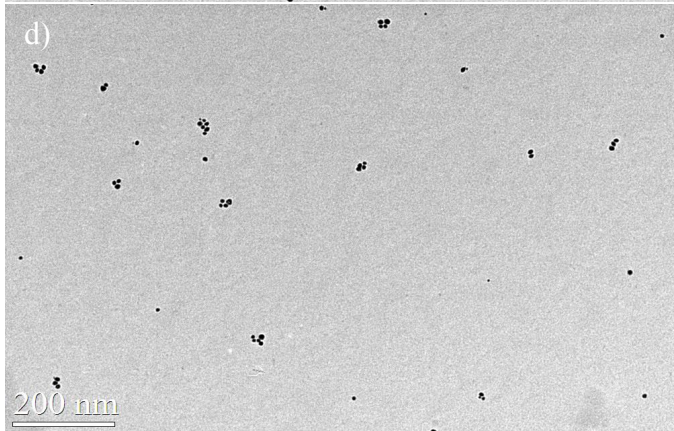
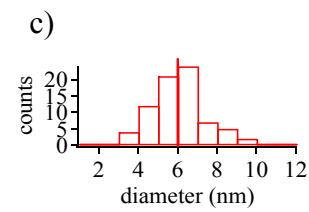
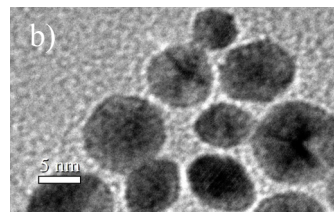
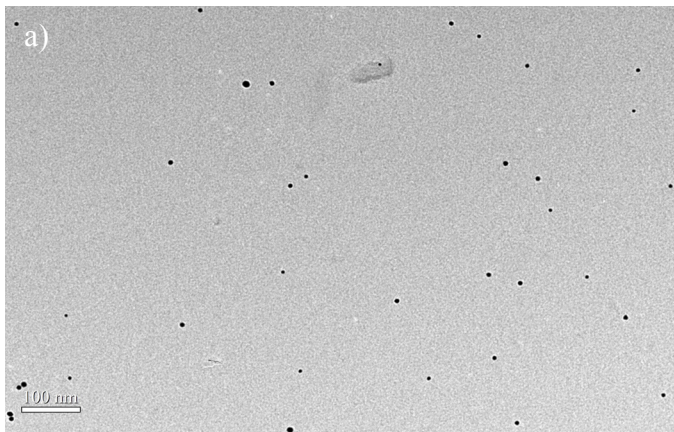


Figure A4.3. TEM images of (a) 6.0 nm Au NPs, (d) 7.8 nm Au@Pt NPs with multiple monolayers of Pt shells, (g) 2.5 nm Au NPs, and j) 3.4 nm Au@Pt NPs with ca. 1-2 MLs thick Pt shells. HR-TEM images of (b) several nano-crystalline Au cubes, (e) a 7.8 nm Au@Pt NPs, (h) a 2.5 nm Au icosahedra, and k) a nanocrystalline Au@Pt spheroid. Size histograms of the particles in (a), (d), (g) and (j) are shown in (c), (f), (i) and (l), respectively.

In Figure A4.4a, a STEM image of the 3.4 nm Au@Pt NPs supported in γ -Al₂O₃ are shown. Particles were conditioned at 200 °C under PROX reaction conditions several times. Several randomly selected nanoparticles were analyzed by EDS. A representative point spectrum is shown in Figure A4.4b. Among 10 Au@Pt NPs analyzed, the lowest elemental Au was ~5% by atom, and the lowest elemental Pt, 8% by atom. In average, particles exhibited a Au:Pt composition of 65:35, which was consistent with the starting composition. Furthermore, no unreacted PtCl₂ was observed by XRD (see XRD section). Since the probe size (1 nm) was smaller than the particle size (average 3.4 nm), the point spectra supported the core shell structure with Au core and Pt shell. EDS line-spectra acquired across single particles indicated that particles had Au rich cores and Pt rich shells. In Figure A4.4, a representative EDS linescan for a ~5 nm Au@Pt particle is shown. Owing to the smallness of the particle and the thinness of the Pt shell, the characteristic shell spectrum with bi-modal Gaussian distribution of X-rays is not clear for the Pt L line. The Pt L spectrum shows a diffuse spatial distribution of X-rays, compared to the compact spatial distribution of X-rays of the Au L spectrum.

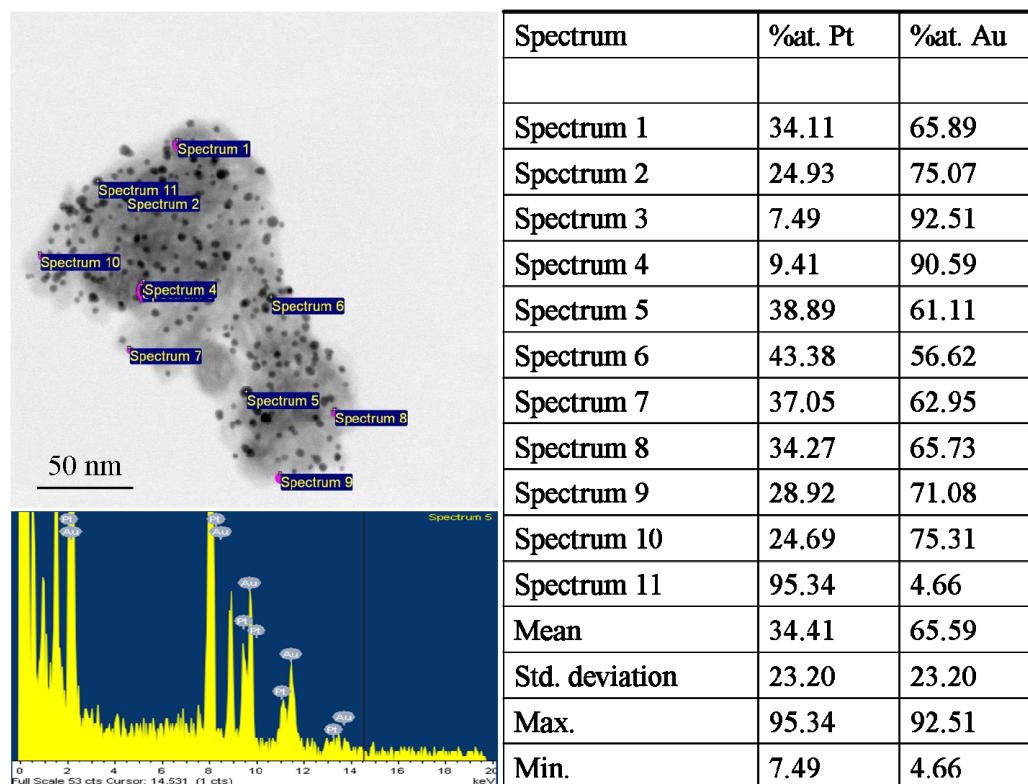


Figure A4.4. STEM-EDS point analysis of 10 randomly chosen Au@Pt NPs supported on γ -Al₂O₃ after conditioning at 200 °C for several hours under PROX reaction. Representative EDS spectrum of the particle 5 is shown below STEM image. Table shows particle composition, and statistical parameters.

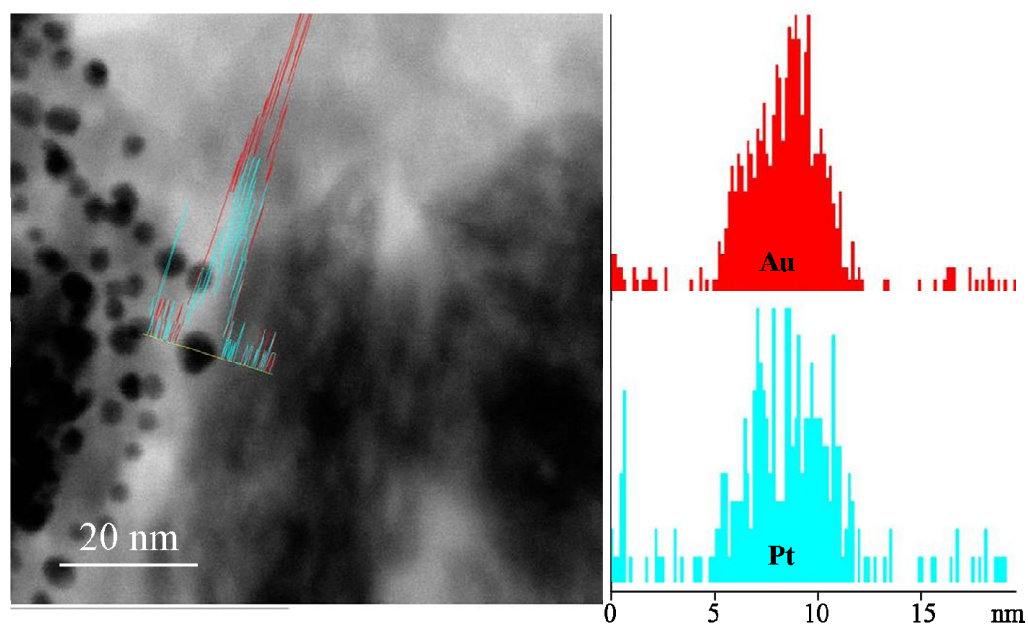


Figure A4.5. Representative STEM-EDS line spectrum of a ~ 3.5 nm Au@Pt NP with ~ 2.5 nm Au core and 1-2 MLs thick Pt shells. Relative atomic % composition (vertical axis) of Au (red) and Pt (blue) are plotted against the line scan probe position (horizontal axis) and are given next to STEM image. A 1.0 nm probe was used to trace 15 – 20 nm scans across each particle. The particle center is at ~ 7 nm.

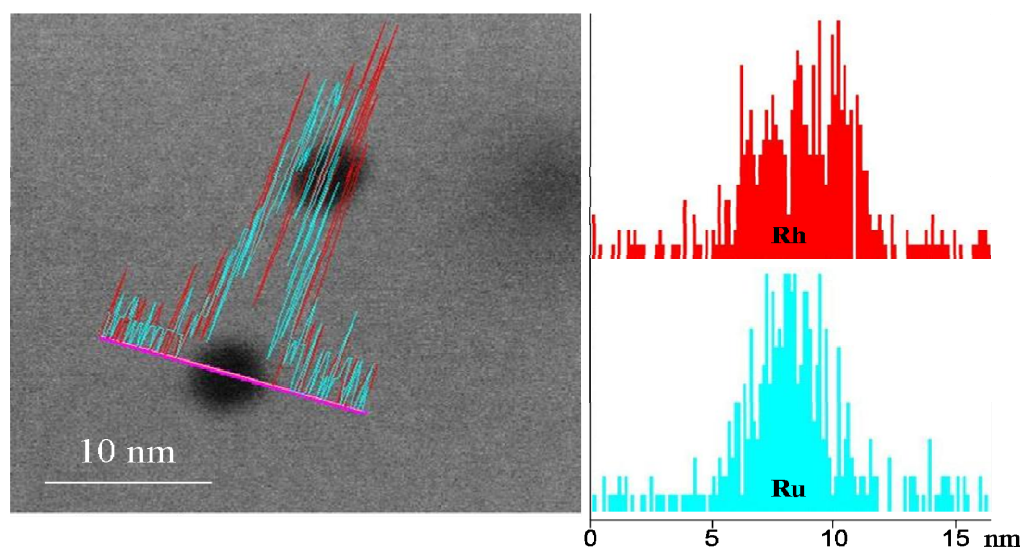


Figure A4.6. Representative STEM-EDS line spectra of a 4.3 nm Ru@Rh NP with 3.0 nm Ru core and 2-3 MLs thick Rh shells. Relative atomic % composition (vertical axis) of Ru (blue) and Rh (red) are plotted against the line scan probe position (horizontal axis) and are given next to STEM images. A 1.5 nm probe was used to trace 15 – 20 nm scans across each particle. The particle center is at ~ 8 nm.

Micro-Raman was employed to investigate the presence of metal-oxide phonon modes in metallic Ru@M NPs. All metals, including Pt group metals, are susceptible to surface oxidation. Therefore the surface metal structure can be monitored by the Raman shift(s) for the metal-oxide stretchings. The observed shifts in the $\nu(\text{M-O})_s$, as well as the $\nu(\text{Ru-O})_s$, of the respective Ru@M NPs compared to those of pure metal NPs were in favor of the core shell formation. Below, the reader will find the details of these micro-structural analyses.

It is expected that the identity of the surface metal atom for the core/shell materials can be monitored via their Raman signatures. The monometallic Pt NPs exhibit

no Raman signal. Ru NPs show three signals: 510 cm^{-1} , 626 cm^{-1} , and 691 cm^{-1} . They are the same Raman-active stretchings as the single-crystal rutile RuO_2 with D_{4h} point symmetry would exhibit.^{237,238} They are assigned to phonon modes for Ru-O with symmetries;^{237,238} E_g , A_{1g} , and B_{2g} respectively (Figure A4.7a). On the other hand, XRD exhibits no rutile RuO_2 phase, but this does not rule out amorphous RuO_2 formation, and indeed explains the low degree of crystallinity in case of Ru NPs (see Figure 4.9, see also Chapter 2). The Raman signals are also red shifted by 20 cm^{-1} with respect to the literature values reported by Katiyar et al. for 800 nm thick RuO_2 film.²³⁷ The nanostructure of the particles accounts for the observed red shifts.²³⁸ It can also be explained using a molecular orbital model that suggests a decrease in Ru-O bond order with an increase in metallic state. On the basis of the present data, as-synthesized Ru NPs are believed to have the Ru@RuO_{2-x} structure. Ru@Pt NPs exhibit identical signals to as-synthesized Ru NPs. However, a closer look at the spectrum reveals spectroscopic signatures of the core/shell architecture. Firstly, the Raman signals for rutile RuO_2 phase are further shifted red by ca. 10 cm^{-1} , which suggests a more metallic character for the Ru cores upon Pt deposition. This argument is also in agreement with EXAFS and PDF results (see Chapter 2, sections 2.3.4.2 and 2.3.4.3) showing the presence of metallic Ru core with short range order and no/little RuO_2 contribution to the nearest neighbor interactions. Secondly, a shoulder appears at ca. 580 cm^{-1} , which is concurrently assigned to amorphous PtO_2 .²³⁹ In addition to Micro-Raman observation of amorphous PtO_2 , EXAFS at Pt L edge reveals the contribution to the nearest neighbor interactions from PtO_2 phase, and thus completes the structural analysis of the Ru@Pt core/shell NPs.

Similarly, other Ru@M (M=Rh and Pd) NPs exhibit the metal-oxide phonon modes. Micro-Raman spectrum of Ru@Rh NPs show signals at 278 cm⁻¹, 422 cm⁻¹ and 568 cm⁻¹, which are shifted blue by ca. 8 cm⁻¹ relative to monometallic Rh NPs and shifted red by 2-12 cm⁻¹ relative to the bulk Rh₂O₃ (Figure A4.7a).^{240,241} The peak at 278 cm⁻¹ is assigned to bending $\nu(\text{Rh-O})$,²⁴⁰ and the peaks at 422 cm⁻¹ and 568 cm⁻¹ to symmetric and asymmetric $\nu(\text{Rh-O})_s$,²⁴¹ respectively, of Rh₂O₃. The single weak signal at 530 cm⁻¹, and the broad asymmetric feature at 610-740 cm⁻¹ range are assigned to rutile RuO₂. The signals for rutile RuO₂ phase is shifted blue by ca. 20 cm⁻¹ relative to monometallic Ru NPs. The 530 cm⁻¹ peak is only observed for Ru@Rh NPs along with other rutile signals and not for monometallic Rh NPs, so that it is attributed to rutile RuO₂, and not to amorphous Rh₂O₃.

Finally, Ru@Pd NPs exhibit signals at 274 cm⁻¹ and 329 cm⁻¹, which are reported to arise from second order (two phonon) scattering,²⁴² 405 cm⁻¹ and 626 cm⁻¹, which are assigned to E_g and B_{1g} phonon modes of PdO,²⁴² and 505 cm⁻¹, ~600 cm⁻¹ and 695 cm⁻¹ for rutile RuO₂. The $\nu(\text{Pd-O})$ peaks are shifted red by 10 cm⁻¹ with respect to those of ca. 6.0 nm Pd NPs, and 25-40 cm⁻¹ red relative to single crystal PdO.²⁴² The $\nu(\text{Ru-O})$ peaks are shifted by 5 cm⁻¹ red relative to those of 3.0 nm Ru NPs. The magnitudes of phonon shifts are less, and the directions opposite compared to Ru@Rh NPs (Figure A4.7a). Figure A4.7a also shows the Ru@Pt@Pd NPs with sandwiched Pt layers at sub-monolayer coverages and ca. 1-2 MLs thick Pd shell. They exhibit a metal-oxide spectrum which looks as if those of the parent 3.7 nm Ru@Pt particles with Pt shells at sub-monolayer coverages with peaks of pure Pd NPs superimposed. The $\nu(\text{Ru-O})_s$ are shifted to red by ca. 10 cm⁻¹ with no pronounced intensity drop as opposed to the

4.5 nm Ru@Pd particles with ca. 1-2 MLs thick Pd shells. The $\nu(\text{Pd-O})$ is slightly red shifted, but its magnitude is less than that of the 4.5 nm Ru@Pd particles with ca. 1-2 MLs thick Pd shells (Figure A4.7b).

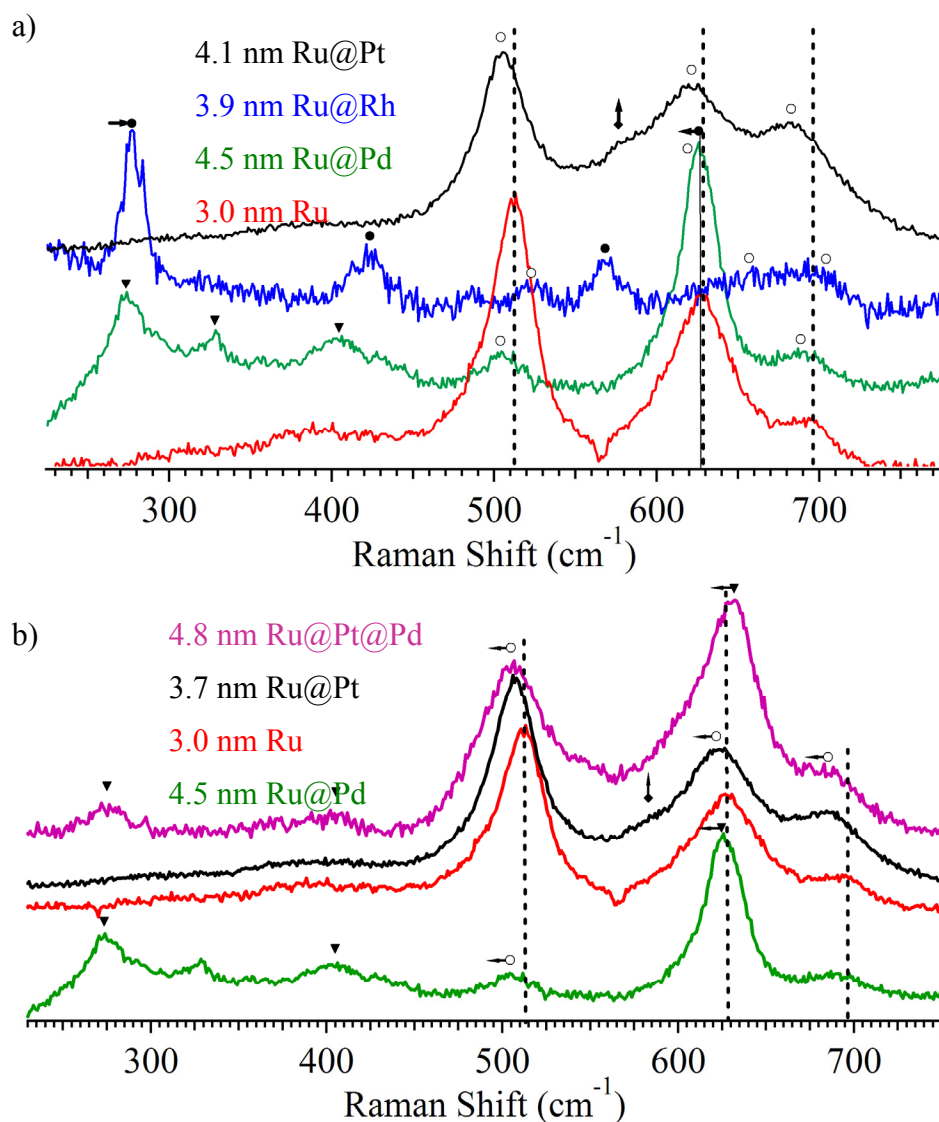


Figure A4.7. Micro-Raman spectra showing $\nu(\text{M-O})\text{s}$ ($\text{M}=\text{Ru}$, Rh , Pd and Pt) of (a) the Ru@M NPs with ca. 1-2 MLs thick M shells and (b) the 4.8 nm Ru@Pt@Pd particles with sandwiched layer of Pt at sub-monolayer coverage and ca. 1-2 MLs thick Pd shells, the parent 3.7 nm Ru@Pt particles and the 4.5 nm Ru@Pd NPs with ca. 1-2 MLs thick Pd shells. Dashed lines mark the positions of Raman active $\nu(\text{Ru-O})\text{s}$ of as-synthesized Ru NPs. ○ marks the $\nu(\text{Ru-O})\text{s}$ in the respective bimetallic NP systems, ● the $\nu(\text{Rh-O})\text{s}$ in the Ru@Rh NPs, ▼ the $\nu(\text{Pd-O})\text{s}$ in the Ru@Pd NPs and ◆ the single $\nu(\text{Pt-O})$ at ca. 590 cm^{-1} . (←, →) arrows show the direction of shifts in $\nu(\text{M-O})\text{s}$ of the bimetallic NPs relative to those of the monometallic NPs.

References

- (1) Proffen, T.; Neder, R. B. *J Appl Crystallogr* **1997**, *30*, 171-175.
- (2) Otsuka, H.; Nagasaki, Y.; Kataoka, K. *Advanced Drug Delivery Reviews* **2003**, *55*, 403-419.
- (3) Mornet, S.; Vasseur, S.; Grasset, F.; Duguet, E. *Journal Of Materials Chemistry* **2004**, *14*, 2161-2175.
- (4) Kovtyukhova, N. I.; Mallouk, T. E. *Chemistry-A European Journal* **2002**, *8*, 4355-4363.
- (5) Feldheim, D. L.; Keating, C. D. *Chemical Society Reviews* **1998**, *27*, 1-12.
- (6) Barnes, W. L.; Dereux, A.; Ebbesen, T. W. *Nature* **2003**, *424*, 824-830.
- (7) Sun, S. H. *Advanced Materials* **2006**, *18*, 393-403.
- (8) Stavroyiannis, S.; Panagiotopoulos, I.; Niarchos, D.; Christodoulides, J. A.; Zhang, Y.; Hadjipanayis, G. C. *Applied Physics Letters* **1998**, *73*, 3453-3455.
- (9) Alivisatos, A. P. *Science* **1996**, *271*, 933-937.
- (10) Mullin, J. W. *Crystallization*; 4th ed.; Reed Educational and Professional Publishing: Oxford, 2001.
- (11) Yin, Y.; Alivisatos, A. P. *Nature* **2005**, *437*, 664-670.
- (12) Milliron, D. J.; Hughes, S. M.; Cui, Y.; Manna, L.; Li, J. B.; Wang, L. W.; Alivisatos, A. P. *Nature* **2004**, *430*, 190-195.
- (13) Hyeon, T.; Lee, S. S.; Park, J.; Chung, Y.; Bin Na, H. *Journal Of The American Chemical Society* **2001**, *123*, 12798-12801.
- (14) Jana, N. R.; Chen, Y. F.; Peng, X. G. *Chemistry Of Materials* **2004**, *16*, 3931-3935.

- (15) O'Brien, S.; Brus, L.; Murray, C. B. *Journal Of The American Chemical Society* **2001**, *123*, 12085-12086.
- (16) Colvin, V. L.; Schlamp, M. C.; Alivisatos, A. P. *Nature* **1994**, *370*, 354-357.
- (17) Peng, X. G.; Schlamp, M. C.; Kadavanich, A. V.; Alivisatos, A. P. *Journal Of The American Chemical Society* **1997**, *119*, 7019-7029.
- (18) Peng, Z. A.; Peng, X. G. *Journal Of The American Chemical Society* **2001**, *123*, 183-184.
- (19) Caseri, W. *Macromolecular Rapid Communications* **2000**, *21*, 705-722.
- (20) Zamborini, F. P.; Leopold, M. C.; Hicks, J. F.; Kulesza, P. J.; Malik, M. A.; Murray, R. W. *Journal Of The American Chemical Society* **2002**, *124*, 8958-8964.
- (21) Pallassana, V.; Neurock, M. *Journal Of Catalysis* **2000**, *191*, 301-317.
- (22) Schulz, J.; Roucoux, A.; Patin, H. *Chem-Eur J* **2000**, *6*, 618-624.
- (23) Su, F. B.; Lv, L.; Lee, F. Y.; Liu, T.; Cooper, A. I.; Zhao, X. S. *Journal Of The American Chemical Society* **2007**, *129*, 14213-14223.
- (24) Ohde, H.; Ohde, M.; Wai, C. *Abstr Pap Am Chem S* **2002**, *223*, U675-U675.
- (25) Jenewein, B.; Fuchs, M.; Hayek, K. *Surf Sci* **2003**, *532*, 364-369.
- (26) Mu, X. D.; Meng, J. Q.; Li, Z. C.; Kou, Y. *J Am Chem Soc* **2005**, *127*, 9694-9695.
- (27) Besenbacher, F.; Chorkendorff, I.; Clausen, B. S.; Hammer, B.; Molenbroek, A. M.; Norskov, J. K.; Stensgaard, I. *Science* **1998**, *279*, 1913-1915.

- (28) Haga, F.; Nakajima, T.; Miya, H.; Mishima, S. *Catalysis Letters* **1997**, *48*, 223-227.
- (29) Sekizawa, K.; Yano, S.; Eguchi, K.; Arai, H. *Appl Catal a-Gen* **1998**, *169*, 291-297.
- (30) Velu, S.; Suzuki, K.; Okazaki, M.; Kapoor, M. P.; Osaki, T.; Ohashi, F. *J Catal* **2000**, *194*, 373-384.
- (31) Knudsen, J.; Nilekar, A. U.; Vang, R. T.; Schnadt, J.; Kunkes, E. L.; Dumesic, J. A.; Mavrikakis, M.; Besenbacher, F. *Journal Of The American Chemical Society* **2007**, *129*, 6485-6490.
- (32) Burch, R.; Shestov, A. A.; Sullivan, J. A. *J Catal* **1999**, *186*, 353-361.
- (33) Lyman, C. E.; Lakis, R. E.; Stenger, H. G. *Ultramicroscopy* **1995**, *58*, 25-34.
- (34) Zhou, S. H.; Varughese, B.; Eichhorn, B.; Jackson, G.; McIlwrath, K. *Angew Chem Int Edit* **2005**, *44*, 4539-4543.
- (35) Minemura, Y.; Ito, S.; Miyao, T.; Naito, S.; Tomishige, K.; Kunimori, K. *Chemical Communications* **2005**, 1429-1431.
- (36) Chin, S. Y.; Alexeev, O. S.; Amiridis, M. D. *J Catal* **2006**, *243*, 329-339.
- (37) Pozdnyakova, O.; Teschner, D.; Wootsch, A.; Krohnert, J.; Steinhauer, B.; Sauer, H.; Toth, L.; Jentoft, F. C.; Knop-Gericke, A.; Paal, Z.; Schlögl, R. *J Catal* **2006**, *237*, 1-16.
- (38) Wee, J. H.; Lee, K. Y. *Journal of Power Sources* **2006**, *157*, 128-135.
- (39) Li, Q. F.; He, R. H.; Gao, J. A.; Jensen, J. O.; Bjerrum, N. J. *J Electrochem Soc* **2003**, *150*, A1599-a1605.

- (40) Camara, G. A.; Ticianelli, E. A.; Mukerjee, S.; Lee, S. J.; McBreen, J. *J Electrochem Soc* **2002**, *149*, A748-a753.
- (41) Igarashi, H.; Fujino, T.; Zhu, Y. M.; Uchida, H.; Watanabe, M. *Phys Chem Chem Phys* **2001**, *3*, 306-314.
- (42) Oetjen, H. F.; Schmidt, V. M.; Stimming, U.; Trila, F. *J Electrochem Soc* **1996**, *143*, 3838-3842.
- (43) Gasteiger, H. A.; Markovic, N. M.; Ross, P. N. *J Phys Chem-US* **1995**, *99*, 8290-8301.
- (44) Gasteiger, H. A.; Markovic, N. M.; Ross, P. N. *Journal of Physical Chemistry* **1995**, *99*, 16757-16767.
- (45) Watanabe, M.; Motoo, S. *J Electroanal Chem* **1975**, *60*, 275-283.
- (46) Watanabe, M.; Motoo, S. *J Electroanal Chem* **1975**, *60*, 267-273.
- (47) Markovic, N. M.; Gasteiger, H. A.; Ross, P. N.; Jiang, X. D.; Villegas, I.; Weaver, M. J. *Electrochim Acta* **1995**, *40*, 91-98.
- (48) Guo, Y. L.; Zheng, D. Q.; Liu, H. Y.; Friedrich, A.; Garche, J. *J New Mat Electr Sys* **2006**, *9*, 33-39.
- (49) Murray, C. B.; Kagan, C. R.; Bawendi, M. G. *Annual Review Of Materials Science* **2000**, *30*, 545-610.
- (50) Xiong, Y. J.; Washio, I.; Chen, J. Y.; Cai, H. G.; Li, Z. Y.; Xia, Y. N. *Langmuir* **2006**, *22*, 8563-8570.
- (51) Johnson, C. J.; Dujardin, E.; Davis, S. A.; Murphy, C. J.; Mann, S. *J Mater Chem* **2002**, *12*, 1765-1770.

- (52) Xiong, Y. J.; McLellan, J. M.; Chen, J. Y.; Yin, Y. D.; Li, Z. Y.; Xia, Y. N. *Journal Of The American Chemical Society* **2005**, *127*, 17118-17127.
- (53) Borodko, Y.; Humphrey, S. M.; Tilley, T. D.; Frei, H.; Somorjai, G. A. *J Phys Chem C* **2007**, *111*, 6288-6295.
- (54) Watzky, M. A.; Finke, R. G. *Journal Of The American Chemical Society* **1997**, *119*, 10382-10400.
- (55) Sugimoto, T. *Journal of Colloid and Interface Science* **2007**, *309*, 106-118.
- (56) Kwon, S. G.; Piao, Y.; Park, J.; Angappane, S.; Jo, Y.; Hwang, N. M.; Park, J. G.; Hyeon, T. *Journal of the American Chemical Society* **2007**, *129*, 12571-12584.
- (57) Kuo, C. H.; Chiang, T. F.; Chen, L. J.; Huang, M. H. *Langmuir* **2004**, *20*, 7820-7824.
- (58) He, B. L.; Chen, Y. X.; Liu, H. F.; Liu, Y. *J Nanosci Nanotechno* **2005**, *5*, 266-270.
- (59) Fleming, D. A.; Williams, M. E. *Langmuir* **2004**, *20*, 3021-3023.
- (60) Zhang, Y. W.; Grass, M. E.; Habas, S. E.; Tao, F.; Zhang, T. F.; Yang, P. D.; Somorjai, G. A. *J Phys Chem C* **2007**, *111*, 12243-12253.
- (61) Tao, A. R.; Habas, S.; Yang, P. D. *Small* **2008**, *4*, 310-325.
- (62) Zhao, J.; Chen, W. X.; Zheng, Y. F.; Li, X.; Xu, Z. D. *J Mater Sci* **2006**, *41*, 5514-5518.
- (63) Chen, J. Y.; Herricks, T.; Xia, Y. N. *Angew Chem Int Edit* **2005**, *44*, 2589-2592.

- (64) Herricks, T.; Chen, J. Y.; Xia, Y. N. *Nano Lett* **2004**, *4*, 2367-2371.
- (65) Bock, C.; Paquet, C.; Couillard, M.; Botton, G. A.; MacDougall, B. R. *J Am Chem Soc* **2004**, *126*, 8028-8037.
- (66) Jin, S. M.; Yuan, L. S.; Zhou, Y.; Qiu, G. Z.; Wan, C. F. *Materials Research Bulletin* **2006**, *41*, 2130-2136.
- (67) Kahlich, M. J.; Gasteiger, H. A.; Behm, R. J. *J Catal* **1997**, *171*, 93-105.
- (68) Pozdnyakova, O.; Teschner, D.; Wootsch, A.; Krohnert, J.; Steinhauer, B.; Sauer, H.; Toth, L.; Jentoft, F. C.; Knop-Gericke, A.; Paal, Z.; Schlogl, R. *J Catal* **2006**, *237*, 17-28.
- (69) Fonseca, G. S.; Umpierre, A. P.; Fichtner, P. F. P.; Teixeira, S. R.; Dupont, J. *Chem-Eur J* **2003**, *9*, 3263-3269.
- (70) Park, K. H.; Jang, K.; Kim, H. J.; Son, S. U. *Angew Chem Int Edit* **2007**, *46*, 1152-1155.
- (71) Bell, A. T. *Science* **2003**, *299*, 1688-1691.
- (72) Roucoux, A.; Schulz, J.; Patin, H. *Adv Synth Catal* **2003**, *345*, 222-229.
- (73) Schulz, E.; Levigne, S.; Roucoux, A.; Patin, H. *Adv Synth Catal* **2002**, *344*, 266-269.
- (74) Ohde, M.; Ohde, H.; Wai, C. M. *Chem Commun* **2002**, 2388-2389.
- (75) Fonseca, G. S.; Domingos, J. B.; Nome, F.; Dupont, J. *Journal Of Molecular Catalysis A-Chemical* **2006**, *248*, 10-16.
- (76) Pillai, U. R.; Sahle-Demessie, E. *Journal Of Molecular Catalysis A-Chemical* **2004**, *222*, 153-158.

- (77) Qi, Z. G.; He, C. Z.; Kaufman, A. *Journal Of Power Sources* **2002**, *111*, 239-247.
- (78) Schmidt, T. J.; Gasteiger, H. A.; Behm, R. J. *J Electrochem Soc* **1999**, *146*, 1296-1304.
- (79) Bratlie, K. M.; Kliewer, C. J.; Somorjai, G. A. *J Phys Chem B* **2006**, *110*, 17925-17930.
- (80) Bratlie, K. M.; Lee, H.; Komvopoulos, K.; Yang, P. D.; Somorjai, G. A. *Nano Letters* **2007**, *7*, 3097-3101.
- (81) Grass, M. E.; Yue, Y.; Habas, S. E.; Rioux, R. M.; Teall, C. I.; Yang, P.; Somorjai, G. A. *Journal Of Physical Chemistry C* **2008**, *112*, 4797-4804.
- (82) Reynolds, P. W. *Journal Of The Chemical Society* **1950**, 265-271.
- (83) Massalski, T. B.; Murray, J. L.; Bennett, L. H.; Baker, H. *Binary Alloy Phase Diagram*; American Society for Metals, 1986; Vol. 1.
- (84) Hills, C. W.; Mack, N. H.; Nuzzo, R. G. *Journal Of Physical Chemistry B* **2003**, *107*, 2626-2636.
- (85) Park, J. I.; Kim, M. G.; Jun, Y. W.; Lee, J. S.; Lee, W. R.; Cheon, J. *Journal Of The American Chemical Society* **2004**, *126*, 9072-9078.
- (86) Hwang, B. J.; Sarma, L. S.; Chen, J. M.; Chen, C. H.; Shih, S. C.; Wang, G. R.; Liu, D. G.; Lee, J. F.; Tang, M. T. *Journal Of The American Chemical Society* **2005**, *127*, 11140-11145.
- (87) Harada, M.; Asakura, K.; Toshima, N. *Journal Of Physical Chemistry* **1993**, *97*, 5103-5114.

- (88) Teng, X. W.; Wang, Q.; Liu, P.; Han, W.; Frenkel, A.; Wen, W.; Marinkovic, N.; Hanson, J. C.; Rodriguez, J. A. *Journal of the American Chemical Society* **2008**, *130*, 1093-1101.
- (89) Campbell, C. T. *Annu Rev Phys Chem* **1990**, *41*, 775-837.
- (90) Greeley, J.; Mavrikakis, M. *Nat Mater* **2004**, *3*, 810-815.
- (91) Baletto, F.; Mottet, C.; Ferrando, R. *Physical Review Letters* **2003**, *90*, 135504.
- (92) Schmid, G. *Nanostructured Materials* **1995**, *6*, 15-24.
- (93) Wang, Y.; Toshima, N. *J Phys Chem B* **1997**, *101*, 5301-5306.
- (94) Gu, H. W.; Yang, Z. M.; Gao, J. H.; Chang, C. K.; Xu, B. *Journal Of The American Chemical Society* **2005**, *127*, 34-35.
- (95) Zhou, S. G.; McIlwrath, K.; Jackson, G.; Eichhorn, B. *J Am Chem Soc* **2006**, *128*, 1780-1781.
- (96) Liu, H. B.; Pal, U.; Medina, A.; Maldonado, C.; Ascencio, J. A. *Physical Review B* **2005**, *71*.
- (97) Ziman, J. M. *The Physics of Metals 1. Electrons*; Cambridge University Press: Cambridge, 1969.
- (98) Zhou, S. H.; Jackson, G. S.; Eichhorn, B. *Adv Funct Mater* **2007**, *17*, 3099-3104.
- (99) Schlapka, A.; Lischka, M.; Gross, A.; Kasberger, U.; Jakob, P. *Phys Rev Lett* **2003**, *91*, -.
- (100) Fan, F. R.; Liu, D. Y.; Wu, Y. F.; Duan, S.; Xie, Z. X.; Jiang, Z. Y.; Tian, Z. Q. *Journal Of The American Chemical Society* **2008**, *130*, 6949-+.

- (101) Mavrikakis, M.; Hammer, B.; Norskov, J. K. *Physical review letters* **1998**, *81*, 2819-2822.
- (102) Greeley, J.; Kreckelberg, W. R.; Mavrikakis, M. *Angew Chem Int Edit* **2004**, *43*, 4296-4300.
- (103) Jakob, P.; Schlapka, A. *SURF SCI* **2007**, *601*, 3556-3568.
- (104) Campbell, R. A.; Rodriguez, J. A.; Goodman, D. W. *PHYS REV B* **1992**, *46*, 7077-7087.
- (105) Lim, B.; Wang, J. G.; Camargo, P. H. C.; Jiang, M. J.; Kim, M. J.; Xia, Y. N. *Nano Letters* **2008**, *8*, 2535-2540.
- (106) Yin, Y. D.; Rioux, R. M.; Erdonmez, C. K.; Hughes, S.; Somorjai, G. A.; Alivisatos, A. P. *Science* **2004**, *304*, 711-714.
- (107) Chou, N. H.; Schaak, R. E. *Chemistry Of Materials* **2008**, *20*, 2081-2085.
- (108) Habas, S. E.; Lee, H.; Radmilovic, V.; Somorjai, G. A.; Yang, P. *Nature Materials* **2007**, *6*, 692-697.
- (109) Tao, F.; Grass, M. E.; Zhang, Y. W.; Butcher, D. R.; Renzas, J. R.; Liu, Z.; Chung, J. Y.; Mun, B. S.; Salmeron, M.; Somorjai, G. A. *Science* **2008**, *322*, 932-934.
- (110) Martin, T. P.; Bergmann, T.; Gohlich, H.; Lange, T. *Journal of Physical Chemistry* **1991**, *95*, 6421-6429.
- (111) Schmid, G. *Chemical Reviews* **1992**, *92*, 1709-1727.
- (112) Aiken, J. D.; Finke, R. G. *J Mol Catal a-Chem* **1999**, *145*, 1-44.
- (113) Chen, Y. M.; Yang, F.; Dai, Y.; Wang, W. Q.; Chen, S. L. *Journal of Physical Chemistry C* **2008**, *112*, 1645-1649.

- (114) Garcia-Gutierrez, D. I.; Gutierrez-Wing, C. E.; Giovanetti, L.; Ramallo-Lopez, J. M.; Requejo, F. G.; Jose-Yacaman, M. *J Phys Chem B* **2005**, *109*, 3813-3821.
- (115) Park, J. I.; Cheon, J. *Journal Of The American Chemical Society* **2001**, *123*, 5743-5746.
- (116) Chou, N. H.; Schaak, R. E. *Journal Of The American Chemical Society* **2007**, *129*, 7339-7345.
- (117) Farrow, C. L.; Juhas, P.; Liu, J. W.; Bryndin, D.; Bozin, E. S.; Bloch, J.; Proffen, T.; Billinge, S. J. L. *J Phys-Condens Mat* **2007**, *19*, -.
- (118) Hills, C. W.; Nashner, M. S.; Frenkel, A. I.; Shapley, J. R.; Nuzzo, R. G. *Langmuir* **1999**, *15*, 690-700.
- (119) Nashner, M. S.; Frenkel, A. I.; Adler, D. L.; Shapley, J. R.; Nuzzo, R. G. *Journal Of The American Chemical Society* **1997**, *119*, 7760-7771.
- (120) Nashner, M. S.; Frenkel, A. I.; Somerville, D.; Hills, C. W.; Shapley, J. R.; Nuzzo, R. G. *Journal Of The American Chemical Society* **1998**, *120*, 8093-8101.
- (121) Lewera, A.; Zhou, W. P.; Hunger, R.; Jaegermann, W.; Wieckowski, A.; Yockel, S.; Bagus, P. S. *CHEM PHYS LETT* **2007**, *447*, 39-43.
- (122) Blyholder, G. *J Phys Chem-Us* **1964**, *68*, 2772-&.
- (123) Pan, C.; Dassenoy, F.; Casanove, M. J.; Philippot, K.; Amiens, C.; Lecante, P.; Mosset, A.; Chaudret, B. *Journal of Physical Chemistry B* **1999**, *103*, 10098-10101.
- (124) Dassenoy, F.; Casanove, M. J.; Lecante, P.; Pan, C.; Philippot, K.; Amiens, C.; Chaudret, B. *Phys Rev B* **2001**, *63*, -.

- (125) Ha, T. H.; Koo, H. J.; Chung, B. H. *Journal Of Physical Chemistry C* **2007**, *111*, 1123-1130.
- (126) Garcia-Gutierrez, D.; Gutierrez-Wing, C.; Miki-Yoshida, M.; Jose-Yacaman, M. *Appl Phys a-Mater* **2004**, *79*, 481-487.
- (127) Rodriguez, J. A.; Campbell, R. A.; Goodman, D. W. *J PHYS CHEM-US* **1990**, *94*, 6936-6939.
- (128) Rodriguez, J. A.; Campbell, R. A.; Goodman, D. W. *J VAC SCI TECHNOL A* **1991**, *9*, 1698-1702.
- (129) Rodriguez, J. A.; Campbell, R. A.; Goodman, D. W. *J PHYS CHEM-US* **1991**, *95*, 5716-5719.
- (130) Rodriguez, J. A.; Goodman, D. W. *Science* **1992**, *257*, 897-903.
- (131) Rodriguez, J. A.; Goodman, D. W. *J PHYS CHEM-US* **1991**, *95*, 4196-4206.
- (132) Hammer, B.; Morikawa, Y.; Norskov, J. K. *Phys Rev Lett* **1996**, *76*, 2141-2144.
- (133) Hammer, B.; Norskov, J. K. *SURF SCI* **1995**, *343*, 211-220.
- (134) Pallassana, V.; Neurock, M.; Hansen, L. B.; Norskov, J. K. *J Chem Phys* **2000**, *112*, 5435-5439.
- (135) Koper, M. T. M.; Shubina, T. E.; van Santen, R. A. *Journal Of Physical Chemistry B* **2002**, *106*, 686-692.
- (136) Ge, Q.; Desai, S.; Neurock, M.; Kourtakis, K. *Journal Of Physical Chemistry B* **2001**, *105*, 9533-9536.

- (137) Greeley, J.; Mavrikakis, M. *Journal Of Physical Chemistry B* **2005**, *109*, 3460-3471.
- (138) Stamenkovic, V. R.; Mun, B. S.; Arenz, M.; Mayrhofer, K. J. J.; Lucas, C. A.; Wang, G. F.; Ross, P. N.; Markovic, N. M. *Nat Mater* **2007**, *6*, 241-247.
- (139) Neurock, M. *Journal Of Catalysis* **2003**, *216*, 73-88.
- (140) Carrette, L.; Friedrich, K. A.; Stimming, U. *Chemphyschem* **2000**, *1*, 162-193.
- (141) Huber, G. W.; Shabaker, J. W.; Dumesic, J. A. *Science* **2003**, *300*, 2075-2077.
- (142) Maroun, F.; Ozanam, F.; Magnussen, O. M.; Behm, R. J. *Science* **2001**, *293*, 1811-1814.
- (143) Enache, D. I.; Edwards, J. K.; Landon, P.; Solsona-Espriu, B.; Carley, A. F.; Herzing, A. A.; Watanabe, M.; Kiely, C. J.; Knight, D. W.; Hutchings, G. J. *Science* **2006**, *311*, 362-365.
- (144) Linic, S.; Jankowiak, J.; Barteau, M. A. *Journal of catalysis* **2004**, *224*, 489-493.
- (145) Zhang, J. L.; Vukmirovic, M. B.; Sasaki, K.; Nilekar, A. U.; Mavrikakis, M.; Adzic, R. R. *Journal of the American Chemical Society* **2005**, *127*, 12480-12481.
- (146) Greeley, J.; Jaramillo, T. F.; Bonde, J.; Chorkendorff, I. B.; Norskov, J. K. *Nature Materials* **2006**, *5*, 909-913.
- (147) Wintterlin, J.; Volkening, S.; Janssens, T. V. W.; Zambelli, T.; Ertl, G. *Science* **1997**, *278*, 1931-1934.

- (148) Yoon, B.; Hakkinen, H.; Landman, U.; Worz, A. S.; Antonietti, J. M.; Abbet, S.; Judai, K.; Heiz, U. *Science* **2005**, *307*, 403-407.
- (149) Tripa, C. E.; Yates, J. T. *Nature* **1999**, *398*, 591-593.
- (150) Zambelli, T.; Barth, J. V.; Wintterlin, J.; Ertl, G. *Nature* **1997**, *390*, 495-497.
- (151) Greeley, J.; Mavrikakis, M. *Catalysis Today* **2006**, *111*, 52-58.
- (152) Brankovic, S. R.; Wang, J. X.; Adzic, R. R. *Electrochemical and Solid State Letters* **2001**, *4*, A217-220.
- (153) Diemant, T.; Hager, T.; Hoster, H. E.; Rauscher, H.; Behm, R. J. *Surface Science* **2003**, *541*, 137-146.
- (154) Lu, C.; Rice, C.; Masel, R. I.; Babu, P. K.; Waszczuk, P.; Kim, H. S.; Oldfield, E.; Wieckowski, A. *Journal of Physical Chemistry B* **2002**, *106*, 9581-9589.
- (155) Gasteiger, H. A.; Markovic, N. M.; Ross, P. N. *Journal of Physical Chemistry* **1995**, *99*, 8945-8949.
- (156) Grgur, B. N.; Zhuang, G.; Markovic, N. M.; Ross, P. N. *Journal of Physical Chemistry B* **1997**, *101*, 3910-3913.
- (157) Lewera, A.; Zhou, W. P.; Vericat, C.; Chung, J. H.; Haasch, R.; Wieckowski, A.; Bagus, P. S. *Electrochimica Acta* **2006**, *51*, 3950-3956.
- (158) Wang, J. X. *Journal of the Electrochemical Society* **2003**, *150*, A1108.
- (159) Guo, J. S.; Sun, G.; Sun, S. G.; Yan, S. Y.; Yang, W. Q.; Qi, J.; Yan, Y. S.; Xin, Q. *J Power Sources* **2007**, *168*, 299-306.
- (160) Liu, C.; Wu, X. W.; Klemmer, T.; Shukla, N.; Yang, X. M.; Weller, D.; Roy, A. G.; Tanase, M.; Laughlin, D. *J Phys Chem B* **2004**, *108*, 6121-6123.

- (161) Nagaveni, K.; Gayen, A.; Subbanna, G. N.; Hegde, M. S. *J Mater Chem* **2002**, *12*, 3147-3151.
- (162) Yan, S. Y.; Sun, G. Q.; Tian, J.; Jiang, L. H.; Qi, J.; Xin, Q. *Electrochim Acta* **2006**, *52*, 1692-1696.
- (163) Ren, J.; Tilley, R. D. *Small* **2007**, *3*, 1508-1512.
- (164) Viau, G.; Brayner, R.; Poul, L.; Chakroune, N.; Lacaze, E.; Fievet-Vincent, F.; Fievet, F. *Chem Mater* **2003**, *15*, 486-494.
- (165) Xiong, Y. J.; Chen, J. Y.; Wiley, B.; Xia, Y. N. *J Am Chem Soc* **2005**, *127*, 7332-7333.
- (166) Xiong, Y. J.; Xia, Y. N. *Adv Mater* **2007**, *19*, 3385-3391.
- (167) Bradley, J. S.; Hill, E. W.; Chaudret, B.; Duteil, A. *Langmuir* **1995**, *11*, 693-695.
- (168) Bradley, J. S.; Hill, E. W.; Behal, S.; Klein, C.; Chaudret, B.; Duteil, A. *Chem. Mat.* **1992**, *4*, 1234-1239.
- (169) Rodriguez, J. A.; Campbell, R. A.; Goodman, D. W. *SURF SCI* **1991**, *244*, 211-220.
- (170) Aleandri, L. E.; Bonnemann, H.; Jones, D. J.; Richter, J.; Roziere, J. *J Mater Chem* **1995**, *5*, 749-752.
- (171) Gilbert, B.; Huang, F.; Lin, Z.; Goodell, C.; Zhang, H. Z.; Banfield, J. F. *Nano Lett* **2006**, *6*, 605-610.
- (172) Masadeh, A. S.; Bozin, E. S.; Farrow, C. L.; Paglia, G.; Juhas, P.; Billinge, S. J. L.; Karkamkar, A.; Kanatzidis, M. G. *Phys Rev B* **2007**, *76*, -.

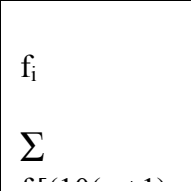
- (173) Juhas, P.; Cherba, D. M.; Duxbury, P. M.; Punch, W. F.; Billinge, S. J. L. *Nature* **2006**, *440*, 655-658.
- (174) Page, K.; Proffen, T.; Terrones, H.; Terrones, M.; Lee, L.; Yang, Y.; Stemmer, S.; Seshadri, R.; Cheetham, A. K. *Chem Phys Lett* **2004**, *393*, 385-388.
- (175) Hahn, T. *International Tables for Crystallography*; 2 ed.; Kluwer Academic Publishers: Dordrecht, 1989; Vol. A.
- (176) Alayoglu, S.; Nilekar, A. U.; Mavrikakis, M.; Eichhorn, B. *Nat Mater* **2008**, *7*, 333-338.
- (177) Greeley, J.; Norskov, J. K.; Mavrikakis, M. *Annu Rev Phys Chem* **2002**, *53*, 319-348.
- (178) Hammer, B.; Hansen, L. B.; Norskov, J. K. *Phys Rev B* **1999**, *59*, 7413-7421.
- (179) Neugebauer, J.; Scheffler, M. *Phys Rev B* **1992**, *46*, 16067-16080.
- (180) Swanson, T. National Bureau of Standards, 1953.
- (181) Pecharsky, V. *Fundamentals of Powder Diffraction and Structural Characterization of Material.*; Springer, Berlin, Germany: Germany, 2005.
- (182) Schlapka, A.; Lischka, M.; Gross, A.; Kasberger, U.; Jakob, P. *Physical review letters* **2003**, *91*, 0161011.
- (183) Bensebaa, F.; Patrino, N.; Le Page, Y.; L'Ecuyer, P.; Wang, D. S. *Journal of Materials Chemistry* **2004**, *14*, 3378-3384.
- (184) Liu, Z. F.; Ada, E. T.; Shamsuzzoha, M.; Thompson, G. B.; Nikles, D. E. *Chemistry of Materials* **2006**, *18*, 4946-4951.

- (185) Wells, A. F. *Structural Inorganic Chemistry*; 5 ed.; Oxford University Press: New York, 1984.
- (186) Toby, B. H. *J Appl Crystallogr* **2001**, *34*, 210-213.
- (187) Chin, S. Y.; Williams, C. T.; Amiridis, M. D. *Journal of Physical Chemistry B* **2006**, *110*, 871-882.
- (188) Dassenoy, F.; Casanove, M. J.; Lecante, P.; Pan, C.; Philippot, K.; Amiens, C.; Chaudret, B. *Physical Review B* **2001**, *63*, 235407.
- (189) German, E. D.; Sheintuch, M. *Journal Of Physical Chemistry C* **2008**, *112*, 14377-14384.
- (190) Koranyi, T. I.; Mihaly, J.; Pfeifer, E.; Nemeth, C.; Yuzhakova, T.; Mink, J. *Journal Of Physical Chemistry A* **2006**, *110*, 1817-1823.
- (191) Liu, Z. L.; Ling, X. Y.; Su, X. D.; Lee, J. Y. *Journal of Physical Chemistry B* **2004**, *108*, 8234-8240.
- (192) Tanaka, K. I.; Shou, M.; He, H.; Shi, X. Y. *Catalysis Letters* **2006**, *110*, 185-190.
- (193) Zhou, S. L.; Yuan, Z. S.; Wang, S. D. *International Journal of Hydrogen Energy* **2006**, *31*, 924-933.
- (194) Suh, D. J.; Kwak, C.; Kim, J. H.; Kwon, S. M.; Park, T. J. *Journal of power sources* **2005**, *142*, 70-74.
- (195) Davies, J. C.; Bonde, J.; Logadottir, A.; Norskov, J. K.; Chorkendorff, I. *Fuel Cells* **2005**, *5*, 429-435.
- (196) Vestergaard, E. K.; Thostrup, P.; An, T.; Laegsgaard, E.; Stensgaard, I.; Hammer, B.; Besenbacher, F. *Physical review letters* **2002**, *88*, 259601.

- (197) de Mongeot, F. B.; Scherer, M.; Gleich, B.; Kopatzki, E.; Behm, R. J. *Surface Science* **1998**, *411*, 249-262.
- (198) Shestov, A. A.; Burch, R.; Sullivan, J. A. *J Catal* **1999**, *186*, 362-372.
- (199) Bligaard, T.; Norskov, J. K.; Dahl, S.; Matthiesen, J.; Christensen, C. H.; Sehested, J. *J Catal* **2004**, *224*, 206-217.
- (200) Zahmakiran, M.; Ozkar, S. *Langmuir* **2008**, *24*, 7065-7067.
- (201) Burch, R.; Shestov, A. A.; Sullivan, J. A. *J Catal* **1999**, *188*, 69-82.
- (202) Tian, P.; Blanchard, J.; Fajerweg, K.; Breysse, M.; Vrinat, M.; Liu, Z. M. *Micropor Mesopor Mat* **2003**, *60*, 197-206.
- (203) Borodko, Y.; Habas, S. E.; Koebel, M.; Yang, P. D.; Frei, H.; Somorjai, G. A. *J Phys Chem B* **2006**, *110*, 23052-23059.
- (204) Park, J. Y.; Zhang, Y.; Grass, M.; Zhang, T.; Somorjai, G. A. *Nano Lett* **2008**, *8*, 673-677.
- (205) Humphrey, S. M.; Grass, M. E.; Habas, S. E.; Niesz, K.; Somorjai, G. A.; Tilley, T. D. *Nano Lett* **2007**, *7*, 785-790.
- (206) Hoefelmeyer, J. D.; Niesz, K.; Somorjai, G. A.; Tilley, T. D. *Nano Lett* **2005**, *5*, 435-438.
- (207) Lima, F. H. B.; Gonzalez, E. R. *Appl Catal B-Environ* **2008**, *79*, 341-346.
- (208) Bergounhou, C.; Blandy, C.; Choukroun, R.; Lecante, P.; Lorber, C.; Pellegatta, J. L. *New J Chem* **2007**, *31*, 218-223.
- (209) Harada, M.; Einaga, H. *J Colloid Interf Sci* **2007**, *308*, 568-572.
- (210) Pasztor, M.; Solymosi, F. *Magy Kem Foly* **1986**, *92*, 321-328.

- (211) Vantblik, H. F. J.; Vanzon, J. B. A. D.; Huizinga, T.; Vis, J. C.; Koningsberger, D. C.; Prins, R. *J Am Chem Soc* **1985**, *107*, 3139-3147.
- (212) Siepen, K.; Bonnemann, H.; Brijoux, W.; Rothe, J.; Hormes, J. *Appl Organomet Chem* **2000**, *14*, 549-556.
- (213) Bonnemann, H.; Britz, P.; Vogel, W. *Langmuir* **1998**, *14*, 6654-6657.
- (214) Reetz, M. T.; Winter, M.; Breinbauer, R.; Thurn-Albrecht, T.; Vogel, W. *Chem-Eur J* **2001**, *7*, 1084-1094.
- (215) Vogel, W. *Cryst Res Technol* **1998**, *33*, 1141-1154.
- (216) Roth, C.; Papworth, A. J.; Hussain, I.; Nichols, R. J.; Schiffrin, D. J. *J Electroanal Chem* **2005**, *581*, 79-85.
- (217) Norskov, J. K.; Bligaard, T.; Logadottir, A.; Bahn, S.; Hansen, L. B.; Bollinger, M.; Benggaard, H.; Hammer, B.; Sljivancanin, Z.; Mavrikakis, M.; Xu, Y.; Dahl, S.; Jacobsen, C. J. H. *J Catal* **2002**, *209*, 275-278.
- (218) Reddington, E.; Sapienza, A.; Gurau, B.; Viswanathan, R.; Sarangapani, S.; Smotkin, E. S.; Mallouk, T. E. *Science* **1998**, *280*, 1735-1737.
- (219) Pallassana, V.; Neurock, M.; Lusvardi, V. S.; Lerou, J. J.; Kragten, D. D.; van Santen, R. A. *J Phys Chem B* **2002**, *106*, 1656-1669.
- (220) Pallassana, V.; Neurock, M. *J Catal* **2002**, *209*, 289-305.
- (221) Sakai, T.; Alexandridis, P. *Journal Of Physical Chemistry B* **2005**, *109*, 7766-7777.
- (222) Ashida, T.; Miura, K.; Nomoto, T.; Yagi, S.; Sumida, H.; Kutluk, G.; Soda, K.; Namatame, H.; Taniguchi, M. *Surf Sci* **2007**, *601*, 3898-3901.

- (223) Hoefelmeyer, J. D.; Liu, H.; Somorjai, G. A.; Tilley, T. D. *J Colloid Interf Sci* **2007**, *309*, 86-93.
- (224) Ikeda, M.; Takeshima, S.; Tago, T.; Kishida, M.; Wakabayashi, K. *Catal Lett* **1999**, *58*, 195-197.
- (225) Lofton, C.; Sigmund, W. *Advanced Functional Materials* **2005**, *15*, 1197-1208.
- (226) Cao, L. Y.; Tong, L. M.; Diao, P.; Zhu, T.; Liu, Z. F. *Chemistry Of Materials* **2004**, *16*, 3239-3245.
- (227) Figuerola, A.; Fiore, A.; Di Corato, R.; Falqui, A.; Giannini, C.; Micotti, E.; Lascialfari, A.; Corti, M.; Cingolani, R.; Pellegrino, T.; Cozzoli, P. D.; Manna, L. *J Am Chem Soc* **2008**, *130*, 1477-1487.
- (228) Chen, W. X.; Zhao, J.; Lee, J. Y.; Liu, Z. L. *Chem Lett* **2004**, *33*, 474-475.
- (229) Campbell, R. A.; Rodriguez, J. A.; Goodman, D. W. *SURF SCI* **1991**, *256*, 272-280.
- (230) Kitchin, J. R.; Norskov, J. K.; Barteau, M. A.; Chen, J. G. *Phys Rev Lett* **2004**, *93*, -.
- (231) Solymosi, F.; Novak, E.; Molnar, A. *J Phys Chem-US* **1990**, *94*, 7250-7255.
- (232) Bertarione, S.; Scarano, D.; Zecchina, A.; Johaneck, V.; Hoffmann, J.; Schauermaun, S.; Frank, M. M.; Libuda, J.; Rupprechter, G.; Freund, H. J. *J Phys Chem B* **2004**, *108*, 3603-3613.
- (233) Borchert, H.; Jurgens, B.; Zielasek, V.; Rupprechter, G.; Giorgio, S.; Henry, C. R.; Baumer, M. *Journal Of Catalysis* **2007**, *247*, 145-154.



- (234) Bartholomew, C. H. *Appl Catal a-Gen* **2001**, *212*, 17-60.
- (235) Kitchin, J. R.; Norskov, J. K.; Barteau, M. A.; Chen, J. G. *J Chem Phys* **2004**, *120*, 10240-10246.
- (236) Du, Y. K.; Qiao, Y.; Zou, C.; Dai, J. T.; Yang, P. *Colloid and Polymer Science* **2007**, *285*, 553-556.
- (237) Bhaskar, S.; Dobal, P. S.; Majumder, S. B.; Katiyar, R. S. *J Appl Phys* **2001**, *89*, 2987-2992.
- (238) Chen, R. S.; Chen, C. C.; Huang, Y. S.; Chia, C. T.; Chen, H. P.; Tsai, D. S.; Tiong, K. K. *Solid State Commun* **2004**, *131*, 349-353.
- (239) McBride, J. R.; Graham, G. W.; Peters, C. R.; Weber, W. H. *J Appl Phys* **1991**, *69*, 1596-1604.
- (240) Zhang, Y.; Gao, X. P.; Weaver, M. J. *J Phys Chem-US* **1993**, *97*, 8656-8663.
- (241) Chan, H. Y. H.; Zou, S. Z.; Weaver, M. J. *J Phys Chem B* **1999**, *103*, 11141-11151.
- (242) McBride, J. R.; Hass, K. C.; Weber, W. H. *Phys Rev B* **1991**, *44*, 5016-5028.